Thilo Hauff

Transport of Energetic Particles in Turbulent Plasmas

2009

Transport of Energetic Particles in Turbulent Plasmas

Dissertation zur Erlangung
des Doktorgrades Dr. rer. nat.
der Fakultät für Naturwissenschaften
der Universität Ulm

vorgelegt von
Thilo Hauff
aus Ulm

2009

Dekan:	Prof. Dr. Axel Groß
Erstgutachter:	apl. Prof. Dr. Frank Jenko
Zweitgutachter:	Prof. Dr. Peter Reineker
Drittgutachter:	Prof. Dr. Tünde Fülöp
Tag der Promotion:	11. November 2009

For we know in part, and we prophesy in part. But when that which is perfect is come, then that which is in part shall be done away.

Saint Paul, 1 Cor. 13, 9-10

Meiner Frau
Cornelia
gewidmet

Abstract

Anomalous transport in magnetically confined fusion plasmas is induced by electrostatic and magnetic turbulence on scales of the Larmor radii of the ions and electrons, and is responsible for the degradation of confinement, strongly complicating the process of achieving the necessary conditions to sustain a burning plasma. The quest to understand the turbulent transport of particles, momentum, and energy in magnetized plasmas remains a key challenge in nuclear fusion research. A basic issue being still relatively poorly understood is the turbulent advection of energetic particles with large drift orbits and gyroradii. Especially the interaction of fast alpha particles or 'beam ions' with the background turbulence is of great interest.

In this thesis, fast particles are treated as passive test particles, and the connection between decorrelation processes (Eulerian or Lagrangian) and the transition to a diffusive regime is shown to be crucial in describing transport processes. To allow for a better understanding of the dependence of the particle diffusivity on the interaction mechanisms between the particle trajectories on one hand and the spatio-temporal structure of a certain type of turbulence on the other hand, a three step approach is applied: Numerical studies with artificially created stream functions in simplified geometries are used alongside analytical models, which are eventually confirmed using self-consistent gyrokinetic simulations with the Gene code. The particle motion is initially restricted to two dimensions and, after having studied the crucial effects there, extended to three dimensions, where additional effects come into play.

In two dimensions (i.e. in the plane perpendicular to the magnetic field), finite gyroradius effects are introduced using the gyroaveraging approximation which means that the gyrating particle is replaced by a charged ring. The Kubo number and the gyroradius are found to be crucial parameters, separating different regimes of transport scaling. Depending on these parameters, regimes can be found where the transport is independent of the energy, or shows a more or less steep decline. The underlying physical mechanisms of this behavior are identified and an analytical approach is developed which favorably agrees with the simulation results. The investigations are extended by introducing anisotropic structures like streamers and zonal flows as well as homogeneous drift effects, leading to quantitative modulations of the gyroradius dependence of the diffusion coefficient. Analytic models are used to explain these various effects, along with numerical simulations. Furthermore, transitions from non-diffusive to diffusive transport regimes are examined.

In three dimensions, the parallel motion of the particles along the magnetic field lines as well as perpendicular excursions due to magnetic drifts become important, in addition to the effects studied in two dimensions. The multitude of different decorrelation mechanisms is studied and a validity condition for 'orbit averaging' is obtained which is shown to be crucial for the level of

fast particle transport and directly related to the magnetic shear. Contrary to popular assumptions, it is shown that 'orbit averaging' is not valid in general, and decorrelation, i.e., the transition to the diffusive regime, occurs on perpendicular, not parallel scales. Furthermore, resonance mechanisms between the perpendicular particle drifts and the diamagnetic drifts of the bulk plasma are observed, due to which the electrostatic transport may stay at significant levels for particle energies up to about ten times the thermal energy of the background plasma. For larger energies, different scaling laws – depending on the plasma parameters and the particle energies – are derived. For electrostatic transport, the diffusion coefficient declines with E^{-1}, which is much slower than orbit averaging would suggest. The turbulent magnetic transport, however, remains constant even for very large particle energies in the case of a large pitch angle. For smaller pitch angles, both the electrostatic and the magnetic transport are modified by a factor of $E^{-1/2}$. The analytical studies are confirmed by means of nonlinear gyrokinetic simulations with the GENE code. Comparing the latter with quasilinear simulations, one finds that it is indeed the turbulent nature of the advecting field which is responsible for the slow decay of the particle transport with increasing energy. The turbulent transport of energetic particles is discussed as a candidate for explaining recent surprising experimental results obtained by the ASDEX Upgrade experiment, finding that our models are able to explain the observed fast broadening of the beam current.

Finally, in order to describe the transport of fast 'runaway electrons', the model is extended to relativistic conditions, exhibiting strong modifications of the scaling laws. They are shown to be able to explain the rather low levels of diffusion found in experimental measurements of this particle species.

Zusammenfassung

Ursache des anomalen Transports in magnetisch eingeschlossenen Fusionsplasmen ist elektrostatische und magnetische Turbulenz von der Größenordnung der Larmorradien der Ionen und Elektronen. Sie ist verantwortlich für die Verschlechterung des Einschlusses, was das Erreichen der "Zündbedingung" stark erschwert. Das Streben nach einem besseren Verständnis des turbulenten Transports von Teilchen, Impuls und Energie in magnetischen Plasmen ist nach wie vor eine der größten Herausforderungen der Kernfusionsforschung. Ein Schlüsselgebiet, welches noch immer relativ wenig verstanden ist, ist der turbulente Transport energiereicher schneller Teilchen mit großen Driftorbits und Larmorradien. Besonders die Wechselwirkung von schnellen Alphateilchen oder 'Beam'-Ionen mit der Hintergrundturbulenz ist hierbei von großem Interesse.

In dieser Dissertation werden die schnellen Teilchen als passive Testteilchen behandelt, und es wird gezeigt, dass der Verbindung von Eulerschen oder Lagrangschen Dekorrelationsprozessen und dem Übergang in ein diffusives Regime bei der Beschreibung des Transportes entscheidende Bedeutung zukommt. Um ein besseres Verständnis der Abhängigkeit der Teilchendiffusivität von den Wechselwirkungsmechanismen zwischen den Teilchenbahnen auf der einen Seite und der räumlichen und zeitlichen Struktur verschiedener Typen von Turbulenz auf der anderen Seite zu erlangen, wird in drei Stufen vorgegangen: Numerische Simulationen mit künstlich erzeugten Potentialen in vereinfachten Geometrien gehen einher mit analytischen Modellen, die zuletzt durch selbstkonsistente gyrokinetischen Simulationen mit dem Gene-Code bestätigt werden. Ferner wird die Teilchenbewegung anfänglich auf die zwei Dimensionen senkrecht zum Magnetfeld eingeschränkt. Nachdem dort die entscheidenden Effekte beschrieben werden, wird die Bewegung auf drei Dimensionen ausgedehnt, und dort auftretende neue Effekte werden der Beschreibung hinzugefügt.

In zwei Dimensionen wird der endliche Larmorradius der Teilchen mittels der Gyromittelungsnäherung beschrieben, bei der das gyrierende Teilchen einfach durch einen geladenen Ring ersetzt wird. Die Kubozahl und der Larmorradius werden als die entscheidenden Parameter erkannt, die verschiedene Transportregime voneinander scheiden. Abhängig von der Wahl dieser Parameter werden Bereiche gefunden, in denen der Transport unabhängig von der Teilchenenergie ist, oder aber mehr oder weniger stark abfällt. Die zugrundeliegenden physikalischen Mechanismen dieses Verhaltens werden identifiziert, und eine analytische Beschreibung wird entwickelt, die mit den Simulationsergebnissen hervorragend übereinstimmt. Weiter werden der Einfluss von anisotropen Strukturen wie "Streamern" und "Zonal Flows" sowie homogener Driften der turbulenten Strukturen untersucht, was zu quantitativen Veränderungen der Larmorradiusabhängigkeit des Diffusionskoeffizienten führt. Analytische Modelle können diese zahlreichen Effekte im Wechselspiel mit numerischen Simulationen erklären. Desweiteren werden Übergänge von nichtdiffusivem zu diffusivem

Transport untersucht und beschrieben.

In drei Dimensionen kommt der Teilchenbewegung entlang der Magnetfeldlinien sowie den Abweichungen durch die magnetischen Driften senkrecht dazu eine besondere Bedeutung zu, zusätzlich zu den Effekten, die zuvor in zwei Dimensionen analysiert wurden. Die Mannigfaltigkeit verschiedener Dekorrelationsmechanismen wird untersucht, und eine Bedingung für die Gültigkeit der "Orbitmittelung" wird aufgestellt. Diese ist entscheidend für das Transportniveau schneller Teilchen und ist eng mit der magnetischen Verscherung des Tokamaks verknüpft. Im Gegensatz zu etablierten Annahmen stellt sich heraus, dass das Orbitmitteln im allgemeinen ungültig ist, und die Dekorrelation schneller Teilchen, also der Übergang ins diffusive Regime, auf Skalen senkrecht zum Magnetfeld, nicht parallel dazu, geschieht. Desweiteren werden Resonanzen zwischen den senkrechten Teilchendriften und der diamagnetischen Drift des thermischen Plasmas beobachtet, die dafür verantwortlich sind, dass der elektrostatische Transport bis zu Energien von etwa dem zehnfachen der thermischen Energie auf einem signifikanten Niveau bleibt. Für größere Energien werden verschiedene Abhängigkeiten des Diffusionskoeffizienten von den Plasmaparametern und der Teilchenenergie gefunden. Der elektrostatische Transport fällt mit E^{-1} ab, was immer noch sehr viel größer ist als nach der Theorie der Orbitmittelung. Der turbulente magnetische Transport jedoch bleibt im Falle großer Pitch-Winkel konstant selbst für sehr hohe Teilchenenergien. Für kleinere Pitch-Winkel fallen sowohl der elektrostatische als auch der magnetische Transport mit einem zusätzlichen Faktor $E^{-1/2}$ ab. Die allgemeinen numerischen und analytischen Studien werden durch nichtlineare gyrokinetische Simulationen mit dem Gene Code bestätigt. Durch den Vergleich letzterer mit quasilinearen Läufen findet man, dass tatsächlich die turbulente Natur der Felder für den langsamen Abfall des Teilchentransports mit der Energie verantwortlich ist. Der turbulente Transport energiereicher Teilchen wird ferner als eine Möglichkeit diskutiert, kürzliche überraschende experimentelle Ergebnisse am ASDEX Upgrade zu deuten. Die in dieser Arbeit vorgestellten Modelle sind hierbei in der Lage, die beobachtete schnelle Verbreiterung des durch Neutralteilcheninjektion getriebenen Stromes zu erklären.

Um den Transport schneller Runaway-Elektronen zu beschreiben, werden die Modelle auf relativistische Bedingungen ausgedehnt, was zu einer starken Modifizierung der Skalierungsgesetze führt. Es wird gezeigt, dass so auch die sehr niedrigen Diffusionskoeffizienten, wie sie für diese Teilchenspezies im Experiment gemessen werden, erklärt werden können.

Contents

Chapter 1

Introduction

The aim of nuclear fusion research is to one day enable the 'production' of energy by the fusion of light nuclei to heavier ones, which is possible for light elements due to the mass defect (Fig. 1.1). Nuclear fusion is the energy source of the stars. In the sun, for example, energy is generated by the successive fusion of four protons to helium:

$$4\mathrm{p} \longrightarrow \mathrm{He}_2^4 + 2\mathrm{e}^+ + 2\nu_\mathrm{e} + 2\gamma + 25.7\,\mathrm{MeV}\,.$$

The partial reactions are:

$$\begin{aligned} \mathrm{p} + \mathrm{p} &\longrightarrow \mathrm{D} + \mathrm{e}^+ + \nu_\mathrm{e} \\ \mathrm{D} + \mathrm{p} &\longrightarrow \mathrm{He}_2^3 + \gamma \\ \mathrm{He}_2^3 + \mathrm{He}_2^3 &\longrightarrow \mathrm{He}_2^4 + 2\mathrm{p}\,. \end{aligned}$$

Since the weak interaction is involved in the first step, the reaction rate of this so-called proton-proton chain reaction is small and therefore technically not feasible under terrestrial conditions. Instead, one focuses on the reaction (Wesson, 1997)

$$\mathrm{D} + \mathrm{T} \longrightarrow \mathrm{He}_2^4 + \mathrm{n} + 17.6\,\mathrm{MeV}\,.$$

Since only the strong interaction is involved, the cross section for that reaction is multiple orders of magnitude larger than for the proton-proton chain. Further, due to a quantum mechanical resonance, the deuterium-tritium reaction is superior to other possible reactions (e.g., D-D or T-T), which is why fusion research concentrates on that process. The maximum cross section of the D-T reaction lies at a relative energy of 64 keV (i.e. $740{\times}10^6$ K). Whereas deuterium has a natural abundance of about one in 6500 atoms of hydrogen in the oceans of the earth, tritium does not appear naturally, since it is radioactive with a half-life of about 12 years. However, it can be bred via the reactions

$$\mathrm{Li}_3^7 + \mathrm{n} \longrightarrow \mathrm{He}_2^4 + \mathrm{T} + \mathrm{n}\,; \qquad \mathrm{Li}_3^6 + \mathrm{n} \longrightarrow \mathrm{He}_2^4 + \mathrm{T}\,.$$

In order to be able to fuse, the nuclei have to overcome the Coulomb wall, which means that their energy has to be quite high. This energy would even be higher if the tunnel effect did not enable them to 'tunnel' through the barrier

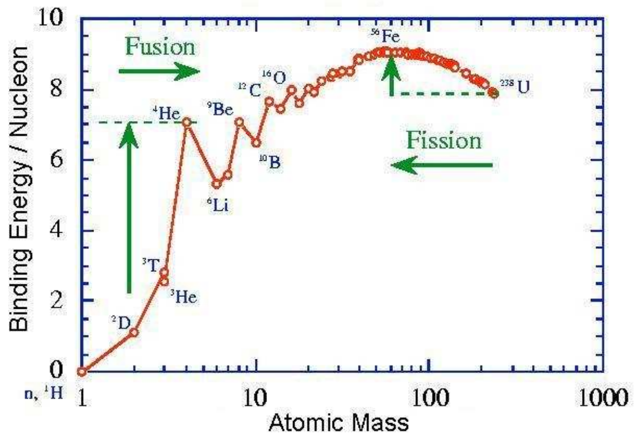

Figure 1.1: Binding energy per nucleon vs. atomic mass. A gain of binding energy corresponds to a loss of mass ($E = mc^2$). Source: IPP Garching.

with a certain probability. The possible solution to energize tritium atoms with a particle accelerator and shoot them onto a deuterium target (*beam-target-fusion*) does not work in practice. It can be shown that the cross section for a Coulomb collision with electrons is larger than for a fusion reaction by a factor $> 10^4$. With such a small probability, more energy would be required for the acceleration of the ions than produced by fusion.

This problem can be avoided by the generation of a very hot and therefore ionized gas (plasma), since energy is not lost by collisions, but redistributed between the atoms. In the thermodynamic equilibrium, the particle distribution in velocity space is governed by Maxwell-Boltzmann statistics. Only particles in the 'tail' of such a distribution are able to fuse. Three fundamental values are decisive for the success of nuclear fusion: The temperature T has to be large, as does the particle density n of the enclosed plasma, since in both cases, more high-energy particles are present. Moreover, the mean energy confinement time τ_E has to be large. An expression for the so-called 'ignition condition' is given by the *Lawson Criterion* (Lawson, 1957; Wesson, 1997): $nT\tau_E > 3{\times}10^{21}\ \mathrm{m}^{-3}\,\mathrm{keV\,s}$. The product of the three parameters has to exceed a certain value, so that the energy gain due to nuclear fusion over-compensates the energy loss due to radiation and convection. Strictly speaking, the value of the constant itself depends on temperature and density of the plasma. The value given above refers to a temperature of $T = 13\,\mathrm{keV}(\approx 140\times10^6\,\mathrm{K})$.

It is obvious that under such conditions, a confinement of the plasma by massive walls is not possible anymore. The most promising and common method is based on confinement by magnetic fields. Apart from collisions, ionized particles can be confined perfectly in the direction perpendicular to a homogeneous magnetic field, since the Lorentz force forces them on helical trajectories about the field lines. Parallel to the magnetic field, however, particles move freely, so that large losses occur at the ends. The installation of so-called 'magnetic mirrors' at the ends of such linear devices is not able to sufficiently reduce these losses, for which reason this method can be excluded. For decades, the most promising architecture is regarded to be the torus geometry, i.e. the magnetic

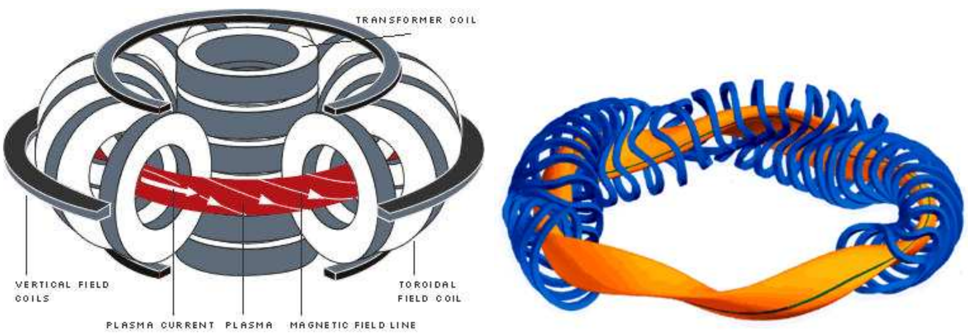

Figure 1.2: *Left*: Schematic view of a tokamak with toroidal coils, plasma current and twisted field lines forming a flux surface. *Right*: Stellarator with optimized field coils and a flux surface. Source: IPP Garching.

field lines are bent to a ring and therefore close in themselves, so that no end losses can occur. However, with the torus geometry, the homogeneity of the magnetic field has to be given up. This leads to particle drifts perpendicular to the field lines, which means that the particles are not well confined anymore. Since these drifts are charge separating, electric fields occur, which in turn lead to additional drifts. In short, avoiding parallel losses leads to perpendicular losses. Nevertheless, those losses can be completely avoided if the magnetic field lines are twisted. Twisting leads to a poloidal rotation of the particles (in addition to the toroidal one), which causes the drifts to cancel. There exist two possibilities to generate the twist of the magnetic field. In the *stellarator*, both toroidal and poloidal field are generated by external coils. In the *tokamak* (Russian abbreviation for 'toroidal chamber with magnetic coils'), only the toroidal field is produced by external coils, while the poloidal field is generated by the plasma itself by inducing a toroidal plasma current. Fig. 1.2 shows both the stellarator and the tokamak schematically. The twisted magnetic field lines are drawn in the tokamak picture. They lie on so-called magnetic flux surfaces, which form nested tori. The transformer coil drives the plasma current by induction. It is the primary coil of a transformer, where the secondary coil is the plasma itself. The toroidal field coils build up the toroidal magnetic field, whereas the vertical field coils provide control of the position of the plasma current. The ratio between the number of toroidal and poloidal cycles is called the *safety factor*

$$q \equiv \frac{N_{\mathrm{tor}}}{N_{\mathrm{pol}}}\,. \tag{1.1}$$

It may vary from one flux surface to another. In a circular geometry, denoting the small torus radius with r, this variation can be described by the *magnetic shear*

$$\hat{s}(r) \equiv \frac{r}{q(r)}\frac{dq}{dr}\,. \tag{1.2}$$

If the ions and electrons of the plasma did not interact with each other, there would be perfect confinement. In reality, however, collisions occur, which are responsible for the so-called 'neoclassical' transport across magnetic flux surfaces (Wesson, 1997). Experimentally, however, much larger values are found for the transport coefficients than can be explained by collisional transport. This highly increased transport is called *anomalous transport* in plasma physics (in contrast to other fields, where 'anomalous' is a synonym for 'non-diffusive'). According to our present knowledge, the anomalous transport is caused by low-scale, turbulent fluctuations of a number of plasma parameters (Liewer, 1985; Wesson, 1997). Density and current density fluctuations induce fluctuations in the electric and magnetic fields, which in turn deflect the particles from their unperturbed orbits. The fluctuations themselves are generated by several microinstabilities, which are driven by the strong density and temperature gradients between the core and the edge of the plasma. The turbulent anomalous transport and, as a result, the reduced energy confinement time, constitute one of the main problems of nuclear fusion research and are by no means completely understood.

Turbulence is a collective phenomenon, and therefore magnetohydrodynamic or kinetic models have to be used to describe its formation. However, the complexity of such self-consistent models may obstruct the view onto the fundamental processes which govern the behavior of certain quantities. Given the fact that the characteristics of the turbulent fields are more or less known – whether it be from self consistent simulations or from experimental measurements – passive test particles can be introduced to measure their transport and mixing properties, as well as their influence on further (diluted) particle species. In doing so, the passive tracer approach enables not only the performance of numerical simulations, but also allows for clear interpretations and even analytical predictions.

The topic of this work is the diffusion of fast test particles like alpha particles and 'beam ions' (ions accelerated and shot into the plasma for heating purposes) in plasma core turbulence. Whereas the former will become important especially in a future burning plasma, the latter are already relevant in present experiments. These fast particles can be treated as test particles for two reasons: First, their dilution is strong enough so that a relevant back-reaction onto the bulk plasma does not occur. This can be shown by comparing test particles with self-consistent simulations. And second, the orbits of fast particles in the tokamak are quite distinct from the ones of thermal particles, which is another justification for treating them separately.

On the basis of the test particle model, the work underlying this thesis has brought new insights concerning the understanding of the interaction between energetic particles with the background plasma core turbulence, as well as the general influence of the scales and structures of turbulent vortices on the transport properties. While this work deals with the turbulent transport in tokamaks, applications of the developed models to astrophysics are also possible, showing their universality.

The remainder of this thesis is organized as follows: In Chapter 2, a comprehensive introduction to the basic concepts underlying this work is given. Among these are particle orbits in a tokamak, plasma turbulence, field aligned coordinates, the concept of diffusion, and the general influence of turbulent structures on particle orbits. This chapter is also thought to be a suitable introduction to the topic for beginners. Chapters 3 to 5 start with the simplified model of electrostatic turbulence in two dimensions, i.e. in a plane perpendicular to the magnetic field. Although not all of the results will carry over to the full three dimensional study, important concepts are developed which are then extended in the following chapters. In Chapter 3 the influence of finite gyroradii onto the particle transport in 2D isotropic electrostatic turbulence is studied. Analytical models are derived and compared to numerical studies, and two times two distinct regimes of transport are found. In Chapter 4, the results of the antecedent chapter are generalized, including anisotropic structures and drifts of the turbulent structures. New regimes of transport are found and studied analytically and numerically. In Chapter 5, emphasis is put onto the question under what conditions transport actually may become diffusive. Only for intermediate time scales, non-diffusive regimes are found.

In Chapters 6 to 10, the 2D approach is extended, and the full particle motion and turbulent interaction in the 3D torus is investigated. In Chapter 6, the interaction of fast particles with electrostatic turbulence is studied numerically, and analytic models are developed which are found to be in excellent agreement with the simulations. Specifically, scaling laws are developed which predict the energy dependence of the diffusion coefficient for a number of different regimes. In Chapter 7, the studies of the preceding chapter are extended to magnetic turbulence. Using a similar analytical model, transport regimes and scaling laws are established for this case. Most notably, it is found that for large energies, the magnetic transport may exceed the electrostatic one. In Chapter 8, the results of the electrostatic and magnetic transport studies are connected to experimentally relevant situations and compared to recent observations in the Garching-based tokamak ASDEX Upgrade. It is found that the model developed in Chapter 7 is able to explain some surprising experimental results. Chapters 6 to 8 form the center of this thesis. Chapter 9 – which can be thought as an excursus, since it does not belong to the step by step structure of this thesis – deals with the question of how thermal electrons are transported by plasma turbulence. Since the large energy limit does not hold for those particles, distinct decorrelation mechanisms are found and explained. In Chapter 10 the insights of Chapter 7 are extended to fast 'runaway electrons'. Since relativistic effects have to be included for this particle species, the scaling laws have to be modified. A new quantitative connection between the diffusion coefficient and the magnetic turbulence amplitude is found, being able to re-interpret some previous experimental measurements. The thesis concludes with a summary of the key results, along with an outlook on possible connections to astrophysics in Chapter 11. Appendix C provides a list of some of the physical abbreviations used in this work.

Chapter 2

Theoretical Background

In this chapter, a theoretical background is given which is essential for the understanding of the subsequent chapters. Basic effects of turbulence, particle transport, and the concept of diffusivity are explained under the special geometric conditions in a tokamak.

2.1 Motion of charged particles in magnetic and electric fields

First, fundamental particle drifts are discussed, which are caused by both the magnetic field inhomogeneity in a tokamak, and by possible perturbations due to electric or magnetic field fluctuations. Whereas the latter are responsible for the anomalous transport in fusion plasmas, the former will turn out to be important as well in order to understand the various interaction effects between particle orbits and turbulent structures.

2.1.1 Lorentz force

The motion of a charged particle with mass m and charge e is governed by the following system of coupled differential equations of first order:

$$\begin{aligned} \dot{\mathbf{x}}(t) &= \mathbf{v}(t), \\ \dot{\mathbf{v}}(t) &= \frac{e}{m}\left(-\nabla\phi(\mathbf{x},t) + \mathbf{v}(t)\times\mathbf{B}(\mathbf{x})\right) . \end{aligned} \tag{2.1}$$

The electrostatic potential is denoted by ϕ, and $\mathbf{B}$ is the magnetic field. In the case of a homogeneous magnetic field, the differential equation system can easily be solved. For $\mathbf{B} \equiv B\mathbf{e}_z$, a possible solution is

$$x(t) = x_0(0) + \frac{v_\perp}{\Omega_g}\sin(\Omega_g t + \varphi_0) \tag{2.2}$$

$$y(t) = y_0(0) + \frac{v_\perp}{\Omega_g}\cos(\Omega_g t + \varphi_0) \tag{2.3}$$

$$z(t) = z(0) + v_\parallel t\,. \tag{2.4}$$

$v_\perp$ and $v_\parallel$ are the initial velocities perpendicular and parallel to the magnetic field, respectively, and the initial coordinates for the center of gyration, denoted by the subscript '0', have been introduced for simplicity. Further, the gyrofrequency and the gyroradius (or Larmor radius) can be introduced:

$$\Omega_g \equiv \frac{eB}{m}; \qquad \rho_g \equiv \frac{v_\perp}{\Omega_g} = \frac{mv_\perp}{eB}\,. \tag{2.5}$$

In such a configuration, the particles are confined perpendicular to the magnetic field, whereas they move freely in the parallel direction.

2.1.2 Magnetic and electric drifts

This subsection partially follows (Chen, 1984) and (Wesson, 1997), where the following derivations can be studied in more detail. It is assumed that the Larmor radius is sufficiently smaller than the variation scales of the magnetic field ($\rho_g|\nabla_\perp B| \ll B$), and that temporal variations of B are significantly smaller than the gyrofrequency ($|\partial B/\partial t| \ll \Omega_g B$). The same argument applies to electric fields. Under those assumptions, the gyration of the particle can be decoupled from the motion of the gyrocenter.

Drift by a force perpendicular to B

We assume an additional force acting on the particle, which can be expressed by the equation

$$m\dot{\mathbf{v}}(t) = \mathbf{F} + e\,\mathbf{v} \times \mathbf{B}\,. \tag{2.6}$$

Forming the scalar product of Eq. (2.6) with $\mathbf{B}$ leads to

$$m\dot{v}_\parallel = F_\parallel\,. \tag{2.7}$$

Taking the cross product of $\mathbf{B}$ with Eq. (2.6), and using the identity $(\mathbf{v} \times \mathbf{B}) \times \mathbf{B} \equiv -B^2\mathbf{v}_\perp$, we find $m\dot{\mathbf{v}} \times \mathbf{B} = \mathbf{F} \times \mathbf{B} - eB^2\mathbf{v}_\perp$, and thus

$$\mathbf{v}_\perp = \frac{\mathbf{F} \times \mathbf{B}}{eB^2} - \frac{m}{eB^2}\dot{\mathbf{v}} \times \mathbf{B} \equiv \frac{\mathbf{F} \times \mathbf{B}}{eB^2} - \dot{\boldsymbol{\rho}}_g\,. \tag{2.8}$$

Since we can identify the last term with the time derivative of the vector of the gyroradius (measured from the gyrocenter), Eq. (2.8) describes a superposition of the ordinary gyration with a constant drift perpendicular to both the direction of the magnetic field and to the force. Since we are not interested in the gyration for the moment (it does not contribute to the perpendicular transport), we can write the drift as

$$\mathbf{v}_D = \frac{\mathbf{F} \times \mathbf{B}}{eB^2}\,. \tag{2.9}$$

E×B drift

The additional force acting on the particle can be caused by an electric field, $\mathbf{F} = e\mathbf{E} = -e\nabla\phi$. Inserting this expression in Eq. (2.9), we find

$$\mathbf{v}_E = \frac{\mathbf{E} \times \mathbf{B}}{B^2} = -\frac{\nabla\phi \times \mathbf{B}}{B^2}\,, \tag{2.10}$$

the so-called $E\times B$ drift. Interestingly, this drift does only depend on the field strengths, not on mass or charge. Once more we want to stress the fact that this expression is only valid if the electric field may be assumed as homogeneous over the distance of the Larmor radius of the particle, and if the variation frequency of the field is on a smaller scale than the gyrofrequency.

Curvature drift

In a tokamak, the magnetic field lines are not straight anymore (see Fig. 1.2). A particle following the curved field lines thus feels a centrifugal force $\mathbf{F}_c = (mv_\parallel^2/R_c^2)\mathbf{R}_c$, where R_c is the radius of curvature. In the absence of currents, $\nabla\times\mathbf{B} = 0$ and it can be shown that $\mathbf{R}_c/R_c^2 = -\nabla B/B$. Inserting the expression for the centrifugal force in terms of the magnetic field into Eq. (2.9), we obtain

$$\mathbf{v}_{\mathrm{curv}} = \frac{mv_\parallel^2}{eB^3}(\mathbf{B}\times\nabla B)\,. \tag{2.11}$$

In reality, we have $\nabla\times\mathbf{B} \neq 0$, since the poloidal component of the magnetic field in the tokamak is created by a plasma current. A detailed calculation leads to a modified expression for the curvature drift (Littlejohn, 1983):

$$\mathbf{v}_{\mathrm{curv}} = \frac{mv_\parallel^2}{eB^3}\left[\mathbf{B}\times\nabla B + B\nabla\times\mathbf{B} - \frac{\mathbf{B}}{B}\left(\mathbf{B}\left(\nabla\times\mathbf{B}\right)\right)\right]. \tag{2.12}$$

Grad-B-drift

In the derivation of the curvature drift, we have only regarded the effect of the centrifugal force caused by the curvature of the field lines. However, a curvature of a magnetic field always is accompanied with a gradient of the absolute value of B. The component $\nabla_\perp B$ is the source of an additional drift. Once more, we first search for an expression for the mean force acting on the particle. Here, the Lorentz force turns out to be important. In a homogeneous magnetic field, the expression $\mathbf{F}_L = e\,\mathbf{v}\times\mathbf{B}$ vanishes, if averaged over one gyration. In an inhomogeneous field, this is not the case anymore. Under the assumption of a constant magnetic field gradient, we can write $\mathbf{B} = \mathbf{B}_0 + (\mathbf{x}\cdot\nabla)\mathbf{B}$. Averaging over one Larmor orbit, we find $\langle F_L\rangle = \mp\frac{1}{2}ev_\perp\rho_g\nabla B$ (Chen, 1984). Inserting this expression into Eq. (2.9), we obtain

$$\mathbf{v}_{\nabla B} = \pm\frac{1}{2}v_\perp\rho_g\frac{\mathbf{B}\times\nabla B}{B^2} = \pm\frac{1}{2}\frac{mv_\perp^2}{eB^3}(\mathbf{B}\times\nabla B)\,. \tag{2.13}$$

This expression can be illustrated taking into account that the gyroradius is larger on the low field side, but smaller on the high field side of the inhomogeneous field. This results in a 2D spiral trajectory, drifting perpendicular to both the magnetic field and its gradient.

Invariance of the magnetic moment

The magnetic moment of a particle is defined as:

$$\mu \equiv \frac{mv_\perp^2}{2B}. \tag{2.14}$$

According to (Landau & Lifshitz, 1960), the action $I \equiv \oint \mathbf{p}\, d\mathbf{q} = const$ under an 'adiabatic' change of the state variable λ ($d\lambda/dt \ll \lambda/T_g$), where T_g is the gyration period. In our case, we have

$$\begin{aligned} I &= \oint \mathbf{p}\, d\mathbf{q} = \oint (m\mathbf{v} + e\mathbf{A})\, d\mathbf{q} = mv_\perp 2\pi\rho_g + e\int_S (\nabla \times \mathbf{A}) d\mathbf{S} \\ &= 2\pi m^2 v_\perp^2/(eB) + e\pi\rho_g^2 B = 3\pi m^2 v_\perp^2/(eB) = const\,. \end{aligned} \tag{2.15}$$

This is the invariance of the magnetic moment,

$$\mu = const\,, \tag{2.16}$$

under the assumption that $\partial B/\partial t \ll \Omega_g B$. In (Kaufman, 1972) it was shown that the adiabatic invariance of the magnetic moment can be broken if the mode frequency of a perturbation (magnetic or electric) gets resonant with a harmonic of the gyrofrequency. However, this is not the case in a tokamak, which is why the magnetic moment is conserved. In Chapter 6, the existence of two more adiabatic invariants is discussed, which are not conserved anymore in the presence of fluctuating fields.

Mirror force

The magnetic field gradient may not only point into the direction perpendicular to the field, but also in the parallel direction ($\nabla_\parallel B \neq 0$). In that case, an additional effect occurs, which can be understood by means of the invariance of the magnetic moment. From Eqs. (2.14) and (2.16) follows that if the magnetic field increases, $v_\perp$ must increase, too, which in turn means that $v_\parallel$ has to decrease, since the kinetic energy of a particle is conserved in static magnetic fields (which we assume). So, there must be a force antiparallel to $\mathbf{B}$. Writing $v_\parallel^2 = v_0^2 - 2B\mu/m$ and using the total derivation $d/dt = \partial/\partial t + (\mathbf{v} \cdot \nabla)$, we obtain $\dot{v}_\parallel = -\frac{\mu(\mathbf{v}_\parallel \cdot \nabla)B}{mv_\parallel} = -\frac{\mu}{m}\nabla_\parallel B$. So we can write the corresponding 'mirror force' as

$$\mathbf{F}_\parallel = -\mu \nabla_\parallel B\,. \tag{2.17}$$

Equations of motion for the gyrocenter

Now we can combine the $E{\times}B$ drift (Eq. (2.10)), the curvature drift (Eq. (2.12)), the grad-B drift (Eq. (2.13)), and the mirror force (Eq. (2.17)) to a new system of equations of motion:

$$
\begin{aligned}
\frac{d\mathbf{X}}{dt} &= \mathbf{v}_\parallel + \frac{B}{B_\parallel^*}\left(\underbrace{\frac{\mu}{eB^2}\mathbf{B}\times\nabla B}_{v_{\nabla B}}\right.\\
&+ \left.\underbrace{\frac{mv_\parallel^2}{eB^3}\left[\mathbf{B}\times\nabla B + B\nabla\times\mathbf{B} - \frac{\mathbf{B}}{B}\left(\mathbf{B}\left(\nabla\times\mathbf{B}\right)\right)\right]}_{v_{\mathrm{curv}}} - \underbrace{\frac{\nabla\phi\times\mathbf{B}}{B^2}}_{v_E}\right),\\
\frac{dv_\parallel}{dt} &= \frac{1}{mv_\parallel}\frac{d\mathbf{X}}{dt}\cdot\left(-e\nabla\phi - \mu\nabla B\right)\,. \qquad (2.18)
\end{aligned}
$$

In addition to the foregoing derivations, a prefactor $B/B_\parallel^*$ has been added, with $B_\parallel^* = B + mv_\parallel/(eB^2)(\nabla\times\mathbf{B})\cdot\mathbf{B}$. It can be derived by a more exact disquisition, and is necessary to exactly preserve the Hamiltonian properties of the system (Littlejohn, 1983). However, the numerical simulations in Chapter 6 will show that this prefactor is negligible as long as the particle energies are not too high. Whereas in a tokamak, electric fields only exist on small scales (due to macroscopic quasi-neutrality), the magnetic field can be divided into a macroscopic static part (generated by the coils and the plasma current) and into small scale turbulent fluctuations. Denoting the small scale turbulent part with a tilde, we can express this as $\phi = \tilde{\phi}(\mathbf{x}, t)$, $\mathbf{B} = \mathbf{B}_0(\mathbf{x}) + \tilde{\mathbf{B}}(\mathbf{x}, t)$.

Finally, it should be emphasized once more that the terms in Eq. (2.18) were derived under the following conditions:
1. The gyroradius of the particle is smaller than typical fluctuation lengths of $\mathbf{E}$ and $\mathbf{B}$: $\rho_g|\nabla_\perp B| \ll B$ and $\rho_g|\nabla_\perp E| \ll E$. If we denote the perpendicular correlation length of the field variations with $\lambda_\perp$, we can write this as $\rho_g \ll \lambda_\perp$.
2. The time variance of the fields is on a larger scale than the gyro frequency: $|\partial B/\partial t| \ll \Omega_g B$ and $|\partial E/\partial t| \ll \Omega_g E$.
Whereas the second constraint is always fulfilled for any kind of turbulence in a tokamak, the first one is not. For energetic particles, the gyroradii as well as the global orbits can become larger than the scales of the electric as well as the magnetic fluctuations. One possible solution for this problem will be treated in Section 2.1.4.

Although Eq. (2.18) looks more complicated than the original equations of motion, Eq. (2.1), it provides a number of fundamental simplifications, which only allow us to continue studying the problem of test particle transport in detail. Those are:
1. The particle motion is split into a motion parallel, and drifts perpendicular to the magnetic field. This is of special importance, since turbulence tends to align along the magnetic field lines, and it is especially the perpendicular drifts which are decisive for the interaction effects.

2. The gyration of the particle is completely excluded. This simplifies both numerical computational effort, and theoretical modeling.

2.1.3 Diamagnetic drift

In the last subsection, we have treated drifts on the basis of a single particle approach. However, there are drifts which only exist in the fluid picture. Although this picture is not relevant for this study of test particles, one important effect shall be described briefly, since it dominates the background plasma, and therefore indirectly the interaction with tracers. In the fluid description of a plasma, a simple equation of motion can be proposed as follows:

$$nm\left(\frac{\partial \mathbf{v}}{\partial t} + \mathbf{v} \cdot \nabla \mathbf{v}\right) = en\left(\mathbf{E} + \mathbf{v} \times \mathbf{B}\right) - \nabla p\,. \tag{2.19}$$

n and $\mathbf{v}$ are the particle density and the mean velocity of a fluid element, and p is the plasma pressure. Neglecting the inertial term on the left hand side, multiplying the equation by $\times\mathbf{B}$, and using the identity $\mathbf{B} \times (\mathbf{B} \times \mathbf{v}) = -B^2\mathbf{v}_\perp$, we arrive at:

$$\mathbf{v}_D = \frac{\mathbf{E} \times \mathbf{B}}{B^2} + \frac{\nabla p \times \mathbf{B}}{enB^2}\,. \tag{2.20}$$

Whereas the first term on the right hand side is the $E \times B$ drift, which we already know, the second term is new and exists only in the fluid description. It is called the diamagnetic drift (Chen, 1984)

$$\mathbf{v}_d = \frac{\nabla p \times \mathbf{B}}{enB^2} = \frac{\kappa T \nabla n \times \mathbf{B}}{enB^2}\,, \tag{2.21}$$

where κ is the heat capacity ratio and T the plasma temperature (with the dimension of an energy). Because of the existence of a density gradient, a net drift results from the gyration of the particles, although the gyrocenters itself keep at rest. Since in a tokamak, $\mathbf{B}$ points (mainly) in the toroidal direction, whereas ∇n is radial, the diamagnetic drift is poloidal and may lead to a poloidal rotation of the whole plasma. Since this effect does not affect single test particles, there is a poloidal motion of the plasma background relative to a single particle, which fundamentally influences the transport, as will become important in Chapter 4 and the following chapters.

2.1.4 Gyroaveraging

Deriving the equations of motion in the gyrocenter limit (Eq. (2.18)), we have stressed the fact that they are only valid in the case of almost homogeneous fields ($E \times B$ drift, curvature drift), or homogeneous gradients (grad-B drift) over the range of a Larmor radius. If the respective field values are fluctuating on that range, this constraint is not fulfilled anymore.

In a tokamak, the particle drifts are always much smaller than the particle velocity ($v_{E,\nabla B,\mathrm{curv},d} \ll v$). This means that the Larmor orbit of a particle can still be assumed as circular in a good approximation. The idea of 'gyroaveraging' is to average the fields over one gyration period, and then to replace the fields in

Eq. (2.18) by new 'gyroaveraged' values, so that the structure of the equations of motion keeps the same. For the electrostatic potential, averaged over one gyroorbit, we write

$$\langle\phi\rangle(\mathbf{x}_0) = \frac{1}{2\pi}\oint d\varphi\,\phi(\mathbf{x}_0 + \boldsymbol{\rho}_g(\varphi))\,, \tag{2.22}$$

where $\mathbf{x}_0$, denotes the value of the center of gyration, and $\boldsymbol{\rho}_g$ is the gyroradius vector pointing from $\mathbf{x}_0$ to the particle position, depending on the angle φ which runs from 0 to 2π. Rewriting this expression as a sum of discrete Fourier modes, we get

$$\begin{aligned} \langle\phi\rangle(\mathbf{x}_0) &= \frac{1}{2\pi}\oint d\varphi \sum_{\mathbf{k}} \phi_{\mathbf{k}} e^{i\mathbf{k}\cdot(\mathbf{x}_0+\boldsymbol{\rho}_g(\varphi))} \\ &= \sum_{\mathbf{k}} \phi_{\mathbf{k}} e^{i\mathbf{k}\cdot\mathbf{x}_0}\frac{1}{2\pi}\oint d\varphi e^{i\mathbf{k}\cdot\boldsymbol{\rho}_g(\varphi)}\,. \end{aligned} \tag{2.23}$$

Setting $\mathbf{k}\cdot\boldsymbol{\rho}_g(\varphi) = k\rho_g \sin\varphi$, the integral can be solved (Bronstein & Semedjajew, 2000; Gradshteyn & Ryzhik, 1994):

$$\frac{1}{2\pi}\oint d\varphi\, e^{ik\rho_g \sin\varphi} = J_0(k\rho_g)\,. \tag{2.24}$$

Here, J_0 is the Bessel function of order zero. In fact, Eq. (2.24) is often used to define the Bessel function. Going back to Eq. (2.23), we can write

$$\langle\phi\rangle(\mathbf{x}_0) = \sum_{\mathbf{k}} \phi_{\mathbf{k}}\, e^{i\mathbf{k}\cdot\mathbf{x}_0} J_0(k\rho_g)\,. \tag{2.25}$$

This so-called *gyroaveraging approximation* can be found in the literature, e.g., in Ref. (Naitou *et al.*, 1979) or (Frieman & Chen, 1982).

The approximation is to replace the electrostatic potential in the drift approximation (Eq. (2.18)) by the new, gyroaveraged potential. The structure of the equations therefore remains unchanged. Instead of $\langle\phi\rangle$, we will denote this new potential with ϕ^{eff} in the following. For the magnetic field fluctuations, the same mechanism can be applied, in general. In the following chapters, we will deal with the question how exactly gyroaveraging modifies the structure and amplitude of electrostatic fluctuations, and how in turn this influences the particle transport.

We now have to ask under which conditions the gyroaveraging approximation is valid. We can state two conditions:
1. The potential must not vary substantially in time during one gyroorbit time. This leads to the condition $|\partial B/\partial t| \ll \Omega_g B$ and $|\partial E/\partial t| \ll \Omega_g E$, which is the same than for the pure gyrocenter approximation. Typical values for tokamak core turbulence are $\Omega_g \sim 10^8\,\text{s}^{-1}$ and $|\partial E/\partial t|/|E| \sim 10^4\,\text{s}^{-1}$, so that this condition is always fulfilled.
2. For the gyrocenter motion, we have had the condition that the potential variation has to be small over the distance of one gyroorbit. This condition is not necessary anymore. Now the potential variation has to be small over the

distance of the Larmor orbit shift after one gyration, which is much shorter. This is because it is the shift which leads to a deviation from the assumed circular gyroorbit. If we denote the variation of the potential with the correlation length $\lambda_\perp$, we can write this condition as $v_D T_g = \frac{2\pi m v_D}{eB} < \lambda_\perp$. Interestingly, this validity expression is independent of the particle velocity v, and therefore, for constant B, of the gyroradius. This means that gyroaveraging can be valid for gyroradii much larger than the fluctuation lengths of the fields. Typical values for core turbulence in a large tokamak are $v_D \sim 10^3\,\mathrm{m/s}, T_g \sim 10^{-8}\,\mathrm{s}$ and $\lambda_\perp \sim 10^{-2}\,\mathrm{m}$, so that this second condition is clearly fulfilled, too.

So we can summarize that gyroaveraging is, under the conditions in plasma core turbulence, always possible. In the remainder of this thesis, this fact will always be presupposed, so that the full Lorentz dynamic as given in Eq. (2.1) is not needed anymore.

2.1.5 Particle orbits in a tokamak

For the moment, we want to neglect all small scale perturbations and therefore set $\phi = 0$, $\mathbf{B} = \mathbf{B}_0(\mathbf{x})$. According to Eq. (2.18), there is a magnetic drift perpendicular to both the magnetic field lines and the direction of their gradient. In a pure toroidal field, this drift would hinder confinement. However, as was already mentioned in the introduction, the twist of the magnetic field lines (i.e. the generation of an additional poloidal field component) is able to compensate this effect. In this section, the reasons for this behavior are explained, and the detailed form of the unperturbed particle trajectories is studied. In order to distinguish two distinct sorts of particle orbits, we introduce the so-called *pitch angle*

$$\eta \equiv \frac{v_\parallel}{v} = \sqrt{1 - \frac{v_\perp^2}{v^2}}\,. \tag{2.26}$$

Passing particles ($\eta \to 1$)

First, we concentrate on particles with a large pitch angle. Since their magnetic moment is small, the mirror force (Eq. (2.17)) is negligible, and the parallel velocity component is approximately constant. As can be seen from Fig. 1.2 (left), the twisted field lines cover so-called magnetic flux surfaces. For the moment, we want to assume their cross section to be circular. We now use cylindrical coordinates (R, z, ζ), as illustrated in Fig. 2.1. Since the magnetic field in a tokamak is axisymmetric, the coordinate ζ can be ignored. The sum of the drifts is now $v_D = v_{\mathrm{curv}} + v_{\nabla B}$, and, since $\mathbf{B} \approx B\mathbf{e}_\zeta$ and $\nabla B \approx |\nabla B|\mathbf{e}_r$, we can approximate $\mathbf{v}_D \propto \mathbf{e}_z$. So we can formulate the following equations of motion (Wesson, 1997):

$$\frac{dR}{dt} = \omega_{\mathrm{pol}} z; \qquad \frac{dz}{dt} = -\omega_{\mathrm{pol}}(R - R_0) + v_D\,. \tag{2.27}$$

The poloidal frequency is $\omega_{\mathrm{pol}} \approx v_\parallel/(qR_0)$, where q is the safety factor defined

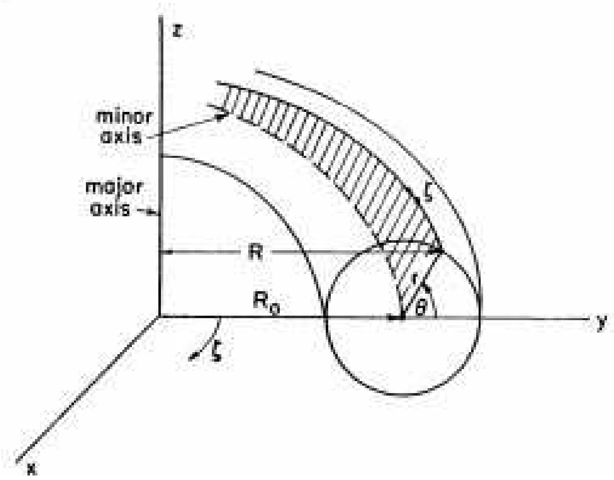

Figure 2.1: Cylindrical coordinates (R, z, ζ) and torus coordinates (r, θ, ζ) for a tokamak. The minor axis is also called the *magnetic axis.* Source: (D'haeseleer *et al.*, 1990).

by Eq. (1.1). The solution of the differential equation is

$$\left(R - R_0 - \frac{v_D}{\omega_{\text{pol}}}\right)^2 + z^2 = const\,, \tag{2.28}$$

which means that the center of the circular orbit in the $R-z$ plane is displaced from the center of the flux surface, resulting in a maximal variance of $\Delta r = 2v_D/\omega_{\text{pol}} = 2qv_D R_0/v_\parallel$. So, it is due to the twist of the magnetic field lines that the magnetic drifts lead only to a shift of the particle trajectories, but not to a constant drift across the flux surfaces. In Chapter 6 it will be shown that this shift is an important issue in the interplay between fast particles and the plasma turbulence, which is responsible for a certain transport behavior. In addition to the radial shift, it is found that the magnetic drifts are responsible for a drift with constant velocity in the ζ direction, which we will denote by v_y (the y coordinate is introduced in Section 2.3.2). It is important to note that this drift is additional to the parallel velocity component just following the magnetic field lines, so that the particles move away from their initial field line with this velocity. A derivation draft of v_y is given in Chapter 6. Using $|\nabla B| = B/R_c \approx B/R_0$ (R_c is the local radius of curvature) together with Eq. (2.26) and $\eta \to 1$, we approximate the magnetic drift $v_D = v_{\text{curv}} + v_{\nabla B}$ by the expression $v_D \approx \frac{m\eta^2 v^2}{eBR_0}$. So we can write the particle orbit circulation time and the maximal radial derivation from the magnetic field line as

$$T_{\text{orbit}} = \frac{2\pi q R_0}{\eta v}; \qquad \Delta r = \frac{2\eta q m v}{eB}\,. \tag{2.29}$$

For the toroidal y (ζ) drift away from the field lines, the approximation

$$v_y = \frac{m\eta^2 v^2 \hat{s}}{eBR_0} \tag{2.30}$$

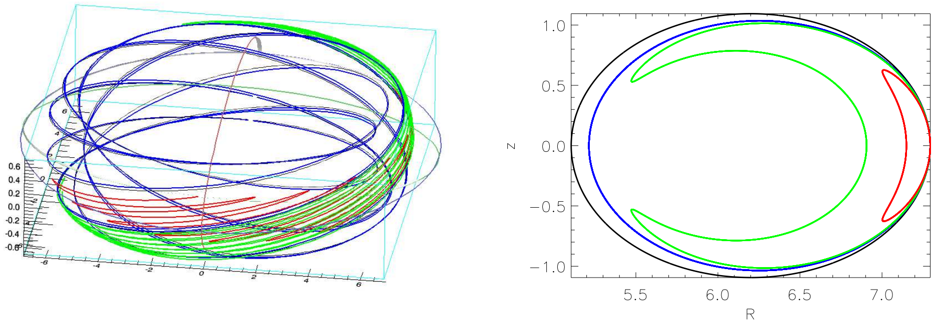

Figure 2.2: Particle orbits for different pitch angles. Blue: $\eta = 0.99$, green: $\eta = 0.3$, red: $\eta = 0.1$, black: magnetic field line. $q = 7/5$, i.e. the magnetic field lines close after 5 toroidal turns. *Left*: Top view of the torus and trajectories. *Right*: The same trajectories in the $R - z$ plane.

can be given (see Chapter 6). Here, the magnetic shear defined in Eq. (1.2) was used. A finite shear means that the safety factor changes with the torus coordinate r. This is the reason why the toroidal components of the magnetic drifts, caused by the poloidal component of the magnetic field, do not compensate exactly anymore, and a toroidal shift remains after one poloidal orbit.

Trapped particles ($\eta \to 0$)

For particles with a small pitch angle, distinct orbits exist. Since their parallel velocity is small, but their magnetic moment is large, the mirror force (Eq. (2.17)) is strong and is able to reflect a particle travelling along the field lines from the outboard (low field) side to the inboard (high field) side. It bounces back and forth on a magnetic field line. Apart from this very distinct behavior compared to the passing particles, the trapped particles show similar effects. Their trajectory shows a radial shift away from their initial field line, and they drift in the toroidal direction with a constant drift velocity. We restrict on presenting the results for their orbits:

$$T_{\text{orbit}} = \frac{2^{3/2}\pi q R_0}{\sqrt{\epsilon(1-\eta^2)}v}; \qquad \Delta r = \frac{2\eta q m v}{eB\epsilon} \qquad (2.31)$$

$$v_y = \frac{m(1-\eta^2)v^2}{2eBR_0}\,.$$

A derivation for the first expressions can be found in (Wesson, 1997), whereas $v_y \equiv v_\zeta$ is further discussed in Chapter 6. The *inverse aspect ratio* of a given magnetic surface is defined as

$$\epsilon \equiv r/R_0\,. \qquad (2.32)$$

Trajectories for passing and trapped particles are shown in Fig. 2.2 in two views, a 3D view onto the torus and a 2D view onto the $R-z$ plane. In the left hand figure, passing and trapped particle orbits can be distinguished, and for both the axial drift can be observed. On the right hand figure, the deflection of both orbits from the original flux surface is evident. Due to their form, the trapped particle orbits are often called 'banana orbits'.

For clarification, it shall be noted that the word 'trapped' is imposed with a double meaning. Apart from the magnetic trapping effect described here, a particle can be trapped by a turbulent vortex, e.g. of the electrostatic potential. 'Vortex trapping' however, only affects the turbulent particle motion perpendicular to the magnetic field lines. This effect is described later in Sec. 2.6.1.

When is a particle trapped or passing?

We have just learned that passing orbits for large pitch angles and trapped particles for small pitch angles are fundamentally distinct. Now the question is: What is the value of the pitch angle η_1 which divides those two regimes, and how many particles are trapped or passing in a tokamak?

At a mirror point, $v_\perp \equiv v$. For a particle starting with a pitch angle η_1 at a field strength B_1 and being reflected at a field strength $B_{\max}$, $\frac{(1-\eta_1^2)v^2}{B_1} = \frac{v^2}{B_{\max}}$ follows from the conservation of energy and magnetic moment. So in that case, all particles with $\eta_1 < \sqrt{1 - B_1/B_{\max}}$ are reflected at the high field side of the tokamak and therefore trapped on the outboard side. We may assume $B(R) \propto 1/R$ (recall Fig. 2.1 for the definition of R). A particle starting at R_1 can reach a maximum field strength of $B_{\max} = B_1 R_1/(2R_0 - R_1)$ on its flux surface so that the trapping criterion becomes $\eta_1 < \sqrt{2 - 2R_0/R_1}$. For $R_0/R_1 = 0.875$ for example, $\eta_1 < 0.5$. Towards the core, less particles are trapped, whereas η_1 is increased on outer flux surfaces.

Assuming an isotropic distribution, a possible expression for the total fraction of trapped particles on a certain flux surface is (Wesson, 1997)

$$f_{\text{trapped}} = \sqrt{\frac{2r}{R_0 + r}} = \sqrt{\frac{2\epsilon}{1+\epsilon}}. \tag{2.33}$$

This means that for instance that for $\epsilon = 0.14$, 50% of the particles are trapped.

2.2 Plasma turbulence

Turbulence is a very general phenomenon, which is neither fully understood, nor easy to define precisely. According to (Hinze, 1959), "turbulent fluid motion is an irregular condition of flow in which the various quantities show a random variation with time and space coordinate, so that statistically distinct average values can be discerned". It is the existence of average values of various quantities (like temperature, amplitude, correlation lengths and times), which only makes the turbulent motion accessible to a mathematical treatment. The source of energy for driving the turbulence "lies either in the non-Maxwellian nature of the distribution functions in velocity space, or in the spatial gradients of the density or temperature of locally Maxwellian distributions." Although it has been known for decades that small scale turbulence must be responsible for the anomalous transport in fusion plasmas (Liewer, 1985), experimental measurements of the fluctuations have been and are still quite difficult to establish

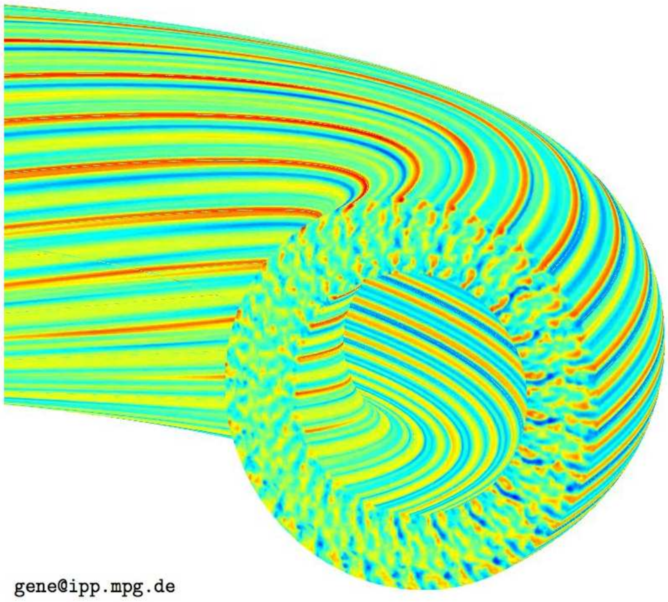

Figure 2.3: Turbulence in a tokamak, simulated with GENE. Shown is the electrostatic potential. A strong elongation along the magnetic field lines can be observed, as well as typical structures perpendicular to the field. Picture generated by Moritz Püschel and Klaus Reuter.

(see, e.g., (Conway, 2008)). Instead, progress in the understanding and prediction of plasma microturbulence has been achieved most notably by numerical simulations. In the research group of Frank Jenko at the IPP Garching, the gyrokinetic Vlasow code "GENE" is used to study the creation, development and saturation of distinct kinds of turbulence. In principle, the code solves the gyrokinetic version of the nonlinear Vlasov equation

$$\frac{df}{dt} = \frac{\partial f}{\partial t} + \dot{\mathbf{x}} \cdot \nabla f + \dot{\mathbf{v}} \cdot \nabla_v f \tag{2.34}$$

for the distribution function $f(\mathbf{x}, \mathbf{v}, t)$, coupled with the field equations, which are derived from Maxwell's equations (Hahm, 1988; Hahm *et al.*, 1988; Brizard, 1989). This is done on a fixed grid in five-dimensional phase space (plus time), keeping the (average) profile gradients fixed. This section shall give a brief overview on three distinct kinds of turbulence which can be found that way, since although this work does not deal with their evolution, the influence of their spatial and temporal structures will turn out to be of great importance. For further information about the GENE code and plasma microturbulence, see (Jenko *et al.*, 2000) and (Dannert & Jenko, 2005), or the PhD theses of (Dannert, 2005; Merz, 2008; Pueschel, 2009; Görler, 2009).

2.2.1 General overview on plasma turbulence in a tokamak

Fig. 2.3 shows typical turbulent structures in a tokamak. The free motion along the magnetic field lines manifests itself in the parallel elongation of the turbu-

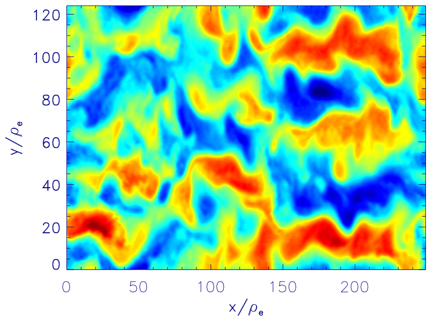

Figure 2.4: ETG turbulence in a plane perpendicular to the magnetic field. The lengths are normalized to the thermal electron Larmor radius, $\rho_e = \frac{\sqrt{T_e m_e}}{eB}$. Data generated with GENE.

lent structures, whereas the correlation lengths in the perpendicular directions are much shorter. The parallel correlation lengths are in the range of a poloidal connection length of a magnetic field line, $\lambda_{\|} \sim 2\pi q R_0$, whereas the perpendicular lengths are of the order of a thermal particle gyroradius, $\lambda_{\perp} \sim \rho_{\rm th}$.

This feature of the fluctuations enables us to consider the interaction of fast particles with the turbulent vortices - in a first approach - as a dominantly *2 dimensional* phenomenon.

In the following, three turbulence modes are introduced, distinct by their drive as well as the dominant scales. For all GENE simulations referred to in this work, double periodic boundary conditions are used, which are adequate if the box lengths are sufficiently larger than the vortex lengths.

2.2.2 Electron temperature gradient (ETG) driven turbulence

ETG turbulence is driven by the gradient of the electron temperature. In general, gradients in a tokamak are extremely strong, since the ion or electron temperature decreases from up to 100 million Kelvin to a few 1000 Kelvin at the edge. Fig. 2.4 shows a contour plot of the electrostatic potential of ETG turbulence. The coordinates x and y are so-called field aligned coordinates and will be defined in the next section. For the moment, we may regard them as perpendicular directions to the magnetic field. Typical for ETG turbulence is the formation of radially elongated vortices, so-called *streamers*. The elongation can be directly observed in Fig. 2.4, but also in the plot of the autocorrelation function in Fig. 2.5, since it is a statistical value, too. On the right hand side of Fig. 2.5, a spatiotemporal plot of the autocorrelation is shown. In this diagram, not only the spatial and temporal decorrelation can be observed, but also the fact that the vortices are moving into the y direction before they decay. This is due to the diamagnetic drift (Section. 2.1.3). In the Chapters 4 and 5, the influence of streamers and the diamagnetic drift on test particles will be studied in general, whereas in Chapter 9, ETG turbulence is examined in particular.

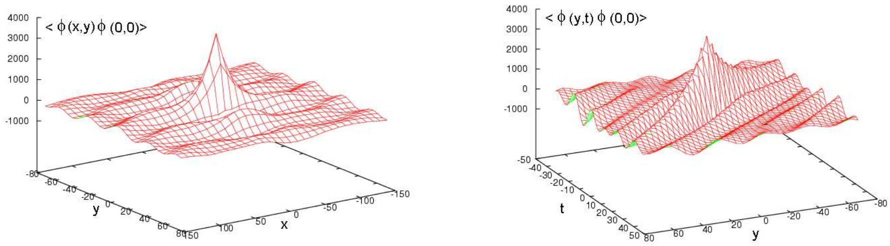

Figure 2.5: *Left*: Spatial (xy) autocorrelation function of the ETG potential of Fig. 2.4. *Right*: Spatiotemporal (yt) autocorrelation function.

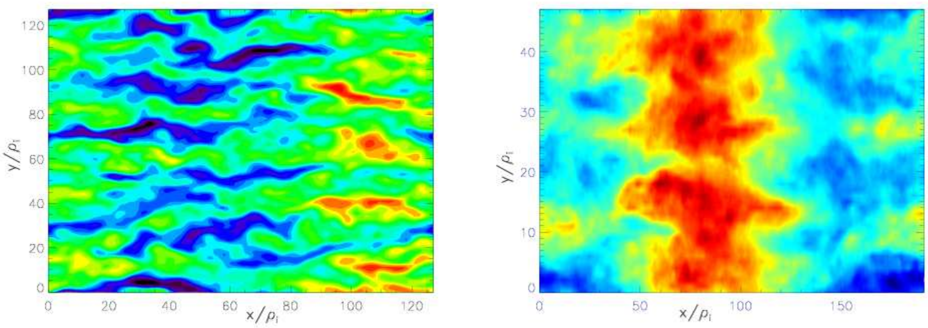

Figure 2.6: ITG turbulence in a plane perpendicular to the magnetic field for different simulation parameters. The lengths are normalized to the thermal ion Larmor radius, $\rho_i = \frac{\sqrt{T_i m_i}}{eB}$. Data generated with GENE.

2.2.3 Ion temperature gradient (ITG) driven turbulence

ITG turbulence is driven by the gradient of the ion temperature. Since ions are dominating, it is on larger scales than ETG turbulence (on the order of the ion Larmor radius instead of the electron Larmor radius). Fig. 2.6 shows two contour plots for ITG turbulence. Although the formation of streamers is similar to ETG turbulence, a new phenomenon occurs: The formation of *zonal flows*, which may, as in the right hand figure, supress the streamer formation. Zonal flows in a plasma are $m = n = 0$ modes of the electrostatic potential (where m and n are the poloidal and toroidal mode numbers), with a purely radial variation. This means that the fluctuations may show only little variation in the y direction, i.e., there is no complete decorrelation. The formation of zonal flows is a phenomenon of self-organization, where energy is transferred to longer wavelengths. A detailed review can be found, for example, in (Diamond *et al.*, 2005). Zonal flow formation is a quite universal mechanism. It is, for example, also responsible for the formation of the bands of clouds on Jupiter. In Chapters 4 and 5, the influence of zonal flows on (fast) particle transport will be studied in detail. It will be found that it is, in particular, the fact that no full decorrelation in the y direction occurs, which strongly influences the

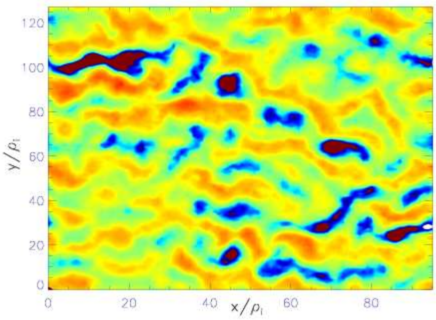

Figure 2.7: TEM turbulence in a plane perpendicular to the magnetic field. The lengths are normalized to the thermal ion Larmor radius, $\rho_i = \frac{\sqrt{T_i m_i}}{eB}$. Data generated with GENE.

transport.

2.2.4 Trapped electron mode (TEM) turbulence

As we have seen in Section 2.1.5, a significant fraction of the particles may be trapped in a tokamak. Trapping in addition to electron temperature or density gradients is able to drive turbulence, too. A contour plot of 'trapped electron mode turbulence' is given in Fig. 2.7. The vortex spatial and temporal scales are similar to ITG turbulence, however, there are, in general, no dominant zonal flows. Similar to ETG turbulence, the vortices are drifting in the y direction before they decay.

The three turbulence types which we have discussed briefly are not completely separable in reality. As was shown in (Kammerer *et al.*, 2008), "various types of microinstabilities, which are usually considered as strictly separated, can actually be transformed into each other via continuous variations of the plasma parameters". Although the drive responsible for the turbulence formation can be attained from numerical simulations, a thorough understanding of the underlying processes is still lacking. For the purpose of this work, as was already emphasized, the formation mechanisms of turbulence are of minor interest. It is the influence of the spatial and temporal scales and patterns on transport which we are interested in, namely radial streamers (all types of turbulence), zonal flows (ITG) and diamagnetic drifts (ETG, TEM).

2.3 Field aligned coordinates

As we have seen in the previous section, plasma turbulence is extremely elongated along the magnetic field lines. Whereas the parallel correlation length is of the order of the torus circumference, the radial correlation lengths are of the order of a few ion (electron) gyroradii, which is a ratio of about 1 : 2000 (1 : 80000). For computational purposes, it is extremely useful to use coordi-

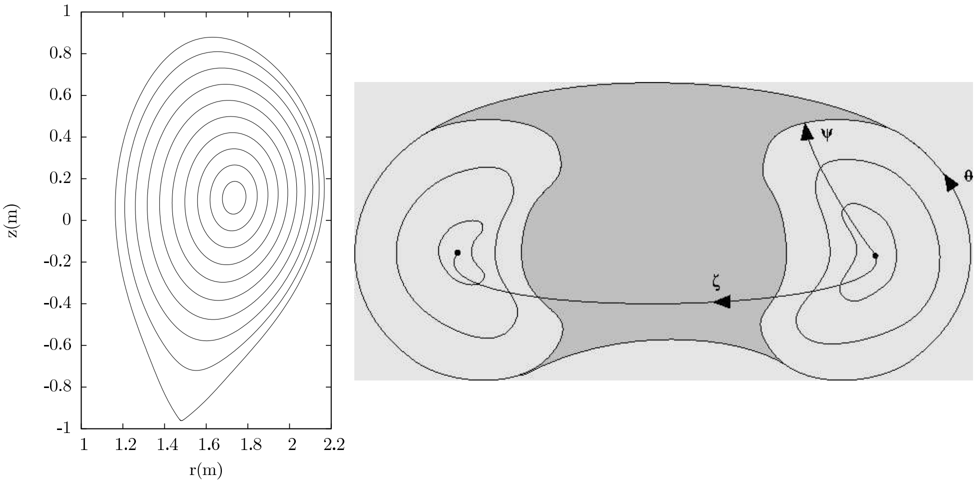

Figure 2.8: *Left*: Flux surfaces in ASDEX Upgrade. Source: (Told, 2008). *Right*: General torus coordinates for arbitrarily formed flux surfaces. Source: (Pinches, 1996).

nates which are aligned along the magnetic field lines, since the computational mesh can be chosen much wider if one direction follows the parallel structures. As will be shown in Chapter 6, the theoretical study of the interaction of 3D particle orbits with the plasma background turbulence is also much simpler to access in field aligned coordinates, since the interaction problem can be reduced to the two perpendicular dimensions.

2.3.1 Field aligned coordinates

In the introduction we have already learned that the magnetic field lines form nested tori. In a first step, general torus coordinates (ψ, ζ, θ) can be introduced (Fig. 2.8, right). As the 'radial' coordinate ψ, the poloidal magnetic flux is typically chosen. In general, the magnetic flux surfaces are not circular. However, especially in the core, they are to good approximation (see Fig. 2.8, left), and this assumption is widely used in numerical codes. It can be shown, as pointed out in Chapter 6, that the difference between an experimental and a circular geometry is only of quantitative nature. So in this thesis, we will restrict to concentric circular flux surfaces. This means we can set $\psi \equiv r$, so that we have the normal torus coordinates r, θ, ζ as drawn in Fig. 2.1, with a major radius R_0 and a distance R from the major axis. We can now unroll such a flux surface, so that we have a $\theta - \zeta$ plane. In such a plane, there are periodic boundary conditions for the particles and magnetic field lines. The field lines are not necessarily straight, but curved, as can be seen in Fig. 2.9. In general, the safety factor q is irrational, i.e. the magnetic field lines do not close. Now before transforming to field aligned coordinates, it is convenient to first introduce a new coordinate system in which the magnetic field lines are straight. The existence of a coordinate system with straight field lines and its mathematical properties have been investigated first in (Kruskal & Kulsrud, 1958; Greene & Johnson, 1962). Therein, it was shown that a general magnetic

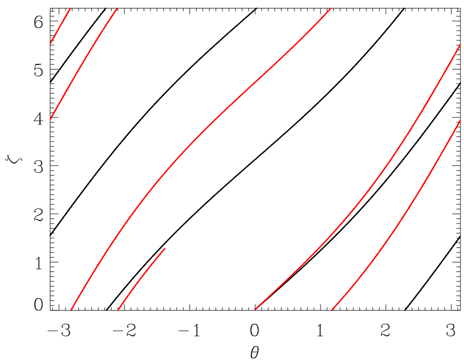

Figure 2.9: Magnetic field line in the $\theta - \zeta$ plane for $q = 3/2$ (black) and an irrational q (red).

field can be written in terms of the so-called Clebsch representation (Kruskal & Kulsrud, 1958) $\mathbf{B} \propto \nabla\beta \times \nabla\Psi$, where $\Psi \equiv r$ in the case of concentric flux surfaces, and $\beta = q(r)\chi - \zeta$. Here, χ is a new "poloidal" coordinate chosen such that the field lines are straight in the $\chi - \zeta$ plane. The new coordinate χ can be found as follows. The safety factor as defined in Eq. (1.1) can be written as

$$q(r) = \frac{1}{2\pi} \int_0^{2\pi} \frac{\mathbf{B} \cdot \nabla\zeta}{\mathbf{B} \cdot \nabla\theta}\, d\theta\,, \tag{2.35}$$

since $\frac{\mathbf{B}\cdot\nabla\zeta}{\mathbf{B}\cdot\nabla\theta}$ is the local relation between the number of toroidal and poloidal turns for a certain poloidal position, i.e. the local gradient in Fig. 2.9. Now if we define a new coordinate $\chi(\theta)$ with the prerequisite that the magnetic field lines are straight in a $\chi - \zeta$ diagram, $q \equiv \frac{\mathbf{B}\cdot\nabla\zeta}{\mathbf{B}\cdot\nabla\chi}$ has to be fulfilled, since the gradient is constant per definition. Together with the expression $\nabla\chi(\theta(\mathbf{x})) = \frac{d\chi}{d\theta}\nabla\theta$, we obtain

$$\chi = \frac{1}{q} \int_0^{\theta} \frac{\mathbf{B} \cdot \nabla\zeta}{\mathbf{B} \cdot \nabla\theta'}\, d\theta'\,. \tag{2.36}$$

Thus we obtain a 'toroidal' coordinate system (r, χ, ζ), in which the magnetic field lines are straight (see Fig. 2.10 (left)) . In Chapter 6, Eq. (2.36) is solved for a concrete magnetic field.

Now the transformation to field aligned coordinates is straightforward. We define

$$\beta \equiv (q\chi - \zeta) \bmod 2\pi\,, \tag{2.37}$$

so that the magnetic field lines are identical to $\beta = const$ lines.

2.3.2 Curvilinear coordinates

We now have to undertake a short excursus concerning curvilinear coordinates, where we refer to (D'haeseleer *et al.*, 1990). We have just derived a coordinate system consisting of the coordinates r, β, χ. In curvilinear coordinates, it is possible to define two kinds of basis vectors, leading to the concept of covariant and contravariant components of a vector (in contrast to Euclidean space, where

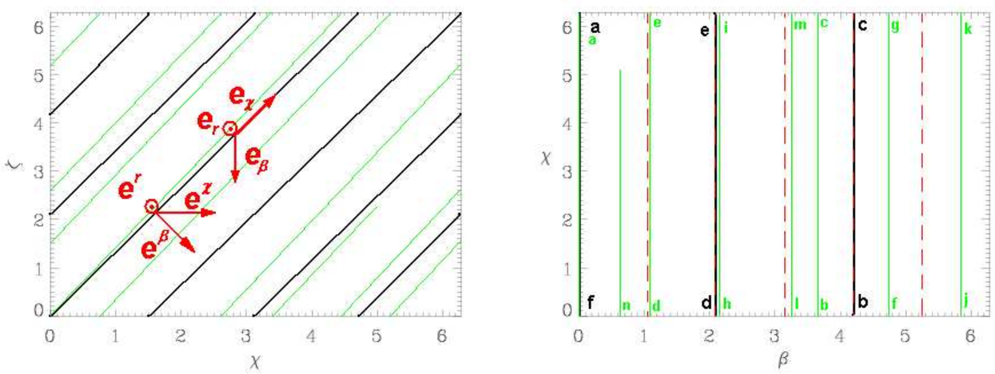

Figure 2.10: *Left*: Magnetic field lines and $r-\beta-\chi$ basis vectors in the $\chi-\zeta$ plane. Black: Magnetic field lines for $q=3/2$. They close after 3 toroidal turns. Green: Magnetic field lines for $q=\sqrt{2}$. The field lines do not close. The co- and contravariant basis vectors are drawn for the $q=3/2$ case. *Right*: The same field lines in the $\beta-\chi$ plane. The boundary conditions in the χ direction are not periodic any more. The field lines jump from a to b, from c to d etc. The red dashed lines indicate a possible division of the flux surface into 6 flux tubes.

such a distinction does not exist). This goes together with two possible sets of basis vectors. The *tangent (covariant) basis vectors* are defined as

$$\mathbf{e}_r \equiv \frac{\partial \mathbf{R}}{\partial r}, \qquad \mathbf{e}_\beta \equiv \frac{\partial \mathbf{R}}{\partial \beta}, \qquad \mathbf{e}_\chi \equiv \frac{\partial \mathbf{R}}{\partial \chi}, \tag{2.38}$$

the *reciprocal (contravariant) basis vectors* are defined as

$$\mathbf{e}^r \equiv \nabla r, \qquad \mathbf{e}^\beta \equiv \nabla \beta, \qquad \mathbf{e}^\chi \equiv \nabla \chi. \tag{2.39}$$

Whereas the covariant basis vectors are parallel to the coordinate curves, the contravariant basis vectors are perpendicular to the constant coordinate surfaces. In Fig. 2.10 (left), straight field lines are drawn in the $\chi-\zeta$ plane for two different safety factors, and the co- and contravariant basis vectors are indicated as defined by Eqs. (2.38) and (2.39). A vector $\mathbf{a}$ can be represented by covariant components $a_i = \mathbf{a}\cdot\mathbf{e}_i$ and by contravariant components $a^i = \mathbf{a}\cdot\mathbf{e}^i$. Since $\mathbf{e}^i\cdot\mathbf{e}_j = \delta^i_j$, the vector $\mathbf{a}$ can be represented in field aligned coordinates as

$$\mathbf{a} = a^r\mathbf{e}_r + a^\beta\mathbf{e}_\beta + a^\chi\mathbf{e}_\chi. \tag{2.40}$$

The basis vectors are the *covariant* unit vectors. $\mathbf{e}_r$ points into the *radial* direction (r in torus coordinates), $\mathbf{e}_\beta$ points into the *toroidal* direction, and $\mathbf{e}_\chi$ points *along the magnetic field lines* (see Fig. 2.10, left). Now the components a^i of $\mathbf{a}$ are the projections onto the *contravariant* basis vectors. This means a^r is the projection onto the *radial* direction, a^β is the projection onto a direction *perpendicular to the field lines as well as to* $\mathbf{e}_r$, and a^χ is the projection onto the 'poloidal' coordinate χ.

Two components of the field aligned coordinates have still the dimension of an angle. In order to convert them into space coordinates, the following transformation can be performed:

$$x \equiv r, \qquad y \equiv \frac{r_0}{q_0}\beta, \qquad z \equiv q_0 R_0 \chi\,. \tag{2.41}$$

The normalization of the coordinate y corresponds to a projection of the contravariant component a^β of a vector onto the poloidal direction. The projection of the full angle $\Delta\beta = 2\pi$ results in a poloidal length of $2\pi r_0/q_0$. The z coordinate is normalized to the length of a magnetic field line at one poloidal circumference. It is important to keep in mind that the direction of a field aligned coordinate is not the same than the corresponding direction onto which the vector is projected. For example, the y (β) coordinate is called both 'toroidal' and 'poloidal' in the literature, depending on whether its co- or contravariant direction is meant. A particle that moves into the y direction in field aligned coordinates moves into the *toroidal* direction in the torus, however, the length it travels is measured in terms of its *poloidal* deviation from its initial field line.

2.3.3 Flux tube coordinates

In radially local simulations, one does not simulate turbulence in the whole torus, but in so-called flux tubes. A flux tube is a tube with rectangular cross section following a magnetic field line for one poloidal turn ($z = 2\pi q_0 R_0$). In Fig. 2.10 (right), for example, the flux surface is divided into six flux tubes. Only one of them is taken as the simulation volume, and in the x (r) and y (β) direction, periodic boundary conditions are used. So x and y can be defined as

$$x \equiv (r - r_0) \bmod (\Delta r), \qquad y = \frac{r_0}{q_0}\Big((\beta - \beta_0) \bmod (2\pi/M)\Big)\,, \tag{2.42}$$

where M is the number of flux tubes to cover the flux surface. The contour plots in Section 2.2 show cross sections of such flux tubes. However, there are complications using the flux tube geometry. As can be seen from Fig. 2.10 (right), there is no natural periodicity in the z (χ) direction, since a magnetic field line exiting at $\chi = 2\pi$ at a certain β re-enters at $\chi = 0$, but at a different β. For a rational safety factor, this problem can be avoided by chosing the right number of flux tubes. In our example, we have $q = 3/2$, and dividing the $\beta - \chi$ plane into $M = 3n$ flux tubes means that although a jump in β occurs, the transit in y as defined by Eq. (2.42) is continuous, as can also be seen in the figure. For an irrational safety factor, however, such a 'trick' is not possible anymore. For turbulence simulations with GENE, the boundary conditions can be adjusted so that when leaving the flux tube in the z direction, the particle makes a jump in the y direction so that in the $\chi - \zeta$ plane, its motion is continuous. For the electrostatic potential, for example, this can be written as $\phi[r, \beta(\chi + 2\pi, \zeta), z(\chi + 2\pi)] = \phi[r, \beta(\chi, \zeta), z(\chi)]$. Another possible - and more simple - 'trick' is to simply enforce $\phi[r, \beta, z = \pm q_0 R_0 \pi] \equiv 0$. In this case, the boundary conditions are irrelevant, given the fact that no correlation shall be preserved. In Chapter 6, we will adopt the latter way, since we will find that the projection of stochastic potentials from flux tube coordinates into the full torus is most convenient to establish in that way and, at the same time, reasonably realistic, given the fact that the turbulent fluctuations tend to peak at the low-field side of the torus.

2.4 Normalization

Particle motion and turbulence in a tokamak occur on a wide range of spatial and temporal scales. For a thermal particle with $E = 10\,\mathrm{keV}$ and a magnetic field of $B = 5\,\mathrm{T}$, for example, the gyroradius is $\rho_i = 2.9\,\mathrm{mm}$ for deuterium ions, and $\rho_e = 0.067\,\mathrm{mm}$ for electrons. The gyrofrequencies are $\Omega_i = 4.8\times10^8\,1/\mathrm{s}$ and $\Omega_e = 8.8\times10^{11}\,1/\mathrm{s}$. For convenience as well as for numerical purposes, it is useful to normalize these quantities to dimensionless values. For studying the interaction between particle orbits and plasma turbulence, it will turn out that transport often scales with dimensionless values, e.g. the ratio between an orbit scale and a turbulence scale. In Chapters 3 to 5, the particle gyroradius is normalized to a correlation length of the turbulent vortices, and the time is normalized to a gyration period.

In gyrokinetic simulations, however, it is common to use different normalizations, which are adopted in this work in Chapters 6 to 10. As a typical length scale for ITG and TEM driven turbulence, the Larmor radius for an ion with thermal velocity $c_i \equiv \sqrt{T_i/m_i}$ is taken, which is $\rho_i = c_i m_i/(eB)$. Alternatively, the ion sound speed $c_s \equiv \sqrt{T_e/m_i}$ can be used, which defines a Larmor radius ρ_s. As a typical time scale, it mostly is not useful to take the gyration period, since the gyration is normally treated via gyroaveraging (see Section 2.1.4). Instead, one uses the time a particle needs to cross a typical macroscopic length in the plasma, $L_\perp/c_{i,s}$. A typical velocity is therefore $\rho_i c_i/L_\perp$. In this work, $L_\perp \equiv R_0$ is used. Denoting the dimensionless values with a hat, we obtain:

$$\hat{x} = x/\rho_i, \qquad \hat{y} = y/\rho_i, \qquad \hat{t} = t\,c_i/R_0, \qquad \hat{v} = v\,R_0/(c_i\rho_i) \qquad \hat{\phi} = \phi\,R_0/(Bc_i\rho_i^2)\,. \tag{2.43}$$

The electrostatic potential is adjusted so that the equations of motion become dimensionless. For example, Eq. (2.10) now reads

$$\hat{\mathbf{v}}_E = -\nabla\hat{\phi}\times\mathbf{e}_z\,. \tag{2.44}$$

One more advantage of dimensionless values is that macroscopic quantities like temperature, magnetic field, or torus radius do not appear anymore in the equations of motion. So the formation of turbulence as well as the interaction with energetic particles can be studied independently from concrete machine parameters. If the real transport values in SI units are needed, one simply has to insert the machine sizes and the temperature into the transformation equations. In the subsequent chapters, the hats are neglected if it is clear that normalized units are used.

2.5 Diffusion

In this work, the transport of test particles is studied primarily in terms of the diffusion coefficient. Diffusion is governed basically by the turbulent structures of the plasma, which makes it essential to establish a connection between diffusivity and the statistical properties of the particles and the plasma. In this section, some basic relations concerning the diffusion coefficient and its relation to Lagrangian and Eulerian statistics are presented, as well as some comments about the diffusive nature of transport in plasma turbulence.

2.5.1 Diffusion coefficient and Taylor formula

The following construction of the diffusion coefficient follows, in part, (Balescu, 2005), Chap. 11.

The density profile $n(\mathbf{x}, t)$ obeys the continuity equation

$$\partial_t n(\mathbf{x}, t) = -\nabla\Gamma(\mathbf{x}, t)\,. \tag{2.45}$$

Assuming that the particle flux Γ consists of two contributions, a *convective* part, characterized by a velocity $\mathbf{u}(t)$, and a *diffusive* part that is phenomenologically related to the density gradient, one obtains 'Fick's law'

$$\Gamma(\mathbf{x}, t) = \mathbf{u}(t)n(\mathbf{x}, t) - D(t)\nabla n(\mathbf{x}, t)\,, \tag{2.46}$$

where $D(t)$ is the *running diffusion coefficient*. Merging the two equations, we arrive at the *advection-diffusion equation*

$$\partial_t n(\mathbf{x}, t) = -\mathbf{u}(t)\nabla n(\mathbf{x}, t) + D(t)\nabla^2 n(\mathbf{x}, t)\,. \tag{2.47}$$

Since $n(\mathbf{x}, t)$ can also be interpreted as the probability density of finding a particle at a point $\mathbf{x}$ at a time t, the average displacement in the x direction can be calculated from Eq. (2.47) to (Balescu, 2005)

$$d_t\langle x(t)\rangle = d_t N^{-1}\int d\mathbf{x}\, x\, n(\mathbf{x}, t) = u_x(t)\,. \tag{2.48}$$

The angular brackets denote ensemble averaging. In the same manner, one obtains

$$d_t\langle x^2(t)\rangle = d_t N^{-1}\int d\mathbf{x}\, x^2 n(\mathbf{x}, t) = 2[d_t\langle x(t)\rangle]\langle x(t)\rangle + 2D_x(t)\,. \tag{2.49}$$

Defining the mean square displacement in the x direction as

$$\langle \delta x^2(t)\rangle = \langle x^2(t)\rangle - \langle x(t)\rangle^2 = \langle [x(t) - \langle x(t)\rangle]^2\rangle\,, \tag{2.50}$$

we finally find the relation

$$D_x(t) = \frac{1}{2}\frac{d}{dt}\langle \delta x^2(t)\rangle\,. \tag{2.51}$$

This relation between the mean square displacement and the diffusion coefficient was first derived by (Einstein, 1905) in his famous disquisition on Brownian motion. It is important to emphasize that if $\nabla n = 0$ and $u = 0$, there is no particle flux ($\Gamma = 0$), however $D \neq 0$ and therefore $\frac{d}{dt}\langle \delta x^2(t)\rangle \neq 0$ are possible. This case is called *self diffusion* or *tracer diffusion*, in contrast to classical *Fickian diffusion* or *chemical diffusion*, which is driven by a concentration gradient and therefore results in a net transport of mass (see Eq. (2.47)). The difference between tracer diffusion and diffusion by fluxes is further discussed in Section 2.5.2.

In the case of a diffusive motion, $D(t \to \infty) \to const$, and the diffusion coefficient is an adequate quantity to describe transport. In that case, it is also possible to define a diffusion coefficient via

$$D'_x(t) = \frac{1}{2}\frac{1}{t}\langle \delta x^2(t)\rangle \,, \tag{2.52}$$

which equalizes Eq. (2.51) for $t \to \infty$. However, transport may also be of nondiffusive nature. In general, the scaling of the mean square displacement can be written

$$\langle \delta x_i^2(t)\rangle \propto t^\mu \,, \tag{2.53}$$

Only for $\mu = 1$, one has standard diffusive behavior, while for $\mu < 1$ and $\mu > 1$, one has sub- and superdiffusive scaling, respectively.

In the next step, it shall be shown under which conditions diffusive behavior can occur. Starting from Eq. (2.51), we can do some transformations:

$$\begin{aligned} D_x(t) &= \frac{1}{2}\frac{d}{dt}\langle x(t)^2\rangle = \langle v_x(t)x(t)\rangle = \langle v_x(t)\int_0^t d\xi\, v_x(\xi)\,\rangle = \\ &= \langle \int_0^t d\xi\, v_x(t)v_x(\xi)\,\rangle = \langle \int_0^t d\xi\, v_x(0)v_x(\xi)\,\rangle \equiv \int_0^t d\xi\, L_{v_x}(\xi) \,. \end{aligned} \tag{2.54}$$

The substitution from $v_x(t)$ to $v_x(0)$ is possible since an autocorrelation function is an even function. Eq. (2.54) is the famous *Taylor formula* first derived by (Taylor, 1920). In the literature, it is sometimes referred to as the *Green-Kubo formula*, according to (Green, 1951) and (Kubo, 1957). However, since it can clearly be attributed to Taylor, his name shall be used in this work. The importance of this formula lies in the connection between the diffusion coefficient and the *Lagrangian* autocorrelation function of the particle velocities,

$$L_{v_x}(t) \equiv \langle v_x(0)v_x(t)\rangle \,. \tag{2.55}$$

It means that the diffusivity becomes a constant if the autocorrelation function decreases to zero. This means that the particle has to decorrelate completely, i.e. it loses all its memory about its initial values. As long as a positive autocorrelation remains, the diffusion coefficient is growing ($\mu > 1$), but if L_{v_x} becomes negative, D is decreasing with time. **The importance of the Taylor formula for this thesis lies in the connection between the concepts of decorrelation and diffusion.** The *Lagrangian* autocorrelation is determined at points following the motion of single particles, i.e. concrete trajectories. However, they are unknown in general. What is known are the statistical quantities of the particle's stream function. In the case of $E \times B$ drift motion, the electrostatic potential $\phi(\mathbf{x}, t)$ is the stream function. We can define the *Eulerian* autocorrelation function to

$$E(\mathbf{x}, t) \equiv \langle \phi(0,0)\phi(\mathbf{x}, t) \rangle \,, \tag{2.56}$$

and, together with Eq. (2.44),

$$E_{v_x}(\mathbf{x}, t) \equiv \langle v_x(0,0) v_x(\mathbf{x}, t) \rangle = -\frac{\partial^2 E(\mathbf{x}, t)}{\partial y^2} \,. \tag{2.57}$$

So the autocorrelation of the particle velocity field is the second derivative of the autocorrelation of the potential. This means, for example, that the correlation lengths are not necessarily identical. This fact will be of some importance in Chapters 6 and 7.

The *Eulerian* autocorrelation functions are defined as statistical averages evaluated at fixed points in the laboratory frame. They can be calculated numerically by replacing the ensemble average by an average over space and time, i.e.

$$E(\mathbf{x}, t) = \lim_{X \to \infty} \lim_{T \to \infty} \frac{\int_{-X}^{X} \int_{-X}^{X} \int_{-T}^{T} \phi(\mathbf{x}', t')\phi(\mathbf{x}' + \mathbf{x}, t' + t) d^2x' dt'}{8X^2 T} \,. \tag{2.58}$$

For our purposes, correlation functions are not normalized to 1, since their absolute values are important.

"The analysis of turbulent diffusion in continuous velocity fields relies on the general problem of relating the Lagrangian and the Eulerian statistical quantities. [...] This is, in a sense, the fundamental problem of turbulence" (Vlad *et al.*, 1998). Many attempts have been made to find a way to calculate Lagrangian quantities out of Eulerian ones, namely the *Corrsin approximation* (Corrsin, 1959) and the *decorrelation trajectory method* (Vlad *et al.*, 1998; Vlad *et al.*, 2004), however, it could be shown that they all are only valid for weak turbulence, but not in cases when effects of vortex trapping become dominant (Hauff, 2006; Hauff & Jenko, 2006), which is the case in tokamak turbulence. So, a simple possibility of calculating particle diffusivities directly out of the statistical values of the stream function does not exist. Nevertheless, there is an important point we can reason. In the case that $E(\mathbf{x}, t)$ (and therefore $E_v(\mathbf{x}, t)$) decays to zero at a typical *correlation time* τ_c and a *correlation length* λ_c, $L_v(t)$ has to do the same, since the particle velocities lose correlation independent from their concrete trajectory. As we will see in the following chapters, such a loss of memory is always given for particles in plasma turbulence (see, for instance, Fig. 2.5). In Chapter 5, possible *coherent structures* in a plasma, i.e. zones in which a finite Eulerian correlation remains, are examined, and it is found that they can support nondiffusive transport (i.e. finite Lagrangian autocorrelations) for longer times, but not forever.

2.5.2 Tracer diffusion and plasma flux

The tracer diffusion coefficient D and the plasma flux Γ are two distinct ways to describe transport in plasmas. The former quantity rather reflects the mixing properties of a turbulent flow, but is not connected with a transport of mass, as long as $\langle \mathbf{v} \rangle = 0$. The latter quantity, in contrast, describes the net transport of a plasma, but it may be zero although there is a finite single particle diffusion. A dependence between the total particle flux and the diffusion coefficient is given by Eq. (2.46), however, the convective part $\mathbf{u}(t)$ is an unknown quantity, if one only knows D or Γ. For example, it is possible that there is an inward flux due to the *pinch effect* (Nycander & Yankov, 1995), which produces an inward density gradient. This density gradient is in turn responsible for an outward diffusive flux, which may balance the inward one. Moreover, a connection as phenomenologically established in Eq. (2.46) does not need to exist at all, since in a plasma, effects like 'up-gradient transport' (Wagner & Stroth, 1993; Nycander & Yankov, 1996) or 'avalanche transport' (Carreras *et al.*, 1999a) may occur, which cannot be described as diffusive processes.

The diffusivity can be measured by inserting test particles into the turbulent field and tracking them. Whereas this method is quite difficult to establish in experimental devices (see, e.g. (Fasoli *et al.*, 1992)), it is easily accessible numerically. The diffusivity is obtained by Eq. (2.51). The particle flux or 'cross-field transport' is obtained measuring $\Gamma = \langle \tilde{n}\tilde{v} \rangle$, where the tildes denote the fluctuating parts of the corresponding quantities. This is the value usually obtained from experimental measurements (see, e.g., (Carreras *et al.*, 1996)), but also from numerical simulations of plasma turbulence. From this definition of Γ, it also becomes clear that the cross-field transport is zero in the case that $\tilde{n}$ and $\tilde{v}$ are out of phase. There are not many works trying to establish a connection between D and Γ, since in general it seems to be accepted that these two views have to be distinguished. However, in (Basu *et al.*, 2003), it was shown via simulations of Hasegawa-Wakatani turbulence (Hasegawa & Wakatani, 1983), that a simple connection via Fick's Law, $D = \Gamma/(\nabla n_0)$, is valid in the case that $L_n \equiv (\nabla n_0/n_0)^{-1} = const.$

2.5.3 The passive particle approach

In this thesis, the energetic particles will be treated as passive particles. This means that, in contrast to active ones, their motion does not act back onto the electric and magnetic fields or onto the motion of the thermal 'bulk' particles. Such passive particles are also labeled as *tracers*. This approximation seems to be well justified by several previous investigations (Estrada-Mila *et al.*, 2006; Dannert *et al.*, 2008; Angioni & Peeters, 2008) in which no significant differences were found between passive and active treatment of the fast particles in the low-density limit. More specifically, Ref. (Angioni & Peeters, 2008) as well as Ref. (Fülöp & Nordman, 2009) find that the passive tracer picture is valid for concentrations up to about 2%. For the fast particles we are interested in, namely alpha particles created in fusion reactions and beam ions inserted from outside for heating purposes, this restriction is, in general, fulfilled.

2.5.4 Turbulent diffusion

The diffusion of particles in turbulent plasmas is dominated (in general) not by collisions as in classical molecular diffusion, but by an advection with the turbulent vortices. It is the randomness of the stream function which enables us to adopt the concept of diffusion. In the gyrocenter approximation, the equations of motion for a particle in a tokamak are given by Eq. (2.18). Turbulent structures which enforce diffusive transport are given by both the electric and the magnetic field. Whereas the electric field is purely turbulent (due to *quasineutrality*, no macroscopic electric field may exist in a plasma), the magnetic field is macroscopic, but has a small turbulent part. Denoting the turbulent parts with a tilde, one can write $\phi(\mathrm{x},t) = \tilde{\phi}(\mathrm{x},t)$ and $\mathbf{B}(\mathrm{x},t) = \mathbf{B}_0(\mathrm{x}) + \tilde{\mathbf{B}}_\perp(\mathrm{x},t)$. It is a common assumption that $\tilde{\mathbf{B}} = \tilde{\mathbf{B}}_\perp$, which is also used in this work and justified for $\tilde{B} \ll B_0$, which is the case in tokamaks.

The turbulent velocity can be expressed as (Liewer, 1985)

$$\tilde{\mathbf{v}}_\perp = -\frac{\nabla\phi \times \mathbf{B}_0}{B_0^2} + v_\parallel \tilde{\mathbf{B}}_\perp / B_0 \,. \tag{2.59}$$

The first term on the right hand side is the $E\times B$ drift which we already know, the second term describes the deviation of a particle from the unperturbed field line caused by the perpendicular turbulent component of B, i.e., it follows the perturbed field line. Since we assume that the perturbed magnetic field is perpendicular, it can be expressed via the vector potential $\tilde{\mathbf{A}}(\mathbf{x}) = \tilde{A}_\parallel(\mathbf{x})\mathbf{e}_z$. So Eq. (2.59) can be rewritten as

$$\tilde{\mathbf{v}}_\perp = -\frac{\nabla\phi \times \mathbf{e}_z}{B_0} + v_\parallel \frac{\nabla\tilde{A}_\parallel \times \mathbf{e}_z}{B_0} \,. \tag{2.60}$$

Interestingly, the mathematical structure of the magnetic part has turned out to be identical to the electrostatic part. For this reason, the main part of this thesis (Chapters 3 to 6) deals with particle transport in electrostatic turbulence, whereas the magnetic part is treated in the last parts (Chapters 7, 8 and 10), mainly by analogy to the electrostatic results.

2.6 Influence of turbulent structures on particle orbits

In this section, an overview of the various interactions between particle orbits and turbulent structures is provided. It will be the basis for the step-by-step approach applied in this thesis.

2.6.1 2D effects (electrostatic)

In a first step, we neglect the effects generated by the 3D structure of the magnetic field (∇B drift, curvature drift, motion parallel to $\mathbf{B}$, see Eq. (2.18)) and restrict to the 2D motion perpendicular to the magnetic field, which is given by Eq. (2.60). Since the electrostatic and the magnetic part have equivalent

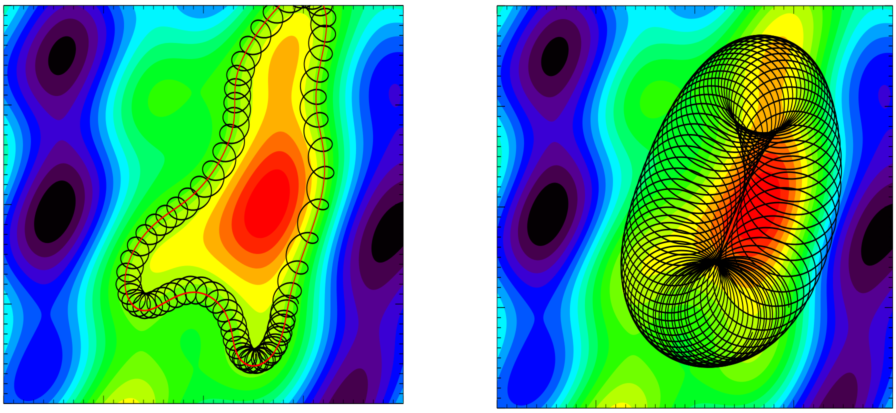

Figure 2.11: Full Lorentz motion of a particle in an electrostatic potential. *Left*: Small Larmor radius. *Right*: Larger Larmor radius

structure, we may further restrict to the $E \times B$ drift part. So in dimensionless units and flux tube coordinates, the differential equation is

$$\begin{aligned} \dot{\mathbf{x}}(t) &= \mathbf{v}_E(t), \\ \dot{\mathbf{v}}_E(t) &= -\nabla\phi(\mathbf{x},t) \times \mathbf{e}_z = \begin{pmatrix} -\partial_y\phi \\ \partial_x\phi \end{pmatrix}. \end{aligned} \tag{2.61}$$

This means that, for a static potential, the particle moves on equipotential lines. To include finite Larmor radius effects, ϕ has to be replaced by the gyroaveraged potential ϕ^{eff}, as described in Sec. 2.1.4. In Fig. 2.11, the full Lorentz motion of a particle is shown for a static potential. Whereas for a small gyroradius (left picture) the particle follows the equipotential lines strictly, for a larger gyroradius this is only roughly the case, since the structure of the gyroaveraged potential is different to the original one. We note in passing that, in Eq. (2.61), x and y are canonical conjugate variables. This means that, although the problem is 2D, there is only one degree of freedom, wherefore the problem is completely integrable, which can be seen in Fig. 2.11.

It is clear that for the $E \times B$ drift to induce a diffusive particle motion, the stream function ϕ has to be time dependent. If the vortex structure is changing, no closed trajectories are possible any more, and - if the changes are irregular - the particle moves in a random, i.e. diffusive, manner. In Fig. 2.12, the (Lorentz) trajectory of a particle in a weakly time dependent potential is shown. The particle circles its initial vortex several times. When the vortex decays, the particle gets free and follows an open equipotential line, until a new vortex emerges and traps the particle again. The question which now arises is: How can the diffusivity be determined from the scales of the stream function? It will turn out that there are two distinct regimes, which can be distinguished by the so-called *Kubo number* (Kubo, 1963; Vlad *et al.*, 1998)

$$K \equiv \frac{V\tau_c}{\lambda_c} \equiv \frac{\tau_c}{\tau_{\text{fl}}}\,. \tag{2.62}$$

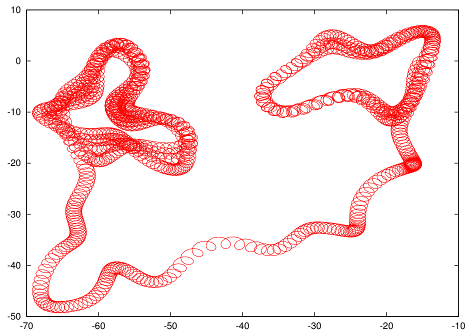

Figure 2.12: Full Lorentz motion of a particle in an slowly time variable electrostatic potential. A sequence of trapping and release processes can be observed.

Here, V denotes the mean $E{\times}B$ drift velocity ($= V_E$) (or, in the magnetic case, the mean perpendicular velocity V_B), τ_c is the correlation time of the turbulent stream function, and λ_c its correlation length, where we assume isotropy for the moment. Following Eq. (2.57), the mean drift velocity V_E can be calculated as

$$V_E = \left(- \left. \frac{\partial^2 E(\mathbf{x}, t)}{\partial y^2} \right|_{\mathbf{x}=t=0} \right)^{1/2} . \tag{2.63}$$

The *mean time of flight* $\tau_{\mathrm{fl}} \equiv \lambda_c / V$, is the average time it takes for a particle to travel the distance of one correlation length, i.e. to 'feel' the topology of the stream function.

Small Kubo number regime

If $K < 1$, $\tau_c < \tau_{\mathrm{fl}}$. This implies that a particle decorrelates before it 'feels' the structure of the vortices, which means that the correlation length λ_c is not able to influence the transport. In this case, only the temporal part of the Eulerian autocorrelation function is important, and we can assume $E = E(t) \equiv L(t)$ or $E_{v_x} = E_{v_x}(t) \equiv L_{v_x}(t)$. Choosing an exponential decrease $L_{v_x}(t) = V_x^2 e^{-t/\tau_c}$, we obtain, solving Eq. (2.54),

$$D_x(t) = V_x^2 \tau_c \left(1 - e^{-t/\tau_c} \right) . \tag{2.64}$$

So the saturation value ($t \to \infty$) of the diffusion coefficient is

$$D_x = V_x^2 \tau_c \,, \tag{2.65}$$

whereas the running diffusion coefficient for $t \ll \tau_c$ is

$$D_x(t) = V_x^2 t \,. \tag{2.66}$$

Thus, the saturation value of Eq. (2.65) is simply the value at $t = \tau_c$. A $D(t)$ curve for a small Kubo number is plotted in Fig. 2.13 (red dashed curve). The superdiffusive regime directly passes into the diffusive regime at $t = \tau_c$. It should be mentioned that small deviations from this expressions may occur,

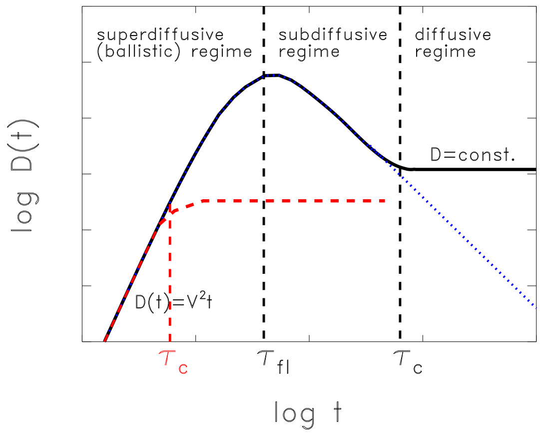

Figure 2.13: Running diffusion coefficient. Black, solid: $D(t)$ for a high Kubo number. The superdiffusive, subdiffusive and diffusive regimes are enlisted. Red, dashed: $D(t)$ in the low Kubo number regime. The saturation value is $D \approx V^2\tau_c$. Blue, dotted: $D(t)$ for a static potential ($K \to \infty$).

depending on the concrete form of $L_{v_x}(t)$. If for example $L_{v_x}(t) = V_x^2 e^{-t^2/\tau_c^2}$ is chosen, the saturation values gives $D_x = \sqrt{\pi}/2\, V_x^2 \tau_c$.

The above relations can be derived in a more simple way, too, referring to the simple example of a classical one dimensional random walk. Here, a particle undergoes a successive sequence of steps with fixed step size Δx and fixed time step Δt. The direction of each step is determined randomly. Then, the diffusion coefficient is determined by (Einstein, 1905) $D_x = (\Delta x)^2/(2\Delta t)$. According to the previous considerations for the small Kubo number limit, we can set $\Delta x \equiv V_x\tau_c$ and $\Delta t \equiv \tau_c$, so that we also obtain Eq. (2.65), apart from a factor 2 which is due to the discretization. For times $t < \tau_c$, $\langle x^2\rangle = (V_x t)^2$, so according to Eq. (2.51), the running diffusion coefficient is given by $D_x(t) = V_x^2 t$, as already derived in Eq. (2.66).

Large Kubo number regime

For $K > 1$ ($\tau_{\mathrm{fl}} < \tau_c$) the particles are able to 'feel' the vortex structure. The particle trajectory plotted in Fig. 2.12 is an example for a large Kubo number regime. As soon as $t > \tau_{\mathrm{fl}}$, the particles are able to circle the vortices; they are trapped. This *vortex trapping* forces a decreasing $\langle x^2(t)\rangle$, which means that $D(t)$ is reduced, too. In a static potential, the particles would be trapped forever, and $D(t)$ would go to zero. However, given a time dependence, decorrelation and saturation of $D(t)$ occur at $t = \tau_c$. The three successive regimes of diffusion are shown in Fig. 2.13 in black.

Is it possible to make a similar quantitative approach for the saturation value D than we just did for the small Kubo number regime? A simple approach would assume particle trapping for a time τ_c, and, when they are released, the particles can travel an average distance of a correlation length λ_c. So setting $\Delta x = \lambda_c$ and $\Delta t = \tau_c$, one would obtain $D = \lambda_c^2/\tau_c$. However, this is not correct, since reality turns out to be much more complex. As can be seen, for example, in the contour plots of Section 2.2, there are equipotential lines which are bound to vortices (typically for large and small values of ϕ), but also equipotential lines which meander between the vortices, without a clear space scale (typically for $\phi \approx 0$). For particles on the latter structures, the small Kubo number expression may be more appropriate, since the particles are not trapped. In reality, in the large Kubo number regime there is always a mixture of trapped and untrapped particles, with exchanges between these two species on the time scale of the correlation time of the stream function. Another, formally widely used approach is the so-called 'Bohm scaling' (see, e.g., (Misguich *et al.*, 1987)). There, the Corrsin approximation (see discussion in Section 2.5.1) is used and leads to a scaling $D \propto \lambda_c V$. It is obvious that this scaling cannot be correct, since it would imply a finite diffusion coefficient even for static potentials, which is impossible due to the trapping effects. So, simple intuitive approaches are not valid in this case.

In fact, finding a scaling law for D with respect to the characteristic turbulence parameters τ_c, λ_c, and V is quite difficult. It was given in the beautiful theoretical work of (Gruzinov *et al.*, 1990), using methods of percolation theory. A general review of percolation theory, including the work of Gruzinov et al., can be found in (Isichenko, 1992). The treatment of Gruzinov starts with a simple model potential $\psi_0(x, y) = \sin x \sin y$, whose separatrices constitute a periodic square lattice. A weak time dependence (modeling very large Kubo numbers) is introduced, which allows for a connection of equipotential lines across the separatrices around the saddle points. An expression for the lifetime τ_h of a contour $\psi = h \ll 1$ (with the maximum of the potential normalized to unity) is estimated by $\tau_h \approx h\tau_c$. Finally, an expression for the diffusion coefficient is found, which is

$$D \approx \lambda_c^{1.3} V^{0.7} \tau_c^{-0.3} \tag{2.67}$$

for $K \gg 1$. In contrast to the simple expressions presented above, there is a quite complex interaction of all three statistical values. Interestingly, although the Gruzinov estimation was achieved using a simplified model, its validity for isotropic turbulence is excellent and has been approved in a number of numerical simulations (Reuss, 1996; Reuss *et al.*, 1998), also in this thesis.

General expression

Since the dimension of D is m^2/s, a general expression for its scaling can be given by $D \propto \lambda_c^2/\tau_c K^\gamma$, or

$$D \propto \lambda_c^{2-\gamma} V^\gamma \tau_c^{\gamma-1} \, . \tag{2.68}$$

Hence, the above expressions are reproduced by setting $\gamma = 2$ for $K < 1$ and $\gamma = 0.7$ for $K > 1$. The wrong expression $D \propto \lambda_c^2/\tau_c$ would be obtained by $\gamma = 0$, which indicates that the true high Kubo number scaling indeed lies between the strict trapping approach and the low Kubo number limit. For $K \approx 1$, we can state $\gamma = 1$, since in that case, $\tau_c \approx \lambda_c/V$.

Once more we want to stress the importance of the scaling laws we just obtained. In the low Kubo number limit, there are no trapping effects, since decorrelation of the particles occurs before they are able to circle the turbulent vortices. Therefore, the diffusion coefficient does not scale with λ_c, but is dependent only on V and τ_c. The diffusivity increases with V and τ_c, since the distance a particle can travel before decorrelating increases in both cases. In the high Kubo number regime, particle trapping becomes important, which makes the specification of a scaling law much more complicated. Because of trapping, the correlation length λ_c influences the diffusivity now, together with V and τ_c. The diffusivity increases with λ_c and V, since in the former case, the distance a particle can travel while being trapped increases, and in the latter case, since a particle which is not trapped moves a wider distance. In contrast to the low Kubo number case, the diffusivity decreases with growing τ_c, since particles are trapped for a longer time, which restricts their motion. The inclusion of finite gyroradius effects into the scaling laws presented here is an important part of this work and discussed in Chapters 3 and 4.

2.6.2 3D effects

So far, we have discussed the scaling of D with the statistical parameters of the stream function in two dimensions. What is the situation in three dimensions, i.e., when Eq. (2.18) is applied? One difference is that a particle can now decorrelate due to its parallel motion along the z axis, i.e. along the magnetic field. Although the vortex lengths along the field lines are much larger than across ($\lambda_\parallel \sim 2\pi q_0 R_0 \gg \lambda_\perp$), it may become possible for fast particles that $\tau_\parallel \equiv \lambda_\parallel / v_\parallel < \tau_c$. In that case, it is the parallel decorrelation time $\tau_\parallel$ which determines decorrelation, not the correlation time of the stream function. The magnetic drifts (∇B drift and curvature drift) are responsible for deviations perpendicular to the magnetic field, as can be inferred from Eq. (2.18). Their influence on the particle orbits has been illustrated in Fig. 2.2. Now the question is, how do these orbits look like in field aligned coordinates, i.e. relative to the magnetic field lines and therefore relative to the perpendicular structure of the turbulence? The answer is given in Fig. 2.14. The trapped and the passing particle orbits show a very similar behavior in field aligned coordinates. An almost circular rotation in the $x - y$ plane is superimposed to a constant drift in the y direction. To our knowledge, this form of the orbits has never been presented in detail before in the literature, and is discussed further in Chapters 6 and 7. Whereas the oscillatory motion in the r (x) direction can also be observed in the plots of the $R - z$ plane, the (oscillatory and constant) motion in the y (toroidal) direction can be seen in the left hand picture of Fig. 2.2. It is obvious that one might try to establish a connection between the treatment of the particle's gyration with its drift orbit motion, since the behavior relative to the perpendicular structures seems to be similar. Indeed, such efforts have been made in the past (Mynick & Krommes, 1979) as well as recently (Zhang *et al.*, 2008), postulating that an 'orbit averaging' effect should be valid similar to the the 'gyroaveraging' presented in Section 2.1.4. In Chapters 6 and 7, this assumption will disputed, based on a detailed study of the orbit trajectories

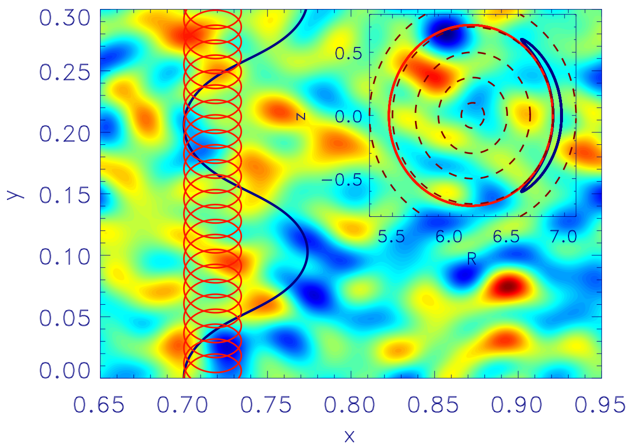

Figure 2.14: Particle orbits (in a fluctuating electrostatic potential) in field-aligned coordinates (left-hand side) and in cylindrical coordinates (embedded). Black: trapped particle with $\eta = 0.2$. Red: passing particle with $\eta = 0.99$. Some magnetic flux surfaces are shown for comparison.

illustrated in Fig. 2.14, and their space and time scales.

Chapter 3

Advection in Isotropic 2D Electrostatic Turbulence

In this chapter, the turbulent $E{\times}B$ advection of charged test particles with large gyroradii is investigated in a 2D geometry, i.e. the transport is governed by the interaction between Eq. (2.61) and the gyroaveraging mechanism described in Section 2.1.4. To this aim, direct numerical simulations are used together with analytical calculations. It is found that for Kubo numbers larger than about unity, the particle diffusivity is almost independent of the gyroradius as long as the latter does not exceed the correlation length of the electrostatic potential. The underlying physical mechanisms leading to this surprising and initially counterintuitive behavior are identified. The key results of this chapter have been published in (Hauff & Jenko, 2006).

3.1 Introductory remarks

As pointed out in the previous chapter, many basic issues of transport in turbulent plasmas are still relatively poorly understood. One such issue is the turbulent $E \times B$ advection of charged test particles with large gyroradii which has important applications both in plasma astrophysics as well as in fusion research. In the latter case, e.g., one is interested in the interaction of α particles or impurities with the background turbulence. To be able to address such topics, a thorough understanding of the dependence of the particle diffusivity on the gyroradius is required. It is the main goal of the work presented in this chapter to shed new light on this old question, thereby revealing novel insights and allowing for more accurate descriptions of such physical systems in the following chapters.

Provided that the temporal changes of the background potential are slow compared to the gyration period and that the potential amplitudes are not too large, the particles' dynamics may be treated in the spirit of gyrokinetic theory (see Section 2.1.4). This means that a gyrating particle is simply replaced by a charged ring. This 'quasiparticle' drifts with an $E{\times}B$ velocity which is computed from a gyroorbit-averaged potential. Since this process of gyroaveraging always reduces the effective drift velocity, one would naively expect that the resulting particle diffusivity is also reduced. It is one of the key findings presented in this chapter, however, that this conclusion is not justified. In fact, we will be able to show that in a strong turbulence situation, the diffusivity is more or less independent of the gyroradius as long as the latter does not exceed the correlation length of the electrostatic potential. Moreover, the underlying physical mechanisms leading to this initially counterintuitive behavior will be identified.

The basic aims of this thesis were inspired, in part, by two papers by M. Vlad and co-workers (Vlad & Spineanu, 2005; Vlad *et al.*, 2005) in which they extended the so-called decorrelation trajectory (DCT) method (Vlad *et al.*, 1998; Vlad *et al.*, 2004) for computing diffusivities from the autocorrelation function of the potential to the case of particles with finite gyroradii. This DCT method was suggested to be able to provide a solution for the old question about connecting Eulerian autocorrelation functions to the Lagrangian ones (see discussion in Section 2.5.1). The results they got were very surprising. In particular, they observed that for sufficiently large Kubo numbers (i.e., for relatively strong turbulence), the diffusivity may *increase* with increasing gyroradius by up to several orders of magnitude. Obviously, this finding is in stark contrast to the usual physical picture sketched above. However, it could be shown in (Hauff, 2006) and (Hauff & Jenko, 2006) that the DCT method does not reproduce the correct diffusivities in the high Kubo number limit, as well as that the extension of the method to large gyroradii was based on a misapprehension. However, these studies motivated us to revisit the problem of turbulent $E \times B$ advection of charged test particles with large gyroradii with a completely new ansatz.

In this chapter, at the beginning of the step-by-step approach underlying this thesis, we will restrict our studies to a rather simple situation, namely the two-dimensional dynamics of test particles in a homogeneous, static magnetic field and a prescribed electrostatic potential which is stochastic and isotropic in space and time. Such models have been used in many previous investigations (see, e.g., (Balescu, 2005) and references therein) mainly due to their accessibility in terms of numerical and analytical methods. Although the relation between the diffusivity obtained from the dispersion of test particles and the diffusion coefficient inferred from the self-consistent turbulent flux is not easy to establish (see discussion in Section 2.5.2), the study of test particle dynamics is still considered quite useful, especially if one is dealing with trace species at low density. It is our main goal at the beginning of this work to study the fundamental physical processes in a fairly clean environment. Specific applications to various situations in fusion research (and astrophysics), including a variety of additional effects, are left for the following chapters.

The dependence of the diffusivity of test particles on the gyroradius ρ has also been the subject of several previous studies beyond the ones already mentioned. E.g., in Refs. (Manfredi & Dendy, 1996; Manfredi & Dendy, 1997; Annibaldi *et al.*, 2002), finite Larmor radius (FLR) effects were studied for test particles in Hasegawa-Mima turbulence using the gyroaveraging approximation. Here, it was found that "FLR effects strongly inhibit stochastic diffusion" (Manfredi & Dendy, 1996), and that the diffusivities drop roughly as ρ^{-1} and $\rho^{-0.5}$ (or $\rho^{-0.35}$) in the low and high Kubo number regimes, respectively (Manfredi &

Dendy, 1997). These results are in agreement with naive expectations and shall also be confirmed in the present, more systematic study. Moreover, in a fairly recent investigation of the same basic type, an additional observation was made. Here, the authors find that "as long as ρ is smaller than or similar to the typical size of the [turbulent] structures, FLR effects are irrelevant" (Annibaldi *et al.*, 2002). In other words, a significant FLR reduction of the diffusivity requires the gyroradius to exceed the correlation length of the potential. While very interesting, this result was not discussed any further, however. In particular, no explanation was given in terms of the underlying physical mechanisms which lead to this behavior, and no mention was made about a possible Kubo number dependence on this effect. In fact, Refs. (Manfredi & Dendy, 1997) and (Annibaldi *et al.*, 2002) seem to contradict each other with respect to the existence of a reduction threshold in ρ. In contrast, the study presented in this chapter offers a much more detailed and systematic investigation of these issues, including the identification of the physical mechanisms at work.

The remainder of this chapter is organized as follows. After some general remarks in Section 3.2, a large number of direct numerical simulations is presented in Section 3.3, and the dependence of the diffusion coefficient on Kubo number and gyroradius is studied. The 'Gruzinov' scaling law (Eq. (2.67)) is confirmed. In Section 3.4, in the limit of small/large Kubo numbers and small/large gyroradii, analytical expressions for the ratio D_ρ/D_0 are derived which agree favorably with the simulation results. We close with some conclusions in Section 3.5.

3.2 General remarks

In this chapter, we want to start our study of the interaction of fast particles with a simple homogeneous, isotropic, stationary, and Gaussian electrostatic potential with stochastic behavior in space and time. We consider the $E \times B$ advection of ions as passive tracers in a plane perpendicular to the background magnetic field, where the corresponding spatial coordinates will be denoted as $\mathbf{x} = (x_1, x_2) = (x, y)$. Such a potential can be generated by means of a superposition of a sufficiently large number of harmonic waves:

$$\phi(\mathbf{x}, t) = \sum_{i=1}^{N} A_i \sin(\mathbf{k}_i \cdot \mathbf{x} + \omega_i t + \varphi_i)\,. \tag{3.1}$$

Its Gaussianity (concerning the distribution of the potential values) can be demonstrated with the help of the central limit theorem, regarding the characteristic numbers of the harmonic waves as a set of independent random variables. The autocorrelation function of such a potential is then easily shown to be (Hauff, 2006)

$$E(\mathbf{x}, t) = \sum_{i=1}^{N} \frac{A_i^2}{2} \cos(\mathbf{k}_i \cdot \mathbf{x} + \omega_i t)\,. \tag{3.2}$$

τ_c and λ_c denote, respectively, the autocorrelation time and length of the electrostatic potential, defined as the e-folding lengths of $E(\mathbf{x}, t)$. The mean drift velocity V can be calculated as

$$V = \left(- \left. \frac{\partial^2 E(\mathbf{x}, t)}{\partial x^2} \right|_{\mathbf{x}=t=0} \right)^{1/2} , \tag{3.3}$$

as in Eq. (2.63). The Kubo number K was already defined in Eq. (2.62). The limits $K \to \infty$ and $K \to 0$ correspond to static and fast fluctuations, respectively. Sometimes, the regime of $K \lesssim 1$ is labeled 'weak turbulence' or 'quasilinear,' while the $K \gtrsim 1$ regime is denoted as 'strong turbulence' or 'nonlinear.' The Kubo number will play an important role in the remainder of this chapter and in this thesis.

According to the discussion in Section 2.1.4, it is possible to bring the finite gyroradius problem into the form of the zero gyroradius one if the original potential is replaced by

$$\langle \phi \rangle(\mathbf{x}) \equiv \phi^{\text{eff}}(\mathbf{x}) \equiv \frac{1}{(2\pi)^2} \int_{-\infty}^{\infty} d\mathbf{k}\, e^{i\mathbf{k}\cdot\mathbf{x}}\, \phi(\mathbf{k})\, J_0(k\rho) \tag{3.4}$$

where $\phi(\mathbf{k}) \equiv \mathcal{F}\{\phi(\mathbf{x})\}$, and ρ is the Larmor radius. The corresponding Eulerian autocorrelation function E^{eff} then reads (Hauff, 2006)

$$E^{\text{eff}}(\mathbf{x}, \rho) = \frac{1}{(2\pi)^2} \int_{-\infty}^{\infty} d\mathbf{k}\, e^{i\mathbf{k}\cdot\mathbf{x}}\, E(\mathbf{k})\, J_0^2(k\rho) \tag{3.5}$$

where we have used the well-known convolution theorem. In contrast to the effective potential, the Bessel function enters squared. So the effective correlations E^{eff} and ϕ^{eff} are simply obtained by multiplying the individual Fourier components of E and ϕ by $J_0^2(k_i\rho)$ and $J_0(k_i\rho)$, respectively.

In order to create an autocorrelation function which is sufficiently smooth in space and time, we are forced to employ a sufficiently large number of partial waves. We ended up using $N = 10^5$ waves with a Gaussian amplitude spectrum of the form $A_i = A_{\max} \exp(-k_i^2/8)$. The wave numbers and frequencies are randomly and homogeneously distributed within the intervals $0 \le |\mathbf{k}_i| \le k_{\max}$ and $0 \le \omega_i \le \omega_{\max}$. We note in passing that random distributions of wave numbers lead to much smoother autocorrelations than regular lattices in wave number space (see, e.g., Ref. (Reuss, 1996)) and are therefore to be preferred. The Kubo number is controlled by varying $\omega_{\max}$. Due to this large number of partial waves, the autocorrelation function is fitted almost perfectly by a Gaussian of the form $E(\mathbf{x}) \propto \exp(-x^2)$. This means that the correlation length (defined as the e-folding length of $E(\mathbf{x})$), is normalized to unity.

Given the large number of partial waves, it is not feasible anymore to compute the potential or the autocorrelation anew for every time step of the numerical simulation. Instead, their values and those of the required derivatives are saved as three-dimensional arrays, e.g., $\phi(x_i, y_j, t_k)$. The values at intermediate space-time points are then recovered by means of cubic interpolations based on the well-known Lagrange formula. For solving the differential equations, a fourth-order Runge-Kutta method is used (Vesely, 1994). The diffusivities are computed according to the definition given in Eq. (2.51). Here, a number of a

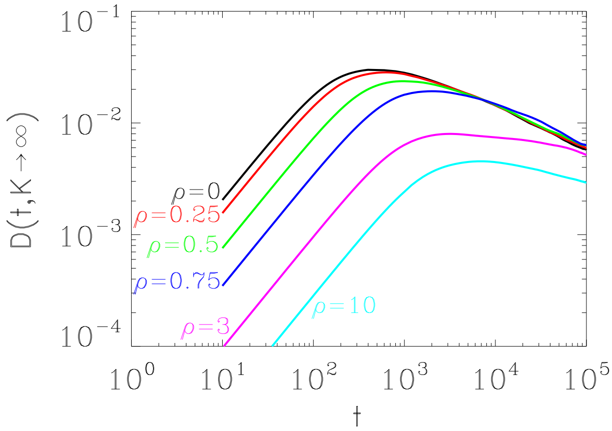

Figure 3.1: Time-dependent diffusivity $D(t)$ in a *static* potential, i.e., for $K \to \infty$, for different gyroradii ρ (normalized to the correlation length of the potential).

few thousand trajectories has been found to be sufficient. A further improvement is obtained via the 'time average' method described in Ref. (Reuss, 1996). Here, the present positions of the particles are saved and reused as new starting points.

3.3 Results of direct numerical simulations

In the present section, we will concentrate on direct numerical simulations performed in a self-generated electrostatic potential described by Eq. (3.1). The amplitude was chosen so that $V \approx 0.007$, which gives $\tau_{\rm fl} \approx 150$. The time-dependent diffusion coefficient $D(t)$ for a static potential ($\tau_c, K \to \infty$) and for a set of different gyroradii is shown in Fig. 3.1. From the discussion of Fig. 2.13 we know already that there is a correspondence between $D(t, K \to \infty)$ and $D(t \to \infty, K)$, since the latter expression can be derived from the former by assuming a transition into the diffusive regime at $t \approx \tau_c$. Therefore one can expect the K-dependent long-time diffusivities to take on similar characteristics. This is indeed the case as can be inferred from Fig. 3.2. Here, we plotted $D(t \to \infty, K)$ for several values of ρ (normalized, again, with respect to the correlation length of the potential). Here, the Kubo number has been varied varying τ_c (by adjusting $\omega_{\rm max}$) From Figs. 3.1 and 3.2, one can extract the scalings $D(t) \propto t$ and $D(K) \propto K$ for small times and small Kubo numbers, respectively, whereas for large times and large K, one finds $D(t) \propto t^{-0.4}$ and $D(K) \propto K^{-0.25}$. The latter scaling – which has a large error bar since it is based on only two points – is very close to Gruzinov's estimate of $D(K) \propto K^{-0.3}$ which is based on percolation theory (Gruzinov *et al.*, 1990) [for numerical confirmations of this theory, see, e.g., Refs. (Reuss, 1996; Reuss *et al.*, 1998)]. At this point, we have to note that, since we have varied K by variation of τ_c, the scaling law is $D(K) \propto K^{\gamma-1}$ according to Eq. (2.68), so that $\gamma = 0.75$ (0.7). For small Kubo numbers, the transport is significantly reduced with increas-

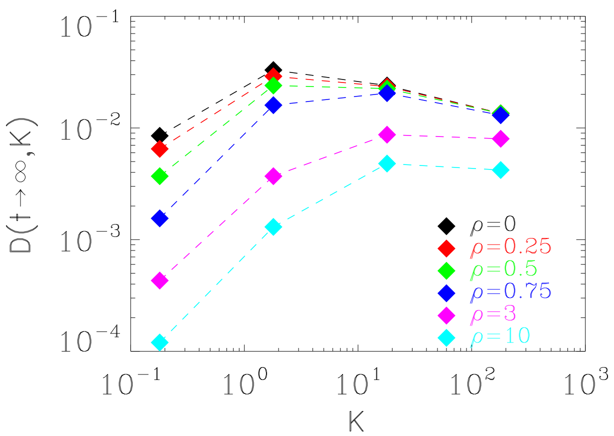

Figure 3.2: Long-time limit of the diffusivity D as a function of the Kubo number K for different gyroradii ρ (normalized to the correlation length of the potential).

ing gyroradius even for $\rho \lesssim 1$. This behavior is in agreement with numerical simulations found in the literature (see, e.g., Ref. (Manfredi & Dendy, 1996)). For larger Kubo numbers, $K \gtrsim 1$, the system's behavior is completely different, however. For $\rho \lesssim 1$, i.e., for gyroradii up to the correlation length, the transport is practically constant or even slightly increased with increasing ρ. In addition, the transport reduction with increasing ρ for $\rho \gtrsim 1$ is much slower than in the low Kubo number regime. These are key results of this first study. They correct *both* the naive expectations *and* the previous DCT-based results. In the following, we shall develop an analytical approach which helps us to understand these findings both qualitatively and even quantitatively.

3.4 An analytical approach

The analytical description of the gyroradius dependence of the diffusivity which we are about to develop will be based directly on the effective autocorrelation function. From the latter, one can infer drift velocities and correlation lengths (as well as correlation times, of course) as a function of ρ. This information can in turn be used together with the well-known Kubo number scalings in the low and high K regimes to derive expressions for the gyroradius dependence of the diffusivity. The formulas obtained this way will be shown to be in good agreement with the results from direct numerical simulations.

Qualitatively speaking, we will find the following scenarios in the case of small and large Kubo numbers. For $K \lesssim 1$, the situation is rather simple. The gyroaveraging merely smoothes out the potential and therefore reduces the effective drift velocity, leading to a significant reduction of the diffusion coefficient. For $K \gtrsim 1$, on the other hand, the presence of trapping effects introduces a new aspect. While the drift velocity is of course still reduced with increasing gyroradii, the gyroaveraging simultaneously enlarges the scales of the equipotential lines. Consequently, the gyrocenter trajectories become more

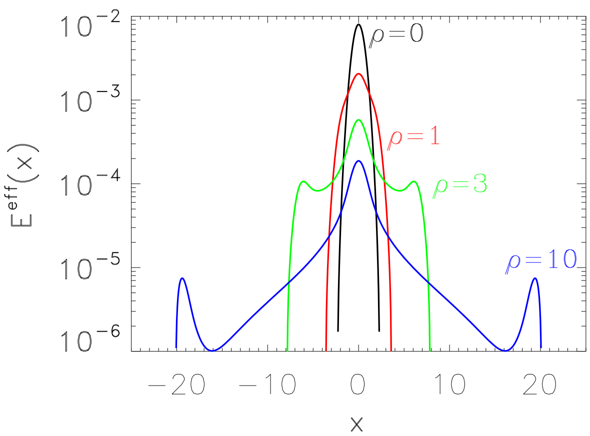

Figure 3.3: Spatial part of the effective autocorrelation function E^{eff} for different gyroradii ρ (normalized to the correlation length of the potential).

extended, counteracting the reduction of the drift velocity. [A similar effect has been discussed in (Vlad & Spineanu, 2005; Vlad *et al.*, 2005) in the context of the DCT method.] In Fig. 3.3, the effective autocorrelation function, calculated according to Eq. (3.5), is plotted for different gyroradii. The reduction of the amplitude as well as the broadening for increasing ρ can be observed. Inferior maxima are at $x = 2\rho$, where the rings surrounding the gyrocenters of the particles are tangent, which means that they get significantly correlated again. In other words, gyroaveraging correlates points in space which are actually uncorrelated.

Starting from these ideas, the goal is to find analytical expressions for both the effective drift velocity V^{eff} and the average extension of a drift trajectory which will be assumed to scale like the correlation length λ_c^{eff}. An expression for the effective autocorrelation of the gyroaveraged potential has already been given in Eq. (3.5). For spatially isotropic autocorrelation functions as we are dealing with here, the angle between $\mathbf{x}$ and $\mathbf{k}$ can be integrated out, yielding

$$E_\rho^{\text{eff}}(x) = \frac{1}{2\pi} \int_0^\infty dk\, k\, E(k)\, J_0^2(k\rho)\, J_0(kx)\,. \tag{3.6}$$

Assuming a Gaussian spatial autocorrelation of the form

$$E(x) = A\, e^{-x^2}\,, \tag{3.7}$$

which is in accordance with Eq. (3.2), we find

$$E_\rho^{\text{eff}}(x) = \frac{A}{2} \int_0^\infty dk\, k\, e^{-k^2/4}\, J_0^2(k\rho)\, J_0(kx)\,. \tag{3.8}$$

Unfortunately, this integral cannot be solved analytically. However, the factor $J_0^2(k\rho)$ can be approximated in the limits of small and large arguments. E.g., for $k\rho \lesssim 1$, we find

$$J_0^2(k\rho) = 1 - (k\rho)^2/2 + 3\,(k\rho)^4/32 - 5\,(k\rho)^6/576 + \mathcal{O}(\rho^8) \tag{3.9}$$

by means of a Taylor expansion. In this case, Eq. (3.8) yields

$$\begin{aligned} E^{\text{eff}}_{\text{small}\,\rho}(x) &= A\,e^{-x^2} - 2A\rho^2\,(1-x^2)\,e^{-x^2} \\ &+ \frac{3A\rho^4}{2}\,(2-4x^2+x^4)\,e^{-x^2} \\ &- \frac{5A\rho^6}{9}\,(6-18x^2+9x^4-x^6)\,e^{-x^2} + \mathcal{O}(\rho^8)\,. \end{aligned} \tag{3.10}$$

Using this expression, we then obtain

$$V^{\text{eff}}_{\text{small}\,\rho} = V\left[1-2\rho^2+5\rho^4/2-5\rho^6/3+5\rho^8/8+\mathcal{O}(\rho^{10})\right] \tag{3.11}$$

for the effective drift velocity. Moreover, a perturbative calculation yields

$$\lambda^{\text{eff}}_{\text{small}\,\rho} = \lambda_c\left[1+\rho^2+\rho^4/4+\mathcal{O}(\rho^6)\right] \tag{3.12}$$

for the effective correlation length. The factor $J_0^2(k\rho)$ in Eq. (3.6) suppresses shorter wavelengths and leads to an increase of the effective λ_c.

For $k\rho \gg 1$, on the other hand, the squared Bessel function is known to oscillate strongly. In this case, we thus approximate it by half of its envelope, i.e., we set

$$J_0^2(k\rho) \approx 1/(\pi k\rho)\,. \tag{3.13}$$

Eq. (3.8) then yields

$$\begin{aligned} E^{\text{eff}}_{\text{large}\,\rho}(x) &= \frac{A}{2\sqrt{\pi}\rho}\,e^{-x^2/2}\,I_0\left(x^2/2\right) \\ = \frac{A}{2\sqrt{\pi}\rho}\,e^{-x^2/2}&\left[1+x^4/16+x^8/1024+\mathcal{O}(x^{12})\right] \end{aligned} \tag{3.14}$$

where I_0 denotes the modified Bessel function of the first kind. From this expression, we obtain

$$V^{\text{eff}}_{\text{large}\,\rho} = V\,(4\sqrt{\pi}\rho)^{-1/2}\,. \tag{3.15}$$

Since the gyroradius ρ enters Eq. (3.14) just a prefactor, the effective correlation length is independent of it. The latter can be determined numerically to be

$$\lambda^{\text{eff}}_{\text{large}\,\rho} \approx 1.73\,. \tag{3.16}$$

For large gyroradii, the term $J_0^2(k\rho)$ in Eq. (3.6) reduces practically the entire k spectrum of the potential in the same way. Therefore the effective correlation length does not increase anymore. In Fig. 3.4, the effective drift velocity and correlation length are plotted for both the small and the high gyroradius approximation.

With the help of the above expressions for V^{eff} and λ_c^{eff} we are now able to estimate the resulting transport levels. In the limit of small Kubo numbers, $K \lesssim 1$, the diffusion coefficient is known to scale like $D \propto \lambda_c V K = \tau_c V^2$ (Eq. (2.65)). Since the correlation time τ_c is not affected by the gyroaveraging, one only has to replace V by V^{eff} to obtain the corresponding diffusion coefficient for finite gyroradii. In the limit of large Kubo numbers, $K \gtrsim 1$, one

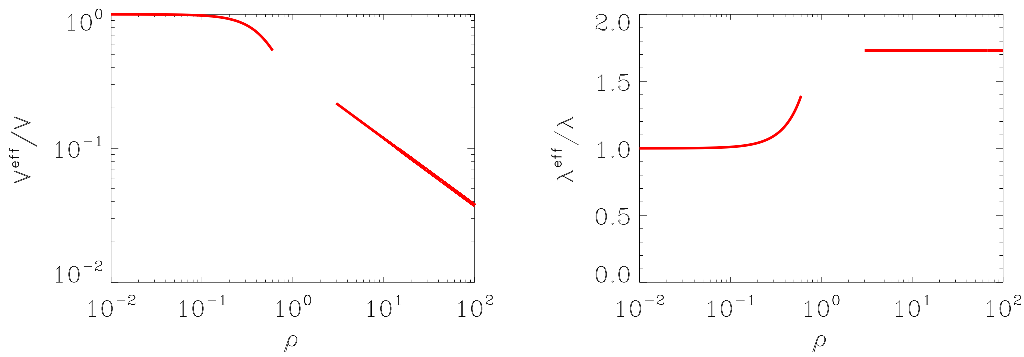

Figure 3.4: *Left*: Effective drift velocity vs. gyroradius according to Eqs. (3.11) and (3.15). *Right*: Effective correlation length vs. gyroradius according to Eqs. (3.12) and (3.16).

has $D \propto \lambda_c V K^{\gamma-1} = \lambda^{2-\gamma} V^\gamma / \tau_c^{1-\gamma}$ instead, with $\gamma = 0.7$ (Eqs. (2.67) and (2.68)) due to trapping effects. [We have observed $\gamma \approx 0.75$ in our numerical simulations.] It should be pointed out that in the large Kubo number regime, both the drift velocity *and* the correlation length are affected, namely in such a way that these two effects tend to cancel each other out. Employing the above formulas for V^{eff} and λ_c^{eff}, we finally obtain

$$\begin{aligned} D_\rho/D_0 \;&\approx\; 1 + [2 - 3\gamma]\,\rho^2 + \left[\frac{3}{2} - \frac{21}{4}\gamma + \frac{9}{2}\gamma^2\right]\rho^4 \\ &+ \left[\frac{1}{2} - \frac{29}{12}\gamma + \frac{27}{4}\gamma^2 - \frac{9}{2}\gamma^3\right]\rho^6 \quad \text{for } \rho \lesssim 1 \end{aligned} \tag{3.17}$$

and

$$D_\rho/D_0 \approx 1.73^{2-\gamma}\,(4\sqrt{\pi}\rho)^{-\gamma/2} \quad \text{for } \rho \gg 1 \tag{3.18}$$

where $\gamma = 2$ for $K \lesssim 1$ and $\gamma \approx 0.75$ for $K \gtrsim 1$. It is interesting to note that for $\gamma = 2/3$, the second and fourth order terms in Eq. (3.17) vanish exactly, i.e., D_ρ/D_0 is constant for small values of ρ up to sixth order corrections. Since this critical value for γ is pretty close to both ours ($\gamma \approx 0.75$) and Gruzinov's ($\gamma = 0.7$) in the large Kubo number regime, the diffusivity depends only weakly on the gyroradius in this case as long as it is smaller than or comparable to the correlation length. This confirms our simulation results in the $K \gg 1$ limit. In the low K regime, we find $D_\rho/D_0 \approx 1 - 4\,\rho^2$ instead, and for large gyroradii, the transport is reduced with increasing ρ like ρ^{-1} or $\rho^{-\gamma/2}$ for $K \lesssim 1$ or $K \gtrsim 1$, respectively. The simulation results shown in Fig. 3.2 are compared to the analytical approximations in Fig. 3.5. In general, we find fairly good agreement for both small and large gyroradii. Only for $K = 180$ and $\rho = 10$, the numerical value is somewhat smaller than the analytical one. In this case, the nonlinear regime is not fully established yet due to the strongly reduced drift velocity. This can be quantified by defining also a new effective Kubo number $K^{\text{eff}} \equiv \frac{V^{\text{eff}}\tau_c}{\lambda^{\text{eff}}}$, which gets smaller than one in this case.

In this chapter, the correlation length of the stochastic potential has been chosen $\lambda_c \equiv 1$ for simplicity. For general studies, the gyroradius ρ has to be

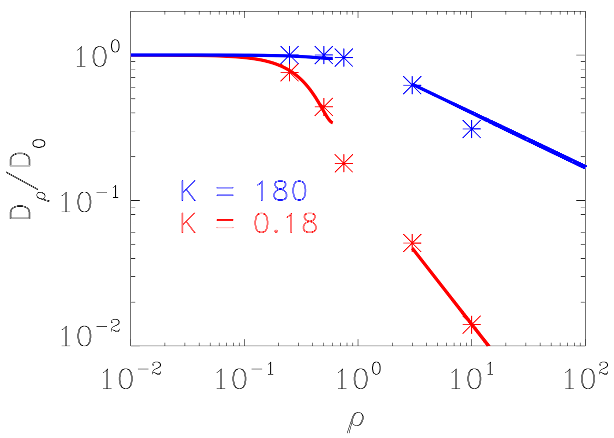

Figure 3.5: Comparison between the numerically determined diffusion coefficients and the analytical formulas, Eqs. (3.17) and (3.18). Here, D_0 and D_ρ denote, respectively, the diffusivity for vanishing and finite gyroradius.

replaced by ρ/λ_c throughout the foregoing discussion.

3.5 Summary and conclusions

In summary, we have used direct numerical simulations and analytical analysis to establish a rather detailed and coherent picture of the turbulent advection of test particles with finite gyroradii. Our results correct *both* the naive expectations *and* the previously published DCT-based results (Vlad & Spineanu, 2005; Vlad *et al.*, 2005). While in the low Kubo number (weak turbulence) regime, the diffusivity falls off rapidly with increasing gyroradius, it is more or less constant in the high Kubo number (strong turbulence) regime as long as the gyroradius does not exceed the correlation length of the electrostatic potential. The physical mechanisms underlying these results were identified and discussed. In short, the gyroaveraging process smoothes out the potential and therefore reduces the effective drift velocity monotonically with increasing gyroradius. On the other hand, the gyroaveraging increases the correlation length of the potential as can be understood by inspection of Eq. (3.5). For $\rho \lesssim 1$, the term $J_0(k\rho)$ mainly suppresses the large wavenumber contributions, narrowing the $\mathbf{k}$ spectrum and therefore widening $E(\mathbf{x})$ in real space. For $\rho \gtrsim 1$, the Bessel function tends to reduce the entire spectrum, and it can be shown that the effective correlation length converges to a fixed value. In particular, we found that for $K \gtrsim 1$, the decrease of the average drift velocity with increasing gyroradius tends to be balanced by an increase of the effective correlation length. Thus the particles are able to travel larger distances, and the diffusivity is practically left unchanged. If the gyroradius clearly exceeds the correlation length, on the other hand, the diffusivity falls off as $\rho^{-\gamma/2}$ with $\gamma = 2$ for $K \lesssim 1$ and $\gamma \approx 0.75$ for $K \gtrsim 1$. This is consistent with previous studies of test particle diffusion in Hasegawa-Mima turbulence (Manfredi & Dendy, 1997).

The main purpose of the present chapter was to investigate the fundamental physical processes responsible for the gyroradius dependence of the diffusivity under various circumstances. In the next chapters, the influence of additional effects like anisotropic structures and diamagnetic drifts is included, but it will turn out that the basic insights and results discussed in this chapter remain relevant. Based on simulations with the nonlinear gyrokinetic code GENE (Jenko *et al.*, 2000; Dannert & Jenko, 2005), we expect the Kubo numbers under realistic experimental conditions to be of the order of unity or even slightly larger. At the same time, the gyroradii of fast beam ions do not exceed the correlation length of the electrostatic potential. Consequently, it is reasonable to expect that the finite Larmor radius reduction of the turbulent diffusion is rendered ineffective, suggesting a significant impact of the turbulence on the beam ion transport. A closer examination of this matter will be given in Chapter 6, including 3D effects.

Chapter 4

Advection in Anisotropic 2D Electrostatic Turbulence

In this chapter, the $E{\times}B$ advection of trace ions in two dimensions is investigated for realistic tokamak microturbulence, which means that certain anisotropies are taken into account. In order to understand the consequences of effects like large gyroradii, fluctuation anisotropies, zonal flows, or poloidal drifts, they are again first studied in the framework of a model which is based on self-created stochastic potentials. Direct numerical simulations are performed, and a semi-analytical model is presented which provides qualitative as well as quantitative insight into the nature of passive tracer transport. Important results are obtained concerning the influence of anisotropic structures on the transport of thermal as well as fast particles. The results of this chapter have been published in (Hauff & Jenko, 2007).

4.1 Introductory remarks

In the present chapter, we will again consider the $E \times B$ advection of trace ions from a rather fundamental point of view. To this aim, we restrict our study to the dynamics of passive tracers in a given perpendicular plane, leaving questions related to parallel dynamics for the Chapters 6 and the following. It will turn out once more that the relative simplicity of this system enables us to obtain qualitative insight into a number of fundamental mechanisms governing transport in turbulent plasmas which would be much harder to extract from more complex models (where it is usually impossible to discriminate between various co-existing effects). Moreover, our approach even allows us to derive quantitative expressions for the resulting particle diffusivities, depending on certain anisotropy parameters. Many of these findings are expected to carry over to more general models, either directly or by analogy.

In this spirit, we will assess the role of effects like large gyroradii (Chapter 3), fluctuation anisotropies (Lin *et al.*, 2005), zonal flows (del Castillo-Negrete, 2000), or poloidal drifts (Annibaldi *et al.*, 2002). Although there exists a significant number of studies addressing their influence on transport, there has been no coherent picture concerning most of them. For the effect of large gyroradii on test particle transport, we have been able to establish such a picture in the previous chapter, temporarily restricting on isotropic turbulence. As far as the strong influence of homogeneous poloidal drifts on the radial transport of tracers is concerned, a clear description of this effect is reported and assessed in this chapter for the first time (to our knowledge), as well as a comprehensive study of the qualitative and (in the former case) quantitative influence of streamers and zonal flows. To begin with, we will study the behavior of tracers in self-created stochastic potentials. Direct numerical simulations are performed, and a semi-analytical model (based on the work in Chapter 3) is presented which is able to capture the main effects quite accurately. Based on these preparatory investigations, we will then analyze the particle dynamics in realistic turbulent fields as described by nonlinear gyrokinetics (Frieman & Chen, 1982). Here, the point is to identify the physical processes controlling the turbulent transport of trace ions in magnetized plasmas, and to characterize their interplay.

The structure of the present chapter is as follows. After providing some basic information about the concepts and definitions of this chapter in Section 4.2, we then deal in detail with fluctuation anisotropies, zonal flows, and poloidal drift effects in Sections 4.3, 4.4, and 4.5, respectively. This is all done in the context of self-created stochastic potentials, in order to be able to isolate and focus on individual effects in a convenient way. In Sec. 4.6, we then discuss the particle diffusion in realistic turbulent potentials as described by nonlinear gyrokinetics. Finally, in Sec. 4.7, we provide a summary along with some conclusions.

4.2 General remarks

In this chapter, the fluctuating electrostatic potentials $\phi(\mathbf{x}, t)$ will either be taken from simulations with the gyrokinetic turbulence code Gene (Jenko *et al.*, 2000; Dannert & Jenko, 2005) or they will be self-created by superposing a sufficiently large number of random harmonic waves, as descriped by Eq. (3.1). The spatiotemporal autocorrelation function of this potential is calculated according to Eq. (3.2). $E \times B$ drift velocity, gyroaveraging approximation, diffusion coefficient etc. are defined as usual, moreover, the same numerical schemes are applied than in the last chapter (e.g. the Runge-Kutta method (Vesely, 1994) and the 'time average method' (Reuss, 1996)). For the self-generated potentials, the values of the potential and those of the required derivatives are given analytically for each point in space and time, whereas for the realistic, gyrokinetic potentials they are given as three dimensional arrays, $\phi(x_i, y_j, t_k)$. The values at intermediate space-time positions are then obtained by means of a suitable interpolation scheme.

4.3 Anisotropic stochastic potentials

Gyrokinetic simulations show that tokamak microturbulence is, in general, not isotropic (see, for example, contour plots in Section 2.2). This calls for a generalization of the ideas developed in Chapter 3. Consequently, we consider next

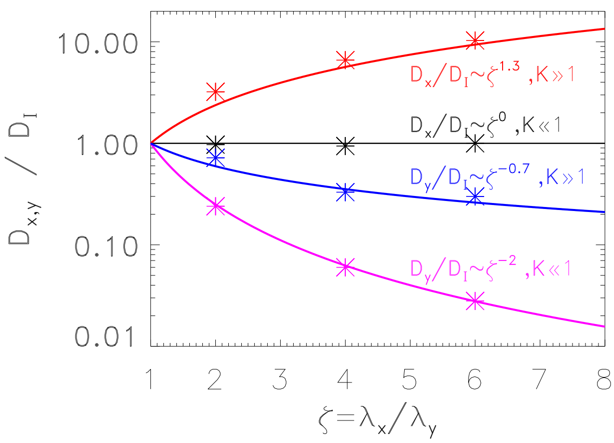

Figure 4.1: Ratio of the diffusion coefficients in anisotropic ($D_{x,y}$) and isotropic (D_I) stochastic turbulence versus the 'anisotropy factor' $\zeta = \lambda_x/\lambda_y$. Solid curves: analytical approach in the low/high Kubo number limit; single points: simulation results for $K_I = 0.07$ and $K_I = 70$.

a spatial autocorrelation function of the form

$$E(\mathbf{x}) \propto e^{-(x/\lambda_x)^2-(y/\lambda_y)^2} \tag{4.1}$$

where $\zeta = \lambda_x/\lambda_y$ may deviate from unity. To realize such autocorrelations, we work now with $N = 10^3$ partial waves, having checked that $E(\mathbf{x})$ is still sufficiently smooth and that the resulting diffusion coefficients are practically unchanged when N is increased.

In a first step, let us consider the limit of vanishing gyroradius. Keeping λ_y (as well as the potential amplitude) fixed and changing only λ_x, one can use $\lambda_I \equiv \lambda_y$ and $V_I = V_x$ as constant reference values denoted by the index I (for *isotropic*). We thus have $\lambda_x = \zeta\lambda_I$ and $V_y = V_I/\zeta$. Inserting these relationships into Eq. (2.68), we find $D_x = \zeta^{2-\gamma}D_I$ and $D_y = \zeta^{-\gamma}D_I$ with $\gamma = 2$ for $K \lesssim 1$ and $\gamma \approx 0.7$ for $K \gtrsim 1$. Here, D_I is the reference diffusion coefficient obtained for the isotropic case, $\zeta = 1$. In Fig. 4.1, these four curves are plotted and compared with direct numerical simulations. The isotropic Kubo number $K_I = V_I\tau_c/\lambda_I$ has again been adjusted by varying τ_c, i.e., $\omega_{\max}$. The linear regime is represented by simulations performed at $K_I = 0.07$, whereas for the nonlinear regime, $K_I = 70$ was chosen. In this context, we would like to point out that if ζ changes, the 'real' Kubo number changes, too, but it keeps the same in both directions as long as $E(\mathbf{x})$ is Gaussian ($K_x = K_y = K_I/\zeta$). As can be seen in Fig. 4.1, the simulation results coincide quite nicely with the analytical predictions. For large Kubo numbers, the diffusion in the x direction is greatly enhanced for $\zeta > 1$. Moreover, invoking mixing length arguments ((Kadomtsev, 1965), Chap. IV 4), it is reasonable to expect that the fluctuation amplitude is proportional to the radial correlation length, yielding $\phi \propto \zeta$. This leads to $D_x = \zeta^2 D_I$ and $D_y = D_I$, independent of K_I. While this estimate might merely set an upper limit, it is clear that the formation of streamers (radially elongated vortices) implies a significant enhancement of D_x with increasing

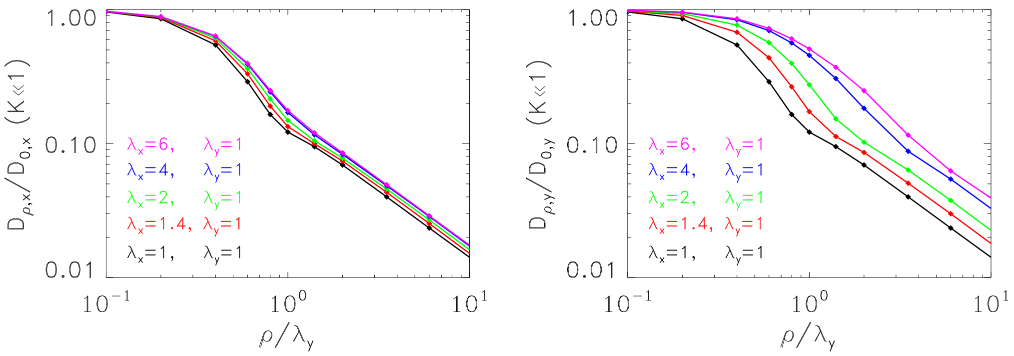

Figure 4.2: *Left*: Relative diffusion $D_{\rho,x}/D_{0,x} = (V_{\rho,x}/V_{0,x})^2$ (semi-analytical approach) for $K \ll 1$ and different anisotropies $\zeta = \lambda_x/\lambda_y$. The subscripts ρ and 0 denote, respectively, cases with finite and vanishing gyroradius. *Right*: The same for the y direction.

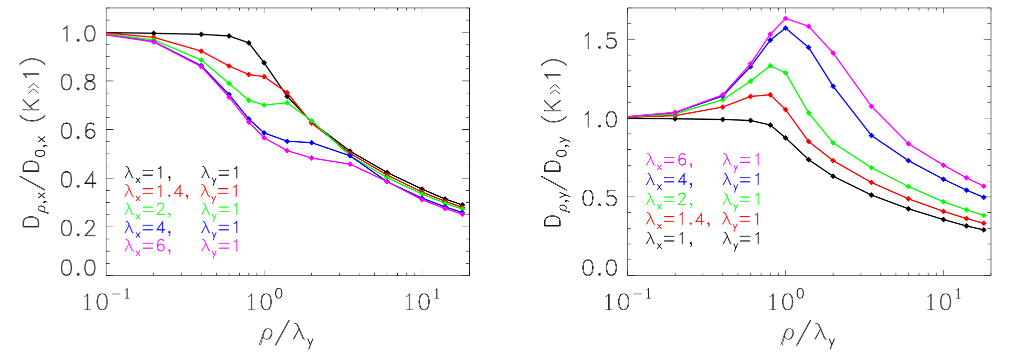

Figure 4.3: *Left*: Relative diffusion $D_{\rho,x}/D_{0,x} = (V_{\rho,x}/V_{0,x})^{\gamma}(\lambda_{\rho,x}/\lambda_{0,x})^{2-\gamma}$, $\gamma = 0.82$ (semi-analytical approach) for $K \gg 1$ and different anisotropies $\zeta = \lambda_x/\lambda_y$. The subscripts ρ and 0 denote, respectively, cases with finite and vanishing gyroradius. *Right*: The same for the y direction. Here, $\gamma = 0.72$.

streamer aspect ratio ζ in a strong turbulence regime.

In a second step, let us now focus on finite gyroradius effects in potentials with given values of K_I and ζ. Our key interest is to find out whether the constant transport regime for $\rho \lesssim 1$ and large K_I (see Fig. 3.5) is still present or not. In order to apply the scaling approach outlined in the previous chapter, we have to determine the effective autocorrelation function for Eq. (4.1) along with the the values of $V^{\text{eff}}_{x,y}$ and $\lambda^{\text{eff}}_{x,y}$. Unfortunately, in the anisotropic case, the integral in Eq. (3.5) cannot be solved analytically anymore, even if the Bessel function is replaced by appropriate approximations. Thus the analysis has to be done numerically, e.g., using MATHEMATICA. Here, the correlation length is defined as $\lambda^{\text{eff}}_x = \sqrt{-2E^{\text{eff}}(x)|_{x=0}/\partial^2_x E^{\text{eff}}(x)|_{x=0}}$, which means that we fit a Gaussian to the central region of $E^{\text{eff}}(x)$ and determine its width. The resulting D_ρ/D_0 curves are shown in Figs. 4.2-4.3. Note that the gyroradius is normalized with respect to λ_y (which is held constant), and that ζ is varied by

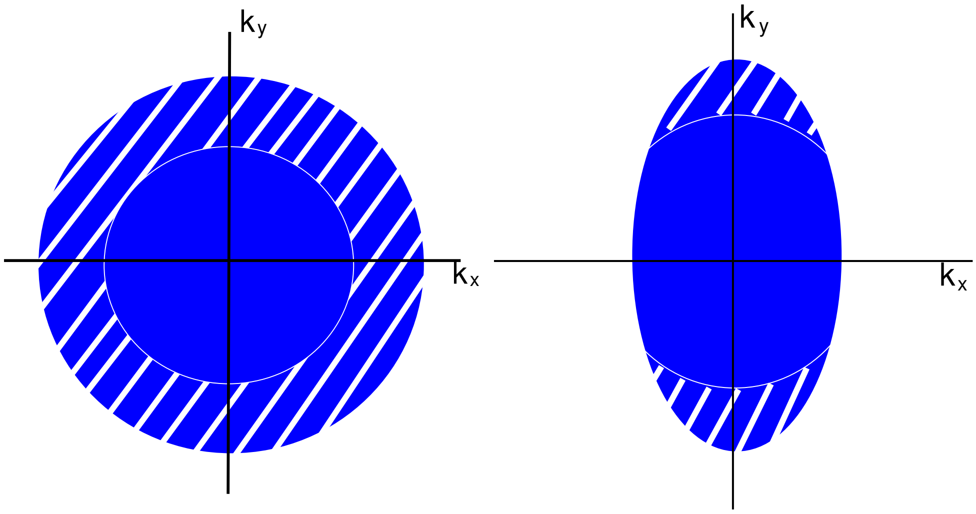

Figure 4.4: *Left*: Isotropic turbulence spectrum and the symbolized narrowing due to gyroaveraging (multiplication with $J_0(\rho k)$. *Right*: The same for an anisotropic turbulence spectrum, symbolizing streamers in the x direction. Only the y component narrows significantly.

varying λ_x. The γ values have been determined from simulations with $\rho = 0$ and varying Kubo numbers. In the x direction, γ deviates substantially from the value obtained by Gruzinov and Isichenko ($\gamma = 0.7$) (Eqs. (2.67) and (2.68)); we find, e.g., that $\gamma = 0.82$ for $\zeta = 4$, which indicates that the trapping effects are weakened with respect to the isotropic case.

In the linear regime ($K \ll 1$), the reduction of D_ρ with increasing ρ is simply a consequence of the reduction of V^{eff}. With increasing anisotropy ζ, this reduction is less severe since the influence of gyroaveraging is weaker for larger structures. In the nonlinear regime ($K \gg 1$), we get a more interesting picture. For the x direction, we see that the increasing anisotropy leads to a stronger reduction of the diffusion for small gyroradii. If ρ in Fig. 4.3 (left) had been normalized with respect to λ_x, this reduction would look even more pronounced. In contrast, for the y direction, we find an increase of D_ρ with increasing anisotropy, and for $\rho \sim \lambda_y$, the diffusion coefficient becomes even larger than in the zero gyroradius limit. These findings can be explained in terms of the behavior of $\lambda_{x,y}^{\text{eff}}$. For potentials with $\lambda_x > \lambda_y$, the autocorrelation spectrum is more extended in the k_y direction than in the k_x direction. If we now multiply this spectrum with the Bessel function [remember Eq. (3.5)], it is clear that for small gyroradii ρ the spectrum is damped mainly in the k_y direction. Therefore, λ_y^{eff} increases strongly, whereas λ_x^{eff} stays roughly constant for quite a while. This behavior is sketched in Fig. 4.4. For isotropic turbulence, we find that for $\rho \lesssim 1$, the increase of the effective correlation length balances the reduction of the drift velocity almost exactly in the nonlinear regime. In the anisotropic case, however, this subtle balance is perturbed. While the change in the x correlation length is observed to be too small, the change of its y counterpart is found to be too large.

The fact that the scaling approach outlined above along with its interpre-

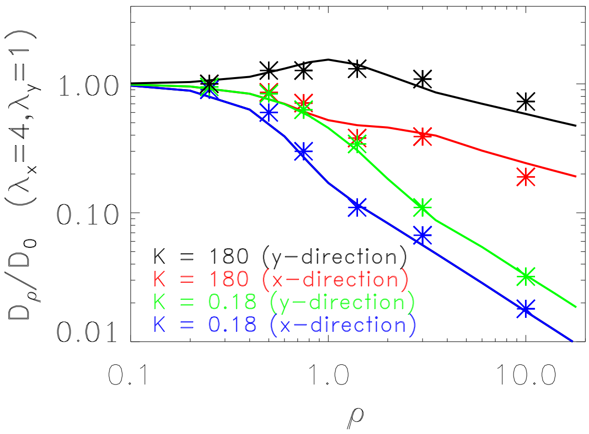

Figure 4.5: Comparison between the simulation results (symbols) for an anisotropic potential with $\zeta = \lambda_x/\lambda_y = 4$ and the semi-analytical approach (solid lines; data taken from Figs. 4.2 through 4.3) for $K \ll 1$ and $K \gg 1$.

tative implications is also applicable to the case of anisotropic fluctuations is demonstrated in Fig. 4.5. Here, we took a potential with $\zeta = 4$ and performed a number of test particle simulations for a set of different gyroradii for both the linear and the nonlinear regime (precisely speaking, $K = 0.18$ and $K = 180$ have been used). As can be inferred from Fig. 4.5, the simulation results and the analytical curves are in good agreement, giving evidence that the model still provides important qualitative as well as quantitative insight.

In summary, we can state that the presence of anisotropic, streamer-like structures (as indicated by $\lambda_x > \lambda_y$) tends to enhance the transport in the x direction in the zero gyroradius limit. On the other hand, one finds a stronger reduction of the transport with increasing gyroradius than in the isotropic case. In the y direction (which is of less interest in a tokamak), the situation is reversed.

4.4 Poloidal shear flow effects

So far, we have focused on the impact of anisotropic vortical structures (streamers) on the radial (and poloidal) diffusivities of trace ions. Such considerations are known to apply, e.g., to trapped electron mode (TEM) turbulence (see Fig. 2.7). However, in the case of ion temperature gradient (ITG) driven turbulence, the system usually spins up poloidal shear flows to fairly high amplitudes (see Fig. 2.6 and related discussion). It is widely accepted that the cross-field transport is reduced or even quenched in the presence of such 'zonal flows (see, e.g., Ref. (Terry, 2000)). Here, we want to investigate the effect of such zonal flows on trace ion transport in detail, with a special consideration of the modifications concerning finite gyroradius effects.

As a model potential, we choose

$$\tilde{\phi}(x, y, t) = \phi(x, y, t) + A_{\mathrm{zf}} \sin(k_{\mathrm{zf}} x)\,. \tag{4.2}$$

Here, ϕ represents the isotropic potential considered already in the previous discussion and generated according to Eq. (3.1) with $N = 10^3$. The corresponding Eulerian autocorrelation function is then easily shown to be

$$\tilde{E}(x, y, t) = E(x, y, t) + \frac{A_{\rm zf}^2}{2}\cos(k_{\rm zf}x)\,, \tag{4.3}$$

where E is the autocorrelation of ϕ. Unfortunately, it is not possible to easily extend the scaling approach introduced in Chapter 3 to cases with strong zonal flows. This is because the last term in Eq. (4.3) completely changes the shape of the autocorrelation, leading to a minimum with large negative values on the x axis and to a plateau on the y axis. Qualitatively, one can expect that the presence of poloidal shear flows will bring about a reduction (an increase) of the diffusivity in the x (y) direction since negative values of $\tilde{E}$ make it less probable for an equipotential line to cross that region, whereas a plateau indicates a larger crossing probability. Quantitative statements have to rely on numerical simulations. But before we turn to those, we would like to insert a brief discussion about the influence of finite gyroradius effects on the transport properties. In this context, one finds the effective autocorrelation function

$$\tilde{E}^{\rm eff}(x, y, t) = E^{\rm eff}(x, y, t) + \frac{A_{\rm zf}^2}{2}\cos(k_{\rm zf}x)J_0^2(k_{\rm zf}\rho)\,, \tag{4.4}$$

i.e., the generic structure of the autocorrelation function is preserved. As we know from Chapter 3, finite gyroradius effects enhance the correlation length inferred from $\tilde{E}^{\rm eff}$ – but they have no influence on the wavelength of the zonal flow term in Eq. (4.4), of course. Considering both terms together, one can thus expect that the gyroaveraging process will lead to an increase of the (effective) correlation length, but this increase will be more moderate than for a potential without zonal components. Moreover, since for realistic parameters, $k_{\rm zf}$ is usually smaller than the average value of $|\mathbf{k}_i|$, the influence of the zonal flow term will increase with increasing gyroradius as long as $k_{\rm zf}\rho \lesssim 1$. So what we expect for the ρ dependence of the transport is a reduction of the plateau regime observed in Figs. 3.2 and 3.5.

Let us now turn to the numerical simulation results. Here, the isotropic potential is created the same way as before, and the zonal flow is characterized by $k_{\rm zf} = 0.76$ and $A_{\rm zf}^2/2 = 0.6\,E(0)$. The latter values are inspired by data from gyrokinetic turbulence simulations with the Gene code (see references given in Section 2.2). The resulting diffusion coefficient for the x direction is shown in Fig. 4.6 for different Kubo numbers and gyroradii. We have chosen the isotropic Kubo number K_I as a parameter, since the Kubo number including the zonal flow term is not unique in the x and y direction anymore. However, as follows from Eqs. (2.62) and (3.3) (note $V_x = (-\partial^2\tilde{E}(\mathbf{x}, t)/\partial y^2|_{\mathbf{x}=t=0})^{1/2} = (-\partial^2 E(\mathbf{x}, t)/\partial y^2|_{\mathbf{x}=t=0})^{1/2}$ and the fact that λ_x is only marginally affected by the zonal flow term), $K_x \approx K_I$. The Kubo number is then again varied by changing τ_c in the isotropic component of the potential.

Compared to Fig. 3.2, we notice two main differences. First, for $K > 1$, the reduction of D_x with K is stronger ($\gamma \approx 0.6$). This is due to the strong negative values of $\tilde{E}^{\rm eff}$, indicating – in the Eulerian picture – that there is a 'transport

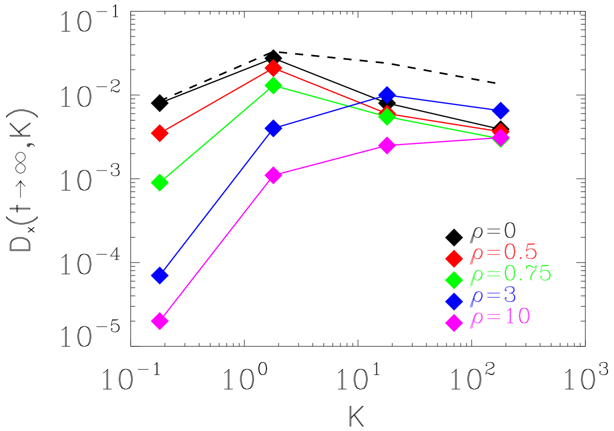

Figure 4.6: Long-time limit of the diffusivity D_x as a function of the Kubo number K for different gyroradii ρ (normalized to the correlation length of the potential) in a potential with a superposed zonal flow [see Eq. (4.2)]. The dashed line represents the case for $\rho = 0$ without zonal flow (data taken from Fig. 3.2).

barrier.' Second, we see that for $K > 1$, a slight reduction of D_x with ρ remains even for $\rho < 1$. This finding is in qualitative agreement with the prediction we made above, studying the effective correlation lengths. The curves for $\rho = 3$ and $\rho = 10$ play a special role. Here, the gyroaveraging filters out the zonal flow term due to $J_0(k_{\rm zf}\rho) \approx 0$, and the $D_x(K)$ curve follows the curve for the pure isotropic case shown in Fig. 3.2. However, this is a direct consequence of our simple choice for the model potential which only features a single zonal mode. In practice, there will always be a superposition of many zonal modes, weakening this effect. In the y direction, on the other hand, the situation is completely different. Here, the particle diffusivity is *increased* by the zonal flow term, and $D(t \to \infty)$ increases further for $\rho \lesssim 1$ when ρ is increased.

The results obtained in the present section may be expected to be prototypical for a large class of systems which can be described as a superposition of background turbulence and zonal flows. They show that the radial particle transport tends to be inhibited by strong zonal flows – as expected – and that the finite gyroradius effects still differ in the low and high Kubo number regimes.

4.5 Poloidal drift effects

While it is not hard to understand (given the huge amount of literature on this topic) that *sheared* poloidal flows can lead to a strong suppression of the radial fluxes of trace species, it is probably easy to overlook that *homogeneous* poloidal drifts may have the same effect. This will be the topic of the present section.

Generally, all microinstabilities in toroidal magnetoplasmas exhibit drifts in the poloidal direction (see, e.g., Fig. 2.5 and related discussion). While ion temperature gradient (ITG) modes tend to drift in the ion diamagnetic direction, electron temperature gradient (ETG) modes and trapped electron modes usually drift in the electron diamagnetic direction. It should be kept in mind, however, that it is also possible for these modes to have only very small drift velocities or even change their drift direction. This is often the case when the gradients which are not responsible for the main drive of the respective mode (e.g., the electron temperature gradient in the case of ITG modes) are increased. As was found in many GENE simulations, these linear drifts tend to carry over into the nonlinear, fully turbulent regime, at least as far as the long-wavelength modes are concerned, i.e., the ones typically responsible for most of the turbulent transport.

In the context of our present stochastic model, we want to define as a 'drifting potential' ϕ_{dr} a (fluctuating or static) potential whose structures move in the poloidal (y) direction with a constant drift velocity v_{dr}. Denoting again the isotropic potential from Chapter 3 by $\phi(x, y, t)$, we thus have

$$\phi_{\mathrm{dr}}(x, y, t) \equiv \phi(x, y - v_{\mathrm{dr}} t, t)\,. \tag{4.5}$$

As we will see in the next section, the model described by Eq. (4.5) is fairly realistic and represents an important and new class of transport effects. Simulations show that the introduction of a drift velocity v_{dr} of the order of V in the y-direction reduces transport in the x direction by up to one order of magnitude, whereas it strongly enhances the transport in the y direction.

4.5.1 Zero gyroradius limit

In order to understand the effect of such a homogeneous drift, it is useful to perform a Galilei transformation to a reference frame moving in the y direction with velocity v_{dr}. Quantities referring to this co-moving coordinate system will be denoted with a prime. Using Faraday's law of induction (in the limit of non-relativistic velocities) this transformation leads to an additional component of the electrostatic field,

$$\mathbf{E}' = \mathbf{E} + \mathbf{v}_{\mathrm{dr}} \times \mathbf{e_z}\,. \tag{4.6}$$

Note that due to our normalization $\mathbf{B}$ is replaced by $\mathbf{e}_z$ (see Section 2.4). Rewriting this equation in terms of the electrostatic potential ($\mathbf{E} = -\nabla\phi$), we thus find

$$\phi'_{\mathrm{dr}}(x, y, t) = \phi_{\mathrm{dr}}(x, y + v_{\mathrm{dr}} t, t) - v_{\mathrm{dr}} x = \phi(x, y, t) - v_{\mathrm{dr}} x\,. \tag{4.7}$$

For the particle motion we then find the (trivial) relation $\mathbf{v}'_E = \mathbf{v}_E - v_{\mathrm{dr}} \mathbf{e}_y$. So in the co-moving frame, which is more easy to access, the law of induction produces an additional electric field, which is responsible for the different behavior compared to a non-drifting potential. An example for such a drift frame potential is shown in Fig. 4.7. It is clear that the second term on the right-hand side of Eq. (4.7) gives the potential a completely new structure. Since it represents an infinite ramp, it prevents the formation of long-ranged equipotential lines in the x direction, whereas open equipotential lines running in the y direction are favored. If we denote the maximum absolute value of the potential ϕ by $\phi_{\max}$, we can estimate from Eq. (4.7) the maximum length of an equipotential line in the x direction to be $x_{\max} \approx 2\phi_{\max}/v_{\mathrm{dr}} \approx 2\,V_x \lambda_y / v_{\mathrm{dr}}$. [Here, λ_y is the y

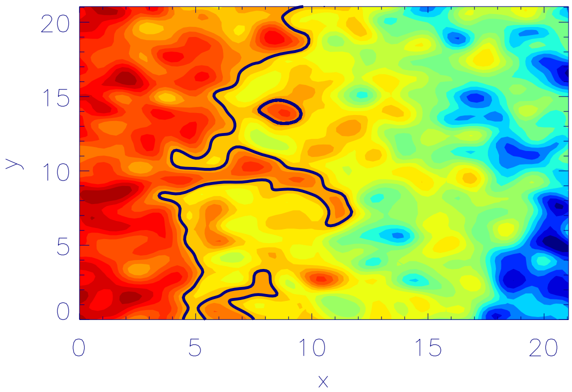

Figure 4.7: Contour plot of the effective (static) potential in the drifting frame, ϕ'_{dr}, for a poloidal drift velocity of $v_{\mathrm{dr}} = 0.0013$ ($V = 0.0052$). Representative open and closed isolines (particle trajectories) are shown as solid lines.

correlation length of ϕ, V_x is the average $E \times B$ drift velocity in the x direction, and, according to Eq. (2.61), the simple approach $V_x \sim \phi/\lambda_y$ is assumed.] Since for a non-fluctuating (but drifting) potential $\phi_{\mathrm{dr}}(x, y, t) = \phi(x, y - v_{\mathrm{dr}}t)$, the length of the trajectory is limited in the x direction, we expect the diffusion coefficient to show a sharp drop to zero. The *'drop time'* can be estimated by the time a particle needs to cross the maximum trajectory length,

$$\tau_{\mathrm{drop}} \approx \frac{x_{\max}}{V_x} = \frac{2\lambda_y}{v_{\mathrm{dr}}} \,. \tag{4.8}$$

Note that λ_y enters this equation, although the motion in the x direction is described. Simulation results show a good correspondence with this estimate (see Fig. 4.8 (left)). Comparing a fluctuating potential (finite τ_c or K) with a non-fluctuating potential ($\tau_c, K \to \infty$), the typical behavior is that the $D(t)$ curves are almost identical for $t \lesssim \tau_c$, whereas for $t \gtrsim \tau_c$, the curve for the fluctuating potential departs from the $K = \infty$ curve and saturates (see Fig. 2.13 and related discussion). Thus we expect that for $\tau_{\mathrm{drop}} \lesssim \tau_c$ or $v_{\mathrm{dr}} \gtrsim 2\lambda_c/\tau_c$, the diffusion will be strongly reduced also at finite K, since in that case, the barrier life time exceeds the time a particle needs to travel the distance $x_{\max}$. On the other hand, as long as $v_{\mathrm{dr}} \ll \lambda_c/\tau_c$, the influence of the homogeneous drift on D_x is relatively small, since decorrelation occurs before the particles are able to 'feel' the barrier, i.e. to cover the distance $x_{\max}$. A schematic draft of the influence of the 'drop time' on the running diffusion coefficient is given in Fig. 4.9. In a number of simulations we found that the relative drift velocity for which the diffusivity drops to $1/e$ of the original value can be expressed as $\Delta_{1/e} v_{\mathrm{dr}} = 2\lambda_y/\tau_c$. This simply means that the diffusivity is reduced by a factor of $1/e$ when $\tau_c = \tau_{\mathrm{drop}}$. It is worth pointing out that this 'resonance width' is thus determined solely by the turbulence properties λ_c and τ_c.

Noting that in the drifting frame, the particles follow the isolines of ϕ'_{dr}, Fig. 4.7 tells us that there are two different classes of particles: trapped ones which in the lab frame move in the y direction with the drift velocity v_{dr} – and passing ones which (even in the lab frame) move against the drift into the

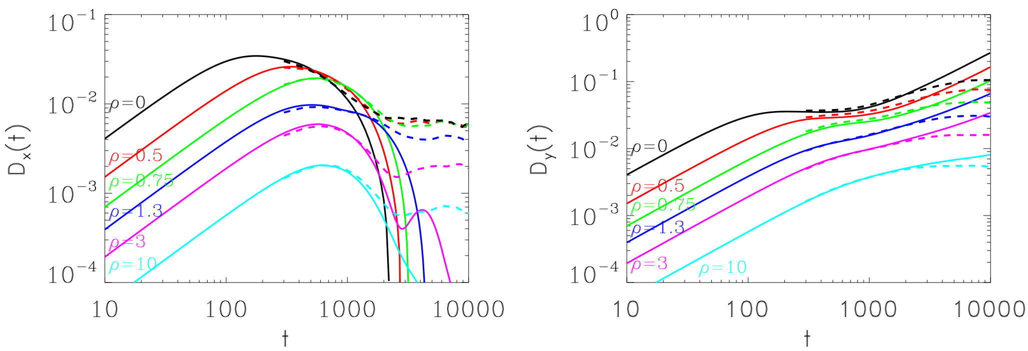

Figure 4.8: *Left*: $D_x(t)$ for a poloidally drifting potential with $v_{\rm dr} = 0.0013$. Solid lines: static potential ($K = \infty$); dashed lines: time-dependent potential ($K = 18$). According to the estimate $\tau_{\rm drop} \approx 2\lambda_c/v_{\rm dr}$, we find $\tau_{\rm drop} \approx (1520, 1920, 2400, 2890, 2630)$ for $\rho = (0, 0.5, 0.75, 1.3, 3)$ and $K = \infty$. These values are in reasonable agreement with the $D_x(t)$ curves. For $K = 18$, we find saturation at $t \sim \tau_c \approx 3000$. *Right*: The same, but for the y direction.

negative y direction. The former dominate for small drift velocities, whereas the latter prevail for large drift velocities when the second term in Eq. (4.7) dominates. Considering the drift frame potential, it is also clear that trapped particles will be found primarily near the extrema of ϕ, whereas particles on open trajectories will be found near $\phi \approx 0$. Such a behavior has already been reported in Ref. (Annibaldi *et al.*, 2002).

Since in the lab frame, we have $\langle \partial_x \phi_{\rm dr} \rangle = 0$ due to symmetry arguments, the quantity $\langle [y(t) - y(0)] \rangle$ always stays zero. This means that the weighted distance of the trapped particles moving into the positive y direction and of the untrapped particles moving into the negative y direction keeps constant. Given that the (average) velocity of the trapped particles is $V_y^{\rm trapped} = v_{\rm dr}$ in the lab frame, the average velocity of the untrapped particles has to be $-V_y^{\rm untrapped} = v_{\rm dr} N^{\rm trapped}/N^{\rm untrapped}$. As $N^{\rm trapped}$ gets smaller when $v_{\rm dr}$ is increased, it is possible for the average velocity of the untrapped particles to stay constant over a certain range of drift velocities. In Fig. 4.10 (left), we display the probability distribution function (PDF) for the particle position in the y direction at a fixed time for a static potential and a series of different drift velocities $v_{\rm dr}$. Sharp peaks of trapped particles can be clearly observed which move to the right with $v_{\rm dr}$, whereas the untrapped particles move to the left (on average). The average velocity of the untrapped particles is observed to stay approximately constant for $v_{\rm dr} \lesssim V$ as pointed out above. Further, it can be estimated that the maximum of $v_{\rm dr} N^{\rm trapped}$ is reached for $V \approx v_{\rm dr}$ which can be interpreted as a resonance condition.

Since we have chosen a static potential, particles stay trapped or untrapped forever. If we introduce a time dependence of the fluctuations, the structures are not constant in time, so that trapped particles can become untrapped and vice versa. This, of course, leads to a dispersion of the structures in the PDF with time increasing, as can be clearly observed in Fig. 4.10 (right). For very

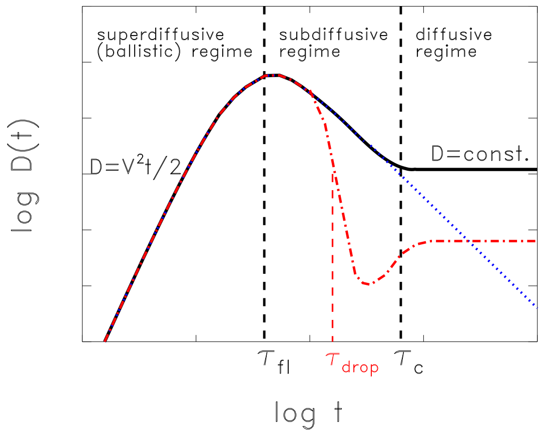

Figure 4.9: Schematic time evolution of the running diffusion coefficient in two dimensions. Black/solid line: time dependent electrostatic potential without background drift. Blue/dotted line: static potential without background drift. Red/dashed dotted line: time dependent potential with background drift and $\tau_{\rm drop} < \tau_c$. Finite gyroradius effects would shift the solid curve downwards ($V^{\rm eff} < V$). Moreover, the maximum would be shifted to the right ($\tau_{\rm fl}^{\rm eff} > \tau_{\rm fl}$).

large times, the PDF turns into a Gaussian. This - more realistic - behavior is left for discussion in Chapter 5.

4.5.2 Finite gyroradius effects

As before, we would like to also study the influence of finite gyroradius effects. To this aim, one has to consider effective gyroaveraged potentials instead of the ones used above. Since the second term on the right-hand side of Eq. (4.7) is not affected by gyroaveraging, we find

$$\phi'^{,\rm eff}_{\rm dr}(x,y,t) = \phi^{\rm eff}(x,y,t) - v_{\rm dr}x\,. \tag{4.9}$$

It thus follows that the effective correlation lengths and drift velocities are simply the ones obtained in the isotropic case (see Chapter 3). Consequently, λ_c increases and V decreases with increasing gyroradius ρ. At the same time, since the gyroaveraging reduces the absolute values of ϕ, the second term in Eq. (4.9) becomes more dominant – which means that the number of trapped particles is reduced with growing ρ.

Fig. 4.8 (left) shows the running diffusion coefficient in the x direction for $v_{\rm dr} = 0.0013$ (for comparison, $V = 0.0052$) for a number of different gyroradii normalized to the correlation length of the potential. The solid lines are obtained from a static (but still drifting) potential. Like discussed above, the diffusion is bound to drop to zero for large times. As can be inferred from the figure, the drop time is well approximated by the expression derived above, $\tau_{\rm drop} \approx 2\lambda_c/v_{\rm dr}$. In particular, since λ_c grows with increasing ρ, $\tau_{\rm drop}$ grows, too. These considerations for a static potential enable us to also interpret the

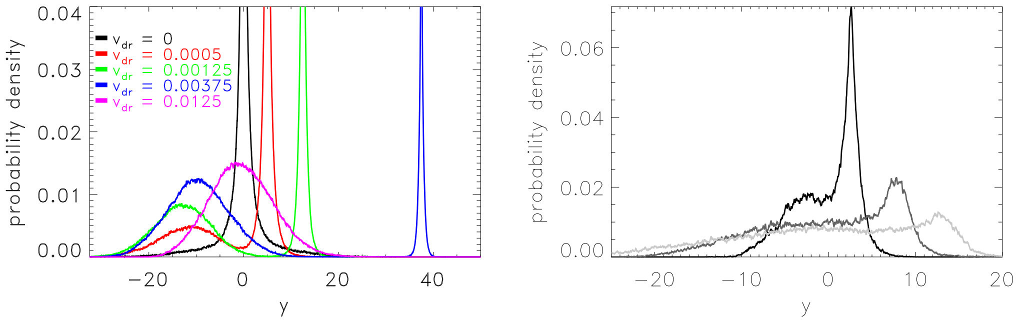

Figure 4.10: *Left*: PDF of the particle displacements in the y direction in a static, drifting potential (for different values of v_{dr}) at $t = 10000$. The number of trapped particles (moving to the right) decreases as v_{dr} increases, and the average position of the untrapped particles (mostly moving to the left) is approximately constant for $v_{\mathrm{dr}} < V = 0.0053$ but decreases rapidly for $v_{\mathrm{dr}} > V$. Note that the right maximum for $v_{\mathrm{dr}} = 0.0125$ is outside the range of the figure. *Right*: Probability density of the particle displacements in the y direction for a time-dependent potential with $K = 18$ and a drift velocity of $v_{\mathrm{dr}} = 0.00125$ at $t = 2000$ (black), $t = 6000$ (dark grey), and $t = 10000$ (light grey).

behavior of $D(t)$ for a fluctuating potential. The dashed lines in Fig. 4.8 (left) show such curves for $K = 18$ and $\tau_c \approx 3000$. As we have already mentioned, the $D(t)$ curves for finite K follow the curves for the static potential up to $t \sim \tau_c$, and then they saturate. In our example, we have $\tau_c \approx \tau_{\mathrm{drop}}$ which is in line with data obtained from Gene simulations of (pure) trapped electron mode turbulence (see Ref. (Dannert & Jenko, 2005) and the results presented in the next section). Since the curves for static potentials in Fig. 4.8 (left) lie close to each other for $t \approx \tau_c$, we can understand why the same is true for time fluctuating potentials. However, as the curves for small gyroradii tend to saturate earlier than the ones for larger gyroradii, this argument is more a qualitative one. We remark that again we have found a regime where the diffusion keeps constant for $\rho \lesssim 1$, and again this effect is due to the increase of the effective correlation length. However, the mechanism leading to this result is different from the one discussed in Chapter 3.

The effect that the different curves do not saturate at exactly the same time although their correlation time is the same is a consequence of a more fundamental effect. In simulations varying the correlation time as well as the Kubo number we found that for $K < 1$, the saturation time coincides quite well with the correlation time, whereas for $K > 1$, the saturation time is reduced compared to τ_c. Thus, the stronger the trapping (i.e., the more circulations around a certain eddy a particle can perform), the more sensitive its motion with respect to small perturbations. In Ref. (Gruzinov *et al.*, 1990), the lifetime τ_h of the contour $\phi = h \ll 1$ (with the maximum of the potential normalized to unity) is estimated by the expression $\tau_h \approx h\tau_c$. Since we know that for large Kubo numbers, the transport is dominated by large-scale trajectories with $h \sim 0$, this confirms our observation. Consequently, an increase of the gyroradius leads to a reduction of the effective Kubo number (see Sec. 4.6.1), and the saturation time increases – although the correlation time stays the same. If, as in our case, $\tau_c \approx \tau_{\mathrm{drop}}$, small changes in the saturation time can cause large changes in the saturation value of D, since the $D(t)$ curve for the static potential changes rapidly around that time. In Fig. 4.8 (left), the increase of D for the static potential is balanced by the slight increase of the saturation time, leading to approximately the same saturation value for different, but small gyroradii.

Fig. 4.8 (right) displays the running diffusion coefficient in the y direction for the same potential as in Fig. 4.8 (left). In the static case (solid lines), we see that the transport is ballistic for large times. Here, the trapped particles move with the drift velocity, whereas – as we have shown above – the untrapped particles move with a constant average velocity into the opposite direction. We have also seen that an increase of the gyroradius leads to a reduction of both the number of trapped particles and the average velocity of the untrapped particles ($-V_y^{\mathrm{untrapped}} = v_{\mathrm{dr}} N^{\mathrm{trapped}}/N^{\mathrm{untrapped}}$). Since the average velocity $\overline{V}_y \equiv (N^{\mathrm{trapped}}|V_y^{\mathrm{trapped}}| + N^{\mathrm{untrapped}}|V_y^{\mathrm{untrapped}}|)/N = (2N^{\mathrm{trapped}}/N)\, v_{\mathrm{dr}}$ does not depend on the effective correlation length but only on the number of trapped particles (and, of course, on the drift velocity), one may expect that D_y drops already for small gyroradii. Fig. 4.8 (right) supports this claim.

4.6 Trace ions in realistic turbulent fields

Until now, we have studied the transport of passive tracers in electrostatic potentials which were created by superposing a large number of plane waves. Applying this method, we were able to model and study a wide number of different effects including anisotropies, zonal flows, poloidal drifts as well as their dependence on the Kubo number of the potential and the gyroradius of the particles. With these results in our hands, we are now in a good position to examine passive tracer transport in realistic turbulent potentials obtained from nonlinear gyrokinetic simulations. Here, some or all of the above effects may be present at the same time and interact with each other.

As an example, we will use simulation data for trapped electron mode (TEM) turbulence in tokamaks obtained with Gene. These simulations have been performed by T. Görler, F. Merz, and M.J. Püschel at the IPP in Garching. As plasma parameters, the nominal values listed in Sec. II.B of Ref. (Dannert & Jenko, 2005) were used. The electrostatic potential in a perpendicular plane on the low-field side is written out frequently and then subjected to post-processing. In this context, it is necessary to make a few remarks about the box and grid size as well as the employed discretization methods. First, Gene uses doubly periodic boundary conditions. So to exclude finite box size effects, we have chosen a simulation domain whose extensions in the x and y directions are much (about 25 times) larger than the respective correlation lengths. This helps to avoid spurious potential correlations and particle trajectories. Second, the choice of the discretization methods was found to be of great importance. Given (only) the electrostatic potential (only) on a two-dimensional x-y grid, it is necessary both to calculate the $E\times B$ drift velocities (i.e. the spatial deriva-

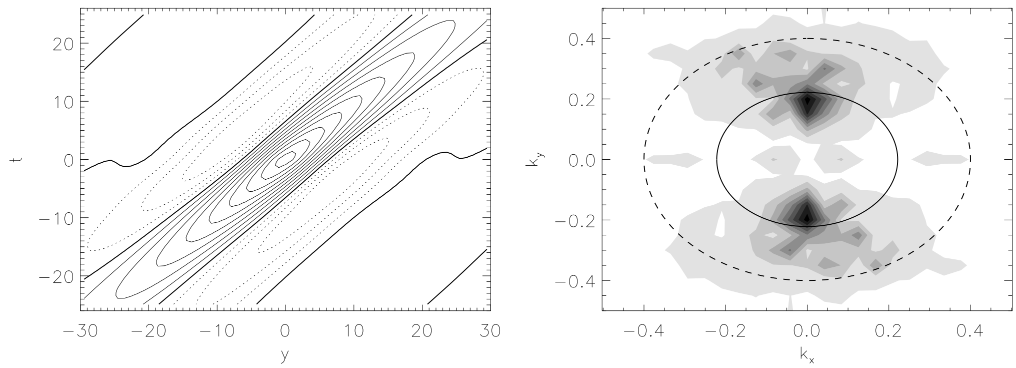

Figure 4.11: *Left*: Autocorrelation function $E(y,t)$ of the electrostatic potential obtained from a gyrokinetic simulation of trapped electron mode turbulence with the GENE code. Solid lines: positive values; dashed lines: negative values. The existence of a poloidal drift is evident. *Right*: Autocorrelation spectrum $E(k_x, k_y)$ of the potential from the left figure. The solid and dashed lines denote, respectively, the points where the squared Bessel function $J_0^2(k\rho)$ drops to $1/e$ times its maximum value and where it has its first zero. Here, $\rho = 6$, for which value both correlation lengths reach their maximum.

tives), and to interpolate between the grid points (for an overview on commonly used interpolation schemes, see Ref. (Yeung & Pope, 1988)). We found that the only method ensuring closed trajectories for static potentials is to both differentiate and interpolate in Fourier space. When using other, numerically less expensive interpolation schemes (e.g., bicubic interpolation), the trajectories are not closed anymore. Although the differences between Fourier and bicubic interpolation tend to be small as long as one is merely interested in *statistical* quantities (like diffusion coefficients) for *time-dependent* potentials, we still prefer to work with the Fourier method – it is most accurate (and works for any Kubo number) while sufficiently effective for our purposes.

We note that from now on, all values are normalized according to Section 2.4. So perpendicular length scales are normalized with respect to $\rho_s = c_s/\Omega_i$ where $c_s = (T_e/m_i)^{1/2}$ is the ion acoustic velocity and Ω_i the ion gyrofrequency, whereas time scales are normalized with respect to $L_\perp/c_s$ where $L_\perp$ is a scale length of the background profiles (which is distinct from, but similar, to R_0). In this section, we will abandon the hats denoting normalized values. The measured correlation lengths of the potential which will be used for our test particle studies are $\lambda_x = 6.1$ and $\lambda_y = 4.2$. Fig. 4.11 (left) displays the contours of the autocorrelation function of this potential plotted versus the coordinate y and time t. It can clearly be observed that while decaying to zero for large times and distances, the whole potential moves in the positive y direction with a velocity of about $v_{\text{dr}} = 0.95$. The components of the average $E \times B$ drift velocity are found to be $V_x = 3.3$ and $V_y = 2.3$. Since $\tau_c \approx 15$ in the co-moving frame, we have $v_{\text{dr}} \gtrsim 2\lambda_y/\tau_c$ ($\tau_{\text{drop}} \lesssim \tau_c$), and poloidal drift effects are expected to be significant. In a first step, however, we will consider a modified potential for which the drift has been removed. Drift effects will then be included in a second step.

4.6.1 First step: Neglecting poloidal drift effects

As was discussed above, the existence and magnitude of a poloidal drift depends on the simulation parameters. Linear gyrokinetic simulations show that if R/L_{T_e} and R/L_{T_i} become comparable, the phase and group velocities of ITG modes or TEMs tend to be rather small. We model such a situation by removing the drift from the original potential, i.e., we work with a new potential $\phi'(x, y, t) \equiv \phi(x, y+v_{\rm dr}t, t)$ where $v_{\rm dr} = 0.95$. Using ϕ', we perform test particle simulations for a set of different gyroradii and discuss the results in the light of the experience we made in Secs. 4.3 and 4.4.

Fig. 4.11 (right) shows the wavenumber spectrum of the TEM potential. We observe a maximum around $|k_y| \sim 0.2$ and $k_x \sim 0$. Since those modes play a prominent role, the autocorrelation function takes on negative values on the y axis in real space around $|y| \sim \pi/0.2 \sim 16$. Obviously, we have $\lambda_x > \lambda_y$, which means that the turbulence exhibits streamers (radially elongated eddies). However, one also observes that that there is significant activity for finite values of k_x – which is important for the understanding of finite gyroradius effects. As we have already discussed in detail, the effective autocorrelation function is obtained by multiplying the spectrum with $J_0^2(k\rho)$. In Fig. 4.11 (right), the $J_0^2 = 1/e$ line and the line of the first zero crossing are plotted for $\rho = 6$. Transforming the gyroaveraged spectra back to real space, one observes an increase of both λ_x and λ_y with increasing gyroradius, reaching their maximum values for $\rho = 6$. However, the increase is much larger in the x direction – in contrast to the findings in Sec. 4.3 where a Gaussian potential was considered. Here, the dominating finite k_y mode is not affected much by the gyroaveraging process, thus leaving λ_y more or less unchanged. This effect is somewhat similar to the one found in the zonal flow model studied in Sec. 4.4 – only that the roles of the x and y directions are reversed. The increase of λ_x is due to the long tails of the spectrum in the k_x direction which are removed under the influence of the Bessel function.

Fig. 4.12 (left) shows the running diffusion coefficient in both directions for a set of different gyroradii. One first notices that the diffusion is smaller in the y direction than in the x direction. This effect can be explained by remembering that the autocorrelation spectrum is characterized by $\lambda_x > \lambda_y$ and the existence of a dominating finite k_y mode. From Secs. 4.3 and 4.4, we already know that both effects lead to a relative decrease of the transport in the y direction. Furthermore, we observe that D_x is roughly constant for $\rho \lesssim 3$ (remember $\lambda_x \approx 6$) and then falls off as ρ is increased further. D_y, on the other hand, is reduced already for small gyroradii. However, this reduction is more moderate for larger ρ than that in the x direction. The ρ dependence of D_x can be interpreted via Fig. 4.13 where the saturation values of D_x (taken from Fig. 4.12 (left)) are plotted together with the estimates obtained from the formula $D_\rho/D_0 = (\lambda^{\rm eff}/\lambda_0)^{2-\gamma}(V^{\rm eff}/V_0)^{\gamma}(\tau^{\rm eff}/\tau_0)^{\gamma-1}$ (see Section 3.4 and 4.3, noting that now an effective correlation time has to be taken into account, too, since the frequencies are no longer independent of the wavenumbers). The effective values have been

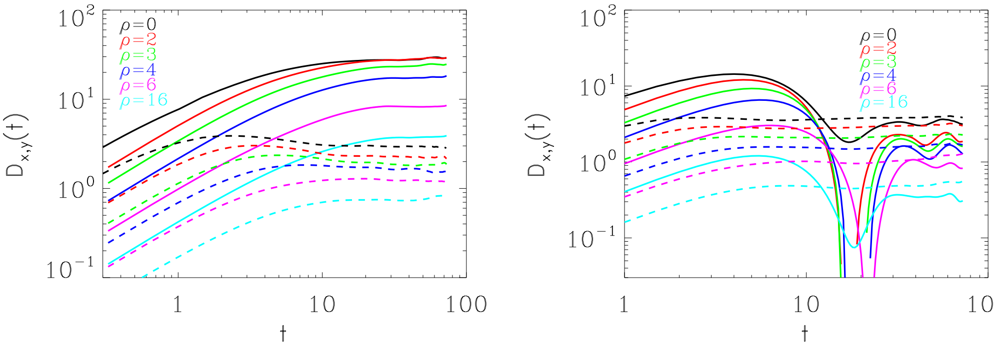

Figure 4.12: *Left*: $D_x(t)$ (solid lines) and $D_y(t)$ (dashed lines) for the potential of Figs. 4.11 (left and right) – but without poloidal drift – for different gyroradii. The Kubo number is $K = 8.6$ and the correlation time/lengths are $\tau_c = 15$, $\lambda_x = 6.1$, and $\lambda_x = 4.2$. *Right*: The same, but including the poloidal drift.

extracted from the gyroaveraged autocorrelation function as before. In the small and large Kubo number limit, we have used $\gamma = 2$ and $\gamma = 0.7$, respectively. As we can infer from Fig. 4.13, the simulation results follow the high Kubo number expectations quite well for small gyroradii, whereas they tend to approach the low Kubo number limit for larger values of ρ. (We note in passing that since $K = 8.6$ for the present case, we cannot expect that the large Kubo number limit is fully established.) This behavior can be understood by introducing effective (i.e., ρ dependent) Kubo numbers, $K^{\text{eff}} = \tau^{\text{eff}} V^{\text{eff}} / \lambda^{\text{eff}}$, and taking into account that γ can vary between 2 (linear regime) and about 0.7 (nonlinear regime). K^{eff} will decrease rapidly if ρ is increased since V^{eff} decreases but λ^{eff} grows. Once K^{eff} approaches unity, we expect the effective value of γ to increase. This fact qualitatively explains the behavior of the simulation results shown in Fig. 4.13. In search of a more quantitative approach, we determined a function $\gamma(K^{\text{eff}}(\rho))$. To this aim, we modified the original TEM data by rescaling the length of the time intervals between the successive steps written out by Gene. This manipulation enabled us to vary the correlation time and therefore the Kubo number of the TEM potential. We then compared the values of $K^{\text{eff}}(\rho)$ with the expression $D(K) = a(K)\, K^{\gamma(K)-1}$ to obtain $\gamma(\rho)$ and $a(\rho)$. Thus, one gets

$$D_\rho / D_0 = \frac{a_\rho \lambda_\rho^{2-\gamma_\rho} V_\rho^{\gamma_\rho} \tau_\rho^{\gamma_\rho - 1}}{a_0 \lambda_0^{2-\gamma_0} V_0^{\gamma_0} \tau_0^{\gamma_0 - 1}} \,. \tag{4.10}$$

The corresponding values are shown as a dashed line in Fig. 4.13. Obviously, they are in good agreement with the simulation results, demonstrating that the form of D_ρ/D_0 is well captured by our effective autocorrelation function approach for a large class of potentials.

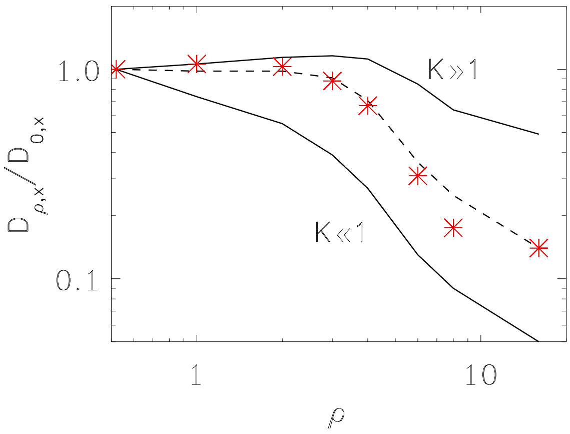

Figure 4.13: Comparison between the simulation results (symbols) from Fig. 4.12 (left) and the semi-analytical approach described in Chapter 3 (solid lines) for $K \ll 1$ and $K \gg 1$. The subscripts ρ and 0 denote, respectively, cases with finite and vanishing gyroradius. The dashed curve is an extension of the usual semi-analytical approach, employing a "dynamical" $\gamma(\rho)$.

4.6.2 Second step: Including poloidal drift effects

Having discussed the behavior of trace ions in a realistic turbulence potential for which poloidal drift effects have been removed, we would now like to include the latter. With $v_{\mathrm{dr}} = 0.95$, we find $\tau_{\mathrm{drop}} = 9.1$ which is slightly smaller but comparable to the correlation time $\tau_c = 15$ (a similar case has been considered in Sec. 4.5). In Fig. 4.12 (right), the running diffusion coefficients D_x and D_y are plotted for a set of different gyroradii. The results are reminiscent of those in self-generated drifting potentials shown in Fig. 4.8 (left and right). First, we observe that D_y is enhanced and D_x is reduced compared to the case with $v_{\mathrm{dr}} = 0$ shown in Fig. 4.12 (left). The physical origin of this behavior has already been identified in Sec. 4.5. Again we have the situation that $\tau_{\mathrm{drop}} \sim \tau_c$ which means that the decorrelation process – the transition into the diffusion regime – occurs in the time segment where the variation of D_x is large. Therefore the saturated value of D_x depends quite sensitively on the saturation time.

In Sec. 4.5, we have already made the observation that the saturation time gets larger compared to the correlation time as the (effective) Kubo number gets smaller, i.e., as the gyroradius increases. In Fig. 4.12 (right), this effect seems to be stronger than in Fig. 4.8 (left); although for $t \sim \tau_{\mathrm{drop}}$, the curves for different ρ lie close to each other, the saturation values decrease rapidly even for small ρ. So in contrast to the case described in Sec. 4.5, we have here the situation that poloidal drift effects lead to a stronger reduction of the diffusion with increasing gyroradius, illustrating the subtle interactions between finite gyroradius and poloidal drift effects. In this context, we would like to point out that for realistic turbulence potentials (like the one considered here) the gyroaveraging also affects the correlation time since the wavenumbers and frequencies of the individual modes are correlated. For example, for $\rho = 3$, the correlation time is increased by a factor of about 1.1, which of course provides a contribution to the increase of the saturation time. – In the y direction, one observes a strong reduction of D_y with increasing ρ compared to Fig. 4.8 (right). This effect has already been described in Sec. 4.5, where we found that it is due to the reduction of the number of trapped particles in the effective potential.

4.7 Summary and conclusions

The main goal of the work presented in this chapter was to investigate the behavior of trace ions in realistic turbulent fields, focusing on the various physical effects determining their particle diffusivities. For simplicity, we have restricted to electrostatic fluctuations and two dimensions as far as the particle trajectories are concerned. Nevertheless, we have used electrostatic potentials taken from three (space) dimensional gyrokinetic simulations with the GENE code. As an example, trapped electron mode turbulence was chosen. In order to be able to study several individual effects in isolation, we also considered potentials which were generated by superposing a large number of random waves. These supplementary studies helped to gain a basic understanding of trace ion transport which is crucial for interpreting the gyrokinetic data.

We found that fluctuation anisotropies like streamers (radially elongated vortices) and zonal flows (poloidal shear flows) may strongly influence the resulting transport levels as well as the gyroradius dependence. Here, the transport may decrease faster or even grow as the gyroradius is increased. Finally, we have shown that poloidal drift effects can have a strong impact on the particle diffusion, enhancing it in the direction of the drift and reducing it in the other (radial) direction. Although the underlying mechanisms are different than for non-drifting potentials, regimes can still be found in which the transport stays constant for gyroradii up to a correlation length.

In many cases, there exist subtle interactions between various effects (e.g., finite gyroradius and finite poloidal drift), leading to fairly complex behavior. Nevertheless, we were able to demonstrate that the diffusivities obtained from tracking particle trajectories in realistic turbulence potentials are usually well described and understood in terms of simple scaling laws employing (effective) correlation lengths, correlations times, and Kubo numbers. This information can be extracted from the autocorrelation function of the (gyroaveraged) potential. Thus, one obtains a fairly coherent picture of (perpendicular) trace ion transport in turbulent plasmas.

The strong dependence on the magnitude of the fluctuations' poloidal drift velocity may – in practice – often be more important than the presence of zonal flows. In Chapter 6, it will turn out that it is especially the poloidal drift of the particles relative to the background potential which dominates transport also in a full three-dimensional environment.

Chapter 5

Non-Diffusive Transport in 2D Electrostatic Turbulence

In this chapter, the studies of the previous chapter are continued, focusing on the question whether and under which conditions the transport may become 'anomalous', i.e. super- or subdiffusive. While in the presence of stochastic fluctuations, the transport always becomes diffusive for large times, coherent flow components like zonal flows or poloidal drifts can induce non-diffusive (non-Gaussian) transport over large intermediate time spans. In order to understand the origin of these phenomena, the simple model employing stochastic potentials is used to complement the analysis based on gyrokinetic turbulence simulations. The results of this chapter have been published in (Hauff *et al.*, 2007).

5.1 Introductory remarks

Until now, we have assumed that transport in turbulent fields as described by tokamak microturbulence is always diffusive, which was also confirmed by our simulation results. Nondiffusive regimes have only been identified for rather 'pathological' situations, like frozen vortices, or on very small time scales. In the fusion community, it is common to portray turbulent transport in tokamaks and stellarators as a standard diffusive process – in spite of its advective nature. However, there also exist several investigations dealing with the possibility of super- or subdiffusive transport, an interesting scenario which should not (and cannot) be excluded *a priori*. Unfortunately, neither the conditions under which such 'anomalous diffusion' is expected to occur nor its physical origin are well understood at present. This is the reason why in the present chapter, we will focus on this question, employing the well-proven connection of self-created pseudo-turbulent velocity fields with data from nonlinear gyrokinetic simulations for parameters which are typical for tokamak core turbulence.

There is a number of well known experimental findings which can be interpreted as evidence for the existence of non-Gaussian transport. Among these are, for instance, the dependence of transport on the system size in low confinement mode plasmas (Perkins *et al.*, 1993), the observed rapid propagation of an induced perturbation (Gentle *et al.*, 1995; Callen & Kissick, 1997), or the measurement of long-range temporal and radial correlations in the plasma edge (Carreras *et al.*, 1998; Carreras *et al.*, 1999b; Zaslavsky *et al.*, 2000). Such observations are sometimes explained in terms of avalanches or self-organized criticality (SOC). Inspired by experimental (and theoretical) evidence for the existence of critical gradients (Baker *et al.*, 2001), the model of the 'stochastic sandpile' (Carreras *et al.*, 1999a) has been developed, for example. It is possible to link numerical simulations of plasma turbulence to the running sandpile by allowing for a temporal evolution of the mean profiles (and the respective gradients which drive the turbulence). Some numerical results are consistent with SOC characteristics (Carreras *et al.*, 1996; Mier *et al.*, 2006), and superdiffusive transport has been found, e.g., for pressure-gradient-driven plasma turbulence and attributed to avalanche effects (Carreras *et al.*, 2001; del Castillo-Negrete *et al.*, 2004). The idea of a critical density gradient acting as a threshold for avalanche transport has also been included into the framework of continuous time random walks (CTRWs), being able to reproduce some of the basic phenomenology of anomalous (superdiffusive) transport scaling in the low confinement mode (van Milligen *et al.*, 2004a; van Milligen *et al.*, 2004b). However, despite the interesting nature of these results, it is far from evident that they carry over to plasma core turbulence in large fusion devices like ITER (ITER, 1999). Most of the experimental results showing superdiffusive transport are achieved for the plasma edge, and to which degree the observation of a 'prompt' perturbation response is of relevance to the usual steady-state conditions is not clear ((Balescu, 2005), p. 418). Moreover, some of the assumptions underlying the 'sandpile' based numerical work are not necessarily justified in the plasma core of larger fusion devices.

Various papers approach the question of anomalous transport from a different perspective. Instead of trying to reproduce or analyze experimental data, they work with more simple turbulence models or analytically given fields in order to study the transition from a diffusive to a superdiffusive regime in detail. An interesting attempt to understand the basic mechanisms of superdiffusive particle transport is the detection of so-called 'chaotic jets' (Afanasiev *et al.*, 1991; Leoncini & Zaslavsky, 2002; Leoncini *et al.*, 2005). Here, the origin of superdiffusion has been ascribed to the existence of long-living bundles of orbits with coherent propagation, constituting an independent structure, a 'hidden order' with almost free motion within the sea of turbulence. The life-time of such 'jets' was found to be much longer than the ordinary 'clump lifetime' of particles with close initial conditions ((Balescu, 2005), Chap. 13). In Ref. (Leoncini & Zaslavsky, 2002), a model of 16 point vortices was introduced, and a connection between superdiffusion and the accumulation of small Lyapunov exponents was established. In Ref. (Leoncini *et al.*, 2005), the same technique was applied to the more realistic model of 2D Hasegawa-Mima turbulence, and similar results were found (see also Ref. (Annibaldi *et al.*, 2002) where superdiffusion was found for small box sizes and large density gradients). However, it is not at all clear if such minimal models – often yielding more or less stationary vortex structures – lead to a good representation of turbulence in fusion devices. It is therefore necessary to analyze data from nonlinear gyrokinetic simulations which are considered to be first-principles based. This approach was chosen for the first time in Chapter 4 in this thesis. Here, it was shown that fluctuating vortices, even when advected with a constant drift velocity, always lead to diffusive behavior for long times. However, in this case, zonal flows – which are a possible source for superdiffusive transport – were rather weak. In another analytic approach, modeling a turbulent bath with a *single* zonal flow as a vortex chain inside a shear layer, superdiffusive transport was found in the 'stochastic layer' where the particles alternate between being trapped in a vortex and moving ballistically with the shear flow (del Castillo-Negrete, 1998; del Castillo-Negrete, 2000). Consequently, superdiffusion was interpreted as a result of the presence of coherent structures in a turbulent background.

In the present chapter, we intend to go through a two-step process, similar to Chapter 4. In the first step (Sec. 5.2), we would like to study test particle transport in random (pseudo-turbulent) fields created by superposition of plane waves. As before, this enables us to have easy control over the field's statistical properties, and allows for the inclusion of additional effects like poloidal drifts and zonal flows which will turn out to be crucial for the existence of non-Gaussian transport regimes. Then, in a second step (Sec. 5.3), we will compare these results with simulations using realistic turbulent fields taken from simulations with the turbulence code GENE. Examining two examples, trapped electron mode (TEM) turbulence and ion temperature gradient (ITG) turbulence, where the effects of poloidal drifts and zonal flows are rather strong, we find that while the transport gets diffusive and Gaussian for large times, there may exist super- and subdiffusive regimes for intermediate times. Given the fact that these (radially local) gyrokinetic simulations are known to be fully consistent with nonlocal ones for sufficiently small values of the normalized ion gyroradius $\rho^* = \rho_s/a$ ($\rho^* \lesssim 1/300$, a minor torus radius) (Waltz *et al.*, 2002; Candy *et al.*, 2004), large-scale devices are expected to be well represented by the data used here. We will close with a summary and some conclusions in Sec. 5.4.

5.2 Diffusion in random fields

5.2.1 Some preliminaries

For the last time, we consider the $E \times B$ advection of ions as passive tracers in a plane perpendicular to the background magnetic field. In Sec. 5.3, the fluctuating electrostatic potentials $\phi(\mathbf{x}, t)$ will be taken from simulations with the GENE code, whereas in the present section, they will be created by superposing a sufficiently large number of random harmonic waves, as described by Eq. (3.1). This approach allows for easy control and variation of the properties of the advecting field, enabling us to get a deeper understanding of the basic mechanisms underlying the transport of passive particles which can them be applied to more realistic cases in a second step.

The motion of passive particles is again described by the (normalized) $E\times B$ drift velocity (Eq. (2.61)). Finite gyroradius effects are neglected here, but could be included in a straightforward fashion as has been done in Chapters 3 and 4. The Kubo number (Eq. (2.62)) stays important for characterizing the velocity field.

The transport is characterized, as usual, by the second moment of the particle displacements,

$$\langle x_i^2(t)\rangle \sim t^\mu \tag{5.1}$$

(see Eq. (2.53) in Sec. 2.5.1). For $\mu = 1$, one has standard diffusive behavior, while for $\mu < 1$ and $\mu > 1$, one has sub- and superdiffusive scaling, respectively. Since we will always find a transition to diffusive scaling for sufficiently long simulation times, we hold on to plot the second moment in the form of the time dependent ('running') diffusion coefficient, as defined in Eq. (2.51). For the particle trajectory simulations, the same numerical methods have been applied as described in the previous chapters.

In a pure isotropic and stochastic potential, transport obviously becomes diffusive as soon as the correlation time of the fluctuations is exceeded, since no memory exists. This important relation is quantified by the Taylor formula, Eqs. (2.54) and (2.55). The introduction of streamers, i.e. structures which are elongated in the x direction, only quantitatively changes the values of D, but preserves the diffusive character, since a complete decorrelation still occurs for $t > \tau_c$ (see Sec. 4.3). Interesting new regimes of transport can be expected only from additional coherent structures with much larger (or infinite) correlation times. In the following, we will modify the stochastic potential given by Eq. (3.1) by adding coherent flow effects. We hereby follow Chapter 4; however, emphasis is now placed on the existence of an intermediate nondiffusive regime and the transition to standard diffusive transport for sufficiently long simulation times.

5.2.2 Poloidal shear flow effects

As a model potential for the simulation of zonal flows, we choose again Eq. (4.2) from the last chapter. Here, the correlation length of the isotropic part is modeled to $\lambda_c = 1$, and the wave number of the zonal flow is chosen to be $k_{\mathrm{zf}} = 0.78$. Varying A_{zf}, the coherent component of the model potential can be changed. For comparison, we note that the root mean square of the stochastic component is $\sqrt{\langle\phi^2\rangle} = 0.03$. In Fig. 5.1, the running diffusion coefficient is plotted for different values of A_{zf}. The Kubo number of the stochastic part has been chosen to be $K = 5$, which is realistic (see Sec. 5.3) and implies reasonably strong trapping events. In the pure stochastic potential ($A_{\mathrm{zf}} = 0$), we observe ballistic transport for small times which – after a short period of subdiffusion due to particle trapping – transitions to a diffusive regime as soon as the potential decorrelates (i.e. for $t \gtrsim \tau_c \approx 120$). With the increase of the zonal flow amplitude A_{zf}, intermediate regimes of subdiffusion and superdiffusion emerge in the x and y direction, respectively. Qualitatively, the increase of transport in the direction of the flow and the decrease in the perpendicular direction are not difficult to understand, since the zonal flow term fundamentally changes the structure of the stream function, favoring open equipotential lines in the y direction and suppressing them in the x direction.

In this context, some interesting quantitative observations can also be made. First, the y direction displays superdiffusive transport with a constant value $1 < \mu < 2$ for a relatively large time intervals, and second, for all values of A_{zf},

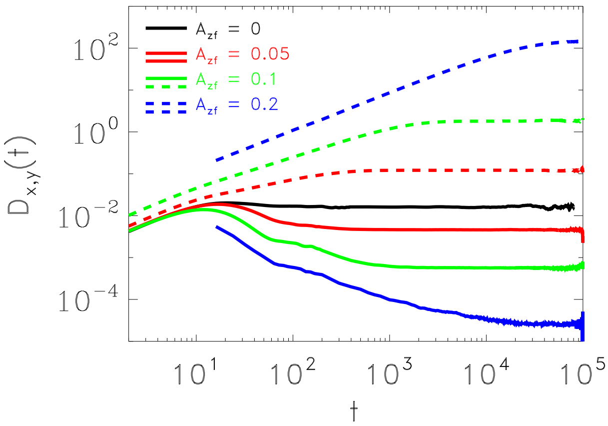

Figure 5.1: Running diffusion coefficient $D(t)$ for different zonal flow amplitudes [Eq. (4.2), $K = 5$]. The solid lines denote the x direction, the dashed lines the y direction. In the y direction, a superdiffusive transitional regime is found for intermediate times. In that regime, we find $\mu \approx 1.5$ for $A_{\text{zf}} = 0.05$, $\mu \approx 1.7$ for $A_{\text{zf}} = 0.1$, and $\mu \approx 1.9$ for $A_{\text{zf}} = 0.2$.

there is a time scale beyond which the transport becomes diffusive. The first effect can be described phenomenologically in terms of a 'continous time random walk' (CTRW) model (Montroll & Weiss, 1965; Metzler & Klafter, 2000; Metzler & Klafter, 2004). Here, the subtle interplay between the stochastic fluctuations and the coherent component is represented by a purely probabilistic model built on waiting time and particle displacement distributions. Asymptotically, the Laplace transformation of the waiting time distribution can be modeled as $\tilde{\psi}(s) = 1 - A\, s^{\beta}$ with $0 < \beta < 1$, and the Fourier transform of the particle displacement distribution as $\tilde{f}(k) = 1 - B\,|k|^{\alpha}$ with $0 < \alpha < 2$. The exponent of the mean square displacement resulting from such a stochastic process can then be expressed as $\mu = 2\beta/\alpha$. Obviously, in the most simple approach, the particle motion underlying Fig. 5.1 can be modeled by slowly decaying distributions of the particle displacements in the y direction and of the waiting time in the x direction. Similar descriptions have already been applied successfully to other superdiffusive transport phenomena (del Castillo-Negrete *et al.*, 2004; Afanasiev *et al.*, 1991).

Trying to understand the second effect mentioned above leads us to consider an additional physical mechanism. Comparing Fig. 5.1 with the probability distribution function (PDF) of the particle displacements in the y direction plotted in Fig. 5.2 (left) for $A_{\text{zf}} = 0.1$, we see that for intermediate times (when the transport is superdiffusive), there are two peaks in the PDF – representing the bulk of particles which is advected ballistically up and down the y direction with the mean shear flow velocity. The peak at $y = 0$ stands for the particles being trapped by vortices at the combs of the potential. The interaction between trapping caused by the stochastically evolving vortices and the free poloidal motion due to the strong zonal flow component leads to a slowly decaying particle displacement distribution and to an exponent $\mu > 1$. Furthermore,

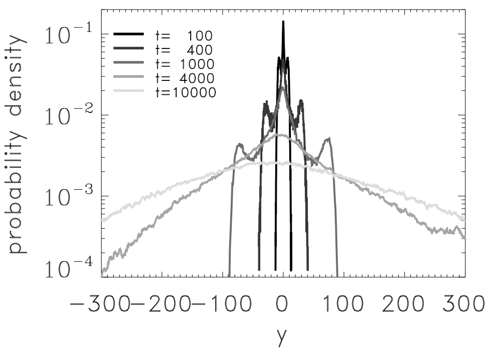

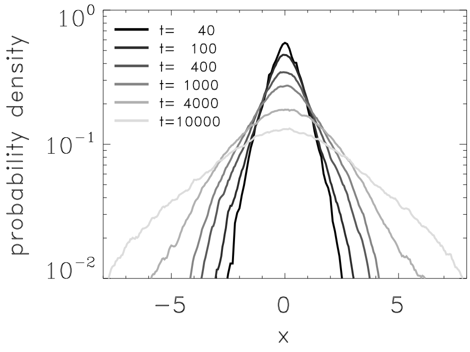

Figure 5.2: *Left*: PDF of the particle displacements in the y direction for $K = 5$ and $A_{\mathrm{zf}} = 0.1$ for different times. [Note that $\tau_c \approx 100$.] For small times, the superdiffusive advection of the tracers with the shear flow can be observed for positive and negative directions. For $t > t_1 \approx 2000$, transitions between different zonal flow channels occur, transforming the distribution into a Gaussian one. *Right*: The same, but for the x direction. For times $t < t_1 \approx 2000$, particles are trapped inside a shear layer of the width $\pi/k_{\mathrm{zf}} \approx 4$. For larger times, a significant number of transitions into neighboring layers occur.

comparing Fig. 5.1 and Fig. 5.2 (left), we notice that the transition to the diffusive regime occurs when the ballistic peaks of the PDF have just vanished. Fig. 5.2 (right) sheds some more light onto this effect. We observe that for $t \lesssim t_1 \sim 2000$ – i.e. during the time span for which the transport is superdiffusive in the y direction and subdiffusive in the x direction – the particle distribution is trapped inside the individual shear flow 'channels' ($-\pi/k_{\mathrm{zf}} < x < \pi/k_{\mathrm{zf}} \approx 4$). For larger times ($t \gtrsim t_1$), we then find that particles may move into a neighboring structure. This means that the direction of the flow is reversed, and a randomization takes place.

In order to make this transition more transparent, we measured the distribution of the first passage time of the particles, i.e. the time interval which particles need to leave a given flow channel and move from an upward to a downward flow or vice versa. This distribution is plotted for $A_{\mathrm{zf}} = 0.1$ in Fig. 5.3 (left). It is clear that if a finite transition probability between the flow structures exists – which will always be the case it a perturbation in form of time dependent fluctuations is introduced – the waiting time distribution will fall off exponentially. For such a function, the first moment exists, and given the fact that we can characterize the particle displacements in the x direction as discrete steps of size $\Delta x = \pi/k_{\mathrm{zf}}$, this in turn means that the transport becomes diffusive (Montroll & Weiss, 1965). Consequently, the dynamics on large time scales can be modeled by an ordinary random walk with $D \sim \Delta x^2/(2\Delta t)$, where Δt is defined as the e-folding length of the passage time distribution. With $\Delta t \approx 9500$ and $\Delta x \approx 4$ we find $D \approx 0.00085$ which favorable agrees with the simulated diffusion coefficient for $A_{\mathrm{zf}} = 0.1$ plotted in Fig. 5.1. In terms of the CTRW model, this situation corresponds to a 'truncated waiting time distribution'. The first passage time of the test particles plotted in Fig. 5.3 (left)

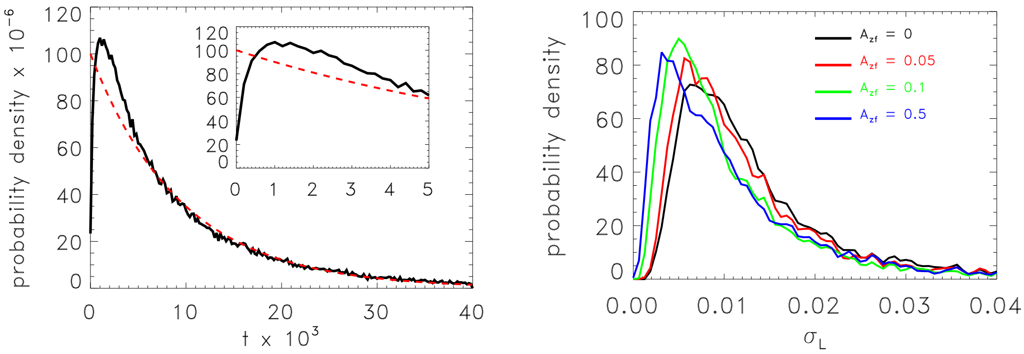

Figure 5.3: *Left*: First passage time of a particle to move from an up- into a downward flow or vice versa for $A_{\mathrm{zf}} = 0.1$. Solid line: PDF of the first passage time from the simulation. Dashed line: $0.0001 \exp(-t/9500)$. *Right*: PDF of the Lyapunov exponent $\sigma_L = T^{-1} \ln(\delta/\epsilon)$ for different values of A_{zf}. Here, $\delta = 0.1$ and $\epsilon = 0.001$. No accumulation near $\sigma_L = 0$ is observed, even for very large zonal flow amplitudes.

shows a sharp increase of $\Psi(t)$ followed by a flat regime of $\Psi(t)$ for intermediate times ($t \lesssim t_1$) and an exponential decay for $t \gtrsim t_1$. Using the CTRW mechanism, such a distribution reproduces the observed diffusivities (Dentz *et al.*, 2004). In particular, we observe that the time scale t_1 inferred from Fig. 5.3 (left) corresponds to the time t_1 in Fig. 5.1. It is clear from this discussion that the intermediate time interval which is characterized by super- and subdiffusion can grow indefinitely as the zonal flow term gets stronger and stronger.

In previous publications, anomalous transport behavior has sometimes been attributed to the existence of 'chaotic jets', i.e. special paths in a generally chaotic environment exhibiting a large stickiness of the advected particles as well as a coherent, ballistic motion (Afanasiev *et al.*, 1991; Leoncini & Zaslavsky, 2002; Leoncini *et al.*, 2005). As an indicator, an accumulation of Lyapunov exponents near zero was identified. In Fig. 5.3 (right), the distribution of Lyapunov exponents is plotted for different values of A_{zf}. These quantities are calculated via (Leoncini & Zaslavsky, 2002)

$$\sigma_L = T^{-1} \ln(\delta/\epsilon)\,, \tag{5.2}$$

where T is the time two particles remain within a distance smaller than δ, and ϵ is the initial separation of the two particles. One typically assumes $\delta \gg \epsilon$ with both quantities chosen to be rather small. We observe, however, that even for very large zonal flow amplitudes [recall that the stochastic component of Eq. (4.2) is $\sqrt{\langle\phi^2\rangle} = 0.03$], there is no accumulation of Lyapunov exponents near $\sigma_L = 0$. This behavior in turn corresponds to the exponential decay of the PDF of the 'sticking time' T which we observed for all the cases displayed in Fig. 5.3 (right). Such a decay is a normal consequence of the 'clump effect' ((Balescu, 2005), Chap. 13), and does not depend on the existence of any special structure. Simply said, two particles starting in a close neighborhood separate when they encounter a hyperbolic fixed point. Since in time dependent potentials this is a stochastic process with a given probability, the 'sticking time' will naturally exhibit an exponential decrease. So although strong coherent structures are present in this model potential, no chaotic jets can be observed. In (Padberg *et al.*, 2007), the recently developed concept of *Lagrangian coherent structures* (Haller, 2000) based on finite time Lyapunov exponents was applied to the 2D turbulent transport of test particles and studied in detail. Using visualizations of the network of repelling and attracting material lines obtained that way, interesting new possibilites for interpreting and analyzing turbulent transport in magnetized plasmas were presented, however, they seem to be more of qualitative nature.

5.2.3 Poloidal drift effects

In Chapter 4 it was shown that homogeneous poloidal drifts may have the same effect on transport as poloidal shear flows. There, a 'drifting potential' ϕ_{dr} was defined as a (fluctuating or static) potential whose structures move in the poloidal (y) direction with a constant drift velocity v_{dr}. Such a potential was modeled in Eq. (4.5). In Chapter 4 it was shown that in order to understand the effect of such a homogeneous drift, it is useful to perform a Galilei transformation to a reference frame moving in the y direction with velocity v_{dr}. This led to the electrostatic potential defined by Eq. (4.7), where the prime denotes quantities in the co-moving system. It has already been discussed that the law of induction produces an additional electric field (second term on the right-hand side of Eq. (4.7)), which gives the potential a completely new structure and is responsible for the differences compared to a non-drifting potential. We have already recognized that this structure shows similarities to that of a zonal flow. As we will see shortly, the particle transport indeed exhibits the same behavior as found in the previous section. This includes, in particular, not only the suppression of transport in the x direction and its increase in the y direction, but also sub- or superdiffusive transport for intermediate time scales.

Fig. 5.4 shows the running diffusion coefficient for different drift velocities v_{dr}. It can clearly be seen that the effect of the poloidal drift is similar to the effect of zonal flows (compare to Fig. 5.1), in both the radial and the poloidal direction. However, the additional term in Eq. (4.7) is not periodic now, but corresponds to an infinite ramp. This makes the transport suppression in the x direction stronger. For large times, we again find a transition to diffusive behavior. The modeling in terms of a random walk model seems to be difficult at first, since in contrast to the zonal flow potential, no reference length scale is given explicitly. On the other hand, it is possible to define an intrinsic length scale via the maximum excursion of an equipotential line in the x direction, $x_{\max} \approx 2\phi_{\max}/v_{\mathrm{dr}} \approx 2V\lambda_c/v_{\mathrm{dr}}$ (see discussion in Sec. 4.5). For the given potential and $v_{\mathrm{dr}} = 0.05$, we find $x_{\max} \approx 2$. The relevance of this limit can clearly be observed in the PDF of Fig. 5.5 (left) for small times, whereas for larger times, the transport becomes diffusive. So the effect is basically the same as in the zonal flow case. In Fig. 5.5 (right), the PDF is displayed for the y direction. Again, we observe a similar behavior as in the zonal flow case (Fig. 5.2 (left)), but we now have a single peak of trapped particles moving upwards with the drift velocity and a bulk of particles moving downwards on

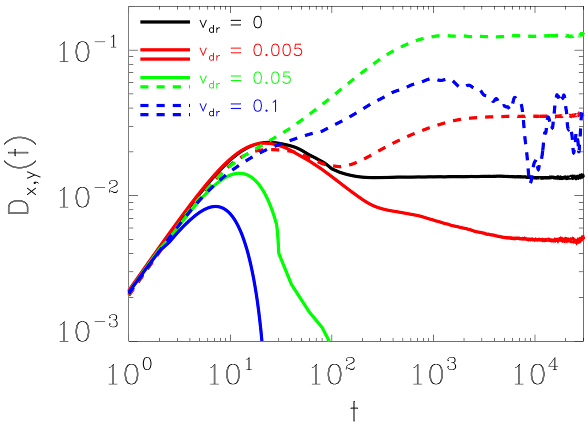

Figure 5.4: Running diffusion coefficient $D(t)$ for different drift velocities [Eq. (4.5), $K = 20$]. The solid lines denote the x direction, the dashed lines the y direction. In the y direction, a superdiffusive transitional regime is found for intermediate times. In that regime, we find $\mu \approx 1.35$ for $v_{\rm dr} = 0.005$, $\mu \approx 1.55$ for $v_{\rm dr} = 0.05$, and $\mu \approx 1.39$ for $v_{\rm dr} = 0.1$. The saturation values for the x direction outside the range of the figure are $D_x = 10^{-4}$ for $v_{\rm dr} = 0.05$ and $D_x = 5 \times 10^{-6}$ for $v_{\rm dr} = 0.1$.

open equipotential lines, whereas in the former case, we found two peaks moving upwards and downwards within a given zonal flow channel. This behavior has already been displayed in Fig. 4.10 (right), however, not in the long time limit, where the transition to a Gaussian distribution function can be observed in the present figure. Here, the transition to a normal diffusive behavior is not caused by the transition to a flow with reversed flow direction, but by the transition from trapped particles advected with the diamagnetic drift to free particles moving against the drift and vice versa. A similar, though more qualitative study of the interplay between free and trapped advected particles can be found in Ref. (Naulin *et al.*, 1999).

In order to further investigate the time evolution of the PDFs shown in the last two subsections, a plot of the kurtoses for all the discussed cases is shown in Fig. 5.6. We define the kurtosis as

$$\gamma_2 = \left\{ \frac{1}{N} \sum_{i=1}^{N} \left[\frac{x_i - \bar{x}}{\sigma} \right]^4 \right\} - 3 \,, \tag{5.3}$$

where N is the number of test particles, x_i is the displacement of a single particle from its origin, $\bar{x}$ is the mean value of x_i and σ is the mean square displacement. As is well known, Gaussian distributions are characterized by $\gamma_2 = 0$, whereas $\gamma_2 > 0$ ($\gamma_2 < 0$) indicates a slower (faster) than Gaussian decay. The kurtoses in Fig. 5.6 are calculated for the same data plotted as PDF in Figs. 5.2 (left and right) and 5.5 (left and right). We clearly observe the transition $\gamma_2 \to 0$ for large times. Interestingly, the kurtosis for the x direction for a drifting potential is close to zero for all times despite the fact that there exists a spatial limit (see Fig. 5.5 (left)). We can explain this observation by the fact that this limit is

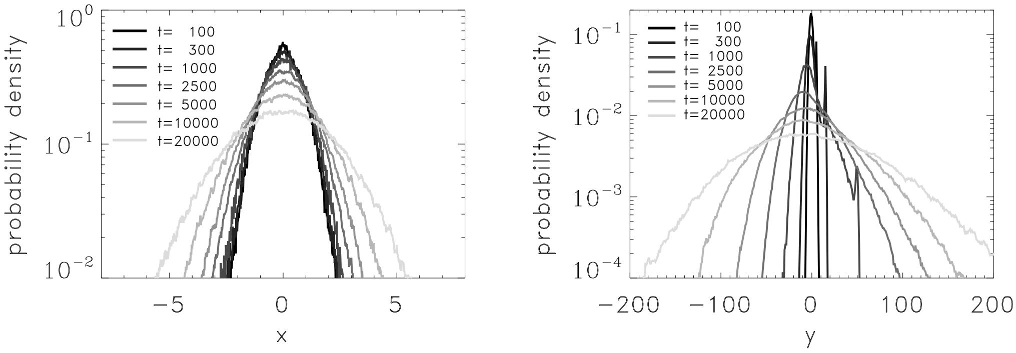

Figure 5.5: *Left*: PDF of the particle displacements in the x direction for $K = 20$, $v_{\rm dr} = 0.05$ for different times. Note that $\tau_c \approx 100$. For times $t < 2000$ particles are trapped inside a threshold of the width $x_{\max} \approx 2\,V\lambda_c/v_{\rm dr} \approx 2$. For larger times, a significant number of transitions into neighboring layers occur. *Right*: The same, but for the y direction. For small times, peaks can be observed at $y = v_{\rm dr}t$, displaying the motion of trapped particles with the diamagnetic flow in the positive y direction. For $t > 1000$, transitions between the trapped upward-moving and the free downward-moving particles evolve, transforming the distribution into a Gaussian one.

not a 'hard' one like in the zonal flow case, but rather a 'soft' one.

Hence we have demonstrated that the existence of large coherent components in a fluctuating potential – represented here by a static zonal flow and a constant drift velocity – can lead to extended regimes of anomalous diffusion for intermediate times, but always shows a transition to the diffusive regimes for large times. In the following, we show that this simple model displays a good correspondence to transport in realistic potentials as described by nonlinear gyrokinetics, and it will turn out that the above interpretations for the simple models carry over to the more realistic ones.

5.3 Diffusion in realistic turbulent fields

Until now, we have studied the transport of passive tracers in electrostatic potentials which were created by superposing a large number of plane waves. Applying this method, we where able to model and analyze the influence of zonal flows and diamagnetic drifts on the transport. The variation of the strength of those additional effects enabled us to study the regime of anomalous diffusion for intermediate times and the conditions for a transition to normal diffusion. Keeping these results in mind, we now want to consider the transport behavior of test particles in realistic electrostatic potentials as they occur for ITG and TEM turbulence. As we will see, these two cases exhibit the same effects as discussed in the previous section.

For this purpose, we use simulation data obtained with Gene code. The data was provided by T. Görler, F. Merz, and M.J. Püschel. As in the previous chapter, the electrostatic potential in a perpendicular plane on the low-field

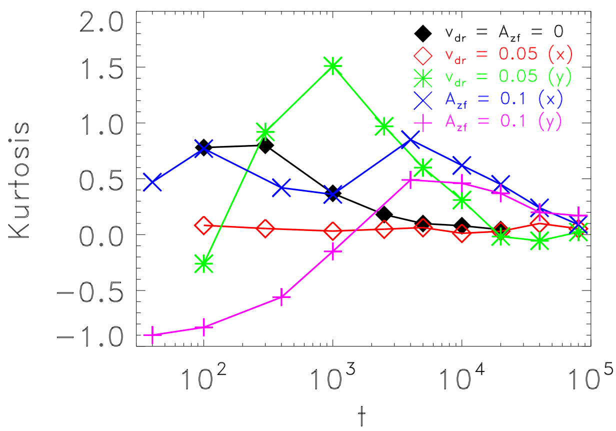

Figure 5.6: Kurtoses for the PDFs shown in Fig. 5.2 (left and right) and 5.5 (left and right). The kurtoses clearly approach zero for large times, indicating the transition to a Gaussian distribution.

side is written out frequently and then subjected to post-processing. However, for spatial interpolation, a simple bicubic scheme is used here. (In order to test its accuracy, comparisons with Fourier interpolation – which is the most exact interpolation method – have been performed for a few test cases, but no significant differences were found.) We note that from now on, perpendicular length scales are normalized with respect to $\rho_s = c_s/\Omega_i$, whereas time scales are normalized with respect to $L_\perp/c_s$ where $L_\perp$ is a scale length of the background profiles (see Sec. 2.4). Since GENE uses periodic radial boundary conditions (keeping the average background gradients fixed), the simulation box sizes were chosen about one order of magnitude larger than the correlation lengths of the turbulence. Therefore, finite size effects do not play a role.

First, we study the test particle transport in ITG turbulence. Here, the so-called Cyclone base case parameter set as described in Ref. (Dimits *et al.*, 2000) is used. A typical contour plot of the electrostatic potential in the outboard midplane is shown in Fig. 5.7 (left). The zonal flow structures are very prominent. As one may expect from this figure, the running diffusion coefficient exhibits a distinct regime of superdiffusion in the y direction for intermediate times, together with a (less distinct) regime of subdiffusion in the x direction (Fig. 5.7 (right)). The curves show a close correspondence to the cases with high zonal flow amplitude in Fig. 5.1. In addition, the PDFs of the particle displacements for a number of different times are given in Fig. 5.8 (left and right). Their shape is again comparable to the PDFs plotted in Fig. 5.2 (right and left). Especially, the threshold of $\Delta x = \pi/k_{\text{zf}} \approx 40$ can be observed in Fig. 5.8 (left), and the disappearance of the ballistic peaks of the y-PDF corresponds again to the transition to diffusive transport.

Second, the transport of test particles in TEM turbulence, which was already studied in Sec. 4.6, is investigated under the aspect of the transition into a diffusive regime. Therein, the correspondence to the studies employing self-created potentials has already been demonstrated. In TEM turbulence, zonal

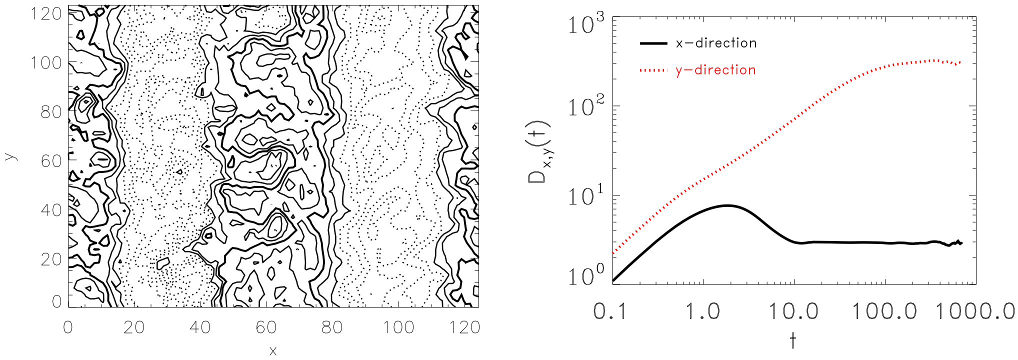

Figure 5.7: *Left*: Contours of the ITG electrostatic potential ('Cyclone base case'). Positive contours are drawn with solid lines, negative contours with dashed lines. Strong zonal flows are present, forming a dominant coherent background. *Right*: Running diffusion coefficient $D(t)$ for the ITG electrostatic potential plotted in Fig. 5.7 (left) ($K \approx 7$). The curves are comparable to the ones obtained by the self-created potential (Fig. 5.1). For the superdiffusive transition regime in the y direction we find $\mu \approx 1.72$ for intermediate times.

flows tend to be rather weak (Dannert & Jenko, 2005), such that diamagnetic drift effects will be more important. The running diffusion coefficient for this case has been plotted in Fig. 4.12. However, since the diamagnetic drift velocity is relatively small in that case, the PDFs do not exhibit a clear threshold effect in the x direction and the ballistic peaks in the y direction, and their shape is quite close to a Gaussian even for small times.

In Fig. 5.9, the kurtoses of the particle PDFs are plotted for the ITG as well as for the TEM potential versus time. Similar to Fig. 5.6, the transition to a Gaussian distribution, expressed by $\gamma_2 \to 0$ for large times, can be observed. Therefore, one may conclude that the studies done in Sec. 5.2 as well as the corresponding results may be considered quite realistic. In the presence of sufficiently strong poloidal flows, sheared or homogeneous, one may expect to find superdiffusion in the y direction and subdiffusion in the x direction of an intermediate time span which grows as the amplitude of the coherent flow component increases.

5.4 Summary and conclusions

The main goal of the present chapter was to investigate the behavior of test particles in realistic turbulent fields, focusing on the question whether and under which conditions the transport may become 'anomalous', i.e. super- or subdiffusive. For simplicity, we have restricted to electrostatic fluctuations and two dimensions as far as the particle trajectories are concerned. Nevertheless, we have used electrostatic potentials taken from three (space) dimensional gyrokinetic simulations with the Gene code. Here, ion temperature gradient and trapped electron mode turbulence cases were chosen, both exhibiting coherent

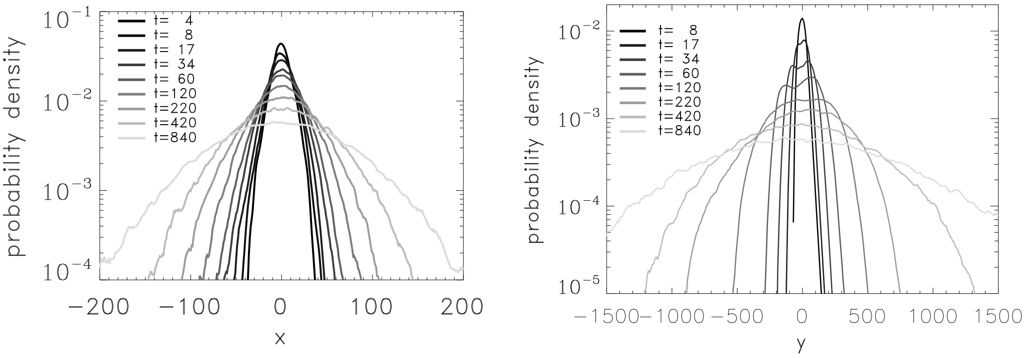

Figure 5.8: *Left*: PDF of the particle displacements in the x direction for the ITG potential for different times. The behavior is comparable to the one shown in Fig. 5.2 (right). *Right*: PDF of the particle displacements in the y direction for the ITG potential for different times. The behavior is comparable to the one shown in Fig. 5.2 (left).

flow components in addition to stochastic fluctuations. In addition, we considered potentials which were generated by superposing a large number of random waves. The variation of the strength of the coherent part (given by the zonal flow amplitude or the drift velocity) enabled us to gain a basic understanding of several transition phenomena.

While in the presence of stochastic fluctuations, one always observes that the particle transport eventually becomes diffusive [in contrast to some previous studies which dealt with less realistic models, observing anomalous diffusion for arbitrarily long times], sufficiently strong poloidal flows, sheared or homogeneous, tend to induce superdiffusion in the y direction and subdiffusion in the x direction over an intermediate time span. The latter grows as the amplitude of the coherent flow component increases, and it may, in fact, become much larger than the correlation time of the fluctuations. Thus, if one is interested in transitional – not steady-state – phenomena, the effects described in the present chapter are likely to be of relevance for the cross-field transport induced by microturbulence.

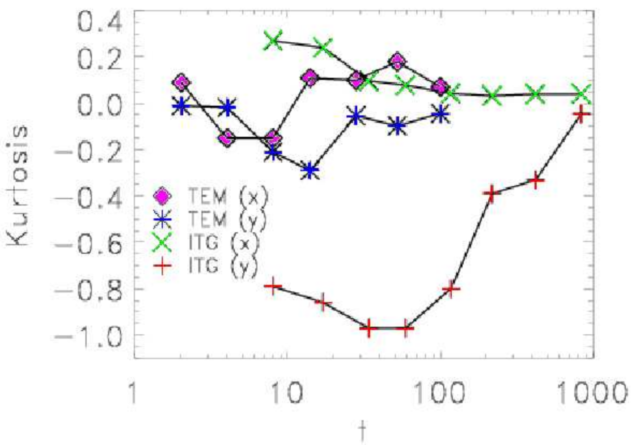

Figure 5.9: Kurtoses for the PDFs shown in Fig. 5.8 (left and right), and for the TEM potential. Again, the kurtoses clearly approach zero for large times, indicating the transition to a Gaussian distribution.

Chapter 6

Advection of Fast Ions in Electrostatic Turbulence in 3D Tokamak Geometry

The diffusion of energetic ions by electrostatic turbulence in 3D tokamak geometry is investigated both analytically and numerically. It is shown that orbit averaging (leading to a significant reduction of the diffusivity) is only valid for low magnetic shear. At moderate or high magnetic shear, a rather slow decrease of the diffusivity is found, proportional to $(E/T_e)^{-1}$ or $(E/T_e)^{-3/2}$ for particles with a large or small parallel velocity component, respectively. The decorrelation mechanisms responsible for this behavior are studied and explained in detail. Moreover, it is found that resonances between the toroidal drift of the particles and the diamagnetic drift of the turbulence can lead to an enhancement of the fast ion transport. The results of this chapter have been published in (Hauff & Jenko, 2008) and (Hauff *et al.*, 2009).

6.1 Introductory remarks

In Chapters 3, 4, and 5, we have studied the advection of energetic ions by microturbulence in a 2D plane perpendicular to the magnetic field, where we have described and understood a variety of different effects, concerning finite gyroradii as well as the structure of the background fluctuations. While this work was in some way the completion of a large number of past publications about particles with large gyroradii in 2D turbulence (Manfredi & Dendy, 1996; Manfredi & Dendy, 1997; del Castillo-Negrete, 1998; del Castillo-Negrete, 2000; Annibaldi *et al.*, 2002; Vlad & Spineanu, 2005; Vlad *et al.*, 2005), the study of fast particles in a turbulent background in 3D toroidal geometry has (re-)gained attention only quite recently (Estrada-Mila *et al.*, 2006; Dannert *et al.*, 2008; Angioni & Peeters, 2008). These investigations were, in part, motivated by recent experimental investigations at ASDEX Upgrade which showed a fast radial broadening of the plasma current profile driven by off-axis neutral beam injection in the absence of any measurable magnetohydrodynamic activity (Günter *et al.*, 2007), and seem to contradict earlier experimental results claiming that such an effect should not exist (see, e.g., Ref. (Heidbrink *et al.*, 1991)). This chapter wants to shed light on this crucial question (especially for future D-T-based experiments like ITER (ITER, 2009)) by studying different decorrelation mechanisms for passive tracers in a 3D turbulent environment. We shall find that the transport levels generally depend on the turbulence characteristics as well as on the orbit parameters of the fast particles in a very sensitive way. This will enable us to explain both situations showing a fast drop of diffusivity with growing particle energy as well as situations in which the transport remains high for a while until it falls off rather slowly, inversely proportional to the particle energy.

In two dimensions, the question of fast particle transport has been solved in a quite complete way in the previous chapters. Here, a fast particle is simply characterized by its gyroradius ρ_g and follows the $E{\times}B$ drift in the gyroaveraged electrostatic potential. It could be demonstrated that for Kubo numbers smaller than unity, the diffusivity is reduced monotonically with growing gyroradius, since gyroaveraging smoothes the potential and therefore reduces the effective drift velocity. In contrast, gyroaveraging increases the correlation lengths of the potential, which for Kubo numbers larger than unity balances the reduction of the drift velocity and therefore keeps the transport constant for gyroradii up to the correlation length. In addition to that, it was shown how a constant drift of the background turbulence affects the transport. This finding will carry over to the 3D case.

In three dimensions, the motion of fast particles is characterized by more than just the gyroradius, of course. Depending on the pitch angle, the particles are passing or trapped (see the detailed discussion in Section 2.1), and in both cases, their motion can be described – in a field-aligned coordinate system – as a superposition of a "circular" (or slightly elliptical) periodic motion and a constant drift in the binormal direction, in analogy with the usual gyromotion (see Section 2.6.2). So we will have to ask whether the effects of gyroaveraging (well understood for the 2D case) will translate into some kind of "orbit averaging" in three dimensions, and to what extent the particle drifts generated by curvature and grad-B drifts (in the 3D case) can lead to effects which resemble those observed in two dimensions. Indeed, it has been claimed in Ref. (Mynick & Krommes, 1979), and only recently in Ref. (Zhang *et al.*, 2008) that gyroaveraging as well as drift orbit averaging both lead to a universal reduction of transport. However, in Ref. (Myra *et al.*, 1993), it was shown that orbit averaging is not valid if the particle is decorrelated by fast parallel dynamics before it can finish its periodic orbit.

In early 3D simulations, studying the interaction of energetic alpha particles with high toroidal mode number instabilities, it was reported that such modes *can* indeed cause significant alpha-particle transport. However, this effect was found to strongly depend on the turbulence properties as well as on the device (Rewoldt, 1988; Rewoldt, 1991). A further explanation of this behavior was not given. In Ref. (Estrada-Mila *et al.*, 2006), alpha particles were modeled as a hot Maxwellian species, and their particle fluxes were determined quasilinearly and nonlinearly. A large increase of the flux of the alphas was reported compared to the particle flux of the thermal background plasma. However, as pointed out in Ref. (Angioni & Peeters, 2008), this interpretation was mainly due to the special normalization used in this work. Furthermore, thermal particles were not distinguished from non-thermal ones. In another recent work (Dannert *et al.*, 2008), beam ions were modeled by means of an asymmetric and anisotropic Maxwellian distribution function with a long tail in the beam direction. In qualitative agreement with our 2D results presented in Chapter 4, it was found that the fast particle transport becomes large when the poloidal drift velocity of the particles matches the diamagnetic drift velocity of the background turbulence. Since resonances can exist for energies up to about 10 times the thermal energy, it was shown that the redistribution of the beam ions may remain significant up to that energy. This has also been found in a recent quasilinear study (Angioni & Peeters, 2008) employing a slowing-down distribution function. Interestingly, according to Ref. (Dannert *et al.*, 2008), fast particles interacting with *turbulent* fields exhibit a rather slow decrease of diffusivity (approximately like $1/E$) instead of the much faster decay observed in quasilinear studies.

It is the aim of this chapter to provide a systematic study of the physical mechanisms responsible for the diffusion of fast particles in a tokamak. As will be shown, the transport is governed, in general, by the combination of a number of different effects, including gyroaveraging, orbit averaging, resonances with the background drift, and decorrelations caused by parallel or perpendicular orbit motion. Furthermore, we will find that it makes a big difference whether orbit averaging is valid or not. Since we are mainly interested in the basic principles underlying the particle-turbulence interactions in a tokamak, we will represent the turbulent background fluctuations by stochastic fields with realistic physical properties, a method used successfully in the 2D studies in the previous chapters. The energetic particles, on the other hand, are still treated as passive tracers (see Section 2.5.3). The transport will be characterized again in terms of diffusion coefficients D corresponding to individual particle trajectories.

The remainder of this chapter is organized as follows. In Secs. 6.2 and 6.3, we provide some information about the construction of the equilibrium magnetic field and the fluctuating electrostatic potentials used in this work. In Sec. 6.4, the validity of orbit averaging is examined, and a number of possible decorrelation mechanisms are discussed. In Sec. 6.5, the latter are investigated for the simple case of a shearless magnetic field. Secs. 6.6 and 6.7 then deal with simulations of energetic ions in a realistic sheared magnetic field, and in Sec. 6.8, some additional information is provided, which generalizes the results. We close with some conclusions in Sec. 6.9.

For clarification, and to avoid possible misunderstandings, it shall be mentioned that in this thesis, the term "orbit motion" refers to the curvature and grad-B drift motion, leading to orbits as shown in Fig. 2.2. and described in Section 2.1.5. The term "gyromotion", in contrast, refers to the simple Larmor orbits described at the beginning of Chapter 2. Although, as was demonstrated in Fig. 2.14, both motions exhibit similarities, they are based on completely different mechanisms and have to be strictly distinguished.

6.2 Equilibrium magnetic and fluctuating electric fields

In the following, we will consider a simple tokamak with circular, concentric flux surfaces, but with a finite aspect ratio. The respective torus coordinates – minor radius, poloidal and toroidal angle – are denoted, respectively, by r, θ, and φ (see Fig. 2.1, where ζ is changed to φ). The distance between the magnetic axis and the symmetry axis is denoted by R_0. In Section 2.3.1, the existence of a field aligned coordinate system $r-\beta-\chi$ with straight field lines has already been introduced. Following Eq. (2.35), the *safety factor* (Eq. (1.1)) q can be expressed by the relation

$$q(r) = \frac{1}{2\pi}\int_0^{2\pi} \frac{\mathbf{B}\cdot\nabla\varphi}{\mathbf{B}\cdot\nabla\theta}\,d\theta = \frac{1}{2\pi}\int_0^{2\pi}\frac{rB_\varphi}{RB_\theta}\,d\theta \tag{6.1}$$

with $R = R_0(1+\epsilon\cos\theta)$ and $\epsilon = r/R_0$. Note that the second equality only holds for the simple geometry of concentric flux surfaces, while the first one is completely generic. The corresponding magnetic field can be written as

$$\mathbf{B} = B_\varphi \mathbf{e}_\varphi + B_\theta \mathbf{e}_\theta = (B_0R_0/R)\,(\mathbf{e}_\varphi + b_\theta \mathbf{e}_\theta) \tag{6.2}$$

where b_θ is assumed to be independent of R. Inserting the components of $\mathbf{B}$ into Eq. (6.1) and integrating over θ, we find the expression

$$B_\theta = \frac{B_0R_0}{R}\,\frac{1}{q(r)}\,\frac{\epsilon}{(1-\epsilon^2)^{1/2}}\,. \tag{6.3}$$

Thus, an arbitrary safety factor profile $q(r)$ may be chosen do define the magnetic field.

We would like to note in this context that the assumption of circular, concentric flux surfaces captures the key features of more complicated geometries. Comparing particle orbits in the simple geometry with orbits in a realistic magnetic field constructed from ASDEX Upgrade data – using the Gourdon code (Gourdon, 1970) – showed that only moderate differences occur which do not affect the dependence on the field and particle parameters. This has been confirmed by recent numerical investigations (Dannert *et al.*, 2008; Belli *et al.*, 2008). Thus, the considerations of this chapter hold also for shaped plasmas.

Next, we have to calculate the function $\chi(\theta)$. For an arbitrary B-field, it was already defined in Eq. (2.36). Inserting the identity under the integral of Eq. (6.1) and the expression for $R(\epsilon,\theta)$, and solving the integral, we finally obtain the relation (Lapillonne *et al.*, 2009)

$$\chi = 2\arctan\left(\sqrt{\frac{1-\epsilon}{1+\epsilon}}\,\tan\frac{\theta}{2}\right)\,. \tag{6.4}$$

In the large aspect ratio limit ($\epsilon\to 0$), we have $\chi\to\theta$, as expected.

Since the turbulent fluctuations in a tokamak plasma are strongly elongated along the magnetic field lines, it is convenient for the construction of fluctuating test potentials to use coordinates which are field-aligned. In the local approximation (see Sections 2.3.2 and 2.3.3) one thus obtains

$$x = r\,, \qquad y = \frac{r_0}{q_0}\,\beta\,, \qquad z = \chi\,. \tag{6.5}$$

Here, unlike the common definition of Eq. (2.41), z remains an angular coordinate. Assuming periodic perpendicular boundary conditions, we can construct a random electrostatic potential according to

$$\phi(\mathbf{x}, t) = g(z) \sum_{i=1}^{N} A_i \, \sin(k_{x,i}\, x + k_{y,i}\, y + \omega_i\, t + \varphi_i)\,, \tag{6.6}$$

which is then mapped back onto a Cartesian spatial grid that is used for calculating the particle trajectories. This is an extension of the 2D potentials constructed by Eq. (3.1). In order to avoid problems with the parallel boundary conditions (see (Beer *et al.*, 1995) and discussion in Section 2.3.3) for our test potentials, for simplicity, we either consider a shearless case, $q(r) \equiv 1.4$, in which the magnetic field lines are closed after 5 poloidal (or 7 toroidal) turns – or we choose the envelope function in Eq. (6.6) to be $g(z) = 0.5\,\cos(z - \sin(z)) + 0.5$ which is quite realistic and renders the parallel boundary conditions at $z = \pm\pi$ irrelevant. In the y direction, the box length is chosen to be $2\pi r_0/q_0$, reflecting the real periodicity of the torus. However, provided one is careful, it is also possible to cover the torus by M copies of a flux tube whose width in the y direction is only $2\pi r_0/(M q_0)$. A discussion of this procedure is presented below, in Sec. 6.6.2.

The physical parameters characterizing the magnetic field and the test potentials in the present study are inspired by the ITER project (ITER, 2009). Thus, we use $R_0 = 6.2$ m and $B_0 = 5.3$ T. For the q profile, we either use $q(r) \equiv 1.4$ or $q(r) = 0.5\,(r/\mathrm{m})^2 + 1.25$. The particles start at a radial position near $r_0 = 0.7$ m. The stochastic electrostatic potential is created according to Eq. (6.6) such that the random field exhibits realistic space and time scales. Using typical values obtained from our experience with the Gene code and renormalizing them to a temperature of $T_i \equiv T_e = 10\,\mathrm{keV}$, we find a typical correlation length of $\lambda_c \approx 1.6$ cm, a correlation time of $\tau_c \approx 1.8 \times 10^{-4}$ s, a mean $E \times B$ drift velocity of $V \approx 900$ m/s, as well as a diamagnetic drift velocity of $v_{\mathrm{dr}} \sim 300$ m/s. However, the latter may vary strongly depending on the gradient drive. Using this values for deuterium ions, we find a thermal Larmor radius $\rho_i \equiv \rho_s = 2.83\,\mathrm{mm}$ and a ion thermal speed $c_i \equiv c_s = 692\,000\,\mathrm{m/s}$. According to Section 2.4, this leads to the following normalized quantities: $\hat{\lambda}_c \approx 6$, $\hat{V} \approx 3$, $\hat{\tau}_c \approx 20$. The characteristic potential parameters lead to a 'classical' Kubo number of $K \equiv V\tau_c/\lambda_c \approx 10$, which is in line with nonlinear gyrokinetic simulations. We note in passing, however, that the value of the Kubo number as defined until now does not affect the key conclusions of the present work, since it will turn out not to be the decisive value anymore, since faster decorrelation mechanisms apply in three dimensions. They lead to a re-definition of the Kubo number using a new, effective decorrelation time. Also, we will only consider fluctuations which are isotropic in the perpendicular plane as in Chapter 3; geometrical effects due to streamer formation (Chapter 4) are not treated.

However, we will see that in the case of fast particles in three dimensions, they are of limited relevance, anyway.

6.3 Particle motion

For simulating the particle trajectories, we now use the full equations of motion as written down in Eq. (2.18). However, ϕ is replaced by ϕ^{eff}, which denotes the gyroaveraged electrostatic potential. The particles are tracked by a modified version of the GOURDON code (Gourdon, 1970), which uses an explicit Adams-Bashforth algorithm to integrate Eq. (2.18).

As already pointed out in Section 2.1.5, particles can circulate around the torus, following the magnetic field lines (passing orbits, large η), or they can be reflected by the mirror force and bounce between two poloidal reversal points (trapped orbits, small η). In both cases, the particles do not follow the magnetic lines exactly anymore, but deviate in an oscillatory fashion in the x as well as in the y direction due to the curvature and ∇B drifts. In addition to that, the particles drift in the y direction with a constant velocity (toroidal precession). In Fig. 2.14, two examples of fast particle orbits in field aligned coordinates in front of the background potential were given. As could be seen, the orbit motion can be described as a superposition of a circular (elliptical) motion in the $x-y$ plane and a constant drift motion in the y direction. Whereas an analytical treatment of the orbit motion in the $R-z$ plane was already derived in Section 2.1.5, a derivation draft of the y drift has been saved for this chapter. In Ref. (Dannert *et al.*, 2008), the z dependent expression $v_y(z) = (v_{\nabla B} + v_{\text{curv}})\, h(z)$ is derived, where $h(z) \equiv \cos z + \hat{s} z \sin z$ and $\hat{s}(r) = r/q(r)\, dq(r)/dr$. Since we are interested in the average value over one orbit turn, we define $\bar{h} = 1/(2z_0) \int_{-z_0}^{z_0} h(z)\, dz$. This yields $\bar{h} = \hat{s}$ for passing particles ($z_0 = \pi$) and $\bar{h} \to 1$ for $z_0 \to 0$ for deeply trapped particles. Absolute values for $v_{\nabla B}$ and v_{curv} are approached from Eqs. (2.12) and (2.13). Since the particles do not move along z with constant velocity, the above approximation is rather crude, though. Moreover, we have $\epsilon \approx 0.1$ in our simulations, such that one may expect finite aspect ratio corrections to play a role. Employing, nevertheless, this simple model, the orbit parameters in the case of passing particles are given by Eqs. (2.29) and (2.30), and in the case of trapped particles by Eq. (2.31). Rewriting this equations in terms of the particle energy, we obtain

$$T_{\text{orbit}} \approx \frac{2\pi q_0 R_0}{\eta} \sqrt{\frac{m}{2E}}\,, \quad \Delta x \approx \frac{2\eta q_0}{eB_0} \sqrt{2mE}\,, \quad v_y \approx \frac{2\eta^2 \hat{s}}{eB_0 R_0} E\,. \tag{6.7}$$

for $\eta \to 1$ (passing particles) and

$$T_{\text{orbit}} \approx 2\pi q_0 R_0 \sqrt{\frac{m}{(1-\eta^2)\epsilon E}}\,, \quad \Delta x \approx \frac{2\eta q_0}{eB_0 \epsilon} \sqrt{2mE}\,, \quad v_y \approx \frac{(1-\eta)^2}{eB_0 R_0} E\,. \tag{6.8}$$

for $\eta \to 0$ (trapped particles).

For our nominal parameters, these expressions read

$$T_{\text{orbit}}/s \approx 1.3 \cdot 10^{-4}\, q_0/\sqrt{E/\text{keV}}\,, \quad \Delta x/m \approx 0.0025\, q_0 \sqrt{E/\text{keV}}\,,$$
$$v_y/(\text{m/s}) \approx 60\, \hat{s}\, E/\text{keV}\,. \tag{6.9}$$

for passing particles and

$$T_{\mathrm{orbit}}/s \approx 5.4 \cdot 10^{-4}\, q_0/\sqrt{E/\mathrm{keV}}\,, \quad \Delta x/m \approx 0.003\,(q_0/r_0)\,\sqrt{E/\mathrm{keV}}\,,$$
$$v_y/(\mathrm{m/s}) \approx 29\, E/\mathrm{keV}\,. \quad (6.10)$$

for trapped particles. The simulation results presented in this chapter show that the expressions for T_{orbit} and Δx fit almost perfectly, whereas the expression for v_y is correct only within about 30%, which may be attributed to finite aspect ratio effects and/or to our simple approach of averaging over z. Later, we present these parameters as simulation results in tables, so that the reader can check the validity of the above expressions on his own. We are not aware of an analytical expression for the diameter of the elliptical motion in the y direction. However, the simulations show that it coincides with the radial diameter up to an error of at most a few 10%. Consequently, in the framework of simple analytical descriptions, it seems reasonable to assume $\Delta y \approx \Delta x$.

A particle motion similar to the one illustrated in Fig. 2.14 has already been the subject of study in Chapter 4, where the interaction of gyrating particles with a background turbulence drifting in the y direction has been investigated and explained. The present case with particles circulating on drift orbits and drifting with respect to the background potential is essentially the same, however, the time scales are distinct. In the former chapter, it was shown that an electrostatic potential drifting with a velocity v_{dr} in the y direction strongly reduces transport in the x direction above a so-called "drop time" $\tau_{\mathrm{drop}} = 2\lambda_c/v_{\mathrm{dr}}$, since, in a frame of reference moving with the drift velocity, Lorentz invariance (in the non-relativistic limit) leads to an additional electric field, acting as a transport barrier. τ_{drop} is the mean time a particle needs to run against the barrier and being reflected. So for $\tau_{\mathrm{drop}} < \tau_c$, a significant transport reduction can be expected, whereas in the opposite case, no significant drift-induced effect is observable, since the barrier does not exist long enough for the particle to feel its presence. The gyroaveraging procedure and its influence on the transport level has also been described before in Chapters 3 and 4.

Now, it is not only the particles which are subject to a drift, but also the background potential (see Section 2.1.3). Depending on the temperature and density gradients of the plasma, this drift can have velocities of up to about $5\,\rho_s c_s/R_0$ (Dannert *et al.*, 2008), which may be as large as several km/s for our nominal parameters. In Ref. (Dannert *et al.*, 2008), the effect of a resonance between the diamagnetic drift of the background potential and the curvature drift of beam ions has already been described. In the following, we will denote the drift of the background potential by v_{dr}, whereas the test particle drifts will be denoted by v_y.

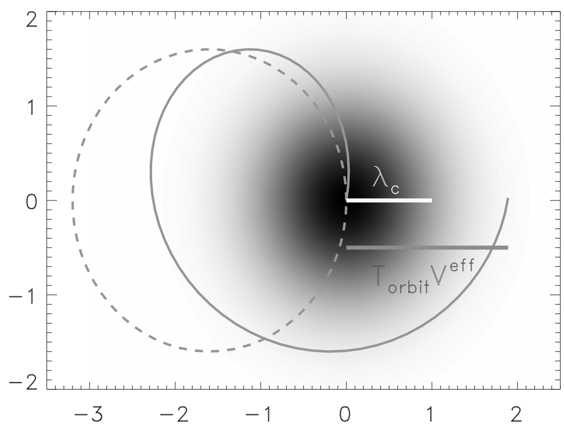

Figure 6.1: The dashed line denotes a circle over which the potential is (orbit-)averaged for a particle starting at the origin, while the solid line denotes a real particle trajectory with a large $E\times B$ drift velocity $\bar{V}^{\rm eff}$. After one period, the particle is displaced by $T_{\rm orbit}\bar{V}^{\rm eff}$ from the origin as well as from the corresponding point on the dashed curve. Therefore, if the particle does not return into the correlated zone [in the background, the autocorrelation function $\langle\phi(0)\phi(\mathbf{x})\rangle$ of an isotropic stochastic potential with correlation length λ_c is plotted], orbit averaging is not valid.

6.4 Fundamental transport and decorrelation mechanisms

6.4.1 Orbit averaging

In Chapter 3, the "gyroaveraging" procedure and its influence on the new effective values of the $E\times B$ drift velocity $V^{\rm eff}$ and the effective correlation length $\lambda_c^{\rm eff}$ have been described. This, in turn, gave us scaling laws for the diffusion coefficient with this values. Now, recalling the discussion concerning Fig. 2.14, we may expect that a similar procedure is possible with respect to the orbit motion of a particle, since, in principle, we just have to replace ρ_g with $\Delta x/2$ and $v_{\rm dr}$ with $v_y - v_{\rm dr}$. In this case, and normalizing to arbitrary correlation lengths, we can get the orbit averaged values by analogy from Eqs. (3.15) and (3.16) for the case that $\Delta x/2 \gtrsim \lambda_c$ (note that ρ is the gyroradius, whereas Δx is the orbit diameter):

$$\bar{V}^{\rm eff} = V\,(2\sqrt{\pi}\Delta x/\lambda_c)^{-1/2}\,, \qquad \bar{\lambda}_c^{\rm eff} = 1.73\,\lambda_c\,. \tag{6.11}$$

From now on we want to use the notation $V^{\rm eff}$ and $\phi^{\rm eff}$ for gyroaveraged values, whereas we write $\bar{V}^{\rm eff}$ and $\bar{\phi}^{\rm eff}$ for orbitaveraged variables. However, we have to remember that the orbit motion takes place on much slower time scales than the gyromotion. So, in a first step, we want to clarify the condition under which orbit averaging is valid.

In Fig. 6.1, the orbit motion of a particle with a rather large $E\times B$ drift velocity is plotted in front of a fluctuating potential symbolized by the contours of its autocorrelation function. As explained in the caption, a criterion for the validity of orbit averaging is the condition $T_{\rm orbit}\bar{V}^{\rm eff} < \lambda_c$, $T_{\rm orbit}$ being the cycle duration. [This criterion corresponds to the criterion for the validity of gyroaveraging, given in Section 2.1.4, condition 2.] Additionally to the $E \times B$ drift, decorrelation can be caused by the curvature drift velocity relative to the diamagnetic drift velocity of the background potential. Moreover, the correlation time of the fluctuations must, of course, be large compared to the cycle duration, $T_{\rm orbit} \ll \tau_c$. Consequently, we can state as a necessary condition for the validity of orbit averaging the relations

$$\Xi_{\rm o.a.} \equiv \max\left\{\bar{V}^{\rm eff}, |v_{\rm dr} - v_y|\right\} \frac{T_{\rm orbit}}{\lambda_c} < 1\,, \qquad T_{\rm orbit} \ll \tau_c\,. \tag{6.12}$$

If one of those inequalities is violated, the particle is decorrelated before it completes one turn, and therefore, orbit averaging is not applicable anymore. If orbit averaging is valid, the gyroradius ρ_g in Eq. (3.4) can simply be replaced by half of the deviation of the particle from the original flux surface, $\Delta x/2$ (where we may assume that $\Delta y \approx \Delta x$), and Eqs. (6.11) apply. As we will see, the first relation of Eq. (6.12) is very critical, and the transport level for fast particles strongly depends on its validity.

6.4.2 Decorrelation mechanisms

We now want to analyze different decorrelation mechanisms for the motion of fast particles in a tokamak. Because of their importance also for this chapter, we briefly repeat the some key points of the previous chapters. As long as a Lagrangian correlation between the current particle velocity and the velocity at its starting position exists, the transport is, in general, not diffusive. For example, for small times, before a particle feels the structure or the time dependence of the turbulent stream function, it moves ballistically, inducing superdiffusive transport. This is the case for $t < \tau_{\rm fl} \equiv \lambda_c/V$, $\tau_{\rm fl}$ being the average time of flight of a particle exploring a typical fluctuation structure. On the other hand, as long as a certain structure persists, the particle can get trapped in it, or be bound by a transport barrier produced by the diamagnetic drift of the background potential. In this case, the transport will be subdiffusive. Only when the particle starts to forget the information concerning its starting point, i.e., when there is no more correlation between the stream function at the current position and at the starting position of the particle, its motion becomes diffusive. This may be seen from the Taylor relation in Eq. (2.54) together with Eq. (2.55). When the Lagrangian velocity autocorrelation $L_{v_x}(t)$ becomes zero, $D_x(t)$ becomes constant.

In two dimensions, the only relevant decorrelation mechanism is the time dependence of the electrostatic potential. This means that the effective decorrelation time of the particle motion is equal to the correlation time of the potential, $\tau^{\rm eff} \equiv \tau_c$ (Vlad *et al.*, 1998). If there is no time dependence at all, the particles simply follow the equipotential lines of the electrostatic potential (the stream function); thus, their dynamics is fully deterministic. In a simple approach, diffusion coefficients can be obtained by following the $D(t)$ curve for a static potential, while the curve is forced to saturate at $t = \tau_c$. If there is a background drift, a sharp drop of the curve occurs at $t = \tau_{\text{drop}}$ if $\tau_{\text{drop}} < \tau_c$. The figures Fig. 2.13 and 4.9 illustrate this type of behavior in two dimensions.

Now, in three dimensions, the situation is basically the same as long as orbit averaging is valid. In this case, the only influence of the orbit motion is the averaging of the background potential which reduces the transport for $\Delta x/2 > \lambda_c$ (in addition to the reduction produced by averaging over the gyroorbit), together with a possible decorrelation by the motion along the magnetic field lines. The situation is quite different, however, if orbit averaging is not valid. In that case, as we have seen while discussing Fig. 6.1, the decorrelation is produced by the orbit motion of the particle perpendicular to the magnetic field. So, as an effective decorrelation time, it is reasonable to take the time a particle needs to cross a distance of one perpendicular *velocity correlation length* during its orbit motion, i.e.,

$$\tau^{\text{orbit}} = \lambda_V / v_{\text{orbit}} = \lambda_V T_{\text{orbit}} / (\pi \Delta x) \,. \tag{6.13}$$

It must be emphasized that now, it is the autocorrelation length of the $E \times B$ drift velocity field, λ_V, defined as the e-folding length of $E_{v_x}(\mathbf{x})$ (Eq. (2.57)), which becomes relevant. This is for the following reason. In two dimensions, the particles follow the equipotential lines of ϕ. Therefore it was essential to approach the distance of this structures, which was done using λ_c. In three dimensions, however, the particles do not feel these structures anymore, instead, they only “scan and skim” them on their orbits (see Fig. 2.14). Now, the disturbing force acting on the particle is governed by the velocity field, not the potential. Therefore, it is the autocorrelation function $E_{v_x}(\mathbf{x})$ and its correlation length λ_V which is decisive. $E_{v_x}(\mathbf{x})$ was defined in Eq. (2.57), where it was already mentioned that the lengths scales may differ from the original function $E(\text{x})$. For example, assuming an Gaussian autocorrelation function for E (as we always do for our self-created potentials) leads to a velocity correlation length $\lambda_V \equiv \lambda_c$ in the x direction, but $\lambda_V \approx 0.51\lambda_c$ in the y direction, assuming the definition of Eq. (2.57). One can argue that it is the smaller correlation length of both directions which governs the decorrelation process. Depending on the spectra, the relation of λ_c and λ_V may be larger or smaller, but in general, $\lambda_V \lesssim \lambda_c$ may be assumed. [We want to note that it seems questionable that in Eq. (6.12), λ_c should not also be changed to λ_V. The answer depends on the question whether the structure of the stream function or the velocity field is decisive in that case. Since the parameter $\Xi_{\text{o}.a.}$ only wants to be a rough approach, we will keep λ_c in the calculation of $\Xi_{\text{o.a.}}$, but take λ_V for the determination of τ^{orbit}.]

The relation of Eq. (6.13) is only valid if $\Delta x/2 \gtrsim \lambda_c$. Only then is the drift orbit wide enough to produce decorrelation. In the opposite case, if $\Delta x/2 \lesssim \lambda_c$, the situation is more complicated. Here, the particle does not necessarily decorrelate at $t = \tau^{\text{orbit}}$, since the orbit radius is smaller than the correlation length; and even if orbit averaging is not valid, the $E\times B$ motion may force the particle to follow the equipotential lines of the stream function. So although it travels a distance larger than λ_c during one orbit turn, it does not necessarily decorrelate. On the other hand, since orbit averaging is not valid, the particle is not strictly bound to the equipotential lines. So, in this case, only a range of time scales can be given at which decorrelation occurs, namely $\tau_{\rm fl} \le \tau^{\rm eff} \le \tau_c$. The behavior of such particles is subject of detailed study in Chapter 9.

As an additional decorrelation mechanism in three dimensions, one obtains the parallel motion of the particles. The relevant time scale is given by $\tau_\parallel = \lambda_\parallel / v_\parallel$ where $\lambda_\parallel$ is the parallel correlation length of the fluctuations.

In summary, we thus have:

$$\begin{aligned} \tau^{\rm eff} &= \min\left\{\tau_c, \quad \tau_\parallel\right\} \quad \forall \quad \Xi_{{\rm o.}a.} \lesssim 1 \\ \tau^{\rm eff} &= \min\left\{\tau_c, \quad \tau_\parallel, \quad \tau^{\rm orbit}\right\} \quad \forall \quad \Xi_{{\rm o.}a.} \gtrsim 1 \,. \end{aligned} \tag{6.14}$$

Here, $\tau^{\rm eff}$ is the effective decorrelation time for which the $D(t)$ curve departs from a reference curve without 3D effects and saturates. For the saturation level, it remains crucial whether the effective decorrelation time is larger or smaller than the drop time $\tau_{\rm drop}$. For the later discussion, it turns out to be important that one typically finds $\tau^{\rm orbit} < \tau_{\rm drop} < \tau_\parallel < \tau_c$, which means that the drift barrier induced by the magnetic drifts of the particles and the diamagnetic drift of the background potential exists if $\Xi_{{\rm o.}a.} < 1$, but not if $\Xi_{{\rm o.}a.} > 1$.

6.4.3 A simple 2D model

To gain a better understanding of the mechanisms we have just explained, it is useful to study the drift orbit motion in the framework of a simple 2D model defined by:

$$\dot{\mathbf{x}} = \mathbf{v} - \frac{1}{B}\nabla\phi^{\rm eff} \times \mathbf{e}_z \,, \quad \dot{\mathbf{v}} = \omega_{\rm orbit}\mathbf{v} \times \mathbf{e}_z \,. \tag{6.15}$$

Eq. (6.15) describes a particle which is forced on an orbit with $\omega_{\rm orbit} = 2\pi/T_{\rm orbit}$, at the same time undergoing $E{\times}B$ drift motion. The orbit radius is set by choosing an appropriate starting velocity of the particle, $v(t=0) = \Delta x\, \omega_{\rm orbit}/2$. In this 2D system, we can also perform orbit averaging of the (already gyroaveraged) potential $\phi^{\rm eff}$ over a circular orbit with radius $\Delta x/2$. Simulation results based on this model will be presented below.

6.5 Beam ions in a shearless magnetic field

Let us now turn to 3D simulations. In a first step, we consider a magnetic field with $q(r) \equiv 1.4, \hat{s}(r) \equiv 0$. Here, the magnetic field lines close after 5 poloidal (7 toroidal) turns, and therefore it is possible to choose $\lambda_\parallel = \infty$ (by $g(z) \equiv 1$ in Eq. (6.6)) which makes comparisons with the simplified model easier. To ensure continuity in the z direction, the flux surface is covered by $M = 5$ identical copies of a flux tube. Moreover, we will see that this special case exhibits many features which are typical for more general weak-shear situations. For the 3D particle simulations with the Gourdon code, we consider deuterium ions with $\eta = 0.99$ and energies ranging from 10 keV to 160 keV which we insert at $r_0 = 0.7$ at the outboard midplane ($\theta = 0$). The characteristic orbit parameters,

E[keV]	T_{orbit}[s]	$\Delta x/2$[m]	$\Delta y/2$[m]	v_y[m/s]	$\Xi_{\mathrm{o.a.}}^{v_{\mathrm{dr}}=0}$	$\Xi_{\mathrm{o.a.}}^{v_{\mathrm{dr}}=300\frac{\mathrm{m}}{\mathrm{s}}}$	$\tau_{\mathrm{drop}}^{v_{\mathrm{dr}}=0}$[s]	$\tau_{\mathrm{drop}}^{v_{\mathrm{dr}}=300\frac{\mathrm{m}}{\mathrm{s}}}$[s]	τ^{orbit}[s]
10	$5.6 \cdot 10^{-5}$	0.0055	0.0050	68	2.0	2.0	$4.8 \cdot 10^{-4}$	$1.4 \cdot 10^{-4}$	$1.4 \cdot 10^{-5}$
20	$4.0 \cdot 10^{-5}$	0.0076	0.0075	136	1.2	1.2	$2.4 \cdot 10^{-4}$	$2.0 \cdot 10^{-4}$	$7.0 \cdot 10^{-6}$
40	$2.8 \cdot 10^{-5}$	0.0110	0.0105	273	0.7	0.7	$1.2 \cdot 10^{-4}$	$1.2 \cdot 10^{-3}$	$3.3 \cdot 10^{-6}$
80	$2.0 \cdot 10^{-5}$	0.0155	0.0148	545	0.6	0.4	$6.0 \cdot 10^{-5}$	$1.3 \cdot 10^{-4}$	$1.7 \cdot 10^{-6}$
160	$1.4 \cdot 10^{-5}$	0.0215	0.0205	1092	0.9	0.6	$3.0 \cdot 10^{-5}$	$4.1 \cdot 10^{-5}$	$8.5 \cdot 10^{-7}$

Table 6.1: Characteristic orbit parameters for beam ions ($\eta = 0.99$) in an ITER-like tokamak with $R_0 = 6.2$ m, $B_0 = 5.3$ T, and $q(r) \equiv 1.4$. The plasma/turbulence parameters are $T = 10$ keV, $\tau_c = 1.8 \cdot 10^{-4}$ s, $\lambda_c = 0.0164$ m, and $V = 900$ m/s. For the calculation of $\Xi_{\mathrm{o.a.}}$, $\bar{V}^{\mathrm{eff}}$ has been determined according to Eq. (6.11). Finite curvature drift velocities v_y are found although the magnetic shear vanishes.

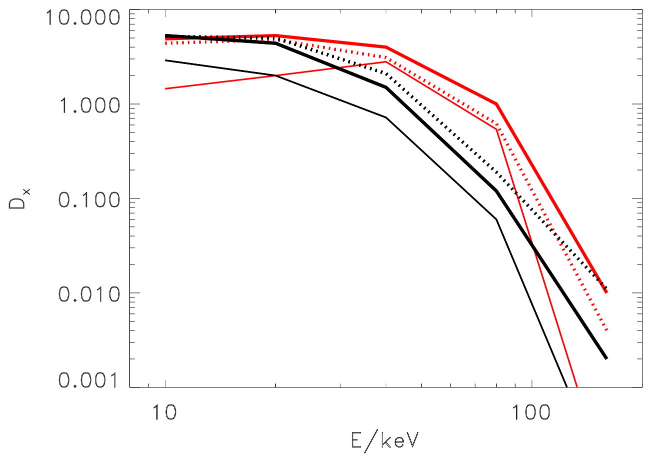

Figure 6.2: Radial diffusion coefficient D_x for different particle energies E and $\eta = 0.99$ in a shearless magnetic field. Black lines: no background drift ($v_{\mathrm{dr}} = 0$). Red lines: background drift ($v_{\mathrm{dr}} = 300$ m/s). Bold solid lines: particles in a tokamak (Eq. (2.18)). Dotted lines: simple 2D model (Eq. (6.15)). Thin solid lines: orbit averaging in the simple 2D model.

obtained from the simulations, can be found in Table 6.1. For comparison, we then recompute these orbits using the simple 2D model of Eq. (6.15), both for the forced drift orbit case as well as for the orbit averaged case. In addition, we do these simulations both with and without a background drift of $v_{\mathrm{dr}} = 300$ m/s. Fig. 6.2 shows the saturated values of the diffusion coefficients for the described cases. We see that the 3D curves, Eq. (2.18), and the 2D curves, Eq. (6.15), agree with each other within a factor of about 1.5, whereas the orbit averaged curves deviate by a larger factor. This behavior can be understood by inspecting the orbit parameters shown in Table 6.1. For the curves without a background drift (black lines), the orbit averaged curves exhibit a rather fast drop for energies exceeding 40 keV, which is due to the fact that $\tau_{\mathrm{drop}} < \tau_c$. The orbit averaged curve with the background drift has its maximum at $E = 40$ keV, since there the drift velocity of the particle is in resonance with the diamagnetic drift velocity, and therefore $\tau_{\mathrm{drop}} \gg \tau_c$. As $\Xi_{o.a.}$ is close to unity for all curves, there are deviations between the orbit averaged and the exact curves, as could

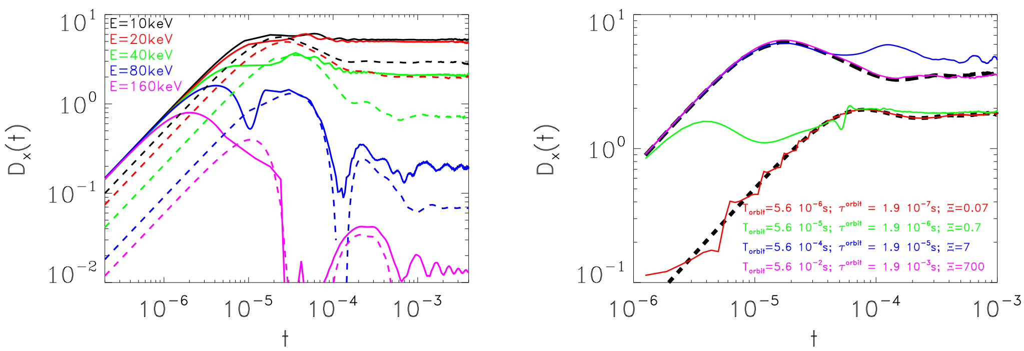

Figure 6.3: *Left*: Running radial diffusion coefficient $D_x(t)$ for different beam energies and $v_{\mathrm{dr}} = 0$. Solid lines: forced orbit motion according to Eq. (6.15). Dashed lines: orbit averaging. The saturation values are the same as in Fig. 6.2. *Right*: Running radial diffusion coefficient $D_x(t)$ for different orbit cycle durations. Here, the orbit radius is kept fixed at $\Delta x/2 \equiv 0.04$ m, and $v_y \equiv v_{\mathrm{dr}} \equiv 0$. Lower dashed line: orbit averaging. Upper dashed line: no orbit motion. Solid lines: full 2D orbit motion. A significant difference in the time evolution for the regimes $\Xi_{\mathrm{o.}a.} < 1$ and $\Xi_{\mathrm{o.}a.} > 1$ can be observed.

be expected. However, the shape of the curves is similar. The correspondence works best between $E = 40$ keV and 80 keV since for these cases, $\Xi_{\mathrm{o.}a.} \ll 1$. Given that the transport is governed by the validity of the orbit averaging approach, one then finds a rather fast decline of $D(E)$ towards higher energies.

More insight into the mechanisms at work can be gained from Fig. 6.3 (left). Here, the running (i.e., time dependent) diffusion coefficient is plotted both for the full 2D dynamics and the respective orbit averaged case for $v_{\mathrm{dr}} = 0$. We first concentrate on the orbit averaged curves. Here, one observes that for small energies (i.e., small curvature drift velocities), the diffusion coefficient first increases linearly in time (ballistic regime), then it decreases slightly (trapping effects), and finally it saturates (decorrelation due to $t > \tau_c$). For larger energies (i.e., larger curvature drift velocities), one has $\tau_{\mathrm{drop}} < \tau_c$, and one observes a strong decrease due to the existence of a "drift barrier." In the ballistic regime, we observe the reduction of the $E \times B$ drift velocity due to the orbit averaging, $D \sim (\bar{V}^{\mathrm{eff}})^2 t$. The curves obtained for the exact 2D orbit motion are similar, but the underlying mechanisms are completely different. For $t < T_{\mathrm{orbit}}$, orbit averaging is not applicable yet. Therefore, it is the original $E \times B$ drift which causes the diffusion of the particles, and for small times, all the curves follow the ballistic diffusion equation, $D = V^2 t$. For larger times, there are now two possibilities. If orbit averaging is valid ($\Xi_{\mathrm{o.}a.} \lesssim 1$), the curve jumps onto the orbit averaged curve within $\tau^{\mathrm{orbit}} \lesssim t \lesssim T_{\mathrm{orbit}}$. This relation describes the time span during which the particle already feels the stochasticity, but the orbit is not complete yet. As can be seen from Fig. 6.3 (left) as well as from Table 6.1, this mechanism applies for $E = 40$ keV to $E = 160$ keV, but the saturation values of the curves are not identical since the validity of orbit averaging seems to be not fully established yet. The second possibility is that orbit averaging is clearly invalid ($\Xi_{o.a.} > 1$). In that case, $D(t)$ simply saturates at $t \sim \tau^{\text{orbit}}$, since, after having crossing the correlated zone once, it never returns to a correlated region. We observe this kind of behavior for small particle energies. For the case with a background potential drift, we obtain similar $D(t)$ curves.

In order to further clarify the decorrelation mechanisms at work, we consider a more idealized situation. In Fig. 6.3 (right), the running diffusion coefficients are plotted for a number of 2D test particles with no drift and the same orbit width, differing only by their orbit circulation time T_{orbit} which, in turn, determines the parameter $\Xi_{o.a.}$. For $T_{\text{orbit}} \leq 5.6 \cdot 10^{-5}$, we have $\Xi_{o.a.} < 1$, and the curves approach the orbit averaged curve between $\tau^{\text{orbit}} < t < T_{\text{orbit}}$. For $T_{\text{orbit}} > 5.6 \cdot 10^{-5}$, orbit averaging is not valid; hence, there is no trend to approach the orbit averaged curve, the diffusion coefficient follows the curve without any orbit effects, until it saturates at $t \sim \tau^{\text{orbit}}$, or, if $\tau^{\text{orbit}} > \tau_c$, at $t = \tau_c (= 1.8 \cdot 10^{-4} s)$. Since in the ballistic regime, $D(t) = (\bar{V}^{\text{eff}})^2 t$ for the orbit averaging case, but $D(t) = V^2 t$ in the case that orbit averaging is not valid (yet), the saturation levels for D are higher in the latter case. So from this figure, it becomes clear how the fact that orbit averaging is not valid can lead to an increase of diffusivity. Also, one can predict that in that case, a reduction of the diffusivity can only occur if the effective decorrelation time $\tau^{\text{eff}} = \tau^{\text{orbit}} = \lambda_V T_{\text{orbit}}/(\pi \Delta x)$ is small enough to be in the ballistic regime where a reduction of τ^{eff} means a reduction of D. Since $\Delta x \propto E^{1/2}$ and $T_{\text{orbit}} \propto E^{-1/2}$, we therefore expect a decrease like $D \propto E^{-1}$ for large energies. More precisely, since the maximum of the static $D(t)$ curve lies at $t = \tau_{\text{fl}} = \lambda_c/V$, the criterion for the E^{-1} decrease is $\tau^{\text{eff}} < \tau_{\text{fl}}$, i.e.,

$$\frac{T_{\text{orbit}} V}{\pi \Delta x} < 1 \,. \tag{6.16}$$

Inserting the equations for T_{orbit} and Δx for our nominal physical parameters and for passing orbits into Eq. (6.16), we obtain the condition $E \gtrsim 15$ keV for the $1/E$ decrease. However, we have to remember that this criterion is valid only if orbit averaging is invalid, and if $\tau_{\text{drop}} > \tau^{\text{orbit}}$. Moreover, for the $T_{\text{orbit}} = 5.6 \cdot 10^{-6}$ curve, the bursty nature of the diffusion can be seen. A burst occurs every time the particles come back into their original zone of correlation, i.e., after $\Delta t = T_{\text{orbit}}$.

6.6 Beam ions in a sheared magnetic field

6.6.1 Simulation results and analytical approach

We now turn to a more realistic scenario by employing a sheared magnetic field with $q(r) = 0.5\,(r/\text{m})^2 + 1.25$. At the same time, we choose the envelope in Eq. (6.6) to be $g(z) = 0.5 \cos(z - \sin(z)) + 0.5$. This ansatz reproduces the typical ballooning structure of plasma turbulence and implies a parallel correlation length of $\lambda_\parallel \sim 2\pi q_0 R_0$ which is in agreement with typical experimental results (Zweben & Medley, 1989; Wootton *et al.*, 1990; Thomsen *et al.*, 2002; Mahdizadeh *et al.*, 2007). The beam ion and turbulence parameters are the same as before, and the beam energies are varied from $E = 10$ keV to $E = 1280$

E[keV]	T_{orbit}[s]	$\Delta x/2$[m]	v_y[m/s]	$\Xi_{\mathrm{o.a.}}^{v_{\mathrm{dr}}=0}$	$\Xi_{\mathrm{o.a.}}^{v_{\mathrm{dr}}=1\,\frac{\mathrm{km}}{\mathrm{s}}}$	$\tau_{\mathrm{drop}}^{v_{\mathrm{dr}}=0}$[s]	$\tau_{\mathrm{drop}}^{v_{\mathrm{dr}}=1\,\frac{\mathrm{km}}{\mathrm{s}}}$[s]	τ^{orbit}[s]
10	$5.6 \cdot 10^{-5}$	0.006	249	2.4	2.6	$1.3 \cdot 10^{-4}$	$4.6 \cdot 10^{-5}$	$1.3 \cdot 10^{-5}$
20	$4.0 \cdot 10^{-5}$	0.008	501	1.3	1.3	$6.7 \cdot 10^{-5}$	$6.4 \cdot 10^{-5}$	$6.0 \cdot 10^{-6}$
40	$2.8 \cdot 10^{-5}$	0.011	1010	1.7	0.6	$3.4 \cdot 10^{-5}$	$1.4 \cdot 10^{-3}$	$3.1 \cdot 10^{-6}$
80	$2.0 \cdot 10^{-5}$	0.016	2040	2.4	1.2	$1.7 \cdot 10^{-5}$	$3.4 \cdot 10^{-5}$	$1.6 \cdot 10^{-6}$
160	$1.4 \cdot 10^{-5}$	0.023	4120	3.3	2.5	$8.4 \cdot 10^{-6}$	$1.1 \cdot 10^{-5}$	$7.5 \cdot 10^{-7}$
320	$1.0 \cdot 10^{-5}$	0.033	8420	4.9	4.3	$4.2 \cdot 10^{-6}$	$4.8 \cdot 10^{-6}$	$4.0 \cdot 10^{-7}$
640	$7.0 \cdot 10^{-6}$	0.047	17300	6.8	6.4	$2.1 \cdot 10^{-6}$	$2.2 \cdot 10^{-6}$	$2.0 \cdot 10^{-7}$
1280	$5.0 \cdot 10^{-6}$	0.067	35800	9.8	9.5	$1.1 \cdot 10^{-6}$	$1.1 \cdot 10^{-6}$	$1.0 \cdot 10^{-7}$

Table 6.2: Characteristic orbit parameters for beam ions ($\eta = 0.99$) in an ITER-like tokamak with $R_0 = 6.2$ m, $B_0 = 5.3$ T, and $q(r) = 0.5(r/\mathrm{m})^2 + 1.25$. The plasma/turbulence parameters are as usual. For the calculation of $\Xi_{\mathrm{o.a.}}$, $\bar{V}^{\mathrm{eff}}$ has been determined according to Eq. (6.11). All parameters are taken from simulations; they are in good agreement with the analytical expressions from Eq. (6.9).

keV. Because of the magnetic shear, the curvature drift velocities v_y are much higher now than in the shearless case. All simulations are performed for a diamagnetic drift velocity of the background fluctuations of either $v_{\mathrm{dr}} = 0$ or $v_{\mathrm{dr}} = 1$ km/s. The characteristic orbit parameters can be found in Table 6.2. The saturated diffusion coefficients (as a function of the beam energies) for the 3D motion, the corresponding 2D orbit motion results, and the orbit averaged 2D cases are shown in Fig. 6.4. For the moment, we want to ignore the dashed bold lines. As can be inferred from Table 6.2, the drift velocities are higher than in the shearless case, leading to an increase of $\Xi_{\mathrm{o}.a.}$. Consequently, the condition $\Xi_{\mathrm{o}.a.} < 1$ is only fulfilled for a single case, namely $E = 40$ keV and $v_{\mathrm{dr}} = 1$ km/s ($v_y \approx v_{\mathrm{dr}}$). In Fig. 6.4, we see that only for these parameters, the orbit averaged value corresponds to the orbit motion value. Moreover, we observe that the 2D orbit curves correspond quite well to the 3D curves, except for $E \sim 100$ keV and $v_{\mathrm{dr}} = 1$ km/s. This may be attributed to the fact that $\Xi_{\mathrm{o}.a.}$ is close to unity in that case, which means that the fast drop in the orbit averaged curves still affects the 2D orbit curves. However, we see that $T_{\mathrm{orbit}} \lesssim \tau_{\mathrm{drop}}$, and in three dimensions, the particle decorrelates at $t \sim T_{\mathrm{orbit}}$ because of its parallel motion. Therefore, it is not affected by the drift barrier. In all the cases where orbit averaging is clearly not valid, decorrelation is produced by $\tau^{\mathrm{eff}} = \tau^{\mathrm{orbit}} = \lambda_V T_{\mathrm{orbit}}/(\pi \Delta x)$, which is always smaller than $T_{\mathrm{orbit}} \sim \tau_{\|}$. Therefore, parallel decorrelation effects are irrelevant in that case, and the 3D motion corresponds to the 2D motion. We note in passing that this would still be valid if the parallel correlation length would be reduced by up to one order of magnitude. Especially for larger beam energies, we observe a very clear $1/E$ decrease which we have already explained in the previous section. Only in the case of the drifting background potential, larger deviations occur because of the existence of a drift resonance around 40 keV.

Based on these insights, the value of D can be estimated. Since the decorrelation due to the orbit motion occurs within the ballistic regime ($\tau^{\mathrm{orbit}} < \tau_{\mathrm{fl}}$), we get $D \sim V^2 \tau^{\mathrm{eff}}$ (low Kubo number limit, Eq. (2.65)). For our nominal parameters, this means $D \sim 114\,\mathrm{m}^2/\mathrm{s}\,(E/\mathrm{keV})^{-1}$, which matches the simulation values within a factor of 1.5. The small deviation can be taken into account

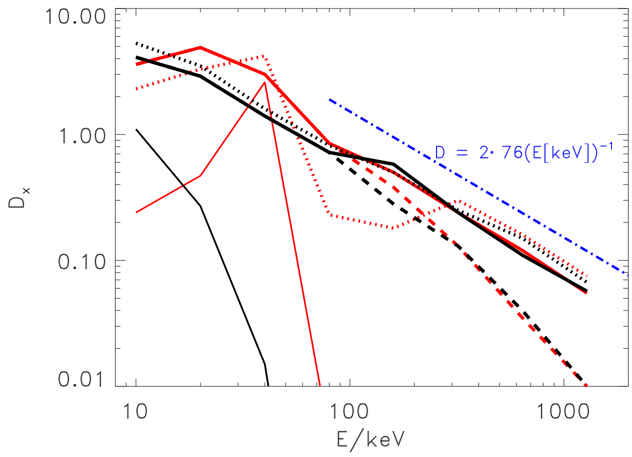

Figure 6.4: Radial diffusion coefficient D_x for different particle energies E and $\eta = 0.99$ in a sheared magnetic field. Black lines: no background drift ($v_{\mathrm{dr}} = 0$). Red lines: background drift ($v_{\mathrm{dr}} = 1$ km/s). Bold solid lines: particles in an annulus. Bold dashed lines: particles an annulus consisting of 10 flux tubes with periodic boundary conditions. Dotted lines: simple 2D model (Eq. (6.15)). Thin solid lines: orbit averaging in the simple 2D model. Blue dashed-dotted line: analytic approach. The blue curve has been multiplied by a factor of two to become distinguishable from the simulation results.

assuming that the decorrelation occurs not exactly at τ^{eff} but already at about $\tau^{\mathrm{eff}} \times 2/3$. [We note in passing that our definition of the correlation time as the e-folding time is in some way arbitrary. A reduction does only mean that the effective decorrelation occurs already at larger values of the autocorrelation function.] Including this correction factor and generalizing to arbitrary physical parameters, we find the relation

$$D \approx \frac{V^2 \lambda_V R_0 B_0 e}{3\eta^2 E} \tag{6.17}$$

for beam ions in electrostatic tokamak microturbulence for $\Xi_{\mathrm{o.a.}} > 1$. We remember $\lambda_V \approx \lambda_c/2$ (see Section 6.4.2).

Using the normalizations that are common in simulations of plasma turbulence it is possible to rescale Eq. (6.17) to arbitrary temperatures and machine sizes. To this aim, we use the normalizations $\hat{V}_E = V_E/(\rho_i c_i/R_0)$ and $\hat{\lambda}_V = \lambda_V/\rho_i$ defined in Section 2.4 where we attribute to T_e (and T_i) the dimension of an energy, so that the Boltzmann constant can be dropped. Inserting these relations into Eq. (6.17), we obtain

$$D(E) \approx \frac{\hat{V}_E^2 \hat{\lambda}_V}{3\eta^2} \left(\frac{E}{T_e}\right)^{-1} \frac{\rho_i^2 c_i}{R_0} \propto \left(\frac{E}{T_e}\right)^{-1} D_{\mathrm{gyroBohm}} \,. \tag{6.18}$$

This is the well known gyro-Bohm diffusion coefficient, $D_{\mathrm{gyroBohm}} = \rho_s^2 c_s/R_0$, multiplied with the inverse of the particle energy normalized with respect to the thermal energy of the background plasma. In this context, we would like to point out that the occurrence of the ratio E/T_e is not trivial since the thermal energy determines the scales of the background turbulence while the particle energy governs the orbit motion of the energetic particles. Both influence the fast particle transport, but they are *a priori* independent. To clarify this point, let us give a counter-example. Assuming that the decorrelation is not caused by the perpendicular orbit motion but by the parallel motion, then the effective decorrelation time would be $\tau^{\text{eff}} = T_{\text{orbit}} \propto E^{-1/2}$ instead of $\tau^{\text{eff}} \propto E^{-1}$. This, in consequence, would lead to the scaling $D(E) \propto (T_e/E^{1/2})\, D_{\text{gyroBohm}}$. Moreover, it should be clear that the structure of the background turbulence (e.g. streamers) is of minor relevance for the transport of fast particles if decorrelation is caused by the orbit motion, since $\tau^{\text{orbit}} < \tau_{\text{fl}}$. This means that the particles are no more able to 'feel' the geometric structure of the turbulent vortices, i.e., a new effective Kubo number is now $K^{\text{eff}} \equiv \tau^{\text{orbit}} V/\lambda_c \ll 1$.

In closing this section, we briefly want to compare the results of Fig. 6.4 with those of previous works. In Ref. (Dannert *et al.*, 2008), a $1/E$ decay of the diffusion coefficient was found for large particle energies in nonlinear gyrokinetic simulations, whereas an approximate $1/E^{2.6}$ decay was found in quasilinear runs based on generalized Maxwellian distributions. An explanation for this behavior with respect to the underlying physics could not be given. In Ref. (Angioni & Peeters, 2008), quasilinear calculations for slowing-down distributions lead to a $1/E^3$ decay. Comparing those results with each other as well as with ours, we may conclude that it is indeed the *turbulent* (i.e., random) nature of the advecting field which is responsible for the slow decay of the particle transport with increasing energy. A more rapid decay (faster than $1/E$) is only obtained in cases for which the particle is not decorrelated after one orbit turn. This applies if orbit averaging is valid ($\Xi_{\text{o.a.}} \lesssim 1$), as we have already seen. In linear simulations, orbit decorrelation does not occur, since there is no turbulence. Hence, orbit averaging remains valid and the reduction of D with E is overestimated.

It is instructive to generalize the expression for the validity of orbit averaging, Eq. (6.12), to arbitrary machine sizes and background temperatures as we have just done for the diffusion coefficient. For very large particle energies, we have $v_y \gg \{v_{\text{dr}}, \bar{V}^{\text{eff}}\}$, and therefore $\Xi_{\text{o.a.}} = v_y T_{\text{orbit}}/\lambda_c$. Inserting the respective terms into that equation, we find

$$\Xi_{\text{o.a.}} = \frac{2^{3/2}\pi\eta\hat{s}qE^{1/2}}{\hat{\lambda}_c T_e^{0.5}} \sim \hat{s}\, q \left(\frac{E}{T_e}\right)^{1/2} . \tag{6.19}$$

Interestingly, this expression is independent of R_0 and B_0. Thus, a reduction of the fast particle transport through a reduction of $\Xi_{\text{o.a.}}$ can be achieved, e.g., through a reduction of the safety factor or the magnetic shear. This result explains, on general grounds, why one can expect orbit averaging to apply and the fast ion transport to drop quickly with increasing particle energy in low-shear regions of a tokamak. Thus, the latter can, in fact, act as kind of "transport barriers" for energetic particles.

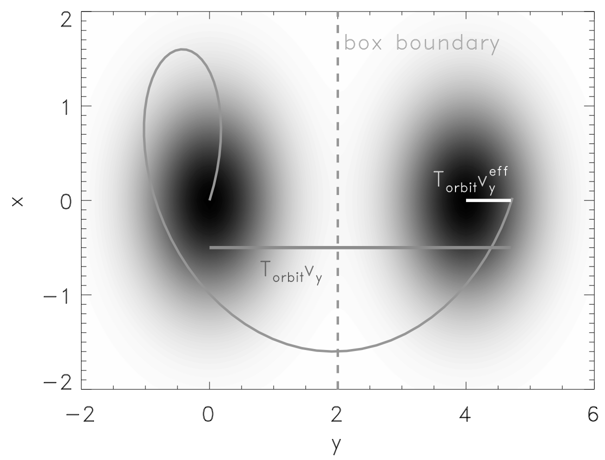

Figure 6.5: This figure is similar to Fig. 6.1. It illustrates the mechanism of unphysical re-correlations if a flux surface is covered by several flux tubes. Here, the real drift velocity v_y is replaced by the effective velocity $v_y^{\text{eff}} = (T_{\text{orbit}} v_y \bmod L_y)/T_{\text{orbit}}$.

6.6.2 Some comments on reduced-volume simulations

At this point, it seems worthwhile to briefly discuss an unphysical aliasing-type effect which can occur if, in energetic particle studies, a flux surface is covered, for convenience, by M identical copies of a thin flux tube, and M is chosen too large. Our standard simulations are performed with $M = 1$, i.e., the box width in the y direction is chosen to be $2\pi r_0/q_0$, and the particles only feel the true periodicity of the flux surface. Now, to reduce the computational effort in setting up the test potential, one might want to use $M > 1$ instead (see Section 2.3.3). Here, one has to be careful, however, as will become clear presently. The dashed lines in Fig. 6.4 have been obtained by using $M = 10$ instead of $M = 1$, corresponding to a box width in the y direction of $L_y \equiv 2\pi r_0/(10 q_0) \approx 0.31$ m. For thermal particle velocities, such a choice would be fully adequate, since the time a particle needs to cross the box is much larger than the turbulence correlation time τ_c. Hence, the particle encounters a new realization when reentering the simulation volume. Now, for $M = 10$, the minimum velocity a particle needs to have to feel the periodicity is $v_{\text{min}} = L_y/\tau_c \approx 1750$ m/s (for $r_0 = 0.7$ m). From Table 6.2, we can infer that the critical velocity is reached at $E \sim 80$ keV, and from Fig. 6.4, we see that this is indeed (at least approximately) the particle energy at which the curves begin to deviate (in fact, since we have only simulated a discrete number of energies, $E = 160$ keV is the first one where we observe the difference).

In Fig. 6.5, the mechanism is explained which leads to an unphysical decrease of the diffusivity for $M = 10$. It displays a trajectory subject to a large drift velocity which takes the particle out of the correlated zone (see also Fig. 6.1). However, because of the imposed periodicity, the particle gets back into the zone of correlation when it reenters the simulation volume. So after one turn, the particle, although having traveled a distance of $T_{\text{orbit}} v_y$, feels a potential which corresponds to the much smaller distance $T_{\text{orbit}}v_y^{\text{eff}}$, where $v_y^{\text{eff}} = (T_{\text{orbit}}v_y \bmod L_y)/T_{\text{orbit}}$. For the transport, this means that the decorrelation does not occur at $\tau^{\text{orbit}} = \lambda_V/v_{\text{orbit}}$ anymore. Since $\Xi_{\text{o.}a.} = T_{\text{orbit}}v_y^{\text{eff}}/\lambda_c < 1$, orbit averaging applies again, and, if $\tau_{\text{drop}} < \min\{\tau_\|, \tau_c\}$, the drift barrier becomes dominant and the transport is reduced. It should be clear that such a re-correlation can only occur if the characteristic time scales are smaller than the correlation time τ_c of the potential. This is true in our case. So, in general, if performing fast particle simulations with $M > 1$, one should always ensure that M is small enough for such aliasing effects not to occur. It is crucial to be aware that the particle is able to 'remember' a former correlation, although being decorrelated at an earlier time.

For the interested reader, a more detailed study of the effect of unphysical re-correlations is provided in Appendix A.

6.6.3 Breaking of adiabatic invariants

Our above findings can also be looked at from a more abstract point of view. As is well known, the radial transport of both thermal and suprathermal particles is fundamentally connected with the breaking of certain adiabatic invariants. From the discussion in Section 2.1.2 we already now the magnetic moment as the first adiabatic invariant in a tokamak. In 3D, the phase space can be parameterized by the three adiabatic invariants $\mathbf{J} = (\mu, J_\phi, J_p)$ and $\theta = (\theta_g, \theta_\phi, \theta_p)$, where μ is the magnetic moment, J_ϕ is the canonical angular momentum, and J_p is the poloidal flux enclosed by the drift surface (Kaufman, 1972; Mynick & Boozer, 2005). The vector θ contains the corresponding phases (the canonical conjugate values to $\mathbf{J}$), and $\Omega_g = \dot{\theta}_g$, $\Omega_\phi = \dot{\theta}_\phi$, and $\Omega_p = \dot{\theta}_p$ are the frequencies of the periodic motions. Diffusion in real space corresponds to a diffusion in $\mathbf{J}$ space which presupposes a breaking of one or more of the adiabatic invariants μ, J_ϕ, and J_p. This may be caused by resonances between the frequencies associated with the respective periodic motions and the perturbation frequencies ω_{turb} of the background turbulence. The resonance condition can be expressed as $\omega_{\text{turb}} = l_g\Omega_g + l_\phi\Omega_\phi + l_p\Omega_p$, ($l_g$,$l_\phi$, l_p integer) (Kaufman, 1972; Mynick & Boozer, 2005). While Ω_g will always be much too large to be in resonance with the turbulence and, for fast ions, $\omega_{\text{turb}}/\Omega_\phi \sim (k_y\rho_s)\,(c_s/R_0)\,(q_0R_0/v_\|) \ll 1$, the frequency corresponding to the third invariant is often found to be comparable to or smaller than the typical frequencies of the fluctuations (Mynick & Krommes, 1979). Since Ω_p is the frequency with which the particles drift around the torus in the toroidal direction, it is given by $\Omega_p = v_y/r_0$. Our test potential was created using a Gaussian frequency spectrum with an e-folding frequency of about 16700 1/s. This frequency is only reached by Ω_p at $E \sim 500$ keV. Therefore, a significant radial transport of fast particles with $E \lesssim 500$ keV is possible due to the breaking of the third adiabatic invariant by the background turbulence.

E[keV]	T_{orbit}[s]	$\Delta x/2$[m]	ρ_g[m]	v_y[m/s]	$\Xi_{\text{o.a.}}^{v_{\text{dr}}=0}$	$\Xi_{\text{o.a.}}^{v_{\text{dr}}=1\,\frac{\text{km}}{\text{s}}}$	$\tau_{\text{drop}}^{v_{\text{dr}}=0}$[s]	$\tau_{\text{drop}}^{v_{\text{dr}}=1\,\frac{\text{km}}{\text{s}}}$[s]	τ^{orbit}[s]
10	$2.6 \cdot 10^{-4}$	0.011	0.0038	237	5.3	12.1	$1.4 \cdot 10^{-4}$	$4.3 \cdot 10^{-5}$	$3.4 \cdot 10^{-5}$
20	$1.8 \cdot 10^{-4}$	0.016	0.0054	472	5.2	5.8	$7.5 \cdot 10^{-5}$	$6.2 \cdot 10^{-5}$	$1.7 \cdot 10^{-5}$
40	$1.3 \cdot 10^{-4}$	0.023	0.0076	938	7.4	1.3	$3.5 \cdot 10^{-5}$	$5.5 \cdot 10^{-4}$	$8.5 \cdot 10^{-6}$
80	$9.0 \cdot 10^{-5}$	0.033	0.011	1860	10.3	4.8	$1.7 \cdot 10^{-5}$	$3.7 \cdot 10^{-5}$	$4.2 \cdot 10^{-6}$
160	$6.4 \cdot 10^{-5}$	0.047	0.015	3680	14.7	10.8	$8.7 \cdot 10^{-6}$	$1.2 \cdot 10^{-5}$	$2.1 \cdot 10^{-6}$
320	$4.5 \cdot 10^{-5}$	0.067	0.021	7270	20.6	17.9	$4.4 \cdot 10^{-6}$	$5.0 \cdot 10^{-6}$	$1.1 \cdot 10^{-6}$
640	$3.2 \cdot 10^{-5}$	0.096	0.031	14300	29.4	27.4	$2.2 \cdot 10^{-6}$	$2.3 \cdot 10^{-6}$	$5.5 \cdot 10^{-7}$
1280	$2.3 \cdot 10^{-5}$	0.139	0.042	28000	41.2	40.8	$1.1 \cdot 10^{-6}$	$1.1 \cdot 10^{-6}$	$2.7 \cdot 10^{-7}$

Table 6.3: Characteristic orbit parameters for ions with $\eta = 0.2$ in an ITER-like tokamak with $R_0 = 6.2$ m, $B_0 = 5.3$ T, and $q(r) = 0.5(r/\text{m})^2 + 1.25$. The plasma/turbulence parameters are as usual. All parameters are taken from simulations; they are in good agreement with the analytical expressions from Eq. (6.10). The finite gyroradius of the particles has been taken into account via gyroaveraging.

6.7 Trapped ions in a sheared magnetic field

Up to now, we have concentrated on beam-like ions, characterized by $\eta \sim 1$. This was, in part, motivated by recent experimental results (Günter *et al.*, 2007) concerning the efficiency of neutral beam injection, and the need to explain them. In the present section, however, we would like to investigate in which way the $D(E)$ behavior is modified if the test particles only have a small parallel velocity component such that they are trapped on the outer side of the torus, moving along banana orbits. Taking $\eta = 0.2$, the respective orbit parameters are shown in Table 6.3. Comparing them with the ones in Table 6.2, one sees that the orbit circulation is slower than for the passing particles with $\eta = 0.99$, as could be expected from comparing Eq. (6.7) with Eq. (6.8). Therefore, $\Xi_{\text{o}.a.}$ is larger, and orbit averaging cannot be applied. Hence, the decorrelation is expected to be caused by τ^{orbit} in all cases. On the other hand, since the particles now have a significant perpendicular velocity component, finite gyroradius effects have to be taken into account. As can be inferred from the table, $\rho_g > \lambda_c$ for $E > 160$ keV. Since τ^{orbit} is larger than for the $\eta = 0.99$ case, we expect the base level of $D(E)$ to be larger, too. However, due to gyroaveraging, the effective $E \times B$ drift velocity is reduced for larger particle energies, leading to a faster drop of the diffusivity. In Fig. 6.6, several $D(E)$ curves are plotted. It can be seen that the fall-off of the diffusivity with growing particle energy is clearly faster than for the beam ion case. It is interesting to compare the $D(E)$ curves obtained with gyroaveraging with those, for which finite gyroradius effects have not been included. In the latter case, the decay is $\propto 1/E$ as in the beam ion case, but on a higher level, indicating that only the increased orbit decorrelation time is at work, but not the reduced $E \times B$ drift. Although orbit averaging is clearly not valid, a peak can be observed at $E = 40$ keV for the case with the background drift, reflecting the existence of a resonance between the particle curvature drift and the drift of the fluctuations. We attribute this behavior to the fact that only for that case, $\tau_{\text{drop}} \gg \tau^{\text{orbit}}$, whereas a small influence of the drift barrier may remain for the other energies.

As in the previous section, we now want to devise a quantitative formula for $D(E)$. To this aim, we again approximate the diffusivity in the large energy

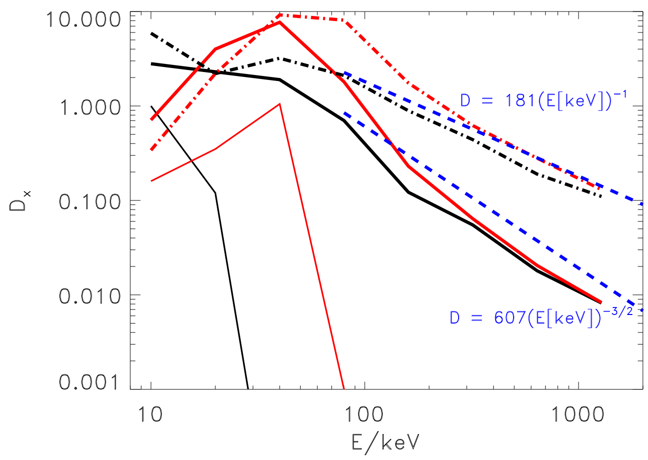

Figure 6.6: Radial diffusion coefficient D_x for different particle energies E and $\eta = 0.2$ in a sheared magnetic field. Black lines: no background drift ($v_{\mathrm{dr}} = 0$). Red lines: background drift ($v_{\mathrm{dr}} = 1$ km/s). Bold solid lines: particles in a tokamak (Eq. (2.18)). Finite gyroradius effects are included via gyroaveraging. Bold dashed dotted lines: the same, but without finite gyroradius effects. Thin solid lines: orbit averaging in the simple 2D model. Blue dashed lines: analytic approach with and without gyroaveraging.

limit by the expression $D \sim (V^{\mathrm{eff}})^2 \tau^{\mathrm{orbit}} \times 2/3$, where the factor 2/3 follows from the observation that in practice, the decorrelation occurs already before the nominal decorrelation time is reached. With Eq. (6.8) we then find

$$D \approx \frac{\sqrt{2}(V^{\mathrm{eff}})^2 \lambda_V^{\mathrm{eff}} R_0^{0.5} r_0^{0.5} B_0 e}{3\eta\sqrt{1-\eta^2}E} \tag{6.20}$$

(again, $\lambda_V \approx \lambda_c/2$). In the case without gyroaveraging, we simply set $V^{\mathrm{eff}} = V$ and $\lambda_c^{\mathrm{eff}} = \lambda_c$. Inserting the nominal physical parameters as introduced in Sec. 6.2 yields $D = 181\,\mathrm{m}^2/\mathrm{s}\,(E/\mathrm{keV})^{-1}$. Fig. 6.6 shows that this approach fits the respective simulation results quite well in the high energy limit. To obtain a realistic description of the behavior for low-η particles, we have to calculate the effective (i.e., gyroaveraged) values. In the large gyroradius limit, they are already known from Eqs. (3.15) and (3.16), where ρ_g is replaced by the relative quantity ρ_g/λ_c. Expressing the gyroradius as $\rho_g = \sqrt{1-\eta^2}\sqrt{2Em}/(eB)$ and inserting the effective values into Eq. (6.20), we get

$$D \approx \frac{1.73\, V^2 \lambda_c \lambda_V e^2 B^2 R_0^{0.5} r_0^{0.5}}{12\sqrt{\pi}\eta(1-\eta^2) m^{0.5} E^{3/2}} \,. \tag{6.21}$$

Employing again the nominal physical parameters, we find $D = 607/(E/\mathrm{keV})^{3/2}$, which, as can be inferred from Fig. 6.6, matches the simulation results quite well in the large energy limit. At this point, we have to recall that the validity condition for this approach is that both the gyroradius and the orbit radius exceed λ_c, such that the effective $E \times B$ drift approach applies, and that the orbit decorrelation is dominant. In Eq. (6.21), a $1/E$ decay is produced by the orbit decorrelation, and an additional $E^{-1/2}$ decay comes from the gyration. We note in passing that for our beam ion case ($\eta = 0.99$), finite gyroradius effects become relevant only for energies exceeding 1 MeV, and that a $E^{-3/2}$ decay may also be expected in this "ultra fast" regime. Moreover, for beam ions where η is clearly smaller than 1, finite gyroradius effects may become important for smaller energies, and a $E^{-3/2}$ decay may be observed, too.

Replacing the parameters characterizing the background potential by dimensionless values, as we have also done in the previous section, one obtains

$$D(E) = \frac{1.73\,\hat{V}_E^2 \hat{\lambda}_c \hat{\lambda}_V \sqrt{\epsilon}}{12\sqrt{\pi}\eta(1-\eta^2)} \left(\frac{E}{T_e}\right)^{-3/2} \frac{\rho_i^2 c_i}{R_0} \propto \left(\frac{E}{T_e}\right)^{-3/2} D_{\text{gyroBohm}} \,. \qquad (6.22)$$

We thus find a slightly faster decay than in the large-η case, which is due to finite gyroradius effects.

6.8 Scaling of fast ion transport for arbitrary orbit parameters

Up to now, we have based our discussion of the high energetic particle scaling in electrostatic turbulence on two constraints:
1. We have parameterized the particles by their pitch angle η and their total energy E, which means that the scaling laws derived in the foregoing sections assume an increase of energy for a constant pitch angle, i.e. energy is uniformly transferred into both parallel and perpendicular direction.
2. Although we have used the parameter η in our scaling laws for D, they are - strictly spoken - only valid in the limits $\eta \to 1$ and $\eta \to 0$. In this section, we will generalize the scaling laws concerning these points.

6.8.1 Scaling laws for arbitrary pitch angles

The orbit parameters given in Eqs. (6.7) and (6.8) have been derived assuming the limits $\eta \to 1$ and $\eta \to 0$, respectively (Wesson, 1997). However, we could demonstrate using particle orbit simulations with the GOURDON code, that the respective expressions can be assumed to be valid for *all* values of η to a good approximation. One only has to ensure whether the particles are trapped or passing. A criterion for this discrimination has already been given at the end of Section 2.1.5. There is no continuous transformation with η from trapped to passing orbits, but a sharp jump.

In Section 6.6, we have assumed that beam ions have a vanishing gyroradius. However, this is true for large energies only if the pitch angle is very large. For this reason, we have assumed $\eta \to 1$ in this section. However, as was shown in Section 2.1.5, passing particles can also have significantly smaller pitch angles ($\sqrt{2 - 2R_0/R_1} \lesssim \eta \leq 1$), where the perpendicular component can be already large enough to produce finite gyroradius effects. We therefore have to include them in the same way as we did for trapped particles in Section 6.7. Moreover, since we have $\tau^{\text{orbit}} < \tau_{\text{fl}}$, decorrelation occurs in the small Kubo number regime, which means that corrections are not only necessary for $\rho_g > \lambda_c$, but already for smaller gyroradii (see red curve in Fig. 3.5).

In Section 6.7, we have included finite gyroradius effects with $\rho_g > \lambda_c$ for all trapped particles. For small particle energies, this does not need to be true, so in this case, Eq. (6.22) should be corrected, too.

Complete equations of motion for the four cases (passing/trapped and small/ large gyroradius) are given in Appendix B. They are a generalization of Eqs. (6.18) and (6.22) to arbitrary pitch angles.

6.8.2 Scaling laws in the $\mu - v_\parallel$ plane

Instead of characterizing a particle by its total energy E and its pitch angle η, it is also possible to chose μ and $v_\parallel$, or $E_\perp$ and $E_\parallel$, respectively, instead. The transformation reads

$$E_\parallel = \eta^2 E\,; \qquad E_\perp = (1-\eta^2)E\,. \tag{6.23}$$

If we replace η and E that way in Eqs. (6.18) and (6.22), we obtain

$$D(E) \approx \frac{\hat{V}_E^2 \hat{\lambda}_V}{3} \left(\frac{E_\parallel}{T_e}\right)^{-1} \frac{\rho_i^2 c_i}{R_0}\,. \tag{6.24}$$

for beam ions with $\eta \to 1$, and

$$D(E) = \frac{1.73\, \hat{V}_E^2 \hat{\lambda}_c \hat{\lambda}_V \sqrt{\epsilon}}{12\sqrt{\pi}} \frac{E_\perp^{-1} E_\parallel^{-1/2}}{T_e^{-3/2}} \frac{\rho_i^2 c_i}{R_0} \tag{6.25}$$

for trapped ions with small η. A systematic scaling draft in the $v_\parallel - \mu$ plane is given in Fig. 6.7. The large pitch angle / vanishing gyroradius regime is given by Eq. (6.24), and the small pitch angle / large gyroradius regime is represented by Eq. (6.25). The two other regimes together with scaling laws for E, η as well as for $E_\parallel, E_\perp$ are given in Appendix B, Eqs. (B.4) to (B.7).

It is interesting to note that regimes exist, where the selective input of energy into a single velocity component does not influence the transport, or weakens the transport more slowly than changing $v_\parallel$ and μ equally.

6.9 Summary and conclusions

In the present chapter, we have studied – in the passive tracer limit – the interaction of energetic ions with electrostatic microturbulence for an idealized ITER-like tokamak, where the full 3D equations of motion were used. It was found that although many findings of the 2D investigations in the previous chapters carry over to the 3D case, the transport mechanisms are in principle of different nature. In this context, several details of both the particle orbit parameters and the properties of the turbulent fluctuations turn out to be important. Nevertheless, it is possible to understand and quantitatively predict the behavior of fast particles both in the high-energy regime, $E/T_e \gg 1$, as well as in the moderate-energy regime, $1 \lesssim E/T_e \lesssim 10$.

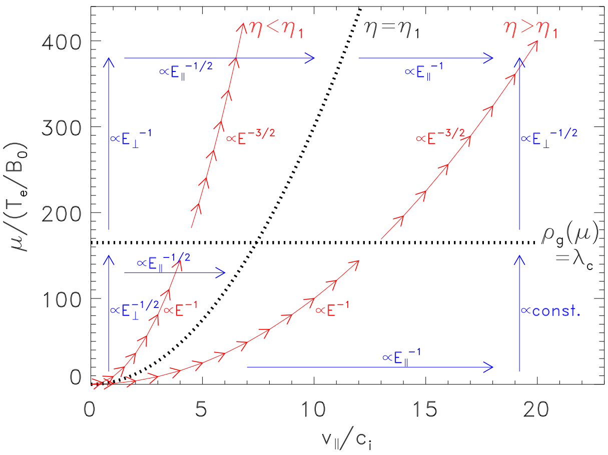

Figure 6.7: Scaling of D with $E_{\parallel}$ and $E_{\perp}$. The axes scale with the parallel velocity (x axis) and with the magnetic moment (y axis). Curves of constant pitch angle have the form $\mu \propto v_{\parallel}^2$. Trapping and passing regimes are separated by the pitch angle η_1, whereas large and small gyroradius regimes are separated by $\rho_g = \lambda_c$ (constant μ).

A first crucial insight is that while, in principle, regimes exist for which it is possible to average the $E\times B$ drift motion over one drift orbit time (for example for very low magnetic shear), such a procedure is usually not valid. In the former case, a particle follows the orbit averaged structures, and the existence of a drift barrier (caused by the poloidal drift of the particles) leads to a strong reduction of the diffusivity with increasing particle energy. In the latter case, however, a particle decorrelates from its original position in the turbulent field already along its orbit. The respective time scale is typically smaller than the autocorrelation time of the fluctuations or the drop time associated with the drift motion. This explains why the observed reduction of the diffusivity is weaker than expected based on orbit averaging arguments. For beam ions, a $(E/T_e)^{-1}$ fall-off has been found analytically as well as numerically, whereas for ions with a smaller parallel and larger perpendicular velocity component, a $(E/T_e)^{-3/2}$ decrease was found, due to additional finite gyroradius effects. Modified scaling laws have been derived by treating $E_{\parallel}$ and $E_{\perp}$ separately.

Besides the high energy limit, we also studied the behavior of particles with $1 \lesssim E/T_e \lesssim 10$. It turned out that the transport of such moderately suprathermal particles may remain on a level comparable to that of thermal particles. This can be attributed to the existence of resonances between the particle drifts and the diamagnetic drift of the background turbulence. In the case of resonance, orbit averaging may become valid, whereas at the same time, the drift barrier does not exist anymore – two effects which work together synergistically. The parallel decorrelation was found to be of minor relevance for all particle energies, since decorrelation due to the perpendicular motion is typically faster by up to one order of magnitude.

By means of these findings and insights, one is able to explain in detail the simulation results reported in Ref. (Dannert *et al.*, 2008). Moreover, they can be applied to try to understand and interpret recent experimental observations (Günter *et al.*, 2007) concerning the efficiency of neutral beam injection. A discussion of the latter problem is the subject of Chapter 8.

Chapter 7

Advection of Fast Ions in Magnetic Turbulence in 3D Tokamak Geometry

The diffusion of energetic ions caused by *magnetic* field fluctuations in 3D tokamak geometry is investigated analytically. In analogy to electrostatic turbulence, it is found that orbit averaging usually is not valid. A regime of constant transport, independent from the particle energy, is found for particles with a large parallel velocity, whereas a decrease with $E^{-1/2}$ is found for particles with a significant perpendicular velocity component. The main results of this chapter have been published in (Hauff *et al.*, 2009).

7.1 Introductory remarks

In Chapter 6, we have studied the variety of mechanisms governing the interaction of the fast particles' orbits with the background electrostatic turbulence. A criterion has been defined for the validity of 'orbit averaging' (Eq. (6.12) or (6.19)). In the case that orbit averaging is not valid, it was shown that the decorrelation time τ^{orbit} (Eq. (6.13)) is the decisive value which governs transport according to the low Kubo number approach $D \approx (V^{\mathrm{eff}})^2 \tau^{\mathrm{orbit}}$, where V^{eff} has to be modified according to the gyroaveraging approach for smaller pitch angles.

The reason why, up to now, we have concentrated on the *electrostatic* turbulent transport was that, according to the discussion in Section 2.5.4, the electrostatic and the magnetic component of the perturbed particle velocity are identical concerning their mathematical structure. In this chapter, we will therefore simply transfer the results of Chapter 6 to magnetic transport, using Eqs. (2.59) and (2.60).

As we know from these equations, the quantity $v_B \equiv v_\parallel(\tilde{B}_r/B_0)$, which represents the projection of the parallel velocity onto the radial direction along a fluctuating field line, takes over the role of the radial component of the $E\times B$ drift velocity in the context of magnetic transport. Here, B_0 is the unperturbed magnetic field and $\tilde{B}_r$ is its radial perturbation. Thus, not unexpectedly, it will

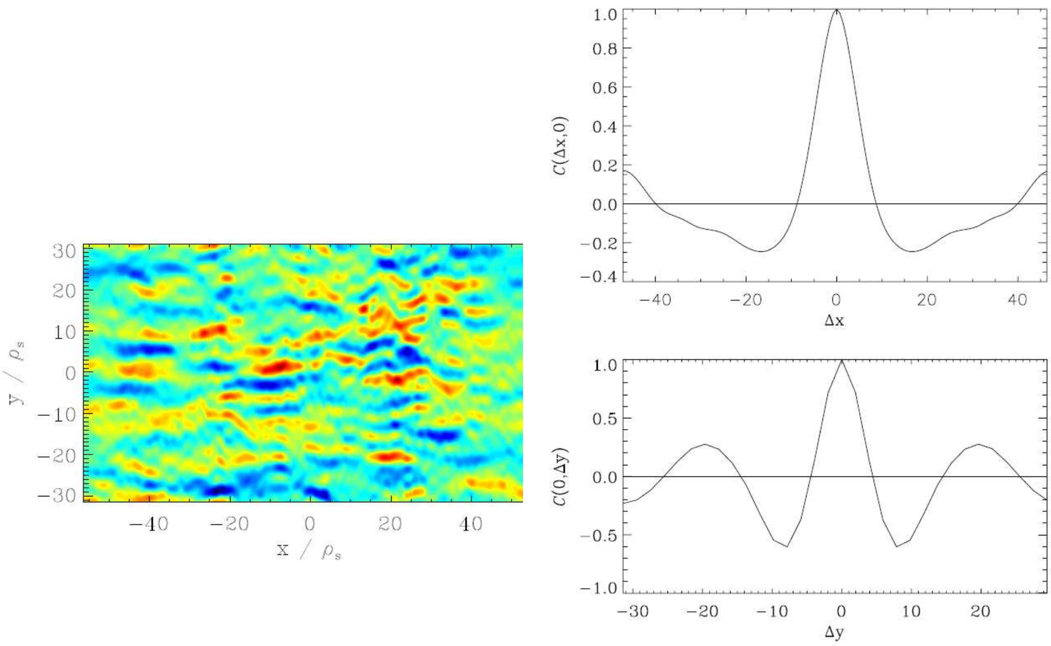

Figure 7.1: *Left*: Contour plot of the radial perturbation part of the magnetic field, $\tilde{B}_r(x, y)$. *Right*: Corresponding autocorrelation functions C in the x and y direction.

turn out that many of the previous findings and insights carry over to this case in a more or less straightforward manner.

7.2 Fast ions in a perturbed magnetic field

It is known, for example from nonlinear electromagnetic GENE simulations, that the structure of the magnetic field line fluctuations (the vector potential $\tilde{A}_{\|}$) is similar to the structure of the turbulent electrostatic field (the electrostatic potential ϕ). In Fig. 7.1, contours of $\tilde{B}_r$ and the corresponding autocorrelation functions are plotted. The correlation length of the radial magnetic field perturbations is found to be comparable to the fluctuations of the electrostatic velocity field, i.e., $\lambda_B \approx 3\rho_i$ in the y direction. This lies between previous assumptions reported in the literature, ranging from $1\rho_i$ (Esposito *et al.*, 1996) to $6\rho_i$ (Mynick & Strachan, 1981).

Simulations of ion temperature gradient turbulence for Cyclone Base Case parameters (Dimits *et al.*, 2000) presented in Ref. (Pueschel *et al.*, 2008) show that the magnetic fluctuation level tends to scale linearly with the 'plasma β'. This parameter is defined as the ratio between the plasma pressure $p_{\text{kin}} = nk_BT$ and the magnetic pressure $p_{\text{mag}} = B^2/(2\mu_0)$:

$$\beta \equiv \frac{p_{\text{kin}}}{p_{\text{mag}}} = \frac{nk_BT}{B^2/(2\mu_0)} \,. \tag{7.1}$$

Although one of the requirements for a commercial fusion reactor is a sufficiently high β, it can be shown that instabilities evolve at higher values of β, when 'ballooning modes' become unstable (Wesson, 1997). We denote the critical value as β_{crit}. So for the fluctuation level of the magnetic field, we specifically find the relation

$$\tilde{B}_r/B_0 \sim C\frac{\beta}{\beta_{\text{crit}}}\frac{\rho_i}{R_0} \tag{7.2}$$

with $C \sim 1$, which is in line with the analytical predictions in Ref. (Waltz, 1985). From now on, $\tilde{B}_r$ will denote the mean value of the magnetic field fluctuations. Consequently, one obtains the estimate

$$V_B \sim \frac{\tilde{B}_r}{B_0}v_\parallel = \frac{\tilde{B}_r}{B_0}\eta\sqrt{\frac{E}{T_e}}\,c_i \sim C\,\frac{\beta}{\beta_{\text{crit}}}\,\eta\sqrt{\frac{E}{T_e}}\,\frac{\rho_i c_i}{R_0} \tag{7.3}$$

for the mean value V_B of the magnetic turbulent velocity v_B. A maximal value can be approached by choosing $\beta = \beta_{\text{crit}}$.

For magnetic transport, the validity condition for orbit averaging is identical to the electrostatic one, except that V_E is replaced by V_B in Eq. (6.12). Since for larger energies $v_y \gg (v_{\text{dr}}, V_B)$, Eq. (6.19) applies, too. Therefore the magnetic values $\Xi_{\text{o.}a.}$ are in general comparable to the electrostatic ones, and orbit averaging is invalid for $E/T_e \gg 1$.

The magnetic orbit decorrelation time is the same as that already defined in Eq. (6.13), only λ_V has to be replaced by λ_B. Subsequently applying the same reasoning that lead to Eq. (6.18) and making the ansatz $D_B \approx V_B^2\tau^{\text{orbit}} \times 2/3$, we obtain the expression

$$D_B(E) \approx \frac{\hat{\lambda}_B}{3}\left(\frac{C\,\beta}{\beta_{\text{crit}}}\right)^2 \frac{\rho_i^2 c_i}{R_0} \tag{7.4}$$

for the diffusion coefficient of beam ions with large pitch angle ($\eta \to 1$). Thus, e.g., for $C = 0.76$ and $\beta/\beta_{\text{crit}} = 0.6$ (Pueschel *et al.*, 2008), one gets $D_B \sim 0.1\,\rho_i^2 c_i/R_0$ ($\approx 0.12\,\text{m}^2/\text{s}$ for ITER parameters as introduced in Sec. 6.2), which is a reasonably large number. It is important to note in this context that the magnetic transport is independent of the particle energy. The reason for this behavior is that the $1/E$ dependence caused by the perpendicular decorrelation is balanced by the increase of the magnetic drift velocity since, in contrast to the electrostatic case, the magnetic perturbation velocity depends on the total parallel particle velocity. For trapped particles, finite Larmor radius effects have to be taken into account as before, and one obtains

$$D_B(E) \approx \frac{1.73\,\hat{\lambda}_B^2\sqrt{\epsilon}\eta}{12\sqrt{\pi}(1-\eta^2)}\left(\frac{C\,\beta}{\beta_{\text{crit}}}\right)^2\left(\frac{E}{T_e}\right)^{-1/2}\frac{\rho_i^2 c_i}{R_0}\,, \tag{7.5}$$

i.e. $D_B(E) \propto E^{-1/2}$. Thus, the magnetic expressions deviate even more profoundly from the expectations based on the validity of orbit averaging.

As in Chapter 6, we have studied only two rather simplified cases here, namely beam ions with vanishing gyroradius ($\eta \to 1$) and trapped ions with large gyroradii ($\rho_g > \lambda_B$). A complete study, including passing particles with finite gyroradius effects as well as trapped particles with small gyroradii, can be found in Appendix B.

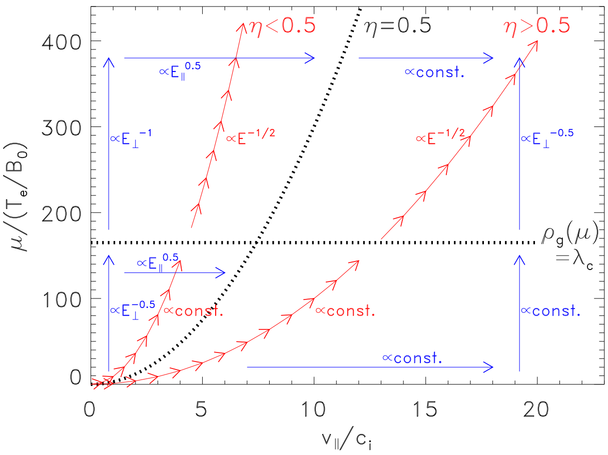

Figure 7.2: Scaling of D with $E_{\parallel}$ and $E_{\perp}$. The axes scale with the parallel velocity (x axis) and with the magnetic moment (y axis). Curves of constant pitch angle have the form $\mu \propto v_{\parallel}^2$. Trapping and passing regimes are separated by the pitch angle η_1, whereas large and small gyroradius regimes are separated by $\rho_g = \lambda_c$ (constant μ).

7.3 Scaling laws in the μ-$v_{\parallel}$ plane

In Section 6.8.2, it was already discussed how the scaling laws change if one parameterizes the energy and the direction of the particles relative to the magnetic field with μ and $v_{\parallel}$, or $E_{\perp}$ and $E_{\parallel}$, respectively. The transformations are given by Eq. (6.23). Replacing the parameters in Eqs. (7.4) and (7.5), we obtain modified scaling laws which are sketched in Fig. 7.2. Additionally, the figure also distinguishes large and small gyroradii for both trapped and passing ions. The complete scaling laws, including all four cases (trapped/passing and small/large gyroradius) are given in Appendix B, Eqs. (B.8) to (B.11). Following $\eta = const$ curves, the scaling laws of Eqs. (7.4) and (7.5) can be observed in the figure. However, a selective input of energy in either the perpendicular or the parallel component leads to different scalings, as we already have seen in Fig. 6.7. For example, a selective input of energy in the parallel direction can lead to an increase of diffusivity in the small pitch angle regime. This is a somewhat peripheral but interesting result.

7.4 Summary and conclusions

Applying the same analytic scaling approach to the transport of fast particles in perturbed magnetic fields in a tokamak as we did to the electrostatic transport in the previous chapter, we found that for beam ions with large pitch angles, the transport is independent of the particle energy, even for very high energies. For trapped ions with a large perpendicular component, we found a rather small reduction of transport with the particle energy, which is $\propto E^{-1/2}$. For arbitrary pitch angles and gyroradii, modified scaling laws have been derived. The relevance of the present results concerning the explanation of recent experimental findings is discussed further in Chapter 8.

Chapter 8

Simulation Results with GENE and Relevance of the Results for Fusion Experiments

Simulation results with the GENE code are presented for passing and trapped particles in electrostatic as well as magnetic turbulence. For this purpose, fast test particles were added as a third passive species. The scaling laws found in Chapters 6 and 7 are confirmed in the E-η plane as well as in the μ-$v_{\|}$ plane. Furthermore, the influence of the now well-confirmed scaling laws on the overall transport in a tokamak is studied, and the ability to explain recent surprising experimental results in ASDEX Upgrade is discussed. This chapter contains some results published in (Hauff *et al.*, 2009).

8.1 Simulation results with the GENE code

In Chapter 6, an analytical model for the scaling of the diffusion coefficient with the particle energy has been developed and confirmed in simulations with the GOURDON code, where artificially produced electrostatic potentials were mapped onto the torus geometry. In Chapter 7, the same model was applied to magnetic turbulence, and modified scaling laws have been found.

In order to test these analytical predictions, we present electromagnetic simulations with the gyrokinetic turbulence code GENE in this section. Here, the particles are put into realistic electrostatic and magnetic turbulent fields, which means that some simplifications of the previous chapters, e.g. the idealized z dependence or the simplified spectrum coming from the self-created stochastic potentials, are not used anymore. For that reason, the GENE simulations may be regarded as the (numerical) test of our model under realistic conditions. They have been performed by Moritz Püschel (IPP Garching), and the data was provided to the author for post-processing.

First efforts to use GENE for fast particle simulations have already been presented by Tilman Dannert (Dannert *et al.*, 2008) for beam ions in electrostatic turbulence. In this context, a first curve for magnetic transport of beam ions has been produced (but was not published), which inspired the work pre-

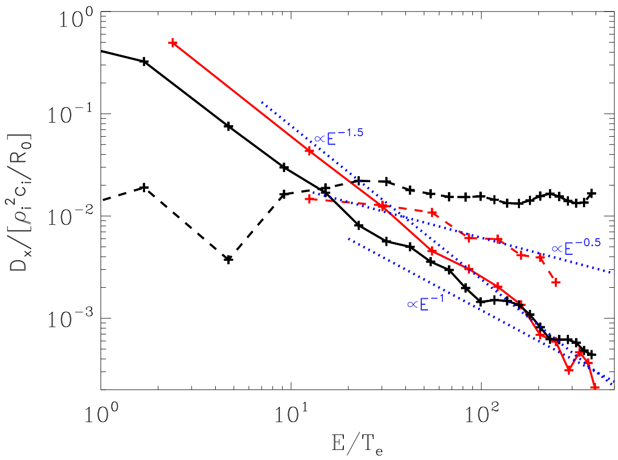

Figure 8.1: Electrostatic (solid lines) and magnetic (dashed lines) particle diffusivities of fast ions for large (black lines) and small (red lines) pitch angles as obtained from GENE simulations. The results agree well with the theoretical expectations (Eqs. (6.18), (6.22), (7.4), and (7.5)) which are shown for comparison.

sented here. For simplicity, our present simulations have been performed in a local flux-tube environment with $\hat{s}$-α geometry (circular flux surfaces). This is a common approximation, and recent numerical investigations show that the resulting turbulence characteristics exhibit moderate quantitative, but no qualitative differences compared to simulations in more realistic geometries (see comments in Section 6.2). We were employing Cyclone Base Case parameters (Dimits *et al.*, 2000) and $\beta/\beta_{\mathrm{crit}} = 0.6$ (as in the simulations presented in Ref. (Pueschel *et al.*, 2008)). Here, we have added an additional passive particle species. Since gyrokinetic δf codes require an equilibrium particle distribution function, we employ an isotropic Maxwellian with $T/T_e = 50$ for the fast ion species. During the saturated turbulent phase, the energy dependent particle transport was written out on a $v_\parallel$-μ grid. The results – normalized with respect to the equilibrium distribution at the respective position in velocity space and interpolated for constant pitch angles – are shown in Fig. 8.1. They are found to be in very good agreement with the previous theoretical considerations. In particular, the magnetic transport is independent of the particle energy for larger energies, and at a level reasonably close to the one predicted by Eq. (7.4). Since the theoretical models and predictions of the previous chapters are not only summarized, but confirmed by simulations based on much more complete models, Fig. 8.1 represents a central result of this thesis. These curves prove that the test particle model based on decorrelation effects is indeed able to explain the observed scaling laws.

For further comparison with our analytical results, plots of the diffusion coefficient in the $E_\perp$-$E_\parallel$ plane are presented in Fig. 8.2 for electrostatic transport. The scaling of D can be compared directly to the theoretical approach constructed in Fig. 6.7, which was based on the scaling laws obtained in Chapter 6, or on the more complete laws given in Appendix B, respectively. In Fig. 8.2,

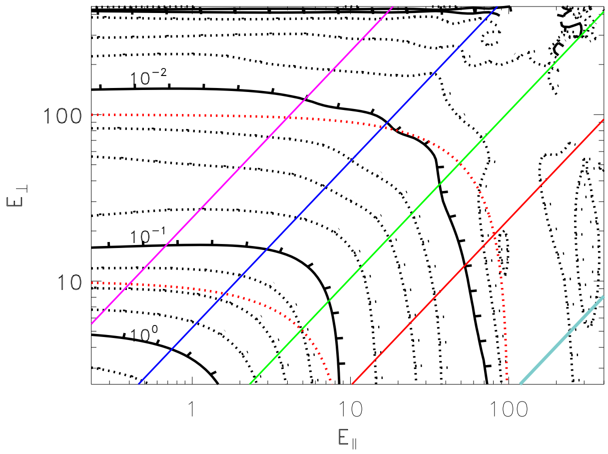

Figure 8.2: Diffusion coefficient in the $E_\parallel$-$E_\perp$ plane for electrostatic transport as obtained from the GENE simulations. The black lines denote equipotential lines of the diffusion coefficient; the solid lines are separated by a factor of 10, the dotted lines by a factor of $10^{1/4} \approx 1.78$. The red dotted lines denote $E \equiv 10$ and $E \equiv 100$. The colored solid lines denote curves of constant pitch angle. *Violet*: $\eta = 0.2$ (trapped). *Blue*: $\eta = 0.4$ (trapped). *Green*: $\eta = 0.7$ (passing). *Red*: $\eta = 0.9$ (passing). *Cyan*: $\eta = 0.99$ (passing).

the E^{-1} decrease for large pitch angles and the $E^{-3/2}$ decrease for small pitch angles can roughly be observed on the $\eta = const$ curves. Moreover, it can be seen that for beam ions with large η, there is practically no dependence of D on $E_\perp$ for small $E_\perp$, and only a weak dependence for large $E_\perp$, as predicted by Eqs. (B.4) and (B.5). Only for small total energies, the predicted scaling laws are not reproduced, e.g., the decline of D with E seems to be much faster than predicted. However, this can clearly be attributed to the fact that orbit averaging is valid in this case (see discussion concerning Fig. 6.4), and therefore the scaling laws do not apply.

In Fig. 8.3, the diffusion coefficient in the $E_\perp$-$E_\parallel$ plane is plotted for magnetic transport. It confirms the scaling draft given in Fig. 7.2, which was based on the approaches in Chapter 7 or, in a more complete way, in Appendix B. Again, a good agreement can be observed. In particular, the constancy of D for large pitch angles is clearly visible, as well as the rather flat $E^{-1/2}$ decrease for small pitch angles and large energies. Furthermore, for trapped particles with large $E_\perp$, an increase of D with increasing $E_\parallel$ can be observed which appears to be even stronger than predicted. For small total energies, we expect orbit averaging to be valid, so that the scaling laws do not apply.

8.2 Overall transport coefficients

Up to now, for electrostatic as well as for magnetic transport, we have treated the diffusion coefficients depending on the particle's energy and pitch angle, $D(E, \eta)$ (or $D(E_\parallel, E_\perp)$). If one aims to understand the transport behavior and

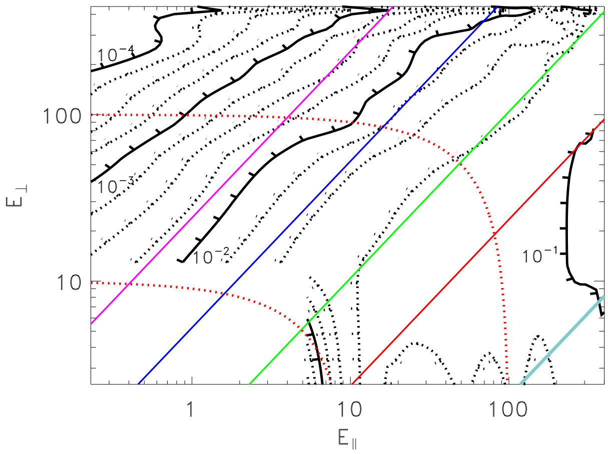

Figure 8.3: Same as Fig. 8.2, but for magnetic transport.

the underlying mechanisms, this is the only feasible method. However, if one looks at the problem from the experimental perspective, it is the overall transport that is of interest since only this quantity is accessible in measurements in a tokamak.

The overall transport coefficients resulting from the derived scalings of the energetic ion diffusivities are treated next, focusing on beam ions. In order to calculate them from our expressions, it is necessary to know the concrete fast particle distribution function. Such a distribution function evolves since fast particles are normally created or inserted at a certain energy, and are then ‘slowed down’ by collisions with other, mainly thermal particles. For example, alpha particles are created at 3.5 MeV, whereas beam ions in ASDEX Upgrade are inserted at energies of about 90 keV (and up to 1 MeV in ITER). The distribution which emerges is the so-called *slowing down distribution*, which can be expressed as (Gaffey, 1976)

$$F_s(v) = \frac{S_0 \tau_s}{4\pi} \frac{H(v_b - v)}{v_c^3 + v^3} \tag{8.1}$$

by solving the Fokker-Planck equation with a delta-function source and assuming isotropy. Here, S_0 is the fast particle source intensity, τ_s is the *slowing down time* (the characteristic collision time, see (Gaffey, 1976) for a definition), v_b is the fast particle birth speed, v_c the *crossover velocity*, which is also defined in Ref. (Gaffey, 1976), and H is the well-known *Heaviside function*. Since $v_c \ll v_b$, the slowing down distribution can be approximated by $F_s(E) \propto E^{-3/2} H(E_b - E)$ for energetic particles (in this case, E_b is the *birth energy*).

So for the overall fluxes of particles (Γ_p), momentum (Γ_m), and energy (Γ_E), the following expressions hold:

$$\begin{aligned}\Gamma_p &\propto \int D(E)\,F_s(E)\,E^{1/2}\,dE \\ \Gamma_m &\propto \int D(E)\,F_s(E)\,E\,dE \\ \Gamma_E &\propto \int D(E)\,F_s(E)\,E^{3/2}\,dE\,.\end{aligned} \tag{8.2}$$

Here, the relation $d\mathbf{v} \propto v^2 dv \propto E^{1/2}dE$ was used. Inserting the high energy approach for $F_s(E)$ together with $D(E) \propto 1/E$ for the electrostatic transport of beam ions, we obtain

$$\begin{aligned}\Gamma_p^{\text{el.stat.}} &\propto -(E_b/T_e)^{-1} + (E_0/T_e)^{-1} \\ \Gamma_m^{\text{el.stat.}} &\propto -(E_b/T_e)^{-0.5} + (E_0/T_e)^{-0.5} \\ \Gamma_E^{\text{el.stat.}} &\propto \ln(E_b/T_e) - \ln(E_0/T_e) = \ln(E_b/E_0)\end{aligned} \tag{8.3}$$

as corrections due to the $1/E$ tail. E_b is the beam energy, T_e the thermal (electron) background temperature, and E_0 is an arbitrary energy with $T_e < E_0 < E_b$, which shall give a lower limit for the fast particles and the applicability of the slowing down distribution, distinguishing them from the thermal ones. This is the case since for $E \sim T_e$, the particles thermalize and rather obey a Maxwellian distribution. We observe from Eqs. (8.3) that, although we have shown in Chapter 6 that the $1/E$ decrease is much slower than assumed or expected in the past, its contribution to the overall particle or momentum fluxes is still fairly small. However, the electrostatic heat flux corrections scale with $\ln(E_b/T_e)$ and therefore constitute a potentially significant influence.

For the magnetic fluxes of beam ions, we insert $D(E) = const$ into Eqs. (8.2) and obtain

$$\begin{aligned}\Gamma_p^{\text{mag.}} &\propto \ln(E_b/T_e) - \ln(E_0/T_e) = \ln(E_b/E_0) \\ \Gamma_m^{\text{mag.}} &\propto \sqrt{E_b/T_e} - \sqrt{E_0/T_e} \\ \Gamma_E^{\text{mag.}} &\propto E_b/T_e - E_0/T_e\,.\end{aligned} \tag{8.4}$$

This means that for magnetic transport, already the particle transport may be influenced significantly by the turbulence, whereas for the heat transport, the influence of fast particles is quite strong and absolutely dominates the transport. However, we have to keep in mind that the prefactors of $D(E)$ are different for electrostatic and magnetic transport. Whereas in the former case, we found $D(E) \approx 8(E/T_e)^{-1}\,\rho_i^2 c_i/R_0$, we obtained $D(E) \approx 0.1\,\rho_i^2 c_i/R_0$ in the latter case, which is a difference of almost two orders of magnitude. In Fig. 8.4, the flux proportionalities of Eqs. (8.3) and (8.4) are weighted with these prefactors, and $E_0/T_e = 5$ is chosen. As can be seen, although the magnetic total fluxes grow faster with energy than the electrostatic ones, the former exceed the latter only for very large particle energies. In a future burning plasma, one can expect $T_e \sim 10\,\text{keV}$, which means that the relative energy of alpha particles is $E_\alpha/T_e \sim 350$. For these energies, the magnetic energy flux may become comparable to the

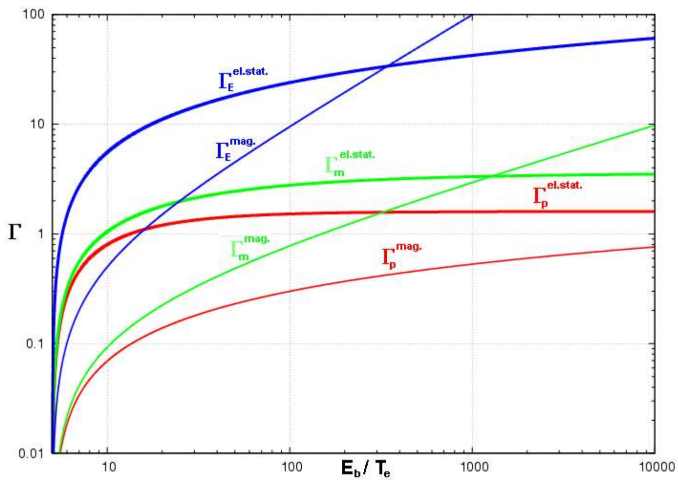

Figure 8.4: Electrostatic and magnetic fluxes of particles, momentum, and energy according to Eqs. (8.3) and (8.4), weighted with the prefactors 8 and 0.1, respectively.

electrostatic one. It is important to note that the choice of E_0/T_e is arbitrary in Fig. 8.4. The relative strength of the magnetic fluxes grows if E_0/T_e is increased.

8.3 Relevance for experimental findings

The discovery of a regime of constant particle transport independent of the particle energy is possibly of great relevance for the explanation of recent experimental findings on ASDEX Upgrade. In (Günter *et al.*, 2007) a fast radial broadening of the plasma current profile driven by off-axis neutral beam injection has been observed. This was attributed to turbulent transport, since no measurable magnetohydrodynamic activity was present. Such a behavior of the beam driven plasma current is of relevance for a future burning plasma, since it is the goal to complement the inductive current drive (see Chapter 1) by a beam ion drive. If the observed behavior carries over to ITER, it could confound this intention. Therefore, an understanding of the mechanism is of great importance. In order to describe the fast broadening of the neutral beam driven current phenomenologically, the ad hoc assumption of a transport coefficient independent of the particle energy was introduced. In (Günter *et al.*, 2007), a diffusion coefficient of $D \equiv 0.5\,\mathrm{m}^2/\mathrm{s}$ was found to describe the observed phenomena. There, simulations were done with the TRANSP code (Pankin *et al.*, 2004) in order to model the beam current distribution. To compare the results of this thesis with the experimental findings, the graphs of Fig. 8.5 where produced by Giovanni Tardini (IPP Garching) using the TRANSP code in the same way as in the forementioned publication, but with different inputs for $D(E)$. The curve with $D \equiv 0.5\,\mathrm{m}^2/\mathrm{s}$ is the one which fits the experimental data best. How does this compare to our results? The diffusion coefficients derived in Chapters 6 and 7 were normalized to $\rho_s^2 c_s/R_0 = m_i^{1/2} T_e^{3/2}/(e^2 B^2 R_0)$.

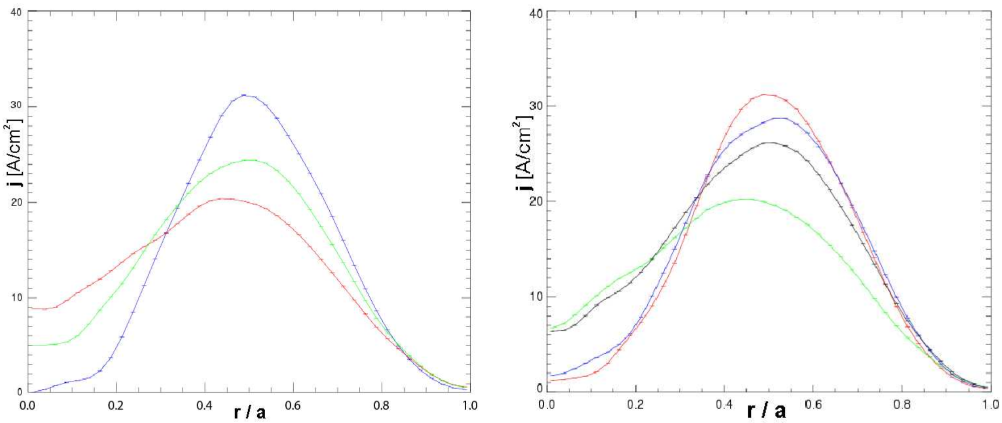

Figure 8.5: Current profiles for an off-axis beam in ASDEX Upgrade simulated with the Transp code. *Left*: Blue: No fast particle diffusion. Green: $D \equiv 0.2\,\mathrm{m}^2/\mathrm{s}$. Red: $D \equiv 0.5\,\mathrm{m}^2/\mathrm{s}$. *Right*: Red: No fast particle diffusion. Blue: $D(E) = (E/T_e)^{-1}\,\mathrm{m}^2/\mathrm{s}$. Black: $D(E) = 5(E/T_e)^{-1}\,\mathrm{m}^2/\mathrm{s}$. Green: $D \equiv 0.5\,\mathrm{m}^2/\mathrm{s}$.

For the values used in Ref. (Günter *et al.*, 2007) – $R_0 = 1.65\,\mathrm{m}$, $B = 2.5\,\mathrm{T}$, $T_e \approx 1.5\,\mathrm{keV}$ – we get $\rho_s^2 c_s/R_0 \approx 0.81\,\mathrm{m}^2/\mathrm{s}$. The pitch angle of the beam was $\eta = 0.78$ (Günter, 2009). Thus, applied to ASDEX, our scaling laws derived in Chapters 6 and 7 give $D(E) \approx 12.0(E/T_e)^{-1}\,\mathrm{m}^2/\mathrm{s}$ for electrostatic transport (Eq. (6.18)) and $D(E) \approx 0.17\,\mathrm{m}^2/\mathrm{s}$ for magnetic transport (Eq. (7.4)). Compared to Fig. 8.5, the results of both approaches seem slightly too small to be able to fully explain the experimental results. Now, whereas the results for the electrostatic transport seem to be quite well established (the parameters $\hat{V}_E$ and $\hat{\lambda}_V$ in Eq. (6.18) are fairly universal), we have already emphasized that this is not the case for magnetic transport. In Eq. (7.4), especially the parameter C has been determined only for a relatively small number of Gene runs and cannot be regarded as universal. For the plasma beta, however, $\beta/\beta_{\mathrm{crit}} \approx 0.6$ can be estimated to be a realistic value for the ASDEX discharge (Günter *et al.*, 2007), so that our previous assumption appears to be justified. However, due to the quadratic dependence of the diffusion coefficient on both the prefactor and the plasma beta, already slight modifications may lead to a significant increase. The same is true for an adjustment of the electron temperature, to which values like λ_B are normalized. Rewriting Eq. (7.4) for ASDEX Upgrade machine sizes and the established value for $\tilde{\lambda}_B$, we obtain

$$D_B \approx 0.44 \times C^2 \left(\frac{\beta}{\beta_{\mathrm{crit}}}\right)^2 (T_e[\mathrm{keV}])^{3/2} \tag{8.5}$$

for the magnetic particle diffusivity in ASDEX Upgrade. Now, in Fig. 8.6, the measured profile of the electron temperature (Günter *et al.*, 2007) is plotted. It increases towards the magnetic axis since the off-axis injection is accompanied by central ECRH (electron cyclotron resonance heating). Although the electron temperature is $T_e \approx 1.5\,\mathrm{keV}$ at the position of the beam, it can be seen in Fig. 8.5 that the most significant deviations of the current profiles with diffusion from

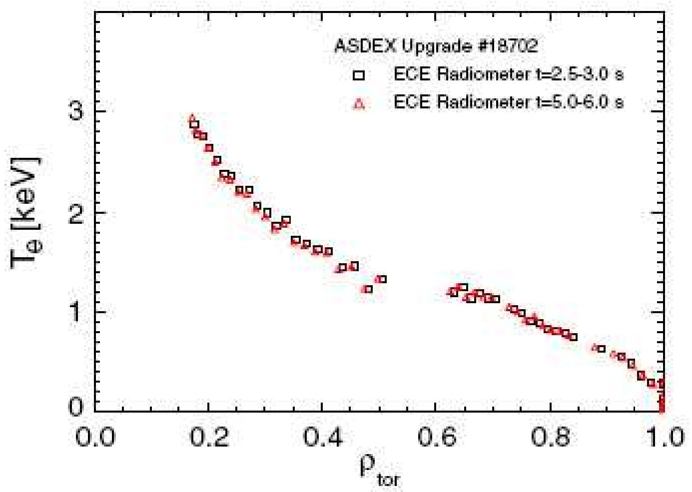

Figure 8.6: Electron temperature profiles for on- and off-axis beam deposition in the ASDEX Upgrade discharge (Günter *et al.*, 2007). $\rho_{\mathrm{tor}} = r/a$.

the non-diffusive one occur towards the magnetic axis, i.e., between $r/a = 0$ and $r/a = 0.2$. There, however, we find $T_e \geq 3\,\mathrm{keV}$. If we keep $C = 0.76$ and $\beta/\beta_{\mathrm{crit}} = 0.6$ in Eq. (8.5) and adjust T_e, we find $D_M = 0.48\,\mathrm{m}^2/\mathrm{s}$, which is more or less the value which was claimed to fit best assuming dominant magnetic transport. In general, even larger values are possible, since the upper limit for beta is $\beta/\beta_{\mathrm{crit}} = 1$. So, although there are some uncertainties about the exact values of C and $\beta/\beta_{\mathrm{crit}}$ as well as on the point where the electron temperature should be measured, it could be shown that the desired value can be reached with our model.

The diffusion coefficient can also be expressed via $\tilde{B}_r/B_0 = C(\beta/\beta_{\mathrm{crit}})\rho_s/R_0$. This way, we can rewrite Eq. (8.5) for the ASDEX parameters:

$$D_B \approx 6.5 \times 10^5 \left(\tilde{B}_r/B_0\right)^2 (T_e[\mathrm{keV}])^{1/2}\,. \tag{8.6}$$

This means that for $T_e = 1.5\,\mathrm{keV}$, a value of $\tilde{B}_r/B_0 = 7.9 \times 10^{-4}$ would be necessary to retain the assumed value of $D = 0.5\,\mathrm{m}^2/\mathrm{s}$, whereas under the assumption of $T_e = 3\,\mathrm{keV}$, a somewhat lower value of $\tilde{B}_r/B_0 = 6.7 \times 10^{-4}$ would be sufficient. Both of these values are rather large. However, values $\tilde{B}_r/B_0 \lesssim 10^{-3}$ have been found in the literature (Entrop *et al.*, 1998; Entrop *et al.*, 2000) and are also expected to be possible for ASDEX Upgrade (Günter, 2009).

Although we have just demonstrated that magnetic transport is in principle able to explain the radial beam broadening found in the experiment, the possibility of a significant electrostatic contribution should still be considered, even though the required level is not known precisely. If we insert the ASDEX parameters (including $\eta = 0.78$) into Eq. (6.18) and use the dimensionless values for $\hat{V}_E$ and $\hat{\lambda}_V$ found in Chapter 6, we obtain

$$D_E \approx 6.5\,(\frac{E}{T_e})^{-1}\,(T_e[\mathrm{keV}])^{3/2}\,. \tag{8.7}$$

With $T_e = 3\,\mathrm{keV}$, this is $D_E \approx 34(E/T_e)^{-1}$. Although such a high prefactor was not simulated with TRANSP, we can extrapolate from Fig. 8.5 that electrostatic transport on this level may probably also be able to explain the experimental observations. However, since in (Günter *et al.*, 2007) only a diffusivity independent of the particle energy has been used for comparison with the measurements, a final answer has to be left to future investigations. It is possible that eventually both magnetic and electrostatic transport will turn out to have significant contributions to the radial beam broadening.

The discussion of Eqs. (8.5) and (8.6) has shown that magnetic transport as introduced in Chapter 7 is a suitable candidate to explain the reported ASDEX Upgrade results, possibly in conjunction with electrostatic transport. If this suspicion turns out to be true, it will have a serious impact on the ITER project, unfortunately not in a positive way, since a well confined beam is needed for an economic current drive which is thought to be a necessary condition for a continuous operation. In order to get more clarity in this matter, a more exact determination of the critical values is still in progress, including a closer collaboration with the experimental side.

8.4 Summary and conclusions

To summarize, self-consistent gyrokinetic simulations were performed with the GENE code, where fast particles were added as a third species. The results support the scaling laws derived in Chapters 6 and 7 and confirm that the test particle model underlying this work is indeed able to describe the diffusion coefficients of fast particles correctly. Moreover, it became clear that the thorough understanding of the underlying processes was possible by reducing the complexity of the transport problem in the way presented here. To allow for a comparison of the scaling laws with experimental observations, their influence on the overall transport of particles, momentum, and energy was studied. It was shown that it is foremost the magnetic energy transport which is influenced significantly by the contributions of fast particles, since it scales linearly with the beam energy. For the magnetic momentum flux and the electrostatic energy flux, the fast particles influence the overall transport moderately, whereas for the electrostatic particle transport, the $1/E$ decrease is too strong for fast particles to constitute a significant influence.

Moreover, the results of the models developed in this thesis were compared with recent experimental measurements on ASDEX Upgrade in Garching. Surprisingly, a fast broadening of the beam ion current was observed to which a rather large constant diffusion coefficient $D(E) = 0.5\,\mathrm{m}^2/\mathrm{s}$ could be fitted. It was shown that this value can be reproduced with the model for magnetic transport. Due to the quadratic dependence on values like C and $\beta/\beta_{\mathrm{crit}}$ which are not definitely established yet, a final answer to the question whether the turbulent magnetic diffusion is responsible for the observed behavior cannot be given at this point. It may have a serious impact on the future fusion project ITER, where neutral beam injection is expected to play a prominent role in the toroidal current drive.

Chapter 9

Advection of Thermal Electrons in 3D Electrostatic Turbulence

In Chapters 6 to 8 the transport of fast particles was studied based on orbit decorrelation. However, this procedure does not apply to thermal particles, which are situated in a regime where orbit averaging is not valid, but at the same time the orbits are too small to support perpendicular decorrelation. In the present chapter an alternative decorrelation process for thermal electrons in electron temperature gradient (ETG) turbulence is studied, and the question if and how streamers (i.e., radially elongated vortices) can lead to an enhancement of the cross-field transport is addressed. A substantial increase of transport is found in a wide region of parameter space; however, the enhancement is reduced compared to the 2D case described in Chapter 4. The results of this chapter have been published in (Hauff & Jenko, 2009b).

9.1 Introductory remarks

In Section 6.4.2, the question how particles are advected if on one hand orbit averaging is invalid, but on the other hand $\Delta r < \lambda_c$, was only raised briefly and was left to a more complete discussion in the present chapter. In this case, the particles do not follow the equipotential lines strictly anymore, as assumed in the discussion in Chapter 4. However, an instantaneous decorrelation due to the orbit motion is also not possible, since the orbit diameter is too small. Here, we want to deal with the transport of thermal electrons in ETG turbulence and the question, whether streamers (radially elongated vortices) lead to an increase of transport (as shown for two dimensions in Sec. 4.3) or not. Since the mechanism described in Sec. 4.3 is valid only in the case that the particles follow equipotential lines for a time larger than the 'flight time' τ_{fl}, the questions of orbit averaging and the influence of streamers are closely linked. We note in passing that since electrons are treated in this chapter, quantities are normalized to the electron gyroradius or the electron thermal velocity. However, the mechanisms described here apply to ions in the same way, of course, provided that the normalized quantities are comparable.

It is well known by now that microturbulence in toroidal magnetized plasmas often tends to form anisotropic structures like zonal flows or streamers. The former are the $E \times B$ flows resulting from purely radial variations of the electrostatic potential (for a review, see Ref. (Diamond *et al.*, 2005)), whereas the latter are radially elongated vortices, generally localized at the outboard side and pointing away from the torus axis (see, e.g., Refs. (Drake *et al.*, 1988; Cowley *et al.*, 1991; Jenko *et al.*, 2000)). Due to their fundamentally different character, a coexistence of both types of structures can be excluded; rather, one (or none) of them will dominate. However, in both cases, it can be expected that the presence of the structures may have a significant impact on the resulting turbulent transport. While in the case of zonal flows, it is widely accepted that the cross-field transport is reduced or even quenched (see the discussion and references in Sec. 4.4), there are only few dedicated investigations concerning the streamer case. It is thus the main goal of the present chapter to address the key issue in this context, namely: To which degree and in which way will the presence of streamers enhance the radial turbulent transport? To this aim, we will systematically study the behavior of passive tracers advected in turbulent electrostatic potentials exhibiting streamers.

This question was raised, in particular, by gyrokinetic simulations which showed that the transport levels in electron temperature gradient (ETG) turbulence can clearly exceed naive mixing length expectations, $\chi_e \gg \rho_e^2 v_e / L_{T_e}$ (Jenko *et al.*, 2000; Dorland *et al.*, 2000; Jenko & Dorland, 2002). Here, χ_e is the electron heat diffusivity, ρ_e is the electron thermal gyroradius, v_e is the electron thermal velocity, and L_{T_e} is a characteristic scale length of the electron temperature profile. For Cyclone Base Case parameters (Dimits *et al.*, 2000), neglecting magnetic electron trapping as well as kinetic ion effects, $\chi_e > 10\,\rho_e^2 v_e / L_{T_e}$ was obtained in these studies. More recently, taking magnetic trapping into account, it was found that the simulations can reach very high transport levels, generally even failing to saturate (see, e.g., Refs. (Idomura, 2006; Bottino *et al.*, 2007; Candy *et al.*, 2007)). Therefore, in the context of a careful comparison between five different gyrokinetic codes, the magnetic shear value was reduced from 0.8 to 0.1 in order to circumvent these problems (Nevins *et al.*, 2006; Nevins *et al.*, 2007). Here, it was found that $\chi_e > 5\,\rho_e^2 v_e / L_{T_e}$ in well-resolved runs for a given box size, and all codes agreed with each other within fairly narrow margins. Finally, recent gyrokinetic simulations including both ion and electron space-time scales self-consistently (but working with a reduced ion-to-electron mass ratio of 400) confirmed these findings in the framework of a more complete and realistic physical setting (Görler & Jenko, 2008). In particular, if ion temperature gradient (ITG) modes are sufficiently close to marginality (as they will be in any experiment) or even stable (as they are in certain dedicated experiments with strong electron heating), one again finds $\chi_e \gg \rho_e^2 v_e / L_{T_e}$. The common feature in all of these simulations is the existence of streamers and relatively weak zonal flow activity. (We note in passing that another such example is trapped electron mode turbulence in the cold ion regime (Dannert & Jenko, 2005; Lang *et al.*, 2007).)

On general grounds, it is reasonable to expect an enhancement of the turbulent transport in the presence of streamers. First, the very existence of streamers is an indicator of the relative weakness of zonal flows, thus allowing for potentially larger fluxes. Second, according to the common notion that in the saturated state, the radial gradients of the background temperature and the temperature fluctuations should be similar (on average), the amplitude of radially elongated streamers should exceed those of isotropic vortices with the same poloidal extension, increasing the resulting transport level. And third, even if the amplitude of the vortices is kept constant, a radial elongation can raise the cross-field diffusivity due to the larger radial correlation length. The latter effect has already been investigated in detail in Sec. 4.3 for particles in two dimensions, and shall be reinvestigated including finite orbit effects as well as parallel effects in the present chapter, establishing a closer link between turbulent structures and corresponding transport levels. To this aim, we will employ the passive tracer description which allows for a simpler, more accessible, and more rigorous treatment of the questions under consideration.

The remainder of this chapter is organized as follows. In Section 9.2, a brief review of pure orbit center motion in anisotropic turbulence is given, and the impact of the invalidity of orbit averaging on the transport of suprathermal particles is reviewed. In Section 9.3, the diffusive motion of thermal test particles is studied in detail, and the consequences of the invalidity of orbit averaging for the decorrelation mechanisms of these particles are examined by means of a simplified model. In Section 9.4, the scaling of the diffusion coefficient with the turbulence amplitude and correlation length is studied for ETG turbulence. Finally, in Section 9.5 we provide a summary along with some conclusions.

9.2 Transport scaling for particle orbit centers and suprathermal particles

At the beginning, we would like to restrict to pure $E\times B$ motion in two dimensions – various generalizations will follow later. In Section 2.6.1, the influence of turbulent structures in an isotropic 2D potential has already been explained in terms of the Kubo number K. As can be inferred from Eq. (2.68), the spatial structure of a turbulent field is only relevant for $\gamma < 2$, i.e., for $K \gtrsim 1$.

In Chapter 4, it was shown that anisotropic structures (like streamers) can be described in a similar way by using λ_x and V_x for the diffusivity in the x direction and λ_y and V_y for the diffusivity in the y direction in Eq. (2.68). Defining an anisotropy factor $\zeta \equiv \lambda_x/\lambda_I$ (the index I denotes the isotropic value), one therefore finds $D_x \propto \zeta^{2-\gamma}$ if λ_y is kept unchanged. This means that in the large Kubo number regime, anisotropic structures enhance the tracer transport. Since realistic Kubo numbers are found (in nonlinear gyrokinetic simulations) to lie between about 1 and 10 (corresponding to γ values somewhere between 0.7 and 1), this effect is relevant if no faster decorrelation mechanism exists (as is the case in two dimensions).

In Section 4.5, the influence of a homogeneous background drift of the turbulence on the transport was also a subject of study. It was shown that a potential drift with velocity v_{dr} in the y direction leads to a strong suppression of transport at a characteristic 'drop time' $\tau_{\text{drop}} \equiv 2\lambda_y/v_{\text{dr}}$. This effect is important for $\tau_{\text{drop}} \lesssim \tau_c$, whereas it has no influence for $\tau_{\text{drop}} \gg \tau_c$. Typically, one finds $\tau_{\text{fl}} < \tau_{\text{drop}} \lesssim \tau_c$, which implies a moderate decrease of the diffusion coefficient compared to a non-drifting case.

In the respective discussion, the only relevant decorrelation mechanism was the time dependence of the electrostatic potential. However, decorrelation may also be caused by the parallel motion of the particles along the magnetic field lines or, if orbit averaging is not valid, by the orbit motion perpendicular to the magnetic field lines. If we denote the respective effective decorrelation time by τ^{eff}, and one has $\tau^{\text{eff}} < \tau_c$, τ_c is to be replaced by τ^{eff} in the preceding discussion to obtain the correct scaling behavior of the diffusion coefficient.

In Eq. (6.12), the parameter $\Xi_{\text{o.a.}}$ was introduced in order to describe the validity of orbit averaging. Following this finding, energetic particles with $E \gg T_{i,e}$ were discussed. Their orbit diameter Δr is much larger than the correlation length of the potential, for both trapped and passing particles. Therefore the particle decorrelates already after a time $\tau^{\text{orbit}} = \lambda_c/v_{\text{orbit}} = \lambda_c T_{\text{orbit}}/(\pi\Delta r)$. Since $\tau^{\text{orbit}} \equiv \tau^{\text{eff}} < \tau_{\text{fl}}$, the particles are in the ballistic regime when they decorrelate, and the diffusion coefficient can therefore be approximated by $D \approx V^2\tau^{\text{orbit}} \propto V^2\lambda_c$. This expression cannot be associated with an exponent γ in the context of Eq. (2.68). Moreover, although the transport in that regime depends on the turbulence correlation length λ_c, it is not affected by structural anisotropies, because the particles do not follow equipotential lines. Instead, they decorrelate due to the orbit motion, which is governed by the smallest correlation length. For radial streamers, this means that only λ_y contributes to D, but not λ_x. Furthermore, it was found that for suprathermal particles, the orbit decorrelation time is smaller than the parallel one ($\tau^{\text{orbit}} < \tau_\parallel$). Hence, the parallel motion was ignorable. In the following sections, we will study to which degree the findings for energetic particles on one hand and for pure $E\times B$ motion in two dimensions on the other hand carry over to thermal particles in a tokamak, namely electrons in ETG turbulence.

9.3 Basic studies of thermal particles in ETG-like turbulence

In order to get an idea of a reasonable choice of various quantities mentioned above, we have performed nonlinear gyrokinetic simulations (in the local limit) of ETG turbulence with kinetic ions for Cyclone Base Case parameters, employing the GENE code. These simulations were done by Tobias Görler (IPP Garching). This way, we found

$$\begin{aligned} \sqrt{\langle\phi^2\rangle} \approx 60\,(\rho_e/R_0)\,(T_e/e), \quad \tau_c \approx 12\,R_0/v_e \\ \lambda_x \approx 23\,\rho_e, \quad \lambda_y \approx 7.0\,\rho_e \\ V_{x,0} \approx 12\,\rho_e v_e/R_0, \quad V_{y,0} \approx 7.5\,\rho_e v_e/R_0 \\ v_{\text{dr}} \approx 2.2\,\rho_e v_e/R_0, \quad \tau_{\text{drop}} \approx 6.4\,R_0/v_e \\ \tau_{\text{fl},x} \approx 1.8\,R_0/v_e, \quad K_x \approx 7\,. \end{aligned} \tag{9.1}$$

Here, R_0 is again the major radius, and the other quantities have already been defined above, however, they are now on electron scales instead of ion scales. These numbers are in good agreement with those obtained in the framework of recent benchmarking simulations (Nevins *et al.*, 2006). Thus, they seem to represent rather typical values for the above quantities. (In global adiabatic-ion simulations of ETG turbulence (Lin *et al.*, 2007), much larger correlation lengths and times have been observed, but the difficulties of using the adiabatic-ion approximation in the presence of trapped electrons mentioned in the introduction make their interpretation hard.) Nevertheless, in the following discussions, we do not want to restrict to those values. Instead, we will study the transport of thermal electrons in ETG turbulence under rather general conditions. This procedure seems to be adequate since we will see that the transport behavior may depend on the interplay of various different time scales in a very sensitive way, rendering it impossible to claim that the transport scaling of a particular realization of ETG turbulence applies universally. In this context, we would like to note that, as before, we have used the e-folding length or time to determine the correlation parameters, since our practical experience shows that this procedure yields the most reliable results. The circulation time and orbit diameter of a thermal electron can be calculated to be $T_{\mathrm{orbit}} = 2\pi q_0 R_0/v_e \approx 9\, R_0/v_e$ and $\Delta r = 2q_0\rho_e \approx 2.8\,\rho_e$, respectively, with q_0 being the safety factor (see Sec. 2.1.5).

To gain a basic understanding of the electron dynamics under such conditions, we simulate the orbit motion of the particles relative to the field aligned coordinates by the simple 2D model of Sec. 6.4.3, which we write

$$\dot{\mathbf{x}} = \mathbf{v} - \nabla\phi \times \mathbf{e}_z\,, \quad \dot{\mathbf{v}} = \omega_{\mathrm{orbit}}\mathbf{v} \times \mathbf{e}_z \tag{9.2}$$

in dimensionless units. Eq. (9.2) describes a particle which is forced on a circular orbit with $\omega_{\mathrm{orbit}} = 2\pi/T_{\mathrm{orbit}}$, at the same time undergoing an $E \times B$ drift motion. The orbit radius is set by choosing an appropriate initial velocity of the particle. This model is very useful for general studies, since all orbit parameters can be varied independently, and the real orbit in field aligned coordinates is fitted well. Its validity has already been demonstrated via direct comparisons with simulations in tokamak geometry in Chapter 6. Of course, no parallel decorrelation effects can be observed with this model. We will include them later.

Using Eq. (6.12), one obtains $\Xi_{\mathrm{o.a.}} \approx 5$, which means that orbit averaging is not valid. Additionally, $T_{\mathrm{orbit}} \approx \tau_c$. So on one hand, the thermal electrons will not follow the equipotential lines of the (orbit averaged) vortex structures exactly. On the other hand, since $\Delta r \ll \lambda_{x,y}$, the particles are not able to significantly depart from their initial equipotential line and decorrelate during one orbit turn. What we therefore expect to happen is that the particles at least roughly follow the turbulent structures, deviating, in particular, at certain positions, e.g., at a saddle point, or at a point where the equipotential line exhibits a sharp bend.

In Fig. 9.1, an electrostatic potential with the scales of Eq. (9.1) is plotted together with trajectories of particles with thermal velocity. The drift in the

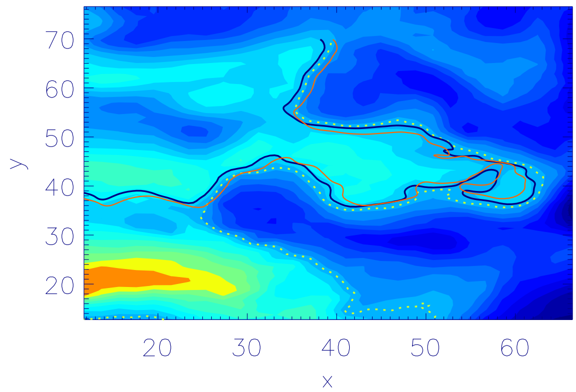

Figure 9.1: ETG-type electrostatic potential with drift in the y direction and particle trajectories, transformed into the co-moving frame (field aligned coordinates). Yellow dashed line: Pure $E\times B$ drift without orbit effects. Solid lines: $E\times B$ drift with particle orbit motion (black line: particle trajectory; red line: orbit center). The deviation from the equipotential lines at a saddle point can be observed.

y direction is kept, but the fluctuations are frozen for the purpose of a better demonstration of the interaction effects. Both the potential and the trajectories have been transformed into the co-moving frame. The potential in that frame is given by Eq. (4.7), and is a superposition of the stochastic part without y drift and a static ramp in the x direction, which acts as a transport barrier. In Fig. 9.1, a pure $E\times B$ drift trajectory without any 2D orbit effects is compared with the trajectory of a thermal particle which undergoes both $E\times B$ drift and orbit motion. As expected, this particle roughly follows the isolines of the stream function due to its small orbit diameter. However, we see that at a point where neighboring lines diverge (this seem to be saddle points coinciding with a sharp bend), the oscillating trajectory diverges from the non-oscillating one. This, in turn, means that the orbit motion of a particle weakens the barrier caused by the background drift of the potential, and defines a time scale on which the transport becomes diffusive, since the departure from the equipotential lines can be interpreted as a random process.

What is the time scale of that random process? It depends on the typical time between two random departures from the equipotential line. The distance between two of these points (saddle points or points of large curvature of the stream function) can be approximated by the extension of the structures of the potential in the co-moving frame. As can be seen in Fig. 9.1 (and was pointed out in Sec. 4.5), there are dominant structures on two scales in the x direction. The first scale is given by the correlation length λ_x (closed equipotential lines in Fig. 9.1), whereas the second scale is given by the maximal extent of the open contours in the x direction, which is $x_{\max} = 2V_x\lambda_y/v_{\mathrm{dr}}$ (Sec. 4.5). In Fig. 9.1, we have $\lambda_x \approx 23$ and $x_{\max} \approx 80$. The respective time scales are $\lambda_x/V_x = \tau_{\mathrm{fl}}$ and $x_{\max}/V_x = \tau_{\mathrm{drop}}$. For a potential with a significant drift velocity v_{dr}, the open equipotential lines are dominating the closed vortices in the co-moving frame. Therefore we will find that the larger scales, $x_{\max}$ or τ_{drop}, on the spatial or

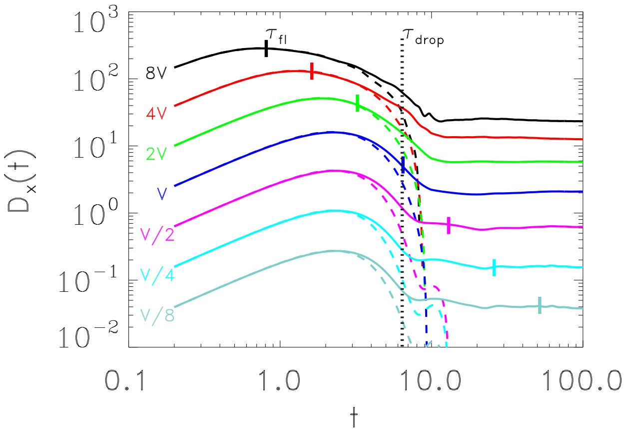

Figure 9.2: Running diffusion coefficient in an artificially created, ETG-like electrostatic potential. For the nominal amplitude V, $\tau_{\text{fl}} \equiv \tau_{\text{drop}}$. V is then varied according to the values plotted left of the curves. Dashed lines: Pure $E \times B$ drift. Solid lines: $E \times B$ drift with 2D orbit effects.

temporal scale, respectively, are dominating the decorrelation process. Here, we would like to note that while the curve in Fig. 9.1 has been chosen to illustrate our argument, the latter can be shown to be generally applicable.

In order to do that, we put a sufficiently high number of test particles into a artificially created electrostatic potential and calculate the diffusion coefficient for both the 2D orbit model of Eq. (9.2) as well as a pure $E \times B$ drift motion without any orbit effects. The electrostatic potential is created as a superposition of 10^3 plane waves, as was shown in the previous chapters, and its scales correspond to the ones of Eq. (9.1) – with two exceptions: the turbulence is frozen (but the y drift is kept), and the amplitude is reduced by a factor of 3.6. The former change is done in order to ignore temporal decorrelation effects for the moment, whereas the latter is done to enforce $\tau_{\text{fl}} = \tau_{\text{drop}}$. Moreover, no parallel dynamics effects are included.

The result is plotted in Fig. 9.2. Here, V is varied, and the actual value of τ_{fl} is indicated. We see that for the pure $E \times B$ motion, the diffusivity drops to zero at $t \sim \tau_{\text{drop}}$ for all amplitudes, since there is no decorrelation mechanism which would allow the particles to cross the barrier produced by the y drift (remember that we have switched the time dependence of the fluctuations off). For the particles on the 2D drift orbit, however, we observe that they decorrelate at $t \sim \tau_{\text{drop}}$, which leads to the saturation of the diffusion coefficient. So in that case, τ_{drop} resumes the role of τ^{eff}, and we can assume that for $\tau_{\text{fl}} \gg \tau_{\text{drop}}$ we will find $D \propto V^2$ ($\gamma = 2$), whereas for $\tau_{\text{fl}} \ll \tau_{\text{drop}}$, we will find $D \propto V^{0.7}$ ($\gamma = 0.7$), which will correspond to an effective low or high Kubo number regime, respectively. From Fig. 9.2, we read $\gamma = 2$ for $\tau_{\text{fl}} \gg \tau_{\text{drop}}$ and $\gamma \approx 0.85$ for $\tau_{\text{fl}} \ll \tau_{\text{drop}}$. This result confirms the claims we have made at the beginning of this section.

Finally, we would like to emphasize one important point. If a V^2 dependence of the transport is observed (ballistic regime), this does not necessarily mean that the particles decorrelate due to the temporal decorrelation of the fluctuations, or due to the parallel motion with a decorrelation time $\tau_{\|} \ll \tau_{\mathrm{fl}}$, as was claimed, e.g., in Ref. (Lin *et al.*, 2007). The perpendicular decorrelation at τ_{drop}, caused by deviations from the equipotential lines due to finite orbit effects at hyperbolic fix points, is able to induce the same behavior. Therefore, decorrelation will occur at $\tau^{\mathrm{eff}} = \min\left\{\tau_{\mathrm{drop}}, \tau_{\|}\right\}$. In the next section, we will examine which decorrelation time is the smaller, i.e., dominating, one.

9.4 Thermal particles in gyrokinetic ETG turbulence

We now return to the gyrokinetic ETG turbulence simulated with Gene, which produces the parameters of Eq. (9.1). In order to obtain the values of the electrostatic potential between grid points, the original data is interpolated via spectral methods, which provides the highest possible spatial accuracy. The differential equation (9.2) is solved via a fourth-order Runge-Kutta algorithm. In order to obtain the scalings of the diffusion coefficient with V_x and λ_x, the original values are modified. In the preceding section, we have discussed the consequences of a decorrelation at τ_{drop}, whereas we have ignored possible decorrelation effects due to the parallel motion of the thermal particles. While for very energetic particles, it could be shown in Chapter 6 that decorrelation due to the perpendicular motion is much faster than due to the parallel one, this is not necessarily the case for thermal particles. This is due to their smaller orbit diameter ($\Delta r < \lambda_c$), which does not bring them out of the correlated zone on a time scale smaller than the orbit time.

The time scales which can be inferred from Eq. (9.1) (and which are close to the values presented in Ref. (Nevins *et al.*, 2006)), imply that $\tau_{\mathrm{drop}} \approx 6.4\,R_0/v_e$, whereas an orbit time for passing particles with a pitch angle of unity can be calculated to be $T_{\mathrm{orbit}} = 2\pi q_0 R_0/v_e \approx 8.8\,R_0/v_e$. Our ETG simulations exhibit $\lambda_{\|} \approx 0.8\pi q_0 R_0$, meaning that $\tau_{\|} \approx 3.5\,R_0/v_e$, which is smaller than τ_{drop} and therefore dominates the decorrelation process.

We mimic the effect of parallel decorrelation by artificially reducing the correlation time of the fluctuations. For example, for passing particles, a reduction to $\tau_c = 3.5\,R_0/v_e$ has the same effect than a decorrelation due to the finite parallel extension of the turbulent structures with $\lambda_{\|} = 0.8\pi q_0 R_0$. This is allowed since for the transition from the initial ballistic regime to a later diffusive regime, it is irrelevant if the decorrelation is temporal or spatial. We have to keep in mind, though, that only the passing particles with large pitch angles are subject to this parallel decorrelation, whereas for trapped particles, the decorrelation comes from temporal or perpendicular effects. For conditions of a particle to be trapped or passing, see Sec. 2.1.5.

Fig. 9.3 (left) shows the saturated diffusion coefficient for a number of different mean drift velocities V_x. The black curve ignores parallel decorrelation effects, whereas the green curve corresponds to a realistic parallel correlation length by reducing τ_c to $3.5\,R_0/v_e$. All curves show a decline of diffusivity when the drift velocity is reduced. The black curve shows a scaling exponent γ growing with the reduction of the mean drift velocity, which can be explained by the

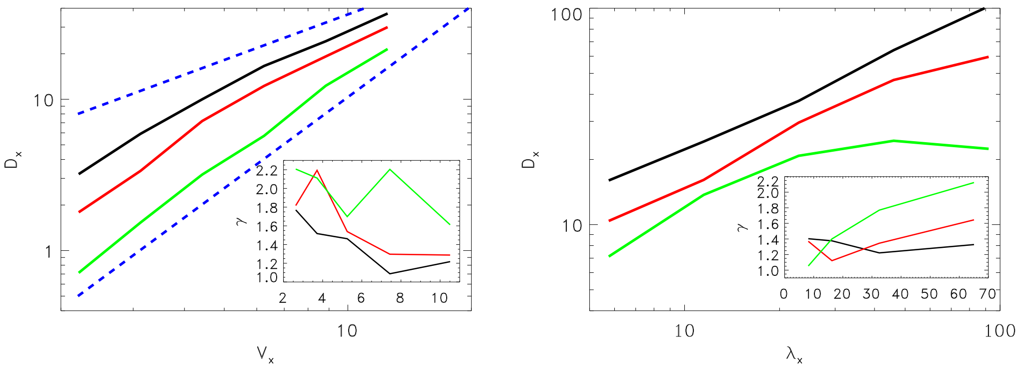

Figure 9.3: *Left*: Saturated diffusion coefficient in a gyrokinetic ETG potential, with V reduced artificially starting from the original value of $V_x = 12.5\,\rho_e v_e/R_0$. Black line: No parallel decorrelation. Red line: Mimicked parallel correlation length $\lambda_\| = 1.6\pi q_0 R_0$ using $\tau_c = 7.0\,R_0/v_e$. Green line: Mimicked parallel correlation length $\lambda_\| = 0.8\pi q_0 R_0$ using $\tau_c = 3.5\,R_0/v_e$. Blue dashed lines: Ideal scaling $D_x \propto V_x^\gamma$, with $\gamma = 1$ (upper line) and $\gamma = 2$ (lower line). Inset: Scaling exponent γ vs. V. *Right*: Same as left figure, but λ_x is varied instead of V_x, starting from the original value of $\lambda_x = 23\,\rho_e$.

fact that τ_{fl} gets larger than τ_{drop} for $V_x < 3.6$. This, in turn, means that the effective decorrelation time moves into the ballistic regime. For the green curve, the effective decorrelation time is $\tau^{\text{eff}} = \tau_\| = 3.5\,R_0/v_e$, which is smaller than τ_{drop} and therefore dominating. Hence, the transition to the ballistic regime $\gamma \to 2$ occurs already at larger V_x.

Fig. 9.3 (right) shows the saturated diffusion coefficient for a number of different radial correlation lengths, while $V_{x,0}$ stays constant. Here, we observe a transition to the ballistic regime for large anisotropy (large λ_x), which is stronger for the curves with parallel decorrelation. τ_{fl} increases with growing λ_x, which means that for large λ_x, it exceeds the effective decorrelation time. Since the latter is smaller with parallel decorrelation effects, the transition occurs earlier in that case. A consequence of that behavior is that, for the green curve (passing particles with parallel decorrelation) there is no increase of the diffusivity for very large radial correlation lengths, since the particles are effectively in the low Kubo number regime.

For the nominal parameters of our ETG simulations with GENE, we find $\gamma \sim 1.2$ for trapped particles (decorrelation at τ_{drop}), and $\gamma \sim 1.6$ for passing particles (decorrelation at $\tau_\|$), which is between the ballistic and the vortex trapping regime. This means that the presence of streamers indeed increases the transport of passive tracers. This increase is less than linear in the streamer length, however. Generally, γ is larger for passing particles with parallel decorrelation than for trapped particles, since decorrelation occurs earlier. For both trapped and passing particles, a transition to ballistic transport ($\gamma = 2$) occurs for small turbulence amplitudes or large radial vortex extension. As a rough criterion for ballistic transport (and therefore no influence of the geometric structure of the streamers), we find $\tau^{\text{eff}} = \min\left\{\tau_{\text{drop}}, \tau_\|\right\} < \tau_{\text{fl}} = \lambda_x/V_x$. This rule of thumb can serve as a first test to find out if a particular turbulence simulation is likely to exhibit streamer-induced transport enhancement or not.

9.5 Summary and conclusions

In the present chapter, we have addressed the question if and how streamers (i.e., radially elongated vortices) can lead to an enhancement of the cross-field transport of passive tracers in a realistic three dimensional environment, including finite orbits and parallel decorrelation. Here, our focus was on the dynamics of thermal electrons in the context of electron temperature gradient (ETG) turbulence, although our results may also be applied to other types of streamer-dominated turbulence, driven, e.g., by trapped electron modes.

We have shown that for thermal electrons in ETG turbulence, orbit averaging is not valid. Nevertheless, due to its small orbit diameter, a particle is not able to decorrelate after one orbit turn and therefore still roughly follows the contour lines of the electrostatic potential. We have seen that decorrelation typically occurs at hyperbolic fixed points, whose typical distance is $x_{\max} = 2V_x\lambda_y/v_{\mathrm{dr}}$. This decorrelation scale is dominated by the potential structure in the frame moving with the diamagnetic background drift of the vortices and leads to an effective decorrelation time of $\tau^{\mathrm{eff}} = \tau_{\mathrm{drop}}$. However, the decorrelation due to the finite parallel extension of the turbulent structures is typically on a smaller time scale, leading to a decorrelation at the minimum value of τ_{drop} and $\tau_{\|}$.

If this effective decorrelation time is significantly smaller than the vortex turnover time $\tau_{\mathrm{fl}} = \lambda_x/V_x$, the transport is in the ballistic regime, which means that $\gamma = 2$ and that the spatial vortex structure has no influence on the transport. This implies that there is an upper limit to the streamer-induced *geometric* transport enhancement – while there still might be an indirect, amplitude-dependent contribution. However, for the nominal turbulence parameters of our simulations (and as well as from other codes), we get $\tau_{\mathrm{fl}} < \tau^{\mathrm{eff}}$, and we find $1 < \gamma < 2$. This amounts to a significant influence of the spatial vortex structure on the transport.

Chapter 10

Runaway Electrons

In this chapter, the mechanisms found for magnetic ion transport in Chapter 7 are extended to the diffusion of runaway electrons. Due to their smaller mass and larger energy, they behave strongly relativistic, for which reason the orbit parameters and scaling laws defined previously have to be modified. We find that due to these changes, the constant magnetic transport regime does not exist anymore, but diffusivity scales with E^{-1} for magnetic transport, or even with E^{-2} in the case that finite gyroradius effects become important. It is shown that our modified analytical approaches are able to explain the surprisingly small values found in experiments, although we can not exclude that possibly other reduction mechanisms are present at the same time. The results of this chapter have been published in (Hauff & Jenko, 2009a).

10.1 Introductory remarks

Until now, we have studied the transport behavior of fast ions with energies up to the MeV range. They are created in fusion processes (alpha particles) or launched into the plasma by neutral beam injection. We applied the test particle approach, since their density is small and their velocities and orbits are clearly distinct from the bulk plasma. In this chapter, we use the mechanisms introduced in Chapters 6 and 7 in order to describe the transport behavior of so-called '*runaway electrons*'. In contrast to alpha particles or beam ions, they are created in the plasma by accident and can have a serious impact on the inner vessel wall as well as on the plasma current. Although, in principle, their orbits are similar to the suprathermal ion orbits, important differences occur. E.g., the transport is now dominated by magnetic fluctuations, and relativistic effects become dominant. Both effects are due to the much larger parallel velocities of the electrons.

The following review of the concept of a critical electric field which is responsible for the runaway generation is based on Ref. (Helander *et al.*, 2002). In a tokamak, situations can occur where large electric fields are induced. In that case, some electrons experience unlimited 'runaway' acceleration. The reason for this behavior is that the friction force $F(v)$ acting on an electron is a non-monotonic function of the particle's velocity, having a global maximum around the thermal speed $v_{\rm th}$. For electrons moving faster, the characteristic collision frequency can be derived to (Wesson, 1997)

$$\nu_e = \frac{e^4 n_e \ln \Lambda}{4\pi\epsilon_0^2 m_e^2 v^3}\,, \tag{10.1}$$

where $\Lambda \equiv \lambda_D/\lambda_L$ is the ratio of the *Debye length* and the *Landau length* of the plasma (Wesson, 1997). [The expression for ν is similar to simple collision models in solid state physics.] Therefore, the friction force is

$$F(v) \equiv m_e \nu_e v \propto v^{-2}\,, \tag{10.2}$$

which means that for a sufficiently fast electron in a sufficiently large field, the friction force gets smaller and smaller, and the particle accelerates until the electric field force is balanced by another mechanism, e.g. the synchrotron radiation of the particle. The requirement for a significant generation of runaway electrons is that the force due to the electric field exceeds the maximum friction force $F(v_{\rm th})$. So a critical electric field can be defined as

$$E_{\rm crit} = \frac{n_e e^3 \ln \Lambda}{4\pi\epsilon_0^2 T_e}\,, \tag{10.3}$$

above which even electrons with thermal velocities are accelerated continuously and become runaway electrons. For particles in the high energy tails of the distribution function, the critical electric field is smaller. Apart from this primary generation mechanism, secondary runaway electrons can be generated by single 'hard' collisions of runaways with thermal electrons, which kick the latter above the threshold, while the former remain above that threshold themselves. This process can cause an 'avalanche' – an exponential growth of the runaway population. Runaway acceleration has also been found to provide a novel mechanism for the electric breakdown in gases, e.g. in the generation of atmospheric lightnings (Gurevich *et al.*, 1992), in addition to the classical ionization avalanche.

What are the conditions under which the electric field becomes large enough so that runaway generation occurs? Due to magnetohydrodynamic instabilities, the equilibrium in a tokamak can be destroyed, which leads to an abrupt and uncontrolled loss of energy. Such an event is called *disruption* (Wesson, 1997). Apart from damages of the vessel wall due to the high thermal impact during a disruption, the fast cooling of the plasma drastically reduces its conductivity ($\sigma \propto T_e^{3/2}$). According to Lenz's law, the sudden reduction of the toroidal current induces a large toroidal electric field. This is the reason why runaway electrons are created mainly during such disruption events. Since synchrotron radiation is nearly the only friction mechanism, they are accelerated to energies of several 10 MeV in existing tokamaks as TEXTOR (Jaspers *et al.*, 1994; Entrop *et al.*, 1998; Entrop *et al.*, 2000) or JET (Esposito *et al.*, 1996), or, as expected for ITER, up to 500 MeV in the worst case scenario (Jaspers *et al.*, 1996). If these fast particles hit the vessel wall, they can cause substantial damage. Although this constitutes a serious concern even in present-day tokamaks, it has been predicted that in ITER, not only the maximum energy of runaways will be increased, but also their number due to the secondary generation caused by the avalanche mechanism. It is therefore obvious that the diffusion mechanisms of runaway electrons are of great interest. Since, as we have seen, runaway electrons are extremely collisionless, the application of the test particle model is justified to an exceptionally high degree.

Similarly to the diffusion of fast ions described in the previous chapters, we find that the basic mechanisms of transport seem to be not completely understood. Most works on this topic find that the experimentally measured transport is by one or more orders of magnitude smaller than the theoretical approach based on magnetic field line diffusion. According to that approach, the particles just follow the turbulent magnetic field lines, which is exactly the situation described by the magnetic part of Eq. (2.59). If we denote the mean perpendicular magnetic drift velocity for a particle just following the magnetic field lines with $V_B \sim \frac{\tilde{B}_r}{B_0} v_\parallel$ and assume a parallel decorrelation at $\tau_\parallel \sim \pi q R_0 / v_\parallel$, we obtain, according to Eq. (2.65) (small Kubo number limit)

$$D_M = \pi q R_0 \left(\frac{\tilde{B}_r}{B_0} \right)^2 v_\parallel \,. \tag{10.4}$$

The electrostatic transport, in contrast, is denoted with

$$D_E = \pi q R_0 V_E^2 / v_\parallel \,. \tag{10.5}$$

This makes clear why for runaway electrons only the magnetic transport is assumed to be relevant, in general. Now, experimental measurements in tokamaks like JET (Esposito *et al.*, 1996), TEXTOR-94 (Jaspers *et al.*, 1994; Entrop *et al.*, 1998; Entrop *et al.*, 2000), or the Madison Symmetric Torus (O'Connell *et al.*, 2003) have shown that the diffusion coefficient of the runaway electrons is by one or more magnitudes smaller than predicted by Eq. (10.4). Experimental values are found to be, for example, $D \approx 0.2\,\mathrm{m}^2/\mathrm{s}$ at JET, $D \approx 0.01\,\mathrm{m}^2/\mathrm{s}$ at TEXTOR-94, and $D \approx 3\,\mathrm{m}^2/\mathrm{s}$ at the Madison Symmetric Torus.

Two possible explanations have been put forward in order to explain the rather low transport level. The first explanation [used, e.g., in (Entrop *et al.*, 2000; Wingen *et al.*, 2006; Esposito *et al.*, 1996; Helander *et al.*, 2002)] attributes the reduction to gyroaveraging and orbit averaging effects similar to which was done in the past for fast beam ions (remember the discussion in Chapter 6). The standard reference which was used in these works is Ref. (Myra & Catto, 1992), where the effect of orbit averaging was included by multiplying Eq. (10.4) with a factor $\Upsilon \equiv \lambda_B / (\sqrt{2\pi} \Delta r / 2)$. This is equivalent (except for the prefactor) to the influence of gyroaveraging for small Kubo numbers which we have derived in Eq. (3.18), replacing ρ_g by $\Delta r / (2\lambda_B)$. However, we find again the same situation that the validity of the orbit averaging approach is taken for granted and not discussed further in the cited publications. Moreover, Eq. (10.4) together with the factor Υ has been used to determine the perturbed magnetic field strength $\frac{\tilde{B}_r}{B_0}$ (Entrop *et al.*, 2000; Esposito *et al.*, 1996), so that the validity of the approach could not be justified.

The second explanation for the transport reduction of runaway electrons which is used in the literature is the assumption that in the torus so-called 'good surfaces' exist, where there is no stochasticity of magnetic field lines and therefore the cross-field transport is suppressed. In (Hegna & Callen, 1993) it was shown that already a small fraction of these 'good surfaces' or magnetic islands inside the 'stochastic sea' can be sufficient to drastically drop the runaway diffusivity, which may easily get even smaller than the thermal transport. In (O'Connell *et al.*, 2003), the transport scaling of Eq. (10.4) could be experimentally confirmed for standard plasmas, however, 'improved confinement' plasmas could be generated where the transport was observed to be independent from the parallel runaway electron velocity, and a reduction of transport from $D \approx 25\,\mathrm{m}^2/\mathrm{s}$ to $D \approx 3\,\mathrm{m}^2/\mathrm{s}$ was observed. A very interesting observation is reported in (Jaspers *et al.*, 1994). After the injection of a deuterium pellet, an increase of runaway electron transport up to $D \approx 300\,\mathrm{m}^2/\mathrm{s}$ was measured, however, after reaching equilibrium again, the remaining runaways were observed to be narrowly localized and had diffusivities of $D \approx 0.02\,\mathrm{m}^2/\mathrm{s}$, which is a reduction by four orders of magnitude. The explanation which was given is that only the pellet injection leads to a full stochastization of the magnetic field fluctuations, which makes Eq. (10.4) to apply. However, small islands would remain, where the fast electrons are not affected. After reaching an equilibrium again, these remaining particles dominate the transport.

At this point, it shall be noted that we are not able to make any contributions to the second explanation, since magnetic islands are beyond the scope of this work. So we concentrate on the possibility of explaining the reduced transport regimes from the assumption of a full ergodized perturbed magnetic field. The importance of this approach is twofold. On one hand, the understanding of the mechanisms of the first explanation will make it easier to decide which mechanism is really responsible for the reduced transport. On the other hand, improvements in the determination of the magnetic field fluctuations are possible, since in reality, Eq. (10.4) is frequently used to determine the fluctuation level $\frac{\tilde{B}_r}{B_0}$ from the diffusivity. This is because due to the synchrotron radiation of the runaway electrons, their position and therefore the diffusion coefficient can be measured quite easily, whereas this is not the case for the field fluctuations. So it is possible that corrections may be necessary not concerning the absolute values of the runaway electron transport, but of the magnetic fluctuations.

10.2 Runaway electron orbits

In the preceding discussion of fast ion orbits (see Secs. 2.1.5 and 6.3), it was not necessary to include relativistic effects, since due to the rather large ion mass, they were not relevant for the observed particle energies. In Fig. 10.1, the particle velocity is plotted versus the kinetic energy for both deuterium ions and electrons. For deuterium ions, the classical approach deviates from the relativistic calculation by 10 per cent only at around 260 MeV, whereas this is the case for electrons already at about 70 keV. For energies exceeding 1 MeV, electrons already approach the speed of light.

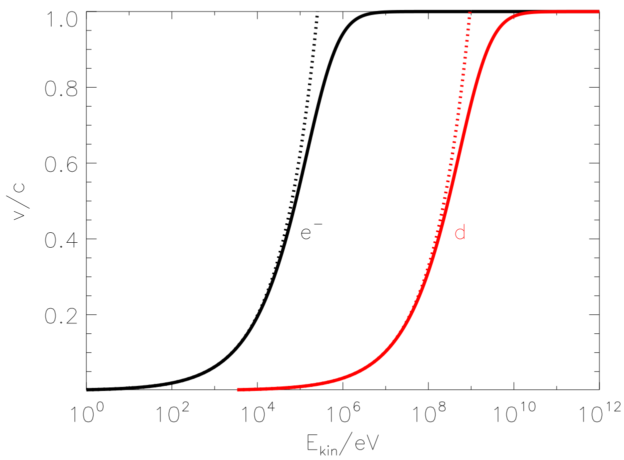

Figure 10.1: Particle velocity vs. kinetic energy for electrons (black) and deuterium ions (red). Solid lines: Relativistic. Dotted lines: Classical limit.

First, we define the well-known Lorentz factor as

$$\gamma \equiv \frac{1}{\sqrt{1-\frac{v^2}{c^2}}} = \frac{E_{\text{kin}}}{m_0 c^2} + 1\,, \tag{10.6}$$

where c is the speed of light. The relativistic relation between energy, mass, and velocity is given as

$$E = mc^2 = \gamma m_0 c^2 = m_0 c^2 + E_{\text{kin}}\,, \tag{10.7}$$

where m_0 is the rest mass and $m = \gamma m_0$ the relativistic mass.

For re-writing the drift orbit parameters of Eqs. (2.29) and (2.30) relativistically in terms of the particle's kinetic energy, it is necessary to replace the rest mass by the relativistic mass, and the classical velocity $v = \sqrt{2E/m_0}$ by the relativistic relation

$$v = c\sqrt{1-\frac{1}{\gamma^2}} = c\sqrt{1-\frac{1}{\frac{E_{\text{kin}}}{m_0c^2}+1}}\,. \tag{10.8}$$

Inserting these changes into Eqs. (2.29) and (2.30), we obtain

$$\begin{aligned}
T_{\text{orbit}} &= \frac{1}{\sqrt{1-\frac{1}{\gamma^2}}}\,\frac{2\pi q R_0}{c} \\
\Delta r &= \sqrt{\gamma^2-1}\,\frac{2 q m_0 c}{eB} \\
v_y &= (\gamma - \frac{1}{\gamma})\,\frac{m_0 c^2 \hat{s}}{eBR_0} \\
\rho_g &= \sqrt{\gamma^2-1}\sqrt{1-\eta^2}\,\frac{m_0 c}{eB}\,.
\end{aligned} \tag{10.9}$$

Since runaway electrons have a pitch angle close to 1 (in (Jaspers *et al.*, 1996), $\eta = 0.98$ was found), the parameter η is neglected here. According to the

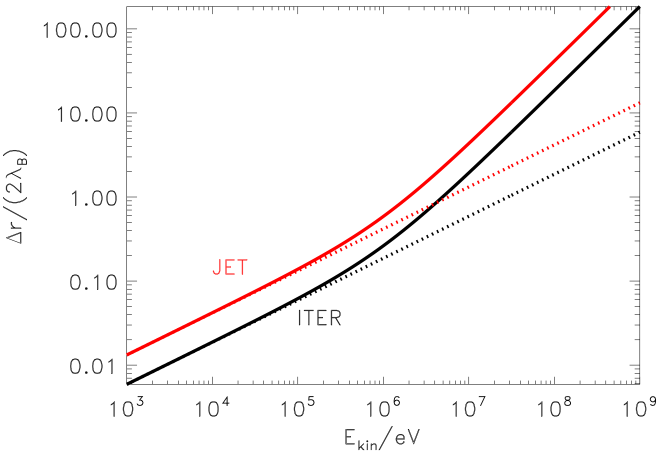

Figure 10.2: Drift orbit radius normalized to the magnetic fluctuation length vs. kinetic energy for runaway electrons with ITER-like (black) and JET-like parameters (red). Solid lines: Relativistic calculation according to Eq. (10.9). Dotted lines: Classical limit.

normalizations defined in Sec. 2.4, we write

$$\begin{aligned} x &\equiv \hat{x}\rho_s = \frac{\hat{x}(T_e m_i)^{1/2}}{eB} \\ v &\equiv \hat{v}\frac{c_s\rho_s}{R_0} = \frac{\hat{v}T_e}{eBR_0} \\ \phi &\equiv \hat{\phi}\frac{Bc_s\rho_s^2}{R_0} = \hat{\phi}\frac{(T_e)^{3/2}m_i^{1/2}}{e^2BR_0}\,. \end{aligned} \tag{10.10}$$

For the normalized values, we chose $\hat{\lambda}_B = 2.5$, $\hat{\lambda}_c = 6$, $\hat{V}_E = 3$, as was found by GENE simulations (Chapters 6 and 7). Further, we set $\tilde{B}_r/B_0 = 10^{-4}$ for the plots presented here, similar to the value found in Chapter 7. We will perform orbit approaches for typical parameters of different fusion devices. For ITER parameters we apply $R_0 = 6.2\,\mathrm{m}$, $B_0 = 5.3\,\mathrm{T}$, and $T_e = 10\,\mathrm{keV}$, whereas for JET parameters, we take $R_0 = 3.0\,\mathrm{m}$, $B_0 = 2.75\,\mathrm{T}$, and $T_e \approx 2\,\mathrm{keV}$. For curves based on TEXTOR data, we apply the parameters $R_0 = 1.75\,\mathrm{m}$, $B_0 = 2.25\,\mathrm{T}$, and $T_e \approx 2\,\mathrm{keV}$. Further, we chose $q = 2$, $\hat{s} = 0.8$ for all three.

It shall be emphasized that while these values may be viewed as typical, they should not be regarded as fixed. The ITER parameters are chosen for comparison with the previous chapters and as a contribution to the future fusion device. The JET parameters are taken in order to compare our scaling approach to results published in (Esposito *et al.*, 1996), where the orbit averaging approach was used. Since larger machine sizes go along with larger fields and temperatures, we will find that the absolute values of the orbits and diffusivities do not differ so much.

Fig. 10.2 shows the drift orbit radius $\Delta r/2$ normalized to the magnetic field correlation length for both the ITER and the JET parameters. Between 2 MeV and 5 MeV, the orbit radius exceeds the correlation length, which means that

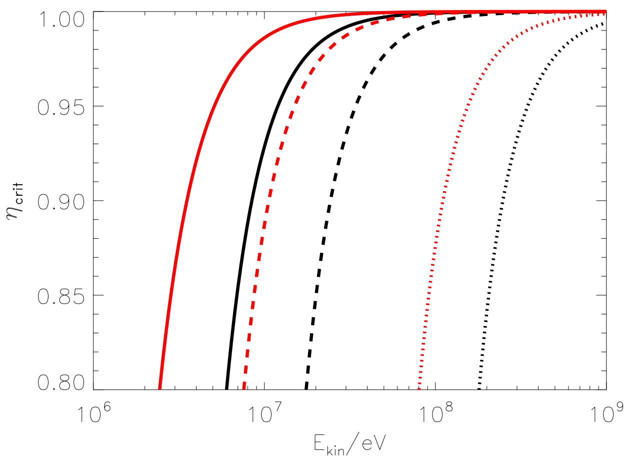

Figure 10.3: Critical pitch angle η_{crit} versus the electron kinetic energy. $\eta_{\text{crit}}(E_{\text{kin}})$ is determined as the curve where $\rho_g \equiv a\lambda_B$. Solid lines: $a = 0.36$. Dashed lines: $a = 1$. Dotted lines: $a = 10$. The curves are drawn for ITER-like (black) and JET-like parameters (red). For $\eta > \eta_{\text{crit}}$ and $a > 0.36$, the large gyroradius approximation as definied in Eq. (B.3) applies. All curves are calculated relativistically according to Eq. (10.9). In the classical limit, finite Larmor radius effects would become relevant only for energies exceeding 1 GeV.

either orbit averaging effects (as described in Sec. 6.4.1) or orbit decorrelation (as described in Sec. 6.4.2) occur. As can also be observed, relativistic effects are responsible for a stronger increase of Δr for large energies.

Further, we want to include the influence of finite gyroradius effects. In the discussion in Appendix B, we have claimed that they become relevant for $\rho_g/\lambda_B \gtrsim 0.36$. In contrast to the orbit radius, the gyroradius has a sensitive pitch angle dependence for large pitch angles, since it is proportional to $\sqrt{1-\eta^2}$. Therefore, in Fig. 10.3 the critical pitch angle (where $\rho_g/\lambda_B = 0.36$) is plotted versus the electron energy. Only for pitch angles exceeding η_{crit}, finite gyroradius effects can be ignored. We see that for $\eta = 0.98$ (as measured in (Jaspers *et al.*, 1996)), they become relevant for energies larger than 10 MeV to 20 MeV, however, they get stronger influence only for higher energies, when the gyroradius clearly exceeds the correlation length.

In Fig. 10.4, the orbit averaging validity parameter $\Xi_{\text{o.a.}}$ as defined in Eq. (6.12) is plotted versus the particle energy. We note that for $E_{\text{kin}} > 10\,\text{keV}$, v_y is the dominating velocity. As can be observed, $\Xi_{\text{o.a.}} > 1$ for E_{kin} exceeding 200 keV to 700 keV, which means that typical runaway electrons are clearly not in an orbit averaging regime.

Before calculating diffusion coefficients, we have to learn more about the decorrelation process responsible for the transition to a diffusive behavior. As pointed out in Sec. 6, it is of special importance which of the times $\tau_{\parallel}, \tau^{\text{orbit}}, \tau_{\text{drop}}$ is the smallest one. As can be inferred from Fig. 10.5, the 'drop time' τ_{drop} is always larger than the minimum of orbit decorrelation time τ^{orbit} and parallel decorrelation time $\tau_{\parallel}$. This means that the drift barrier due to the toroidal

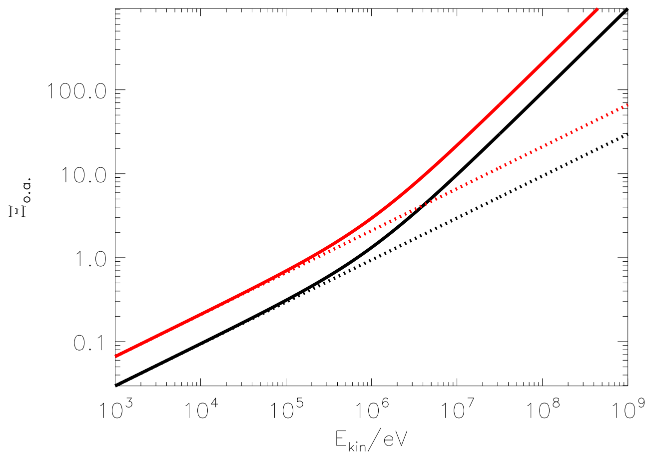

Figure 10.4: Orbit averaging validity parameter $\Xi_{\text{o.a.}}$ vs. kinetic energy. for runaway electrons with ITER-like (black) and JET-like parameters (red). Solid lines: Relativistic calculation according to Eq. (10.9). Dotted lines: Classical limit.

precession drift (as described in Sec. 4.5) has no influence, since decorrelation always occurs on a smaller time scale. For energies smaller than about 500 keV to 1 MeV, the parallel motion provides the relevant decorrelation mechanism, whereas for larger energies, decorrelation occurs due to the perpendicular orbit motion, as described already in Sec. 6.

So we can state:

1. For the orbit decorrelation scaling to be valid, the following assumptions have to be fulfilled: $\Xi_{\text{o.a.}} > 1, \Delta r > 2\lambda_B, \tau^{\text{orbit}} > \tau_{||}$. So according to Figs. 10.2, 10.4, and 10.5 it is the orbit diameter which is the limiting value, leading to the precondition that $E_{\text{kin}} \gtrsim$ 'some MeV'. For larger values ($E_{\text{kin}} \gtrsim 10\,\text{MeV}$ for $\eta \approx 0.98$), finite gyroradius effects have to be taken into account additionally.

2. On the contrary, for the particles following the perturbed magnetic field lines, only $\Xi_{\text{o.a.}} < 1$ has to be fulfilled, i.e. $E_{\text{kin}} \lesssim$ 'some hundred keV'. In that case, the parallel motion leads to decorrelation at $\tau_{||}$ and to the saturation of the diffusion coefficient. In the range between these extremes, orbit averaging is not valid, however, the orbit diameter is still too small for orbit decorrelation to occur. Here we are in a regime which corresponds to the one studied in Chapter 9, however, we will not examine this more closely here.

10.3 Diffusion coefficient assuming field line diffusion

First, we want to derive the diffusion coefficients for case 2, i.e. the assumption that the particles strictly follow the perturbed magnetic field lines (or, for electrostatic transport, the equipotential lines). Finite gyroradius or drift orbit averaging effects can be neglected, since they become relevant only for energies where the assumption does not hold anymore. For magnetic transport, we

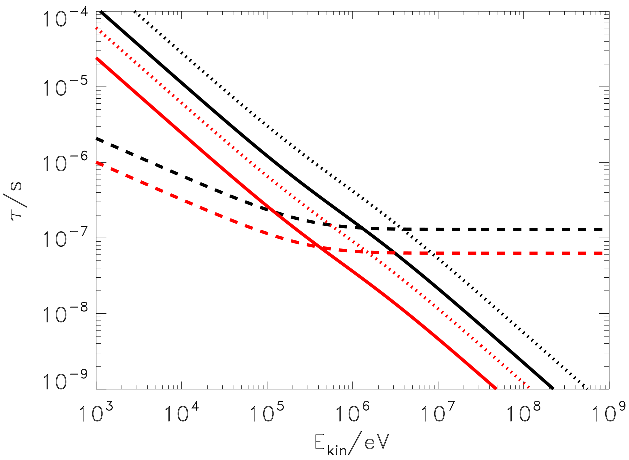

Figure 10.5: Relevant time scales for the particle diffusivity vs. kinetic energy. Solid lines: Orbit decorrelation time $\tau^{\text{orbit}} \equiv \frac{\lambda_B T_{\text{orbit}}}{\pi \Delta r}$. Dashed lines: Parallel decorrelation time $\tau_{\|} \equiv \lambda_{\|}/v_{\|} \sim \pi q R_0/v_{\|}$. Dotted lines: 'Drop time' $\tau_{\text{drop}} \equiv 2\lambda_B/v_y$. The curves are drawn for ITER-like (black) and JET-like parameters (red) and calculated relativistically according to Eq. (10.9).

therefore obtain

$$D_M \approx V_B^2 \tau_{\|} = \pi q R_0 \left(\frac{\tilde{B}_r}{B_0}\right)^2 v_{\|} = \pi q R_0 \left(\frac{\tilde{B}_r}{B_0}\right)^2 c\sqrt{1 - \frac{1}{\gamma^2}}\,. \tag{10.11}$$

Similarly, neglecting finite gyroradius and drift orbit effects, electrostatic transport obeys to the equation

$$D_E \approx V_E^2 \tau_{\|} = \frac{\pi q R_0}{v_{\|}} V_E^2 = \frac{\pi q R_0 V_E^2}{c} \frac{1}{\sqrt{1 - \frac{1}{\gamma^2}}}\,. \tag{10.12}$$

If we now – despite its invalidity – include drift orbit averaging, we have to multiply V_E and V_B with the factor $(4\sqrt{\pi}\Delta r/(2\lambda_{E,B}))^{-1/2}$ (see Eq. (3.15)), which is valid for $\Delta r/(2\lambda_{E,B}) \gtrsim 0.36$, i.e. $E_{\text{kin}} \gtrsim 1\,\text{MeV}$. Small orbit corrections can be treated via an adjustment of Eq. (3.11). For including finite gyroradius effects, Eqs. (3.15) and (3.11) are applied directly.

In Fig. 10.6 both electrostatic and magnetic diffusivity are plotted versus the electron's kinetic energy. The curves neglecting finite orbit effects saturate as soon as the particle velocity approaches the velocity of light, since the diffusivity is proportional (inversely proportional) to the parallel velocity. Additionally, orbit averaging effects are included for the magnetic transport. For large energies, the orbit averaging leads to a $1/E$ decrease of the diffusion coefficient, which can be attributed to the increase of the relativistic particle mass. From Fig. 10.6 we learn that relativistic effects strongly reduce the magnetic particle diffusivity in the field line diffusion limit, which is on one hand due to the limited particle velocity, and on the other hand due to the relativistic increase of

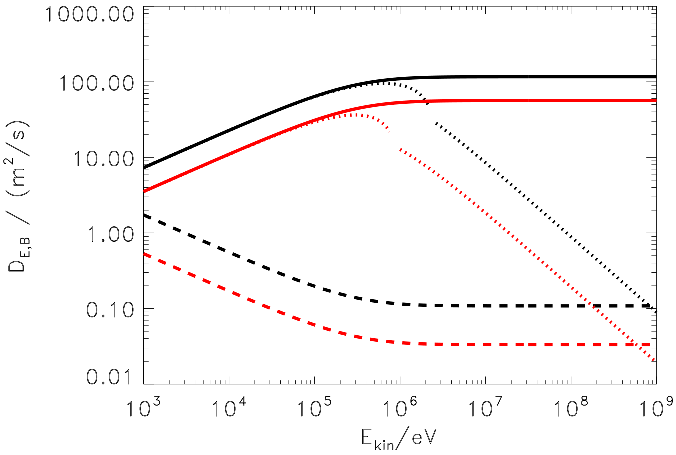

Figure 10.6: Diffusion coefficients vs. kinetic energy according to the model that particles follow the perturbed field lines (magnetic transport, Eq. (10.11)) or the equipotential lines (electrostatic transport, Eq. (10.12)). For magnetic transport $\tilde{B}_r/B_0 = 10^{-4}$ has been assumed, whereas for electrostatic transport, $V_E = 912\,\mathrm{m/s}$ was taken (as used in Chapter 6). Solid lines: Magnetic transport (no orbit effects). Dashed lines: Electrostatic transport. Dotted lines: Magnetic transport with orbit averaging. The curves are drawn for ITER-like (black) and JET-like parameters (red) and calculated relativistically using the orbit parameters defined in Eq. (10.9).

the particle mass, leading to a stronger increase of the orbit diameter compared to the classical case. We want to add that for particle energies larger than about 10 MeV, finite gyroradius effects have to be included, leading to an additional $1/E$ decrease, which means an overall decrease of $D(E) \propto E^{-2}$. However, since this effect strongly depends on the pitch angle (see Fig. 10.3), we have neglected it for the moment. We would like to emphasize the strong (quadratic) dependence on $\tilde{B}_r/B_0$. In the figure, $\tilde{B}_r/B_0 = 10^{-4}$ was chosen similar to the GENE results underlying Chapter 7, however, smaller values are possible in tokamaks, which can drastically reduce the magnetic runaway diffusion. In Sec. 10.5, we will re-determine the fluctuation strength based on measurements of the runaway diffusion coefficients in JET (Esposito *et al.*, 1996).

10.4 Diffusion coefficient assuming orbit decorrelation

Now, we want to establish relations for case 1, i.e., the orbit decorrelation mechanism already discussed in Chapters 6 and 7. As we have seen above, this is the correct description for $E_{\mathrm{kin}} \gtrsim$ 'some MeV'. According to the model applied in Sec. 7.2, using the orbit parameters of Eq. (10.9), we obtain

$$D_M \approx \frac{2}{3} V_B^2 \tau^{\mathrm{orbit}} = \frac{2}{3}\left(\frac{\tilde{B}_r}{B_0}\right)^2 v_\parallel^2 \frac{\lambda_B T_{\mathrm{orbit}}}{\pi \Delta r} = \frac{2}{3}\left(\frac{\tilde{B}_r}{B_0}\right)^2 \frac{\lambda_B R_0 e B}{m_0}\frac{1}{\gamma}. \tag{10.13}$$

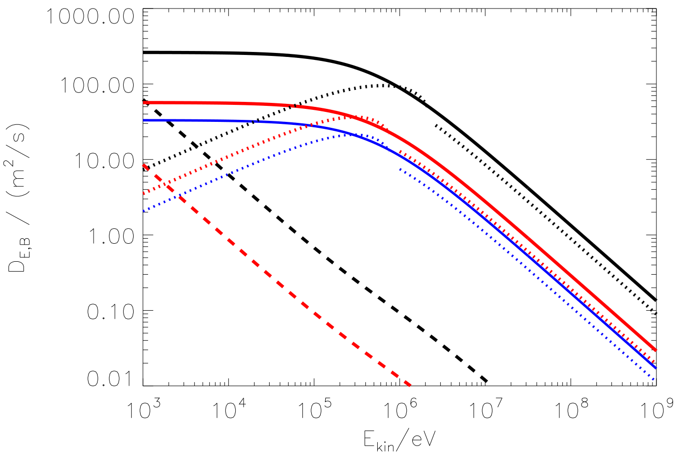

Figure 10.7: Diffusion coefficients vs. kinetic energy according to the orbit decorrelation model for magnetic transport (Eq. (10.13)) and electrostatic transport (Eq. (10.12)). The orbit averaging curve for magnetic transport from Fig. 10.6 is given for comparison. $\tilde{B}_r/B_0 = 10^{-4}$ was chosen. The values inserted for $\tilde{B}_r/B_0$ and V_E correspond to the ones Fig. 10.6. Solid lines: Magnetic transport (orbit decorrelation). Dashed lines: Electrostatic transport (orbit decorrelation). Dotted lines: Magnetic transport with orbit averaging. The curves are drawn for ITER-like (black), JET-like (red), and TEXTOR-like parameters (blue) and calculated relativistically according to Eq. (10.9).

Similarly, for electrostatic transport, we find (see Sec. 6.6)

$$D_E \approx \frac{2}{3} V_E^2 \tau^{\text{orbit}} = \frac{2}{3} \frac{V_E^2 \lambda_V R_0 e B}{m_0 c^2} \frac{1}{\gamma - 1/\gamma} \,. \tag{10.14}$$

These curves, adjusted for the JET-like and ITER-like parameters, are drawn in Fig. 10.7, together with the orbit averaged curve for the magnetic transport from Fig. 10.6. Possible finite gyroradius effects are still neglected. We recall that the orbit decorrelation approach is valid only in the range $E_{\text{kin}} \gtrsim 1\,\text{MeV}$, whereas below, the field line diffusion approach (dotted lines) is valid. Interestingly, for magnetic transport, a $1/E$ decrease for large electron energies is found which not only corresponds to the (invalid) orbit averaging approach concerning the energy scaling, but also very well in the absolute values. Is this a systematic effect or pure chance? To answer this question, we compare Eq. (10.11) with Eq. (10.13). Although distinct in the ansatz, they become similar if Eq. (10.11) is multiplied with the orbit averaging correction factor $(4\sqrt{\pi}\Delta r/(2\lambda_B))^{-1}$, so that it attains the same dependence on $1/\Delta r$ as in Eq. (10.13). However, this dependence comes from the reduction of the average magnetic drift velocity due to orbit averaging, whereas in the orbit decorrelation case, it comes from the reduction of the effective decorrelation time. So, it is reasonable to attribute the similarity to an accidental coincidence. If the effective Kubo number was larger than one, the orbit averaging scaling would be different and the curves would differ from each other again.

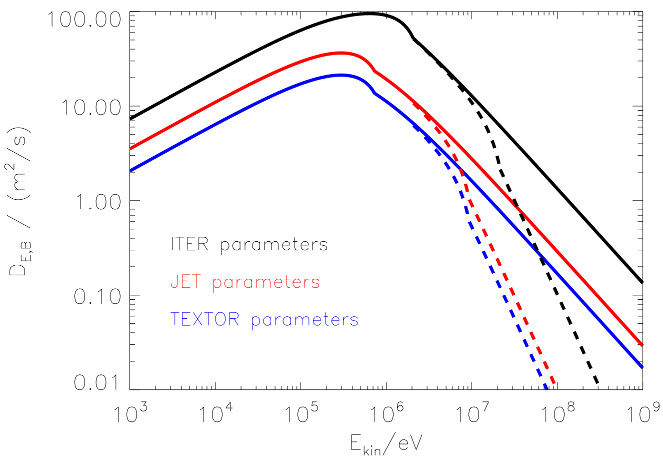

Figure 10.8: Diffusion coefficients vs. kinetic energy. Combined approach taking the field line diffusion model with orbit averaging (Eq. (10.11)) for small energies ($\Xi_{\text{o.a.}} < 1, \Delta r/2 < \lambda_B$) and the orbit decorrelation model (Eq. (10.13)) for large energies ($\Xi_{\text{o.a.}} > 1, \Delta r/2 > \lambda_B$) As before, $\tilde{B}_r/B_0 = 10^{-4}$ was chosen. Solid curves: No finite gyroradius effects ($\eta \to 1$). Dashed lines: Finite gyroradius effects included for $\eta = 0.98$, using gyroaveraging. The curves are drawn for ITER-like (black), JET-like (red), and TEXTOR-like parameters (blue) and calculated relativistically according to Eq. (10.9).

In Fig. 10.8, the field line diffusion (including orbit averaging corrections for $\Delta r/2 < \lambda_B$) for small kinetic energies is combined with the orbit decorrelation for large kinetic energies to a continuous curve, which gives something like the expected real behavior of runaway diffusivity. The solid curves neglect finite gyroradius effects as before, whereas the dashed curves include them for an assumed pitch angle of $\eta = 0.98$, as found in (Jaspers *et al.*, 1996). They lead to an additional factor E^{-1}, which results in an overall scaling of $D_M(E) \propto E^{-2}$. Depending on the pitch angle, this last transition can occur at larger or smaller energies. Once more it shall be emphasized that the difference between the scaling laws illustrated in Fig. 10.8 and the ones presented in Chapter 7 lies only in the relativistic behavior of the runaway electrons. Since the gyroradius and orbit radius grow stronger with energy than in the classical limit, but the orbit circulation time is limited due to the upper limit for the particle's velocity, the decline of diffusivity according to Eq. (10.13) is stronger.

At this point, one question is forced upon the watchful reader. Why have we just found that for runaway electrons, orbit averaging – despite its clear invalidity – leads to the same results than the correct orbit decorrelation approach, whereas in Chapters 6 and 7, we have claimed that this would not be the case? In Chapter 6, it was already emphasized that the reason for the strong reduction of transport in the case that the orbit averaging mechanism is applied (as can be seen, e.g., in Figs. 6.4 and 6.6) is not just the reduction of the turbulent drift velocity due to orbit averaging itself, but the fact that due to the toroidal precession drift v_y, the 'drift barrier' (as described in Sec. 4.5) dominates the transport. We have learned that this barrier strongly reduces transport in the case that $\tau_{\text{drop}} < \tau^{\text{eff}}$, i.e., if the drop time is smaller than the effective decorrelation time. For fast ions, this was the case for orbit averaging, but not for orbit decorrelation, since we found $\tau^{\text{orbit}} < \tau_{\text{drop}} < \tau_{\|}$ for large ion energies (see Tables 6.2 and 6.3). For runaway electrons, it can be seen in Fig. 10.5, that τ_{drop} is always larger than τ^{orbit}, i.e. as for ions, the drift barrier has no influence onto the orbit decorrelation mechanism. However, if orbit averaging is applied, we see that for $E_{\text{kin}} \gtrsim 2\,\text{MeV}$ to $5\,\text{MeV}$, τ_{drop} gets smaller than $\tau_{\|}$, so that we have indeed the same situation than in Figs. 6.4 and 6.6. The drift barrier leads to a very strong decrease of $D(E)$. This effect has not been included in the dotted lines in Fig. 10.7. Therefore we can state that the coincidence of the orbit averaging approach and the orbit decorrelation mechanism is not only accidental in the sense that different approaches lead to the same scaling law, it is also only possible since in the former case the effect of the drift barrier is completely ignored. So it should be allowed to state that the interpretation of experimental results based on the orbit averaging approach as done by (Entrop *et al.*, 2000; Wingen *et al.*, 2006; Esposito *et al.*, 1996; Helander *et al.*, 2002), is correct due to a 'lucky strike', where a combination of two wrong assumptions (orbit averaging and omission of the drift barrier) leads to almost the correct result by chance.

10.5 Comparison with the literature

We now want to compare the consequences of our results with the approaches of previous publications, where we want to turn a special attention to the determination of $\tilde{B}_r/B_0$. At the JET tokamak (Esposito *et al.*, 1996), the diffusion coefficient of runaway electrons was measured in the energy range between 133 keV and about 1.5 MeV using a FEB (fast electron bremsstrahlung) diagnostic. A diffusion coefficient averaged over that energy range was determined to $D = 0.2\,\text{m}^2/\text{s}$. Since finite orbit effects are negligible for the smallest energy which was measured, $E_{\text{kin}} = 133\,\text{keV}$, the magnetic field fluctuations were determined according to Eq. (10.11) to be $\tilde{B}_r/B_0 \approx 8 \times 10^{-6}$. However, this value was regarded as a lower limit, since it was claimed that for larger energies, the finite orbit influence would increase, therefore the magnetic field perturbation should increase to obtain the measured value of D. The red dotted curves in Fig. 10.6 and Fig. 10.7 describe the field line diffusion model including orbit averaging effects and have been normalized exactly to the values of (Esposito *et al.*, 1996), except that $\tilde{B}_r/B_0 = 10^{-4}$ was taken. If we replace that value by $\tilde{B}_r/B_0 \approx 8 \times 10^{-6}$ in Eq. (10.11), this would lead to a reduction in the $D(E)$ curves by a factor of 156, which would give a maximum value of exactly $D = 0.2\,\text{m}^2/\text{s}$. However, it was pointed out in (Esposito *et al.*, 1996) that the maximum runaway electron energy is about 30 MeV. Here, according to Fig. 10.8, the diffusion coefficient should be expected to be smaller than the value around 300 keV by a factor of about 30 (without finite gyroradius effects), i.e. $D \approx 0.007\,\text{m}^2/\text{s}$. Assuming $\eta = 0.98$, we would even find $D \approx 0.0009\,\text{m}^2/\text{s}$. Unfortunately, diffusivities were not measured in the high energy limit in (Esposito *et al.*, 1996).

At the TEXTOR tokamak, different diffusion regimes were found, which were explained by a different level of stochastization of the magnetic field lines (Jaspers *et al.*, 1994). By synchrotron emission, a population of 30 MeV runaway electrons was observed. After pellet injection, a rapid loss has been detected with diffusion coefficients up to $300\,\mathrm{m}^2/\mathrm{s}$. If we apply Eq. (10.13) (or adjust Fig. 10.8), we find the corresponding magnetic field perturbation to be $\tilde{B}_r/B_0 = 2.3 \times 10^{-3}$ if finite gyroradius effects are neglected, which is a rather large value. However, if we remember Eq. (7.2), we can approximate the maximal possible value to $(\tilde{B}_r/B_0)_{\max} \sim \rho_i/R_0 \approx 2.9 \times 10^{-3}$, which means that such a large value can in principle be possible. Since the pellet injection raises the plasma pressure and, according to Eq. (7.1), also the plasma beta, such a behavior can qualitatively be understood. Including the effects of a finite gyroradius with the assumption $\eta = 0.98$, we would obtain $(\tilde{B}_r/B_0)_{\max} \approx 7 \times 10^{-3}$, a value which would actually be too large. However, it must be emphasized that the real pitch angle is unknown in that experiment. Moreover, in (Jaspers *et al.*, 1994) it is assumed that all runaway electrons have 30 MeV, which need not be true. If a significant number of lower energetic electrons exists, their diffusivity can reach the measured value for smaller values of $(\tilde{B}_r/B_0)$. Now in (Jaspers *et al.*, 1994), after pellet injection, a remaining runaway electron population with an extremely slow diffusivity of $D \lesssim 0.02\,\mathrm{m}^2/\mathrm{s}$ was detected, which was attributed to the existence of intact magnetic islands within the chaotic sea. However, if we assume stochasticity also here and apply the standard orbit decorrelation approach without gyroradius effects, this corresponds to $\tilde{B}_r/B_0 \approx 1.9 \times 10^{-5}$, which is still a reasonably large number. Assuming again $\eta = 0.98$ and including the finite gyroradius effects resulting from this choice, we would even obtain $\tilde{B}_r/B_0 \approx 1.7 \times 10^{-4}$, which would be an ordinary magnitude. The diffusion coefficients derived that way correspond to findings of Ref. (Entrop *et al.*, 2000), reported from TEXTOR, too, where $\tilde{B}_r/B_0 \approx 5 \times 10^{-5}$ was found for Ohmic plasmas, but $\tilde{B}_r/B_0 \approx 10^{-3}$ if an NBI (neutral beam injection) current is applied. Similar findings are reported from the Tore Supra tokamak (Zou *et al.*, 1995). Here, the determination of the magnetic field fluctuations was done directly via the polarization change of electromagnetic waves scattered by the fluctuations, thus independent from a determination of the diffusion coefficient. So it may possibly be that the concept of 'good surfaces' and magnetic islands is not necessary for explaining the observed small diffusion coefficients, since they can also be explained conventionally by our model, assuming stochastic field fluctuations of the order of 10^{-5} to 10^{-4}, as reported in the literature. However, an exact determination of $\tilde{B}_r/B_0$ depends on the knowledge of the pitch angle, which is normally not known from measurements. In the literature reviewed here, finite gyroradius effects have always been neglected, which indicates that in general, the determination of the field fluctuations has led to values which are too small.

10.6 Summary and conclusions

We have applied the same mechanisms to fast runaway electrons that were previously applied to fast ions. As before, orbit averaging was found to be invalid for large particle energies, so that the orbit decorrelation mechanism has to be used to describe transport correctly. Due to their smaller mass and higher energy, runaway electrons behave strongly relativistically, which leads to different scaling laws compared to the non-relativistic ions described in Chapters 7 and 8. For example, the magnetic transport drops with $1/E$ for large energies as long as the pitch angle is large enough for finite gyroradius effects to be neglected. If this is no more the case, we obtain even $D \propto E^{-2}$. It was found that despite the wrong ansatz, orbit averaging leads to almost the same result in the case that the influence of the toroidal precession drift is neglected. Whereas the transport is found to be weak for runaway electrons close to saturation, a maximum is found around 1 MeV, which may strongly exceed the thermal transport. Due to the quadratic dependence, the magnetic field perturbation was shown to be a crucial parameter. Perturbations as measured in experiments are found to be – in principle – sufficient to explain the weak transport for large kinetic energies, however, the determination of $\tilde{B}_r/B_0$ from the diffusion coefficient strongly depends on the pitch angle, which is a quantity often unknown.

Chapter 11

Conclusions

In the course of this Ph.D. project, a number of new and important contributions concerning the transport of fast particles in tokamak microturbulence have been made. In many cases, previous models and assumptions, often based on rather rough approximations and sometimes contradicting each other, were improved and corrected by careful and detailed analyses, based on first principles. Moreover, new results were obtained in areas disregarded in the past, like the magnetic transport of fast particles. By comparison with complex gyrokinetic codes as well as with measurements on ASDEX Upgrade, the results of the analytical models could be confirmed, and, vice versa, the start of new experimental campaigns was inspired.

A short overview of the main results of this thesis is given in the following; detailed summaries can be found at the end of each chapter.

11.1 Summary

Fast particles in 2D electrostatic turbulence

Based on analytical studies of the gyroaveraged autocorrelation function of turbulent electrostatic potentials, expressions for the dependence of the diffusion coefficient on the Larmor radius were derived. As for the transport of pure gyrocenters, the Kubo number was identified as an important parameter in distinguishing different regimes and scaling laws. Concerning the large Kubo number regime (in which realistic tokamak turbulence was found to lie) both naive expectations and previously published results were corrected. It was found that transport is not affected by finite Larmor radius effects for radii up to the correlation length of the electrostatic potential, whereas for radii exceeding this value, the decay of diffusivity is more moderate than expected in the low Kubo number regime.

The influence of geometric structures like radially elongated vortices and zonal flows has been studied. For the former, the resulting increase of transport could be observed and described analytically, whereas for the latter a decrease was confirmed. The modification of finite gyroradius effects by these structures was described both qualitatively and quantitatively. Moreover, the influence of homogeneous poloidal drifts of the background turbulence was studied, and its action as a transport barrier for the radial particle transport was demonstrated, as well as its modification by finite Larmor radius effects. In particular, the 'drop time' was introduced as the decisive time scale, above which the transport barrier begins to act, provided that the decorrelation time of the fluctuations is larger. These studies were later found to be of great relevance in three dimensions, where – due to magnetic effects – the particles themselves are subject to a poloidal drift.

The identification of zonal flows and homogeneous poloidal drifts as transport barriers was the start of further investigations concerning the nature of diffusion within these structures. Although they can give rise to non-diffusive regimes for rather large times, it was found that the stochastic parts of the stream function always induce a transition to diffusive transport above a certain threshold in time. The processes underlying this transition were studied qualitatively, comparing them to continuous time random walk models. Moreover, effects like 'chaotic jets' which were claimed to appear by some authors, could not be confirmed to apply under realistic conditions.

Fast particles in 3D electrostatic turbulence

Many results of the two dimensional studies were found to carry over to three dimensions, especially the gyroradius dependence and the poloidal drifts acting as transport barriers. However, a number of new effects could be identified. Among the most important is the identification of the *perpendicular* drift orbit motion (relative to the magnetic field lines) of fast particles as the decisive decorrelation mechanism governing the transition to a diffusive regime. This result was found to be in contrast to older as well as more recent publications, assuming that decorrelation occurs due to the motion *parallel* to the magnetic field lines, i.e., on much larger time scales. From this finding, it followed that the assumption of 'orbit averaging' (i.e., averaging the electrostatic or magnetic potentials over one drift orbit) – which has been widely used by many authors and together with the poloidal drift barrier would lead to a drastic reduction of transport with the particle energy – is not valid for typical conditions in a tokamak. Instead, an analytical model based on the perpendicular decorrelation of particles experiencing the pure potential was developed. This model led to analytical expressions for the diffusion coefficient depending on parameters like the correlation length of the fluctuations and the energy of the fast particles. In particular, a decrease of diffusivity with E^{-1} ($E^{-3/2}$) was found for beam ions (trapped ions) which is much more moderate than applying the orbit averaging mechanism. Comparing our analytical formula with simulations with the GOURDON code as well as with the gyrokinetic GENE code, an excellent agreement was found. Moreover, it was shown that the diffusion coefficient is maximal when the toroidal precession drift of the particles is in resonance with the homogeneous diamagnetic drift of the background potential, since in this case, the drift barrier as described for the 2D case is weak.

Fast particles in 3D magnetic turbulence

Applying the mechanisms of electrostatic transport of fast particles to magnetic transport, even more interesting scaling laws were derived. It was found that for beam ions, the diffusion coefficient does not depend on the particle energy anymore, even for very high energies, provided that the pitch angle is sufficiently large. For trapped ions or beam ions with smaller pitch angle, a rather weak $E^{-1/2}$ dependence was found. These analytical findings could be confirmed by simulations with the GENE code. Whereas in the past, magnetic transport was mostly disregarded as a candidate for fast ion transport due to the smaller amplitudes of the turbulent magnetic fields compared to the electrostatic ones, it was shown that for large beam energies, this effect is balanced by the constant level of diffusion for arbitrary energies, so that magnetic transport should be considered as a hot candidate for governing the transport of fast particles.

Comparison with experimental measurements

It was shown that our analytical approach for magnetic transport is able to reproduce the almost exact value introduced ad hoc at ASDEX Upgrade in order to describe the radial NBI (neutral beam injection) broadening observed in measurements. Whereas this observation had been quite surprising at the beginning, the results obtained in this thesis provided them with a well-founded theoretical basis. Although the main emphasis was laid on an explanation via magnetic transport (which was mainly due to the ad hoc assumption of a constant diffusion coefficient from the experimental side), it was shown that, in principle, electrostatic transport can lead to a similar broadening of the current beam according to the respective scaling laws. So whereas one can state that likely, both magnetic and electrostatic transport can contribute, a definite answer to the question of the nature of diffusion in that specific case has to be left to future experimental examinations. Particularly, energy-resolved measurements of the beam current are required in that case. Such investigations are currently underway.

Runaway electrons

Extending the scaling laws derived for ions to relativistic ‘runaway’ electrons, it could be demonstrated that the experimentally measured low diffusivities can, in principle, be explained by the orbit decorrelation model, possibly making different explanations reported in the literature redundant. In particular, it was found that it is the relativistic behavior in conjunction with finite gyroradius effects which leads to an E^{-2} decrease of the magnetic transport, strongly differing from the ion transport.

11.2 Outlook – Applications in astrophysics

In this thesis, the diffusive transport of fast particles due to electrostatic and magnetic field fluctuations has been studied for the conditions in a tokamak. The purpose of these studies was the modeling and understanding of fast particle phenomena in present and future fusion devices. As far as the transport of passive test particles is concerned, their discussion can probably be regarded as more or less complete.

At the end of this work, an outlook shall be given in which way the basic transport and decorrelation mechanisms derived here can be applied to astrophysical scenarios, particularly the transport of highly energetic 'cosmic rays' (i.e. particles) within intergalactic, interstellar, or interplanetary magnetic fields. Due to the interstellar or solar wind plasma, these fields often exhibit a turbulent nature, as can be observed, for example, for the fields within the spiral arms of galaxies (Beck, 2003) or for the fields trapped in the solar wind (Zimbardo, 2005; Tu & Marsch, 1995). This leads to scattering of the cosmic rays perpendicular to the background field which is in principle the same as the diffusive magnetic transport in a tokamak, although the scales are extremely different.

The highest measured energies of cosmic rays are larger than 10^{20} eV. While the acceleration of particles to energies up to 10^{14} eV can be explained by shock waves in supernovae, the origin of cosmic rays with larger energy remains unknown (Shalchi, 2007). The form of the observed magnetic fields often shows a spiral shape like in the arms of spiral galaxies or in the solar wind ('Parker Spiral'), but it can also show a cell-type shape as observed in intracluster gas, or a helical shape in synchrotron jets (Vallée, 2004). The strength of these fields ranges from 10^{-14} T in the intergalactic space to 10^{-8} T in the solar wind in the neighborhood of the earth. Although the absolute value of these fields is small, the turbulent part is quite high. For the solar wind, e.g., one finds $\tilde{B}/B_0 \approx 0.5$ - 1 (Zimbardo, 2005; Tu & Marsch, 1995). Moreover, the fluctuations in the solar wind do not show a strong elongation along the magnetic field lines. Instead, satellite measurements find $\lambda_\parallel \sim \lambda_\perp \sim 10^6$ km (Tu & Marsch, 1995). The nature of these fluctuations does not seem to be fully understood yet. Possibly, they are either passive remnants of coronal processes or an example for dynamically evolving MHD (magnetohydrodynamic) turbulence, or a mixture of both (Tu & Marsch, 1995).

If the knowledge from the tokamak is applied to the amplitudes and scales of, e.g., the solar wind magnetic field, it is found that the effective magnetic Kubo number $K_{\mathrm{mag}} = \tilde{B}/B_0\,\lambda_\parallel/\lambda_\perp$ is of order unity. This is in the transition zone between the high and the low Kubo number regime, so that, using the experience from Chapter 3, different regimes of the scaling of transport with the particle energy can be expected if the scales of the magnetic field are varied. Moreover, it can be shown that for large cosmic ray energies, gyroaveraging is not valid anymore. This means that the same mechanisms as described in Chapters 6 and 7 concerning the invalidity of orbit averaging can be applied if the parameters concerning the drift orbits are replaced by the ones concerning the gyromotion. Rough estimates show this to happen for particle energies exceeding 1 GeV.

More exact expressions and models strongly depend on a better knowledge of the amplitudes and scales of the turbulent magnetic fields. This has to be left to future work, possibly in cooperation with researchers from the field of astrophysics.

Appendix A

Some more Comments on Reduced-volume Simulations

This annex is a continuation of the discussion in Section 6.6.2. The mechanisms which determine artificial re-correlation effects are described in more detail by means of the running diffusion coefficient.

Fig. A.1 shows the running diffusion coefficients for the saturated values already plotted in Fig. 6.4. The orbit decorrelation times τ^{orbit} range from $1.2 \cdot 10^{-5}\,\mathrm{s}$ for $E = 80\,\mathrm{keV}$ to $1.0 \cdot 10^{-7}\,\mathrm{s}$ for $E = 1280\,\mathrm{keV}$ and are outside the plot range. Now, caused by the mechanisms explained in Section 6.6.2, the large energy curves show a drop at times larger than this orbit decorrelation time, which is responsible for the reduction of transport. We assume that this drop is caused by the 'drift barrier' at $\tau_{\mathrm{drop}} = 2\lambda_c/v_y^{\mathrm{eff}}$. What is the value of v_y^{eff} (the value of v_y is known to be 31256 m/s)? Since in our 3D simulations, the starting points of the tracers were split from $r_0 = 0.6$ to $r_0 = 0.8$, it does not make sence to study one single orbit in detail, since the dependence on transport is very sensitive (see the discussion with respect to Fig. A.2) and we can only expect to observe an average over a number of slightly different orbits by studying Fig. A.1. Instead, we use a probabilistic approach. The particle gets re-correlated if, by moving into the neighbor box, it returns into the correlated zone. This happens with a probability of λ_c/L_y, which is 0.053 in our case. The first chance for a re-correlation is after two turns, since $2T_{\mathrm{orbit}}v_y \approx L_y$, this is, at $1 \cdot 10^{-5}\,\mathrm{s}$. After 12 of these double orbits, approximately 50% of the particles are re-correlated ($(1 - 0.053)^{12} \approx 0.5$). Indeed, the time span from $1 \cdot 10^{-5}\,\mathrm{s}$ to $1 \cdot 10^{-4}\,\mathrm{s}$ is roughly the range where the drop occurs. For larger times, the potential itself gets decorrelated (remember $\tau_c = 1.8 \cdot 10^{-4}\,\mathrm{s}$), and so the remaining particles do not get re-correlated again.

Last, we want to study the effect of re-correlation in more detail. To this aim, we use the well established 2D approach, where it is possible to arbitrarily vary the orbit parameters, here the drift velocity v_y. The box width is kept as $L_y = 0.31\,\mathrm{m}$. For $E = 1280\,\mathrm{keV}$, we have $T_{\mathrm{orbit}} = 5 \cdot 10^{-6}\,\mathrm{s}$, therefore $L_y/T_{\mathrm{orbit}} =$ 62831 m/s is the velocity where the particle gets re-correlated exactly after one orbit. In Fig. A.2 we can see that, after a first saturation around $\tau^{\mathrm{orbit}} \sim 10^{-7}\,\mathrm{s}$, the transport increases in steps of $\Delta t = T_{\mathrm{orbit}}$, until it saturates around $\tau_c =$

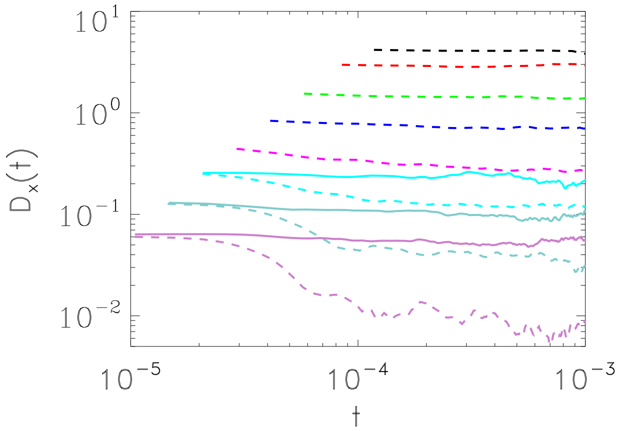

Figure A.1: Running diffusion coefficient for the 3D values already plotted in Fig. 6.4. The dashed lines represent $D(t)$ for a torus filled with 10 identical fluxtubes. The energies vary from $E = 10\,\mathrm{keV}$ to $E = 1280\,\mathrm{keV}$ top down. The solid lines, in contrast, show the curve $D(t)$ for energies from $E = 320\,\mathrm{keV}$ to $E = 1280\,\mathrm{keV}$, if the torus is filled by only one fluxtube, i.e. no aritificial periodicity is present. As can be seen clearly, this avoids the drop around $t \sim 5 \cdot 10^{-5}s$.

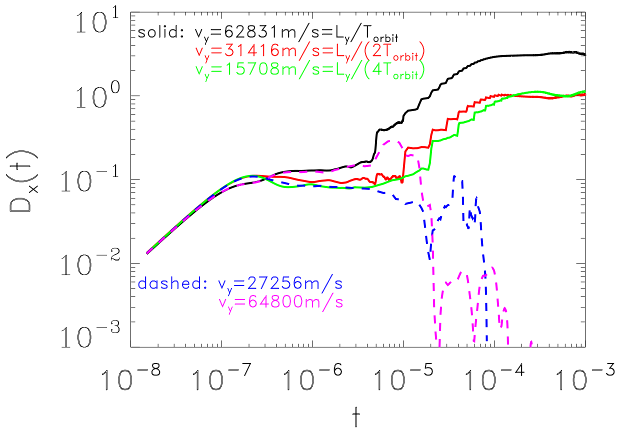

Figure A.2: Running diffusion coefficient with the parameters for $E = 1280\,\mathrm{keV}$ (see Tab. 6.2), but with variable curvature drift v_y. The curves are simulated using the 2D approach (Eq. 6.15). As can clearly be seen, the diffusivity depends on the curvature drift velocity in a very sensitive way. Whereas transport is large for the resonance cases (solid lines, $v_y T_{\mathrm{orbit}} \bmod L_y = 0$), it shows rapid drops if there is no exact resonance (dashed lines).

1.8 m/s. If we reduce the drift velocity by a factor of 2 or 4, the step width increases by the same factor, since now, the particle must circulate for 2 or 4 times until it reaches the correlated zone in the neighbor box. Since we have an effective drift velocity of $v_y^{\mathrm{eff}} = 0$, there is no drift barrier and the transport is high. The dashed lines in Fig. A.2 describe situations, where there is no exact resonance. For the particle with $v_y = 64800\,\mathrm{m/s}$, the relative position to the correlation maximum after one turn is $(v_y T_{\mathrm{orbit}} \bmod L_y) L_y = 0.0098\,\mathrm{m}$, which is smaller than λ_c, and we expect orbit averaging to be valid (since $\Xi_{\mathrm{o}.a.} < 1$). The effective curvature drift velocity would be $v_y^{\mathrm{eff}} = 0.0098\,\mathrm{m}/T_{\mathrm{orbit}} = 1968\,\mathrm{m/s}$, which leads to a drop time of $\tau_{\mathrm{drop}} = 2\lambda_c/v_y^{\mathrm{eff}} = 1.7 \cdot 10^{-5}\,\mathrm{s}$. This is what we observe in the figure. For the case where $v_y = 27256\,\mathrm{m/s}$, the particle is outside the correlated zone after one orbit turn. It can easily be shown that the particle needs 7 orbit circulation periods to return inside a radius of λ_c of the correlation maximum. In that time, it crosses 3 boxes. We find $(7 v_y T_{\mathrm{orbit}} \bmod L_y) L_y = 0.011\,\mathrm{m} < \lambda_c$. This leads to a effective drift velocity of $v_y^{\mathrm{eff}} = 0.011\,\mathrm{m}/(7T_{\mathrm{orbit}}) = 314\,\mathrm{m/s}$ and a drop time of $\tau_{\mathrm{drop}} = 1 \cdot 10^{-4}\,\mathrm{s}$, which also corresponds quite well to the observation in Fig. A.2.

From this discussion, it should become clear how aliasing effects caused by box sizes which are smaller than the distance a fast particle travels within the correlation time of the fluctuations influence the transport. For well defined orbits, this leads to an arbitrary behavior of the diffusion coefficient. We have seen that in the discussion of Fig. A.2. For an ensemble of slightly different orbits, averaging effects lead to a reduction of diffusivity, since the non-resonant particles dominate the more or less resonant ones (Fig. A.1). This effect seems to be very important to consider if simulations of fast particles are done in the common flux tube approach. It is crucial to recall that the particle is able to 'remember' a former correlation, although being decorrelated at an earlier time. This re-correlation is responsible for the re-validity of orbit averaging, which in turn forces the particle transport into a completely different regime compared to the non-periodic case.

Appendix B

Scaling Laws for Arbitrary Pitch Angles and Gyroradii

B.1 Gyroradius effects

In Chapters 6 and 7, we have already mentioned that the Equations (6.18) and (6.22), as well as (7.4) and (7.5), strictly spoken only describe the cases $\eta \to 1$ and $\eta \to 0$, since we have assumed either beam ions with very small gyroradii $\rho \ll \lambda_c$, where the gyroradius can be neglected, or trapped ions with small η, where it was assumed that the energy is substantially in the perpendicular component ($v_\perp \sim v$) and therefore large gyroradii $\rho \gtrsim \lambda_c$ occur, where the large gyroradius approach can be used. In this annex, we will expand these equations to arbitrary pitch angeles and gyroradii. In the following equations, we include FLR effects for both the case $0 < \rho < \rho_{\text{crit}}$ and $\rho > \rho_{\text{crit}}$, where we refer to the formulas for V^{eff} and λ^{eff} derived in Eqs. (3.11), (3.12), (3.15), and (3.16). However, for the sake of simplicity, we restrict the expansions for the small gyroradius limit to second order, and we set the 'critical gyroradius' ρ_{crit} to the value where the small gyroradius approach for $D(E)$ equalizes the large gyroradius approach. Moreover, the second order expressions are modified so that they fit the higher order expressions of Chapter 3 in the limit $\rho < \rho_{\text{crit}}$. For our approaches of the diffusion coefficient, the product $(V^{\text{eff}})^2\lambda^{\text{eff}}$ is decisive. We approach this expression in second order by

$$(V^{\text{eff}}_{\text{small}\,\rho})^2\lambda^{\text{eff}}_{\text{small}\,\rho} = V^2\lambda_c(1 - \frac{5}{2}\frac{\rho^2}{\lambda_c^2})\,, \tag{B.1}$$

$$(V^{\text{eff}}_{\text{large}\,\rho})^2\lambda^{\text{eff}}_{\text{large}\,\rho} = 1.73\,V^2(4\sqrt{\pi}\rho/\lambda_c)^{-1}\,. \tag{B.2}$$

As a criterion for distinguishing the small from the large Larmor radius regime, we find

$$\frac{\hat{\rho}^2}{\hat{\lambda}_c^2} = \frac{E}{\hat{\lambda}_c^2 T_i}(1-\eta^2) <> 0.132\,. \tag{B.3}$$

This is where $(V^{\text{eff}}_{\text{small}\,\rho})^2\lambda^{\text{eff}}_{\text{small}\,\rho} \approx (V^{\text{eff}}_{\text{large}\,\rho})^2\lambda^{\text{eff}}_{\text{large}\,\rho}$.

B.2 Electrostatic transport for passing ions

For beam ions with small gyroradius effects, we obtain (modified Eq. (6.18)):

$$\begin{aligned} D_{\mathrm{small}\rho}(E) &\approx \frac{\hat{V}_E^2\hat{\lambda}_V}{3\eta^2}\left(\frac{E}{T_e}\right)^{-1}\left[1-\frac{5}{2\hat{\lambda}_c^2}\frac{E}{T_e}(1-\eta^2)\right]\frac{\rho_i^2 c_i}{R_0} \\ &\propto \frac{1}{\eta^2 E}\left[1-\frac{5}{2\hat{\lambda}_c^2}\frac{E}{T_e}(1-\eta^2)\right] = \frac{1}{E_\parallel}\left[1-\frac{5}{2\hat{\lambda}_c^2}\frac{E_\perp}{T_e}\right] \\ &\qquad \text{for} \quad \frac{E}{\hat{\lambda}_c^2 T_i}(1-\eta^2) = \frac{E_\perp}{\hat{\lambda}_c^2 T_i} < 0.132\,. \end{aligned} \tag{B.4}$$

In Chapter 6, the term in angular brackets was neglected, since we assumed $\eta \to 1$ (i.e. $\rho \to 0$). For large gyroradii this expression changes to:

$$\begin{aligned} D_{\mathrm{large}\rho}(E) &\approx \frac{1.73\,\hat{V}_E^2\hat{\lambda}_c\hat{\lambda}_V}{12\sqrt{\pi(1-\eta^2)}\eta^2}\left(\frac{E}{T_e}\right)^{-3/2}\frac{\rho_i^2 c_i}{R_0} \\ &\propto \frac{1}{\sqrt{1-\eta^2}\eta^2 E^{3/2}} = \frac{1}{E_\perp^{1/2}E_\parallel} \\ &\qquad \text{for} \quad \frac{E}{\hat{\lambda}_c^2 T_i}(1-\eta^2) > 0.132\,. \end{aligned} \tag{B.5}$$

For beam ions, both cases can occur. Whereas for example for $\eta = 0.99$, $E/T_i \gtrsim 500$ for reaching the large gyroradius regime this value reduces to $E/T_i \gtrsim 9$ for $\eta = 0.7$, where particles can still be in the passing regime.

B.3 Electrostatic transport for trapped ions

For trapped ions with small gyroradius effects, we obtain:

$$\begin{aligned} D_{\mathrm{small}\rho}(E) &\approx \frac{2\hat{V}_E^2\hat{\lambda}_c\sqrt{\epsilon}}{3\sqrt{\eta^2(1-\eta^2)}}\left(\frac{E}{T_e}\right)^{-1}\left[1-\frac{5}{2\hat{\lambda}_c^2}\frac{E}{T_e}(1-\eta^2)\right]\frac{\rho_i^2 c_i}{R_0} \\ &\propto \frac{1}{\eta\sqrt{1-\eta^2}E}\,[...] = \frac{1}{E_\parallel^{1/2}E_\perp^{1/2}}\,[...] \\ &\qquad \text{for} \quad \frac{E}{\hat{\lambda}_c^2 T_i}(1-\eta^2) < 0.132\,. \end{aligned} \tag{B.6}$$

However, since η is small for trapped ions, this will only be the case for energies not exceeding the thermal energy very much. Since for those small energies, orbit averaging is valid in general, one can assume that Eq. (B.6) does not apply in reality.

For large gyroradii, what can be assumed for almost all fast particles with small η, this expression changes to (Eq. (6.22)):

$$\begin{aligned} D_{\mathrm{large}\rho}(E) &\approx \frac{1.73\hat{V}_E^2\hat{\lambda}_c\hat{\lambda}_V\sqrt{\epsilon}}{12\sqrt{\pi}\eta(1-\eta^2)}\left(\frac{E}{T_e}\right)^{-3/2}\frac{\rho_i^2 c_i}{R_0} \\ &\propto \frac{1}{\eta(1-\eta^2)E^{3/2}} = \frac{1}{E_\parallel^{1/2}E_\perp} \\ &\qquad\text{for}\quad \frac{E}{\hat{\lambda}_c^2 T_i}(1-\eta^2) > 0.132\,. \end{aligned} \tag{B.7}$$

B.4 Magnetic transport for passing ions

For beam ions with small gyroradius effects, we obtain (modified Eq. (7.4)):

$$\begin{aligned} D_{B,\mathrm{small}\rho}(E) &\approx \frac{(C\,\beta/\beta_{\mathrm{crit}})^2\hat{\lambda}_B}{3}\left[1-\frac{5}{2\hat{\lambda}_c^2}\frac{E}{T_e}(1-\eta^2)\right]\frac{\rho_i^2 c_i}{R_0} \\ &\propto \mathit{const}\times[...] \\ &\qquad\text{for}\quad \frac{E}{\hat{\lambda}_c^2 T_i}(1-\eta^2) < 0.132\,. \end{aligned} \tag{B.8}$$

For beam ions with large gyroradius effects, the relation becomes

$$\begin{aligned} D_{B,\mathrm{large}\rho}(E) &\approx \frac{1.73(C\,\beta/\beta_{\mathrm{crit}})^2\hat{\lambda}_B^2}{12\sqrt{\pi(1-\eta^2)}}\left(\frac{E}{T_i}\right)^{-1/2}\frac{\rho_i^2 c_i}{R_0} \\ &\propto \frac{1}{\sqrt{1-\eta^2}E^{1/2}} = \frac{1}{E_\perp^{1/2}} \\ &\qquad\text{for}\quad \frac{E}{\hat{\lambda}_c^2 T_i}(1-\eta^2) > 0.132\,. \end{aligned} \tag{B.9}$$

B.5 Magnetic transport for trapped ions

For trapped ions with small gyroradius effects, we obtain

$$\begin{aligned} D_{B,\mathrm{small}\rho}(E) &\approx \frac{2(C\,\beta/\beta_{\mathrm{crit}})^2\hat{\lambda}_B\sqrt{\epsilon}\eta}{3\sqrt{1-\eta^2}}\left[1-\frac{5}{2\hat{\lambda}_c^2}\frac{E}{T_e}(1-\eta^2)\right]\frac{\rho_i^2 c_i}{R_0} \\ &\propto \frac{\eta}{\sqrt{1-\eta^2}}[...] = \frac{E_\parallel^{1/2}}{E_\perp^{1/2}}[...] \\ &\qquad\text{for}\quad \frac{E}{\hat{\lambda}_c^2 T_i}(1-\eta^2) < 0.132\,. \end{aligned} \tag{B.10}$$

Analogue to the electrostatic case, since η is small for trapped ions, this will only be the case for energies not exceeding the thermal energy very much. Since for those small energies, orbit averaging is valid in general, one can assume that Eq. (B.10) does not apply in reality.

If finite gyroradius effects for large gyroradii are included, what can be assumed for almost all fast particles with small pitch angles, this expression changes to (Eq. 7.5):

$$
\begin{aligned}
D_{B,\mathrm{large}\rho}(E) &\approx \frac{1.73(C\,\beta/\beta_{\mathrm{crit}})^2\hat{\lambda}_B^2\sqrt{\epsilon}\eta}{12\sqrt{\pi}(1-\eta^2)}\left(\frac{E}{T_e}\right)^{-1/2}\frac{\rho_i^2 c_i}{R_0} \qquad \text{(B.11)}\\
&\propto \frac{\eta}{(1-\eta^2)E^{1/2}} = \frac{E_\parallel^{1/2}}{E_\perp}\\
&\qquad\qquad \text{for} \quad \frac{E}{\hat{\lambda}_c^2 T_i}(1-\eta^2) > 0.132\,.
\end{aligned}
$$

B.6 Pitch angle dependence

Although the above expressions have been modified for arbitrary pitch angles concerning the FLR effects, they are, strictly spoken, still only valid in the limits $\eta \to 1$ for passing particles and $\eta \to 0$ for trapped particles, since the formulas for the orbit circulation time and the shift away from the magnetic flux surfaces are derived in this limit (Wesson, 1997). However, as we could demonstrate using particle orbit simulations with the GOURDON code, the concerning expressions can be assumed to be valid for *all* values of η in a good approximation. One only has to ensure whether the particles are trapped or passing, so there is no continous transformation with η from trapped to passing orbits, but a sharp jump. The question whether a particle is trapped or passing can be obtained the normal way, see the discussion at the end of Section 2.1.5.

Appendix C

List of Physical Abbreviations

B	magnetic field
B_0	constant background part of B
$\tilde{B}$	turbulent part of B (local *or* mean value)
c	velocity of light
C	parameter (~ 1)
$c_e = \sqrt{T_e/m_e}$	thermal electron velocity
$c_i = \sqrt{T_i/m_i}$	thermal ion velocity
$c_s = \sqrt{T_e/m_i}$	ion sound speed
$D(t) = \frac{1}{2}\frac{d}{dt}\langle\delta x^2(t)$	test particle diffusion coefficient
e	(elementary) charge (pos. or neg.)
e (index)	electron
E	test particle energy *or* Eulerian autocorrelation function *or* electric field
i (index)	ion (mostly deuterium)
$K = \tau_c V/\lambda_c$	Kubo number
$K^{\text{eff}} = \tau^{\text{eff}} V/\lambda_c$	effective Kubo number
L	Lagrangian autocorrelation function in general, in particular of the electrostatic potential
L_{v_x}	Lagrangian autocorrelation function of the velocity field (x direction)
$L_\perp$	typical perpendicular global scale length
M	number of fluxtubes filling the torus
$p_{\text{mag}} = B^2/(2\mu_0)$	magnetic pressure
$q = N_{\text{tor}}/N_{\text{pol}}$	safety factor
r	radial torus coordinate (Fig. 2.1)
$\Delta r \equiv \Delta x$	max. deviation of the drift orbit from the magnetic flux surface, 'orbit diameter'
R	distance from major axis (Fig. 2.1)
R_0	major radius of a tokamak (Fig. 2.1)
R_c	curvature radius
$\hat{s}(r) = r/q(r)\, dq/dr$	magnetic shear

T	background plasma 'temperature' in dimension of energy (Joule or eV)
$T_g = 2\pi m/(eB)$	gyro (Larmor) period
T_{orbit}	drift orbit period
v, $(v_\perp, v_\parallel)$	particle velocity (component)
$v_B = v_\parallel \tilde{B}/B_0$	turbulent magnetic drift velocity
$v_{\nabla B}$	gradient-B drift velocity
v_{curv}	curvature drift velocity
v_d	diamagnetic drift velocity
v_{dr}	poloidal (diamagnetic) drift velocity of the background turbulence
v_D	drift velocity in general
v_E	$E \times B$ drift velocity
$v_y \equiv v_\zeta$	toroidal precession drift velocity
V	mean turbulent drift velocity in general, in particular $E \times B$ drift
V_E	mean $E \times B$ drift velocity
V_B	mean turbulent magnetic drift velocity
x, y, z	cartesian *or* fluxtube coordinates
$\Delta x \equiv \Delta r$	max. deviation of the drift orbit from the magnetic flux surface, 'orbit diameter'
$\beta = (q\chi - \zeta) \mod 2\pi$	field line coordinate
$\beta = p/p_{\text{mag}}$	'plasma beta'
β_{crit}	maximal value for β before kinetic ballooning modes appear
$\gamma \quad (D \propto \lambda_c^{2-\gamma} V^\gamma \tau_c^{\gamma-1})$	diffusion scaling exponent
$\gamma \equiv \frac{1}{\sqrt{1-\frac{v^2}{c^2}}} = \frac{E_{\text{kin}}}{m_0 c^2} + 1$	'Lorentz factor'
$\Gamma = \langle \tilde{n}\tilde{v} \rangle$	cross-field transport (particle flux)
$\Gamma = D\nabla n_0$	diffusive particle flux
$\epsilon = r/R_0$	inverse aspect ratio
ζ	toroidal torus coordinate (Fig. 2.1)
$\zeta = \lambda_x/\lambda_y$	'anisotropy parameter'
$\eta = v_\parallel/v$	pitch angle
θ	poloidal torus coordinate (Fig. 2.1)
$\lambda_c, \lambda_\perp$	perpendicular correlation length in general, in particular of the electrostatic potential
λ_x, λ_y	correlation lengths in x or y direction
λ_V	perpendicular correlation length of the $E \times B$ velocity field
λ_B	perpendicular correlation length of the magnetic field
$\mu = mv_\perp^2/(2B)$	magnetic moment
$\Xi_{o.a.} \equiv \max\left\{\bar{V}^{\text{eff}}, \lvert v_{\text{dr}} - v_y \rvert\right\} \frac{T_{\text{orbit}}}{\lambda_c}$	orbit averaging validity parameter

$\rho_e = m_e c_e/(eB)$	electron thermal gyro (Larmor) radius
$\rho_g \equiv \rho = mv_\perp/(eB)$	particle gyro (Larmor) radius
$\rho_i = m_i c_i/(eB)$	ion ($Z_i = 1$) thermal gyro (Larmor) radius
$\rho_s = m_i c_s/(eB)$	gyro (Larmor) radius of a ion ($Z_i = 1$) with $v = c_s$
τ	correlation time in general
τ_c	correlation time of the electrostatic (magnetic) potential
$\tau_{\mathrm{drop}} = 2\lambda_y/v_{\mathrm{dr}} \quad (2\lambda_y/v_y)$	'drop time'
τ^{eff}	effective decorrelation time responsible for transition to diffusive regime
$\tau_{\mathrm{fl}} = \lambda_c/V$	flight time
$\tau^{\mathrm{orbit}} = \lambda_V T_{\mathrm{orbit}}/(\pi\Delta x)$	perpendicular orbit decorrelation time
$\tau_\parallel = \lambda_\parallel/v_\parallel$	parallel decorrelation time
ϕ	electrostatic potential
ϕ^{eff}	gyroaveraged electrostatic potential
$\bar{\phi}^{\mathrm{eff}}$	orbit averaged electrostatic potential
φ	phase
$\varphi \equiv \zeta$	toroidal torus coordinate
χ	modified (straight) 'poloidal' coordinate
$\Omega_g = eB_0/m$	gyro (Larmor) frequency

Bibliography

Afanasiev, V.V., Sagdeev, R.Z., & Zaslavsky, G.M. 1991. Chaotic jets with multifractal space-time random walk. *Chaos*, **1**, 143.

Angioni, C., & Peeters, A.G. 2008. Gyrokinetic calculations of diffusive and convective transport of alpha particles with a slowing-down distribution function. *Physics of Plasmas*, **15**, 052307.

Annibaldi, S. V., G., Manfredi, & O., Dendy R. 2002. Non-Gaussian transport in strong plasma turbulence. *Physics of Plasmas*, **9**, 791.

Baker, D.R., Greenfield, C.M., & Burrell, K.H. 2001. Thermal diffusivities in DIII-D show evidence of critical gradients. *Physics of Plasmas*, **8**, 4128.

Balescu, R. 2005. *Aspects of Anomalous Transport in Plasmas*. Institute of Physics Publishing.

Basu, R., Jessen, T., Naulin, V., & Rasmussen, J. J. 2003. Turbulent flux and the diffusion of passive tracers in electrostatic turbulence. *Physics of Plasmas*, **10**, 2696.

Beck, R. 2003. *Kosmische Magnetfelder*. Tätigkeitsbericht, Max-Planck-Institut für Radioastronomie.

Beer, M.A., Cowley, S.C., & Hammett, G.W. 1995. Field-aligned coordinates for nonlinear simulations of tokamak turbulence. *Physics of Plasmas*, **2**, 2687.

Belli, E.A., Hammett, G.W., & Dorland, W. 2008. Effects of plasma shaping on nonlinear gyrokinetic turbulence. *Physics of Plasmas*, **15**, 092303.

Bottino, A., Peeters, A.G., Hatzky, R., Jolliet, S., & McMillan, B.F. et al. 2007. Nonlinear low noise particle-in-cell simulations of electron temperature gradient driven turbulence. *Physics of Plasmas*, **14**, 10701.

Brizard, A. 1989. Gyrokinetic energy-conservation and poisson-bracket formulation. *Physics of Fluids B*, **1**, 1381.

Bronstein, I. N., & Semedjajew, K. A. 2000. *Taschenbuch der Mathematik*. Verlag Harri Deutsch.

Callen, J.D., & Kissick, M.W. 1997. Evidence and concepts for non-local transport. *Plasma Physics and Controlled Fusion*, **39**, B173.

Candy, J., Waltz, R.E., & Dorland, W. 2004. The local limit of global gyrokinetic simulations. *Physics of Plasmas*, **11**, L25.

Candy, J., Waltz, R.E., Fahey, M.R., & Holland, C. 2007. The effect of ion-scale dynamics on electron-temperature-gradient turbulence. *Plasma Physics and Controlled Fusion*, **49**, 1209.

Carreras, B.A., Newman, D., Lynch, V.E., & Diamond, P.H. 1996. A model realization of self-organized criticality for plasma confinement. *Physics of Plasmas*, **3**, 2903.

Carreras, B.A., van Milligen, B., Pedrosa, M.A., Balbin, R., & Hidalgo, C. et al. 1998. Long-range time correlations in plasma edge turbulence. *Physical Review Letters*, **80**, 4438.

Carreras, B.A., Lynch, V.E., Newman, D.E., & Zaslavsky, G.M. 1999a. Anomalous diffusion in a running sandpile model. *Physical Review E*, **60**, 4770.

Carreras, B.A., van Milligen, B., Pedrosa, M.A., Balbin, R., & Hidalgo, C. et al. 1999b. Experimental evidence of long-range correlations and self-similarity in plasma fluctuations. *Physics of Plasmas*, **6**, 1885.

Carreras, B.A., Lynch, V.E., & Zaslavsky, G.M. 2001. Anomalous diffusion and exit time distribution of particle tracers in plasma turbulence model. *Physics of Plasmas*, **8**, 5096.

Chen, F. F. 1984. *Introduction to Plasma Physics and Controlled Fusion.* Plenum Press.

Conway, G.D. 2008. Turbulence measurements in fusion plasmas. *Plasma Physics and Controlled Fusion*, **50**, 124026.

Corrsin, S. 1959. *In:* Frenkiel, F., & Sheppard, P. (eds), *Atmospheric Diffusion and Air Pollution.* Academic Press, New York.

Cowley, S.C., Kulsrud, R.M., & Sudan, R. 1991. Considerations of ion-temperature-gradient-driven turbulence. *Physics of Fluids B*, **3**, 2767.

Dannert, T. 2005. *Gyrokinetische Simulation von Plasmaturbulenz mit gefangenen Teilchen und elektromagnetischen Effekten.* Ph.D. thesis, Technische Universität München, Max-Planck-Institut für Plasmaphysik, Garching.

Dannert, T., & Jenko, F. 2005. Gyrokinetic simulation of collisionless trapped-electron mode turbulence. *Physics of Plasmas*, **12**, 072309.

Dannert, T., Günter, S., Hauff, T., Jenko, F., & Lauber, P. 2008. Turbulent transport of beam ions. *Physics of Plasmas*, **15**, 062508.

del Castillo-Negrete, D. 1998. Asymmetric transport and non-Gaussian statistics of passive scalars in vortices in shear. *Physics of Fluids*, **10**, 576.

del Castillo-Negrete, D. 2000. Chaotic transport in zonal flows in analogous geophysical and plasma systems. *Physics of Plasmas*, **7**, 1702.

del Castillo-Negrete, D., Carreras, B.A., & Lynch, V.E. 2004. Fractional diffusion in plasma turbulence. *Physics of Plasmas*, **11**, 3854.

Dentz, M., Cortis, A., Scher, H., & Berkowitz, B. 2004. Time behavior of solute transport in heterogeneous media: transition from anomalous to normal transport. *Advances in Water Resources*, **27**, 115.

D'haeseleer, W.D., Hitchon, W.N.G., Callen, J.D., & Shohet, J.L. 1990. *Flux Coordinates and Magnetic Field Structure*. Springer-Verlag.

Diamond, P.H., Itoh, S.-I., Itoh, K., & Hahm, T.S. 2005. Zonal flows in plasma - a review. *Plasma Physics and Controlled Fusion*, **47**, R35.

Dimits, A.M., Bateman, G., Beer, M.A., Cohen, B.I., & Dorland, W. et al. 2000. Comparisons and physics basis of tokamak transport models and turbulence simulations. *Physics of Plasmas*, **7**, 969.

Dorland, W., Jenko, F., Kotschenreuther, M., & Rogers, B.N. 2000. Electron temperature gradient turbulence. *Physical Review Letters*, **85**, 5579.

Drake, J.F., Guzdar, P.N., & A.B., Hassam. 1988. Streamer formation in plasma with a temperature-gradient. *Physical Review Letters*, **61**, 2205.

Einstein, A. 1905. Über die von der molekularkinetischen Theorie der Wärme geforderte Bewegung von in ruhenden Flüssigkeiten suspendierten Teilchen. *Annalen der Physik*, **17**, 549.

Entrop, I., Lopes Cardozo, N.J., Jaspers, R., & Finken, K.H. 1998. Diffusion of runaway electrons in TEXTOR-94. *Plasma Physics and Controlled Fusion*, **40**, 1513.

Entrop, I., Lopes Cardozo, N.J., Jaspers, R., & Finken, K.H. 2000. Scale size of magnetic turbulence in tokamaks probed with 30-MeV electrons. *Physical Review Letters*, **84**, 3606.

Esposito, B., Solis, R.M., & vanBelle, P. 1996. Runaway electron measurements in the JET tokamak. *Plasma Physics and Controlled Fusion*, **38**, 2035.

Estrada-Mila, C., Candy, J., & Waltz, R. E. 2006. Turbulent transport of alpha particles in reactor plasmas. *Physics of Plasmas*, **13**, 112303.

Fasoli, A.F., Skiff, F.N., Good, T.N., Paris, P.J., & Tran, M.Q. 1992. Test-ion diffusion in a magnetized plasma. *IEEE Transactions on Plasma Science*, **20**, 655.

Frieman, E.A., & Chen, L. 1982. Non-linear gyrokinetic equations for low-frequency electromagnetic-waves in general plasma equilibria. *Physics of Fluids*, **25**, 502.

Fülöp, T., & Nordman, H. 2009. Turbulent and neoclassical impurity transport in tokamak plasmas. *Physical of Plasmas*, **16**, 032306.

Gaffey, J.D. 1976. Energetic ion distribution resulting from neutral beam injection in tokamaks. *Journal of Plasma Physics*, **16**, 149.

Gentle, K.W., Bravenec, R.V., & Cima, G. 1995. An experimental counterexample to the local transport paradigm. *Physics of Plasmas*, **2**, 2292.

Görler, T. 2009. *Multiscale effects in plasma microturbulence*. Ph.D. thesis, Universität Ulm, Max-Planck-Institut für Plasmaphysik, Garching.

Görler, T., & Jenko, F. 2008. Scale separation between electron and ion thermal transport. *Physical Review Letters*, **100**, 185002.

Gourdon, C. 1970. *Programme optimisé de calculs numériques dans les configurations magnétiques toroidales*. CEN, Fontenay aux Roses.

Gradshteyn, & Ryzhik. 1994. *Table of Integrals, Series, and Products*. Academic Press, Harcourt Brace and Company.

Green, M.S. 1951. Brownian motion in a gas of noninteracting molecules. *Journal of Chemical Physics*, **19**, 1036.

Greene, J.M., & Johnson, J.L. 1962. Stability criterion for arbitrary hydromagnetic equilibria. *Physics of Fluids*, **5**, 510.

Gruzinov, A. V., Isichenko, M. B., & Kalda, Y. L. 1990. Two-dimensional turbulent diffusion. *Soviet Physics JETP*, **70**, 263.

Günter, S. 2009. private communication.

Günter, S., Conway, G., daGraça, S., Fahrbach, H.-U., & Forest, C. et al. 2007. Interaction of energetic particles with large and small scale instabilities. *Nuclear Fusion*, **47**, 920.

Gurevich, A.V., Milikh, G.M., & Rousseldupre, R. 1992. Runaway electron mechanism of air breakdown and preconditioning during a thunderstorm. *Physics Letters A*, **165**, 463.

Hahm, T.S. 1988. Nonlinear gyrokinetic equations for tokamak microturbulence. *Physics of Fluids*, **31**, 2670.

Hahm, T.S., Lee, W., & Brizard, A. 1988. Nonlinear gyrokinetic theory for finite-beta plasmas. *Physics of Fluids*, **31**, 1940.

Haller, G. 2000. Finding finite-time invariant manifolds in two-dimensional velocity fields. *Chaos*, **10**, 99.

Hasegawa, A., & Wakatani, M. 1983. Plasma edge turbulence. *Physical Review Letters*, **50**, 682.

Hauff, T. 2006. *Gyrierende Testteilchen in turbulenten Magnetoplasmen*. Diploma thesis, Universität Ulm, Max-Planck-Institut für Plasmaphysik, Garching.

Hauff, T., & Jenko, F. 2006. Turbulent ExB advection of charged test particles with large gyroradii. *Physics of Plasmas*, **13**, 102309.

Hauff, T., & Jenko, F. 2007. ExB advection of trace ions in tokamak microturbulence. *Physics of Plasmas*, **14**, 092301.

Hauff, T., & Jenko, F. 2008. Mechanisms and scalings of energetic ion transport via tokamak microturbulence. *Physics of Plasmas*, **15**, 112307.

Hauff, T., & Jenko, F. 2009a. Runaway electron transport via tokamak microturbulence. *Physics of Plasmas*, **16**, 102308.

Hauff, T., & Jenko, F. 2009b. Streamer-induced electron transport in electron temperature gradient turbulence. *Physics of Plasmas*, **16**, 102306.

Hauff, T., Jenko, F., & Eule, S. 2007. Intermediate non-Gaussian transport in plasma core turbulence. *Physics of Plasmas*, **14**, 102316.

Hauff, T., Pueschel, M.J., Dannert, T., & Jenko, F. 2009. Electrostatic and magnetic transport of energetic ions in turbulent plasmas. *Physical Review Letters*, **102**, 075004.

Hegna, C.C., & Callen, J.D. 1993. Plasma transport in mixed magnetic topologies. *Physics of Fluids B*, **5**, 1804.

Heidbrink, W.W., Barnes, C.W., Hammett, G.W., Kusama, Y., & Scott, S.D. et al. 1991. The diffusion of fast ions in ohmic TFTR discharges. *Physics of Fluids B*, **3**, 3167.

Helander, P., Eriksson, L.-G., & Andersson, F. 2002. Runaway acceleration during magnetic reconnection in tokamaks. *Plasma Physics and Controlled Fusion*, **44**, B247.

Hinze, J.O. 1959. *Turbulence. An Introduction to its Mechanism and Theory.* McGraw-Hill Book Company.

Idomura, Y. 2006. Self-organization in electron temperature gradient driven turbulence. *Physics of Plasmas*, **13**, 080701.

Isichenko, M. B. 1992. Percolation, statistical topography, and transport in random media. *Reviews of Modern Physics*, **64**, 961.

ITER, Homepage. 2009. *www.iter.org.*

ITER, Physics Basis Editors. 1999. *Nuclear Fusion*, **39**, 2137.

Jaspers, R., Lopes Cardozo, N.J., Finken, K.H., Schokker, B.C., Mank, G., Fuchs, G., & Schuller, F.C. 1994. Islands of runaway electrons in the TEXTOR tokamak and relation to transport in a stochastic field. *Physical Review Letters*, **72**, 4093.

Jaspers, R., Lopes Cardozo, N.J., Schuller, F.C., Finken, K.H., Grewe, T., & Mank, G. 1996. Disruption generated runaway electrons in TEXTOR and ITER. *Nuclear Fusion*, **36**, 367.

Jenko, F., & Dorland, W. 2002. Prediction of significant tokamak turbulence at electron gyroradius scales. *Physical Review Letters*, **89**, 225001.

Jenko, F., Dorland, W., Kotschenreuther, M., & Rogers, B. N. 2000. Electron temperature gradient driven turbulence. *Physics of Plasmas*, **7**, 1904.

Kadomtsev, B. B. 1965. *Plasma Turbulence*. Academic, London.

Kammerer, M., Merz, F., & Jenko, F. 2008. Exceptional points in linear gyrokinetics. *Physics of Plasmas*, **15**, 052102.

Kaufman, A.N. 1972. Quasilinear diffusion of an axisymmetric toroidal plasma. *Physics of Fluids*, **15**, 1063.

Kruskal, M.D., & Kulsrud, R.M. 1958. Equilibrium of a magnetically confined plasma in a toroid. *Physics of Fluids*, **1**, 265.

Kubo, R. 1957. Statistical-mechanical theory of irreversible processes. 1. General theory and simple applications to magnetic and conduction problems. *Journal of the Physical Society of Japan*, **12**, 570.

Kubo, R. 1963. Stochastic Liouville equations. *Journal of Mathematical Physics*, **4**, 174.

Landau, L. D., & Lifshitz, E. M. 1960. *Course of Theoretical Physics, Vol.1*. Pergamon Press.

Lang, J., Chen, Y., & Parker, S.E. 2007. Gyrokinetic delta f particle simulation of trapped electron mode driven turbulence. *Physics of Plasmas*, **14**, 082315.

Lapillonne, X., Brunner, S., Dannert, T., Jolliet, S., Marinoni, A., Villard, L., Görler, T., Jenko, F., & Merz, F. 2009. Clarifications to the limitations of the s-α equilibrium model for gyrokinetic computations of turbulence. *Physics of Plasmas*, **16**, 032308.

Lawson, J. D. 1957. Some criteria for a power producing thermonuclear reactor. *Proceedings of the Physical Society. Section B*, **70**, 6.

Leoncini, X., & Zaslavsky, G.M. 2002. Jets, stickiness, and anomalous transport. *Physical Review E*, **65**, 046216.

Leoncini, X., Agullo, O., Benkadda, S., & Zaslavsky, G.M. 2005. Anomalous transport in Charney-Hasegawa-Mima flows. *Physical Review E*, **72**, 026218.

Liewer, P. C. 1985. Measurements of microturbulence in tokamaks and comparison with theories of turbulence and anomalous transport. *Nuclear Fusion*, **25**, 543.

Lin, Z., Chen, L., & Zonca, F. 2005. Role of nonlinear toroidal coupling in electron temperature gradient turbulence. *Physics of Plasmas*, **12**, 056125.

Lin, Z., Holod, I., Chen, L., Diamond, P.H., Hahm, T.S., & Ethier, S. 2007. Wave-particle decorrelation and transport of anisotropic turbulence in collisionless plasmas. *Physical Review Letters*, **99**, 265003.

Littlejohn, R. G. 1983. Variational-principles of guiding center motion. *Journal of Plasma Physics*, **29**, 111.

Mahdizadeh, N., Greiner, F., Happel, T., Kendl, A., & Ramisch, M. et al. 2007. Investigation of the parallel dynamics of drift-wave turbulence in toroidal plasmas. *Plasma Physics and Controlled Fusion*, **49**, 1005.

Manfredi, G., & Dendy, R. O. 1996. Test-particle transport in strong electrostatic drift turbulence with finite larmor radius effects. *Physical Review Letters*, **76**, 4360.

Manfredi, G., & Dendy, R. O. 1997. Transport properties of energetic particles in a turbulent electrostatic field. *Physics of Plasmas*, **4**, 628.

Merz, F. 2008. *Gyrokinetic simulation of multimode plasma turbulence*. Ph.D. thesis, Westfälische Wilhelms-Universität Münster, Max-Planck-Institut für Plasmaphysik, Garching.

Metzler, R., & Klafter, J. 2000. The random walk's guide to anomalous diffusion: a fractional dynamics approach. *Physics Reports*, **339**, 1.

Metzler, R., & Klafter, J. 2004. The restaurant at the end of the random walk: recent developments in the description of anomalous transport by fractional dynamics. *Journal of Physics A*, **37**, R161.

Mier, J.A., Garcia, L., & Sanchez, R. 2006. Study of the interaction between diffusive and avalanche-like transport in near-critical dissipative-trapped-electron-mode turbulence. *Physics of Plasmas*, **13**, 102308.

Misguich, J. H., Balescu, R., Pecseli, H. L., Mikkelsen, T., Larsen, S. E., & Xiaoming, Q. 1987. Diffusion of charged particles in turbulent magnetoplasmas. *Plasma Physics and Controlled Fusion*, **29**, 825.

Montroll, E. W., & Weiss, G. H. 1965. Random walks on lattices. *Journal of Mathematical Physics*, **6**, 167.

Mynick, H.E., & Boozer, A.H. 2005. The effect on stellarator neoclassical transport of a fluctuating electrostatic spectrum. *Physics of Plasmas*, **12**, 062513.

Mynick, H.E., & Krommes, J.A. 1979. Particle diffusion by magnetic perturbations of axisymmetric geometries. *Physical Review Letters*, **43**, 1506.

Mynick, H.E., & Strachan, J.D. 1981. Transport of runaway and thermal electrons due to magnetic microturbulence. *Physics of Fluids*, **24**, 695.

Myra, J.R., & Catto, P.J. 1992. Effect of drifts on the diffusion of runaway electrons in tokamak stochastic magnetic fields. *Physics of Fluids B*, **4**, 176.

Myra, J.R., Catto, P.J., Mynick, H.E., & Duvall, R.E. 1993. Quasi-linear diffusion in stochastic magnetic fields - reconciliation of drift-orbit modification calculations. *Physics of Fluids B*, **5**, 1160.

Naitou, H., Kamimura, T., & Dawson, J.M. 1979. Kinetic effects on the convective plasma-diffusion and the heat-transport. *Journal of the Physical Society of Japan*, **46**, 258.

Naulin, V., Nielsen, A. H., & Rasmussen, J. J. 1999. Dispersion of ideal particles in a two-dimensional model of electrostatic turbulence. *Physics of Plasmas*, **6**, 4575.

Nevins, W.M., Candy, J., Cowley, S., Dannert, T., & Dimits, A. et al. 2006. Characterizing electron temperature gradient turbulence via numerical simulation. *Physics of Plasmas*, **13**, 122306.

Nevins, W.M., Parker, S.E., Chen, Y., Candy, J., & Dimits, A.M. et al. 2007. Verification of gyrokinetic delta f simulations of electron temperature gradient turbulence. *Physics of Plasmas*, **14**, 084501.

Nycander, J., & Yankov, V.V. 1995. Anomalous pinch flux in tokamaks driven by the longitudinal adiabatic invariant. *Physics of Plasmas*, **2**, 2874.

Nycander, J., & Yankov, V.V. 1996. Turbulent equipartition and up-gradient transport. *Physica Scripta*, **T63**, 174.

O'Connell, R., Den Hartog, D.J., Forest, C.B., Anderson, J.K., & Biewer, T.M. et al. 2003. Observation of Velocity-Independent Electron Transport in the Reversed Field Pinch. *Physical Review Letters*, **91**, 045002.

Padberg, K., Hauff, T., Jenko, F., & Junge, O. 2007. Lagrangian structures and transport in turbulent magnetized plasmas. *New Journal of Physics*, **9**, 400.

Pankin, A., McCune, D., Andre, R., Bateman, G., & Kritz, A. 2004. The tokamak Monte Carlo fast ion module NUBEAM in the National Transport Code Collaboration library. *Computer Physics Communications*, **159**, 157.

Perkins, F.W., Barnes, C.W., & Johnson, D.W. 1993. Nondimensional transport scaling in the tokamak fusion test reactor - is tokamak transport Bohm or gyro-Bohm. *Physics of Fluids B*, **5**, 477.

Pinches, S.D. 1996. *Nonlinear interaction of fast particles with Alfvén waves in tokamaks*. Ph.D. thesis, University of Nottingham.

Pueschel, M.J. 2009. *Electromagnetic effects in gyrokinetic simulations of plasma turbulence*. Ph.D. thesis, Westfälische Wilhelms-Universität Münster, Max-Planck-Institut für Plasmaphysik, Garching.

Pueschel, M.J., Kammerer, M., & Jenko, F. 2008. Gyrokinetic turbulence simulations at high plasma beta. *Physics of Plasmas*, **15**, 102310.

Reuss, J. D., Vlad, M., & Misguich, J. H. 1998. Percolation scaling for transport in turbulent plasmas. *Physics Letters A*, **241**, 94.

Reuss, J. D. and Misguich, J. H. 1996. Low-frequency percolation scaling for particle diffusion in electrostatic turbulence. *Physical Review E*, **54**, 1857.

Rewoldt, G. 1988. Alpha-particle effects on high-normal instabilities in tokamaks. *Physics of Fluids*, **31**, 3727.

Rewoldt, G. 1991. Comparison of high-N instabilities including alpha-particle effects in BPX and TFTR. *Nuclear Fusion*, **31**, 2333.

Shalchi, A. 2007. *Nonlinear effects in cosmic ray transport theory.* Professorial dissertation (Habilitationsschrift), Ruhr-Universität Bochum.

Taylor, G. I. 1920. Diffusion by continuous movements. *Proceedings of the London Mathematical Society*, **20**, 196.

Terry, P.W. 2000. Suppression of turbulence and transport by sheared flow. *Reviews of Modern Physics*, **72**, 109.

Thomsen, H., Endler, M., Bleuel, J., Chankin, A.V., Erents, S.K., & Matthews, G.F. 2002. Parallel correlation measurements in the scrape-off layer of the Joint European Torus. *Physics of Plasmas*, **9**, 1233.

Told, D. 2008. *Gyrokinetische Turbulenzsimulationen für den Tokamak ASDEX Upgrade.* Diploma thesis, Universität Ulm, Max-Planck-Institut für Plasmaphysik, Garching.

Tu, C.-Y., & Marsch, E. 1995. *MHD structures, waves and turbulence in the solar wind.* Kluwer Academic Publishers.

Vallée, J. P. 2004. Cosmic magnetic fields – as observed in the universe, in galactic dynamos, and in the milky way. *New Astronomy Reviews*, **48**, 763.

van Milligen, B.P., Sanchez, R., & Carreras, B.A. 2004a. Probabilistic finite-size transport models for fusion: Anomalous transport and scaling laws. *Physics of Plasmas*, **11**, 2272.

van Milligen, B.P., Carreras, B.A., & Sanchez, R. 2004b. Uphill transport and the probabilistic transport model. *Physics of Plasmas*, **11**, 3787.

Vesely, F. J. 1994. *Computational Physics.* Plenum Press, New York.

Vlad, M., & Spineanu, F. 2005. Larmor radius effects on impurity transport in turbulent plasmas. *Plasma Physics and Controlled Fusion*, **47**, 281.

Vlad, M., Spineanu, F., Misguich, J. H., & Balescu, R. 1998. Diffusion with intrinsic trapping in two-dimensional incompressible stochastic velocity fields. *Physical Review E*, **58**, 7359.

Vlad, M., Spineanu, F., Misguich, J. H., Reuss, J. D., Balescu, R., Itoh, K., & Itoh, S. I. 2004. Lagrangian versus Eulerian correlations and transport scaling. *Plasma Physics and Controlled Fusion*, **46**, 1051.

Vlad, M., Spineanu, F., Itoh, S. I., Yagi, M., & Itoh, K. 2005. Turbulent transport of ions with large Larmor radii. *Plasma Physics and Controlled Fusion*, **47**, 1015.

Wagner, F., & Stroth, U. 1993. Transport in toroidal devices - the experimentalists view. *Plasma Physics and Controlled Fusion*, **35**, 1321.

Waltz, R.E. 1985. Numerical simulation of electromagnetic turbulence in tokamaks. *Physics of Fluids*, **28**, 577.

Waltz, R.E., Candy, J.M., & Rosenbluth, M.N. 2002. Gyrokinetic turbulence simulation of profile shear stabilization and broken gyroBohm scaling. *Physics of Plasmas*, **9**, 1938.

Wesson, J. 1997. *Tokamaks*. Oxford Science Publications.

Wingen, A., Abdullaev, S.S., Finken, K.H., Jakubowski, M., & Spatschek, K.H. 2006. Influence of stochastic magnetic fields on relativistic electrons. *Nuclear Fusion*, **46**, 941.

Wootton, A.J., Carreras, B.A., Matsumoto, H., McGuire, K., & Peebles, W.A. et al. 1990. Fluctuations and anomalous transport in tokamaks. *Physics of Fluids B*, **2**, 2879.

Yeung, P.K., & Pope, S.B. 1988. An algorithm for tracking fluid particles in numerical simulations of homogeneous turbulence. *Journal of Computational Physics*, **79**, 373.

Zaslavsky, G. M., Edelman, M., Weitzner, H., Carreras, B., McKee, G., Bravenec, R., & Fonck, R. 2000. Large-scale behavior of the tokamak density fluctuations. *Physics of Plasmas*, **7**, 3691.

Zhang, W., Lin, Z., & Chen, L. 2008. Transport of energetic particles by microturbulence in magnetized plasmas. *Physical Review Letters*, **101**, 095001.

Zimbardo, G. 2005. Anomalous particle diffusion and Lévy random walk of magnetic field lines in three-dimensional solar wind turbulence. *Plasma Physics and Controlled Fusion*, **47**, B755.

Zou, X.L., Colas, L., Paume, M., Chareau, J.M., & Laurent, L. et al. 1995. Internal magnetic turbulence measurement in plasma by cross polarization scattering. *Physical Review Letters*, **75**, 1090.

Zweben, S.J., & Medley, S.S. 1989. Visible imaging of edge fluctuations in the TFTR tokamak. *Physics of Fluids B*, **1**, 2058.

List of Publications

Publications in peer-reviewed journals

T. Hauff and F. Jenko,
Turbulent $E\times B$ advection of charged test particles with large gyroradii,
Physics of Plasmas **13**, 102309 (2006).

T. Hauff and F. Jenko,
$E\times B$ advection of trace ions in tokamak microturbulence,
Physics of Plasmas **14**, 092301 (2007).

K. Padberg, T. Hauff, F. Jenko, and O. Junge,
Lagrangian structures and transport in turbulent magnetized plasmas,
New Journal of Physics **9**, 400 (2007).

T. Hauff, F. Jenko, and S. Eule,
Intermediate non-Gaussian transport in plasma core turbulence,
Physics of Plasmas **14**, 102316 (2007).

S. Günter, G. Conway, S. daGraça, H. -U. Fahrbach, C. Forest, M. Garcia Muñoz, T. Hauff, J. Hobirk, V. Igochine, F. Jenko, K. Lackner, P. Lauber, P. McCarthy, M. Maraschek, P. Martin, E. Poli, K. Sassenberg, E. Strumberger, G. Tardini, E. Wolfrum, H. Zohm, and ASDEX Upgrade Team,
Interaction of energetic particles with large and small scale instabilities,
Nuclear Fusion **47**, 920 (2007).

T. Dannert, S. Günter, T. Hauff, F. Jenko, and P. Lauber,
Turbulent transport of beam ions,
Physics of Plasmas **15**, 062508 (2008).

T. Hauff and F. Jenko,
Mechanisms and scalings of energetic ion transport via tokamak microturbulence,
Physics of Plasmas **15**, 112307 (2008).

T. Hauff, M.J. Pueschel, T. Dannert, and F. Jenko,
Electrostatic and magnetic transport of energetic ions in turbulent plasmas,
Physical Review Letters **102**, 075004 (2009).

T. Hauff and F. Jenko,
Streamer-induced transport in electron temperature gradient turbulence,
Physics of Plasmas **16**, 102306 (2009).

T. Hauff and F. Jenko,
Runaway electron transport via tokamak microturbulence,
Physics of Plasmas **16**, 102308 (2009).

Presentations at conferences

T. Hauff and F. Jenko,
Turbulent $E \times B$ advection of energetic particles (oral presentation),
IPP Theory Meeting, November 2006, Schloss Ringberg, Germany.

T. Hauff, T. Dannert, and F. Jenko,
Redistribution of energetic particles by background turbulence (oral presentation and conference proceedings),
3rd IAEA Technical Meeting on the Theory of Plasma Instabilities, March 2007, University of York, United Kingdom.

T. Hauff, T. Dannert, and F. Jenko,
Redistribution of energetic particles by background turbulence (poster presentation),
12th European Fusion Theory Conference, September 2007, Madrid, Spain.

T. Hauff, T. Dannert, and F. Jenko,
Redistribution of energetic particles by background turbulence (oral presentation),
IPP Theory Meeting, November 2007, Sellin, Germany.

T. Hauff, M.J. Pueschel, T. Dannert, and F. Jenko,
Electrostatic and magnetic transport of energetic ions in turbulent plasmas (oral presentation),
50th Annual Meeting of the Division of Plasma Physics of the American Physical Society, November 2008, Dallas, Texas.

T. Hauff, M.J. Pueschel, S. Guenter, T. Dannert, and F. Jenko,
Electrostatic and magnetic transport of energetic particles in turbulent plasmas (oral and poster presentation),
Joint EU-US Transport Task Force Workshop, April/May 2009, San Diego, California.

Danksagung

Die vorliegende Dissertation wurde am Max-Planck-Institut für Plasmaphysik in Garching bei München angefertigt.

Ganz herzlich danke ich Prof. Frank Jenko für die Ermöglichung dieser Arbeit und die Betreuung in den vergangenen drei Jahren. Seine Motivation und sein Vertrauen waren ein entscheidender Antrieb für mich und haben viel zum Gelingen beigetragen. Aus unseren Gesprächen und seinen von großer Intuition geprägten Hinweisen ergaben sich oftmals neue Ideen, aus denen wichtige Teile dieser Dissertation hervorgingen. Gleichzeitig konnte ich mich immer frei fühlen, neue Themengebiete auszuwählen und meine eigenen Wege zu gehen. Danken möchte ich ihm auch für die Ermöglichung des Besuchs zahlreicher Konferenzen und die stetige Anregung zu Publikationen, durch die ich viele wichtige Erfahrungen sammeln und meine Arbeiten bekannt machen konnte.

Ebenso danke ich meinen Zimmerkollegen Tobias Görler, Florian Merz und Moritz J. Püschel herzlich für die Diskussionsbereitschaft und Hilfe bei allen physikalischen und numerischen Fragen und die Durchführung einer Reihe von Gene-Simulationen, ganz besonders aber für die tolle und freundschaftliche Atmosphäre und die ungezählten Diskussionen über Politik, Gesellschaft und Glauben. Mein Dank gilt in gleicher Weise allen Mitgliedern unserer Arbeitsgruppe. Bei Moritz J. Püschel, Tobias Görler und Daniel Told bedanke ich mich außerdem für die gründliche Durchsicht von Teilen des Manuskripts, bei Klaus Reuter für die versierte Hilfe bei der endgültigen Formatierung.

Erika Strumberger und Elisabeth Schwarz danke ich für die Hilfe bei der Anwendung des Gourdon-Codes und Giovanni Tardini für die Simulation und Überlassung der Transp-Graphen.

Prof. Peter Reineker danke ich für die Übernahme der Zweitkorrektur dieser Dissertation.

Mein Dank gilt auch Prof. Sibylle Günter für ihre Unterstützung und die Verbindungen zu den experimentellen Ergebnissen, die durch sie hergestellt wurden.